Integration of short-term solar variability in the sizing and simulation of industrial microgrids

Louis Polleux

To cite this version:

Louis Polleux. Integration of short-term solar variability in the sizing and simulation of industrial microgrids. Optimization and Control [math.OC]. Université Paris sciences et lettres, 2022. English. NNT : 2022UPSLM014 . tel-04043181

HAL Id: tel-04043181
https://pastel.hal.science/tel-04043181v1

PSL
UNIVERSITÉ PARIS

THÈSE DE DOCTORAT
DE L'UNIVERSITÉ PSL

Préparée à MINES Paris-PSL

Integration of short-term solar variability in the sizing and simulation of industrial microgrids

Intégration de la variabilité de l'ensoleillement dans les méthodes de simulation et de dimensionnement des micro-réseaux industriels

Soutenue par
Louis Polleux
Le 25 mars 2022

École doctorale n°84
Sciences et technologies de l'information et de la communication

Spécialité
Contrôle, Optimisation, Prospective

Composition du jury :

Bruno François Professeur, Centrale Lille	*Président du jury*
Jan Kleissl Professeur, UCSD	*Rapporteur*
Gilles Guerassimoff Professeur, Mines Paristech	*Directeur de thèse*
Jean-Paul Marmorat Dir. de recherche, Mines Paristech	*Examinateur*
Sophie Demassey Prof. Associée, Mines Paristech	*Examinateur*
Vincent Leclere Chargé de recherche, ENPC	*Examinateur*
Sami Ghazouani Ingénieur de recherche, TotalEnergies	*Examinateur*

MINES PARIS | PSL

INTEGRATION OF SHORT-TERM SOLAR VARIABILITY IN THE SIZING AND SIMULATION OF INDUSTRIAL MICROGRIDS

POLLEUX LOUIS

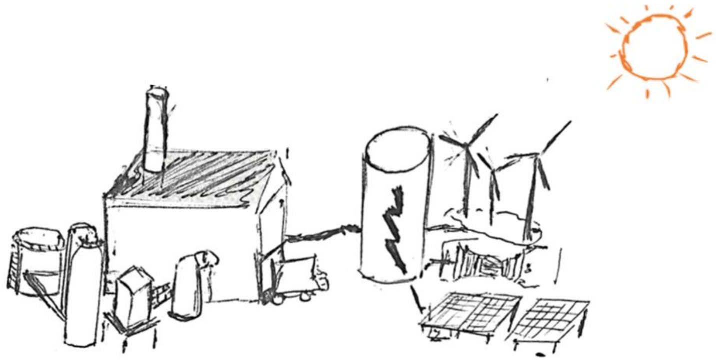

A thesis submitted for the degree of Doctor of Philosophy

Mar. 2022

Polleux Louis: *Integration of short-term solar variability in the sizing and simulation of industrial microgrids,* A thesis submitted for the degree of Doctor of Philosophy, © Mar. 2022

AVANT-PROPOS

Quel que soit son sujet, un doctorant commence par énoncer un problème et interroge la communauté sur les méthodes existantes. Vient ensuite une question existentielle : Quelle sera ma contribution ?

Avant de plonger dans la complexité d'une description mathématique abstraite, il n'est en effet pas inutile de s'interroger sur le but profond de son travail. En ces temps de changements climatiques irréversibles, l'adage de Rabelais "Science sans conscience n'est que ruine de l'âme" est plus vrai que jamais. Il pourrait même être complété par la "ruine du monde". Mais d'aucuns (et surtout les jeunes étudiants) pourraient être pétrifiés par un tel niveau de gravité.

Et si notre travail pouvait faire partie d'une contribution positive à l'humanité au lieu d'une revendication vigoureuse pour éviter la ruine et la terreur ?

Au cours de ces trois ans de thèse, seul le parallèle avec l'art m'aura donné une distance suffisante pour entrevoir une réponse. Dans son traité sur le contrepoint, Johann Joseph Fux attribue à l'art une qualité toute particulière : " il imite et perfectionne la nature, mais ne la détruit jamais". On peut trouver dans cette phrase une façon d'entreprendre la recherche scientifique avec plus de légèreté, en la mettant au service de la nature.

Ponctués par ces quelques considérations, les travaux présentés dans cette thèse résultent d'un travail de trois ans au Centre de Mathématiques Appliquées de Mines ParisTech (Université Paris Science et Lettre). Les recherches ont été menées en collaboration avec le département Recherche et Développement de TotalEnergies et financées par la bourse CIFRE (Convention industrielle de formation par la recherche) n° 2018/3264. Bien que ce travail n'adresse qu'une petite partie des enjeux climatiques, j'espère que le lecteur trouvera quelques réponses pour un futur plus harmonieux.

Pour appréhender ce document, le lecteur se référera à la table des matières générale. Des tables des matières détaillées sont ensuite disponibles au début de chaque chapitre. Les symboles mathématiques, indices et ensembles sont définis pour chaque chapitre de manière indépendante et sont listés dans des sections ad hoc.

FOREWORD

Regardless its speciality, a doctoral student shall start by stating a problem and asking the community about the lack to solve it. Then comes the existential question : what will be my contribution ?

Before diving into the complexity of an abstract mathematical description, it is indeed not useless to ask ourselves the profound aim of our work. In times of irreversible climate changes, Rabelais's adage "Science without conscience is nothing but the ruin of the soul" is more true than ever. It might even be completed by the "ruin of the world". But one (and especially young students) might be ossified by such a level of solemnity.

What if our work could be a part of a positive contribution to humankind instead of a vigorous claim to avoid ruin and terror ? A question that art is undoubtedly able to answer. Art, as referred by Johann Joseph Fux in his counterpoint treaty, "Imitates and perfects nature, but never destroys it". One might find in this sentence a lighter way of undertaking scientific research.

Such considerations has informed this work which results from the collaboration between the Center for Applied Mathematics of Mines Paristech (member of the Paris Science et Lettres University) and the R&D department of TotalEnergies. The research was funded by TotalEnergies thanks to the CIFRE (Convention industrielle de formation par la recherche) grant n° 2018/3264. Even though this scantly contributed to our world's challenges, I hope that one might find modest answers for a more sustainable and harmonious future.

When apprehending this document, the reader may refer to the general table of contents for an overview of the work and shall find a detailed table of contents at the beginning of each chapter. Mathematical symbols, indices, and sets are defined for each chapter independently and listed in ad hoc sections.

REMERCIEMENTS

Je tiens à remercier Monsieur Bruno François pour m'avoir fait l'honneur de présider le Jury de Thèse. Je remercie les rapporteurs Pr. Bruno François et Pr. Jan Kleissl pour leur lecture exigente de ce document. Je remercie également Sophie Demassey et Vincent Leclère d'avoir examiné cette thèse. Je remercie finalement l'ensemble du jury pour les échanges lors de la soutenance.

Je remercie très chaleureusement Gilles Guerassimoff pour avoir encadré ces travaux de thèse. Merci pour son soutien, ses relectures et sa confiance. Merci également à Jean-Paul Marmorat d'avoir secondé l'encadrement et d'avoir toujours su se rendre disponible.

Un grand merci à Sami Ghazouani pour avoir assuré l'encadrement industriel de cette thèse dans sa dernière année, pour les relectures attentives de ce document et ses nombreux conseils. Merci à Thierry Schuhler, pour sa confiance depuis les prémices de ce sujet, jusqu'à son départ en retraite.

Je veux remercier chaleureusement mes collègues de TotalEnergies pour leur acceuil et l'intêret qu'ils ont porté à mes travaux. Je me dois de donner une mention particulière à John Sandoval, qui a toujours eu une oreille attentive et amicale.

J'ai également une pensée pour toute l'équipe du CMA. Merci à toutes ces formidables individualités qui font de cette équipe un spécimen unique en son genre. ll existe peu de lieux où l'air se parfume d'un tel mélange de bienveillance et de génie.

A mes parents, Isabelle Etienne et Marc Polleux, je veux dire toute ma gratitude pour leur soutien indéfectible et leur bienveillance à toute épreuve. Merci de m'avoir rendu capable, confiant, heureux. Ma reconnaissance va bien au delà de ces études. Merci à ma soeur, Claire, à qui je souhaite de trouver sa voie comme j'ai trouvé la mienne.

Bien que ce mot en dise trop peu, "Merci" à Noémie, de m'accompagner chaque jour. Peu d'hommes ont la chance de trouver une telle source de courage, d'abnégation et de force au quotidien.

A tous mes amis les plus proches, merci pour votre présence chaleureuse, les encouragements sincères, les défis sportifs, les discussions idéalistes, les nuits sans fins. Ne pouvant tous vous nommer, je sais que chacun se reconnaîtera dans ces mots. Je pense à vous.

Enfin, j'achève ma thèse avec une pensée émue pour mes grands parents Christianne Decroix et Jean Etienne, dont l'histoire de vie m'inspire chaque jour. Leur générosité, leur détermination, mais aussi le souvenir de leur musique me guideront sans aucun doute dans les défis qui m'attendent.

ABSTRACT

Recent policies and markets evolutions have pushed the industry to invest in new electricity supply technologies with the aim of reducing its environmental footprint. In developing countries with unreliable grids or large off-grid areas, industrial facilities rely on on-site fossil generation. For economic and safety reasons, the electricity supply follows strict reliability specifications in terms of power plant availability and power quality. The integration of a large-scale solar power plant in off-grid industrial power systems brings new challenges related to the short-term variability. If fossil generators cannot quickly compensate for the solar power drops, a fast-responding storage system must take over to guarantee electrical stability. Therefore, the long-term planning of industrial microgrids must now integrate the relationship between renewable penetration, short-term variability, and power quality which alters the techno-economic optimization paradigm.

The objective of this thesis is to integrate the short term solar-photovoltaic (PV) variability in the performance evaluation of optimal management strategies and in the sizing optimization process of off-grid industrial power systems.

After a general introduction (Chapter 1), the concept of industrial micro-grid is defined and the main research challenges for solar power integration are presented in Chapter 2. In Chapter 3, the modeling and characterization of large-scale solar power plant variability are investigated. A methodology is proposed to identify solar irradiance profiles among a year long dataset allowing fast grid simulations. In Chapter 4, a simulation framework is proposed to evaluate the operability and economical performances of an industrial micro-grid. An energy management optimization layer is coupled with a dynamic electrical model to reproduce the behavior of the power plant and evaluate grid frequency deviations, fuel consumption, and CO2 emissions. Finally, the process of optimal and robust sizing of a solar-powered industrial microgrid is developed in Chapter 5. First, a preliminary optimization technique is presented to evaluate the optimal size of the PV and storage system while ensuring resiliency over cloud passage. The mathematical formulation embeds linear frequency constraints and worst-case ramp scenarios. Then, the optimal solution found at the first step is assessed by the operational simulator developed in Chapter 4 to verify the operability of the architecture and refine the size of the storage system. The power generation of a liquefied natural gas processing plant is used as a case study and illustrates the ability of the method to provide optimal and robust sizing of the hybrid architecture.

RÉSUMÉ

Les récentes politiques climatiques et l'évolution des marchés ont conduit le secteur industriel à investir dans de nouvelles technologies de production d'électricité dans le but de réduire son empreinte environnementale. Dans les pays en développement ne disposant pas d'un accès fiable à l'electricité ou possédant de large zones sans réseau, les sites industriels produisent leur propre électricité. Par ailleurs, la production d'électricité est soumise à des spécifications strictes en termes de continuité d'approvisionnement et de qualité de courant pour des raisons de sécurité industrielle. Dans ce contexte, les centrales solaires photovoltaiques de grande puissance amènent de nouveaux défis lié à la gestion de leur intermittence. Lors des passages nuageux, les variations de l'ensoleillement doivent être compensées par les générateurs fossiles ou par un système de stockage rapide pour garantir la stabilité électrique. La planification long-terme des microréseaux industriels doit donc intégrer les liens entre la variabilité de l'ensoleillement et la qualité d'approvisionnement ce qui modifie le paradigme d'optimisation technico-économique.

L'objectif de cette thèse est d'intégrer la variabilité court terme de l'ensoleillement dans les processus de simulation des stratégies de gestion optimales et d'optimisation du dimensionnement de centrales électriques industrielles hors-réseau.

Après une introduction générale (Chapitre 1), le concept de microréseau industriel et ses principales problématiques de recherche sont détaillés dans le Chapitre 2. Le Chapitre 3 explore la caractérisation et la modélisation de la variabilité de l'ensoleillement. Des profils d'ensoleillement tenant compte de la variabilité court terme sont identifiés à partir d'un jeu de données annuel pour simplifier les simulations électriques. Le Chapitre 4 présente un cadre de simulation pour évaluer les performances opérationnelles d'une centrale électrique hybride. Une couche d'optimisation de la gestion de l'énergie est couplée à un modèle électrique dynamique afin d'évaluer les écarts de fréquence sur le réseau, la consommation de carburant et les émissions de CO_2. Enfin, une méthode de dimensionnement est proposée dans le Chapitre 5. Une optimisation préliminaire est réalisée pour évaluer les investissement optimaux du couple photovoltaique-stockage tout en garantissant la stabilité électrique lors de perte d'ensoleillement. Le simulateur opérationnel présenté dans le Chapitre 4 est ensuite utilisé pour vérifier l'opérabilité de l'architecture et raffiner la taille du système de stockage. Une usine de liquéfaction de gaz est utilisée comme cas d'étude pour illustrer le potentiel de la méthode.

PUBLICATIONS

PUBLICATIONS IN SCIENTIFIC JOURNALS

L.Polleux, T. Schuhler, G. Guerassimoff, JP. Marmorat, J. Sandoval-Moreno, S. Ghazouani. "On the relationship between battery power capacity sizing and solar variability scenarios for industrial off-grid power plants" In: *Applied Energy* 302 (Nov. 2021), p. 117–553.

L.Polleux, G. Guerassimoff, JP. Marmorat, J. Sandoval-Moreno, T. Schuhler. "An overview of the challenges of solar power integration in isolated industrial microgrids with reliability constraints." In: *Renewable and Sustainable Energy Reviews* 155 (March. 2022) p.111-955.

Submitted:

E. Fernando Alves, L. Polleux, M. Korpås, E. Tedeschi, G. Guerassimoff. "Allocation of spinning reserves in autonomous grids considering frequency stability constraints and short-term solar power variations." Submitted in January 2023 to *IEEE Access*.

PUBLICATIONS IN CONFERENCES

L Polleux, J. Sandoval-Moreno, G. Guerassimoff, and JP. Marmorat. "Impact of thermal generation flexibility on power quality and LCOE of industrial off-grid power plants." In: *11th International Conference on Applied Energy (ICAE2019).* Västeraas, Sweden (Aug. 2019).

L. Polleux, T. Schuhler, G. Guerassimoff, JP. Marmorat, and J. Sandoval-Moreno. "Increasing the accuracy of PV plants and power system dynamic models: a comparison of benefits for battery capacity sizing." In: *12th International Conference on Applied Energy (ICAE2020).* Bangkok, Thailand, (Dec. 2020).

L. Polleux, S. Ghazouani, G. Guerassimoff, JP. Marmorat. "Optimal and robust sizing of industrial solar powered microgrids with cloud passage resiliency constraints." In: *Congrès annuel de la Société Française de Recherche Opérationnelle et d'Aide à la Décision (ROADEF 2022).* Lyon, France, (Feb. 2022).

PATENT CLAIMS

L. Polleux, S. Ghazouani, J. Sandoval-Moreno, G. Guerassimoff, JP. Marmorat. "Multi-layer simulation of isolated industrial hybrid power plants." European patent claim n°EP22305193.9 applied on February 22, 2022.

CONTENTS

ACRONYMS

API	Application Programming Interface
ASAI	Average Service Availability Index
ASUI	Average Service Unavailability Index
CAIDI	Customer Average Interruption Duration Index
CAPEX	Capital Expenditures
CCGT	Combined cycle gas turbine
CFD	Computational fluid dynamics
DC	Direct Current
EENS	Expected Energy Not Supplied
EMS	Energy management system
ESS	Energy Storage System
FCUC	Frequency Constrained Unit Commitment
GE	Gas Engines
GHG	Greenhouse gases
GHI	Global horizontal irradiance
GT	Gas turbine
HIL	Hardware in the loop
ICE	Internal combustion engine
IEA	International energy agency
ISO	International Organization for Standardization
LCOE	Levelized costs of electricity
LNG	Liquefied natural gas
LP	Linear programming
MG	Microgrid
MILP	Mixed integer linear programming
MPC	Model Predictive control
NREL	National Renewable Energy Laboratory
O&G	Oil and gas
O&M	Operation and maintenance
OPEX	Operational expenditures

PID	Proportional Integral Derivative
PTONRR	Percentage of time over normal ramp rate
PV	Photovoltaic
R&D	Research and development
RDA	Ramp detection algorithm
TFD	Time of frequency disturbances
TONRR	Time over normal ramp-rate
TSO	Transmission system operator
VIGV	Variable inlet guide vane
WVM	Wavelet variability model

1

GENERAL INTRODUCTION

Thanks to growing environmental policies, the industrial sector is more and more committed to reducing its greenhouse gases emissions. When no utility grid is available, industrial facilities rely on on-site generation to power their processes. In many industrial sectors such as upstream and downstream Oil&Gas, chemical or mining industries, the continuity of electricity supply is a priority for operators for both economical and safety reasons. This explains the wide use of fossil fuels for electricity generation as conventional generators have a high level of reliability. However, this contradicts sustainable industrial development.

Integration of renewable electricity is a promising lever to reduce carbon emissions. In particular, solar photovoltaic (PV) generators have now reached a low break-even point which leads the industry to explore hybrid power plants solutions (or microgrids) featuring fossil generators and large-scale solar systems. On the other hand, the variability of solar resources puts the continuity of electricity supply at risk. Short-term solar variations can cause a temporary mismatch between production and consumption leading to large electrical instabilities and a loss of electricity supply. To mitigate electrical perturbations, storage systems can be installed but come at high costs which reduce the profitability of the system.

Therein lies the problem of autonomous industrial hybrid power plant development: improve the environmental footprint of electricity production with the best economical performances while guaranteeing the reliability of electricity supply against solar power short-term variations.

The motivation of this thesis is to provide methods helping industrial architects with the preliminary assessment process of such systems. Operational philosophy for the optimal management of PV power and fossil generators must be investigated to evaluate the costs, CO_2 emissions, and electrical stability of the system over its lifetime. In addition, an integrated sizing method is necessary to provide a robust and optimal solution for the installed capacities of PV and primary support storage systems. To properly assist industrial developers, the development of numerical tools and methods shall be adapted to preliminary technical studies : (1) most of the technical inputs such as grid topology or PV and fossil unit technology characteristics are not available at this step; (2) the computational complexity should be kept minimal to allow screening a wide range of solutions in a limited amount of time with standard computational resources.

Lots of highly detailed electrical models are available to evaluate electrical stability of micro grids but only a few of them provide a focus on the impact of short-term solar variability and combine PV systems with large scale fossil generators. In particular, ramping constraints on fossil generation is generally not considered. Detailed electrical models require complex technological blocks with many input parameters and require large computational resources to simulate large time windows such as daily irradiance timeseries.

The majority of these models are focused on electrical stability whereas economical and environmental performances evaluation of the plant is separately carried out by high level energy models. This may lead to discrepancies between short-term and hourly level behaviour.

Sizing tools currently available are based on high level energy models with a 15 minutes to 1h time-decompositions. Consequently, electrical stability problems are not considered. Alternatively, non-linear optimization and meta-heuristics have been proposed to address the grid stability in case of a generator contingency or wind power variations. The literature highlights the interest of Mixed Integer Linear Programming (MILP) formulations to avoid convergence to local optimum but only a few work ave addressed grid resiliency in a linear optimization framework. Regardless of the sizing optimization technique, the grid resiliency to short term solar variability remains poorly covered.

Bearing in mind the state-of the art methods, this thesis contributes to the research field on industrial micro-grid development in the following manners:

1. A pre-treatment procedure for 1-second solar irradiance time series is proposed to reduce the number of solar input scenario to consider in grid simulations. The method applies the Wavelet-Variability-Model to simulate a MW-scale equivalent irradiance and uses Kmeans clustering to obtain a set of representative time series.

2. A methodology to identify worst-case solar ramps is proposed to perform fast grid simulation and integrate solar ramps in high-level energy model. The methodology is based on a ramp-detection algorithm and a convex-hull representation of linear solar drops.

3. A multi-layer simulation framework is developed to simultaneously consider power quality control and energy management optimization. The short term model is based on a reduction of detailed electrical models to improve its computational performances and is adapted for better consideration of gas turbines physical limitations. The energy management optimization

model reproduces the planning strategy of an industrial power plant.

4. The use of a reduced set of solar irradiation time series composed of representative days and a worst-case scenario allows the multi-layer simulation to provide an evaluation of the lifetime performances of the power plant as well as the minimum required storage installed capacity to ensure electrical stability.

5. A MILP optimization model is formulated to provide optimal and robust sizing of PV and storage installed capacities. The model ensure the plant's resiliency to fossil generators contingencies thanks to redundancy constraints. The resiliency against fast-cloud passage is ensured thanks to linear frequency deviations constraints and solar ramp convex hulls previously identified.

6. All these tools are assembled into a sizing procedure which provides validated architecture to power plants architects. The MILP sizing model is used is as a preliminary optimization step for fast screening of potential solutions. Then, the selected architectures are evaluated thanks to the multi-layer simulation to provide refined storage requirement and lifetime performances.

The contributions mentioned above are developed throughout this document as follows:

- Chapter 2 provides an overview of the challenges and state-of the art research on industrial micro-grids and highlights the main knowledge gaps.

- The methodology for solar irradiance time series pre-processing and scenario generation is developed in Chapter 3.

- The multi-layer simulation framework for operational simulation is detailed in Chapter 4 after a description of electrical and energy management models.

- In Chapter 5, the sizing optimization model is formulated and discussed. Then, the full sizing process is presented and applied to a case study aiming at sizing the PV and storage capacities for the power generation of a Liquefied Natural Gas (LNG) processing plant.

- Conclusions are drawn in Chapter 6 as well as recommendations for industrial microgrids development and future research.

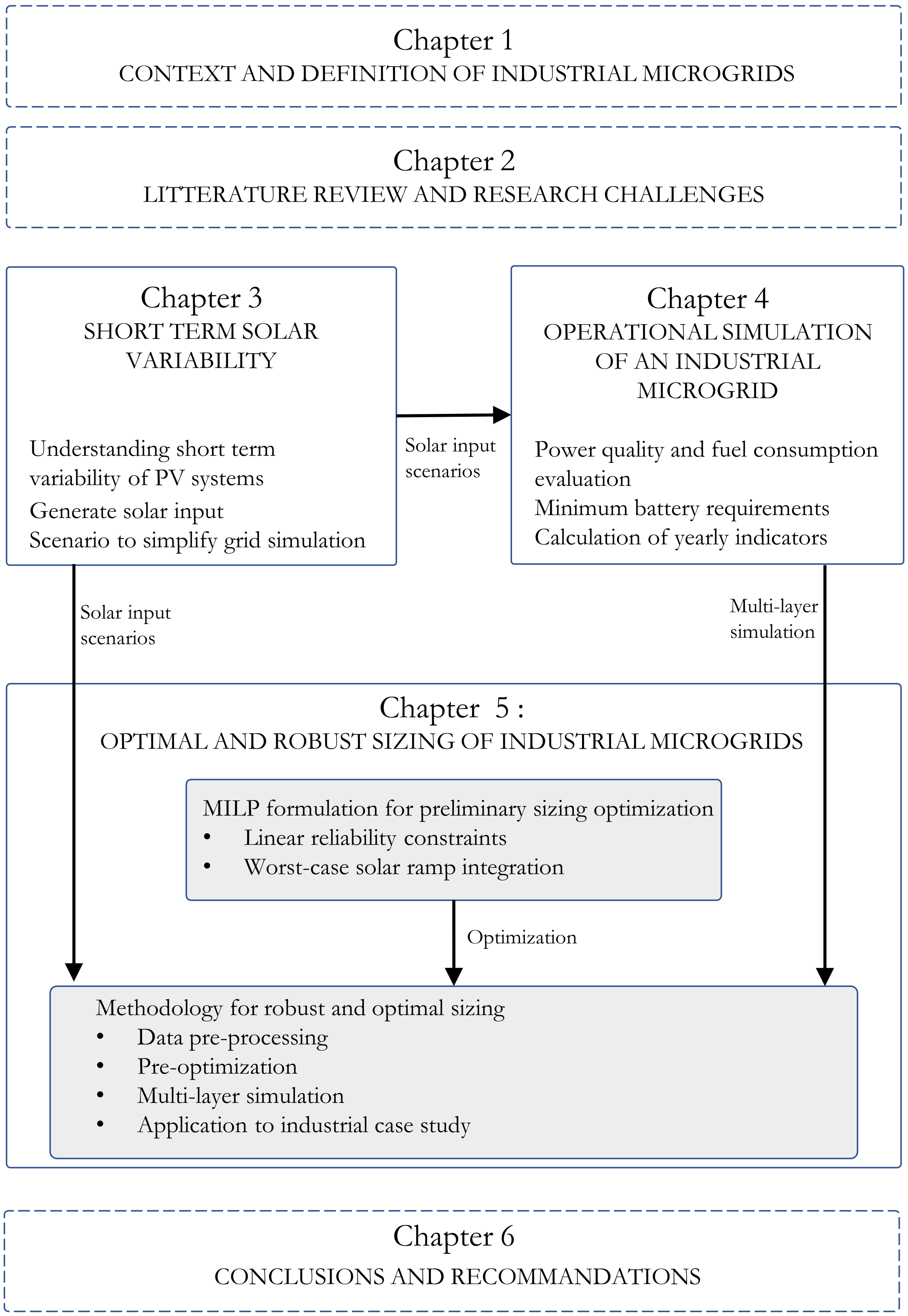
Chapter 1
CONTEXT AND DEFINITION OF INDUSTRIAL MICROGRIDS
Chapter 2
LITTERATURE REVIEW AND RESEARCH CHALLENGES
Chapter 3
SHORT TERM SOLAR VARIABILITY
Understanding short term variability of PV systems
Generate solar input
Scenario to simplify grid simulation
Solar input scenarios
Chapter 4
OPERATIONAL SIMULATION OF AN INDUSTRIAL MICROGRID
Power quality and fuel consumption evaluation
Minimum battery requirements
Calculation of yearly indicators
Solar input scenarios
Multi-layer simulation
Chapter 5 :
OPTIMAL AND ROBUST SIZING OF INDUSTRIAL MICROGRIDS
MILP formulation for preliminary sizing optimization
• Linear reliability constraints
• Worst-case solar ramp integration
Optimization
Methodology for robust and optimal sizing
• Data pre-processing
• Pre-optimization
• Multi-layer simulation
• Application to industrial case study
Chapter 6
CONCLUSIONS AND RECOMMANDATIONS

2

SOLAR POWERED INDUSTRIAL MICROGRIDS

This chapter defines the concept of industrial microgrids and reviews existing applications. The challenges of dynamical modeling of fossil generation and PV systems are presented and state-of-the-art relevant power control and energy management strategies are set out. This work has been published in Elservier's Renewable and Sustainable Energy Reviews [1].

Ce chapitre définit le concept de micro-réseaux industriels à partir d'une revue les applications existantes. Les défis principaux liés à la modélisation dynamique des générateurs fossiles photovoltaïques sont présentés. L'état de l'art des stratégies de contrôle et de gestion de l'énergie est finalement exposé. Ce travail a été publié dans la revue scientifique Renewable and Sustainable Energy Reviews [1].

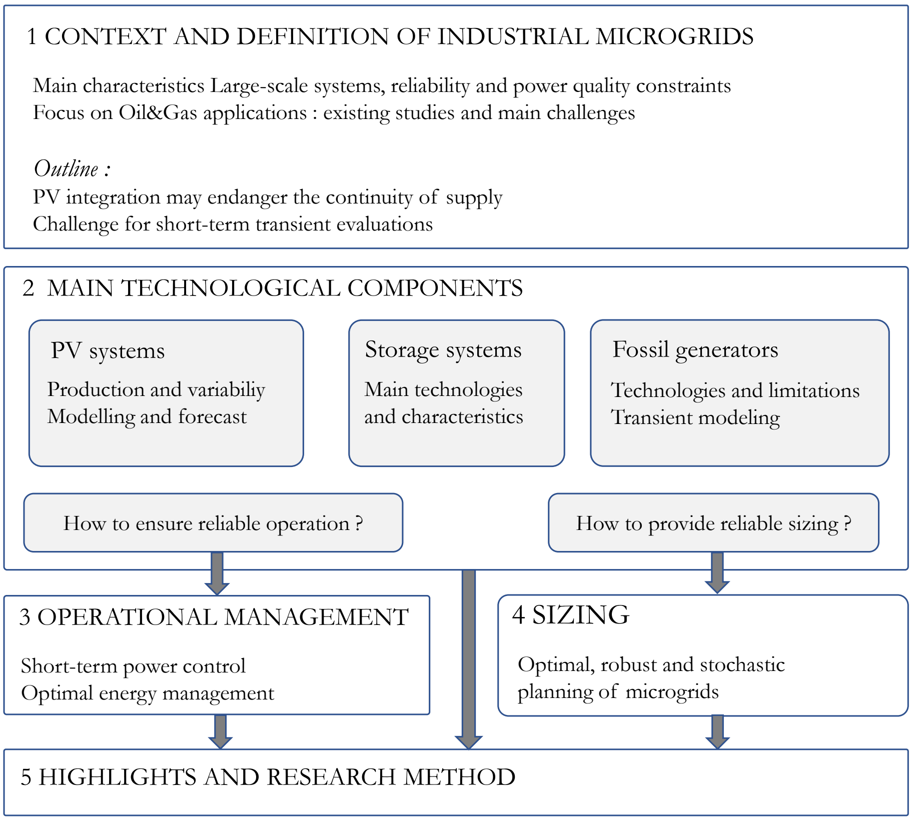

Contents

2.1 THE CONCEPT OF INDUSTRIAL MICROGRID

2.1.1 *General context*

In 2019, the General assembly of the United Nations (UN) stated that "eradicating poverty in all its forms and dimensions, [. . .] is the greatest global challenge and an indispensable requirement for sustainable development" [2]. Meanwhile, the majority of the representatives of the states and governments, enlightened by the IPCC (International panel on climate change) and IPBES (The Intergovernmental Science-Policy Platform on Biodiversity and Ecosystem Services), agree on the increasing danger of climate change and its effects on lands, ocean, biodiversity and populations. At the COP25, The IPCC executive secretary Espinosa stated that meeting our CO2 reduction objectives is "absolutely necessary to the health, safety and security of everyone on this planet—both in the short- and long-term" [3].

At the beginning of the 2020 decade, these two major challenges pile up together and bring the world a double issue to solve as quickly as possible. Among all the dimensions of these problems, the role of energy is of major interest as it is the link between climate and growth.

On one hand, the access to energy – and more specifically electricity - is a key lever for poverty alleviation and socio-economic development.

Electricity access is necessary to satisfy the basic needs of populations and improve their well-being. It is crucial for clean and safe cooking, health infrastructures and scholar development which is why the UN's development program has included 'access to electricity' to its "Multidimensional Poverty Index" [4]. Recently, the IEA warned that the covid-19 crisis reversed electricity access progress and highlighted the need to put it at the core of recovery plans and development programs [5].

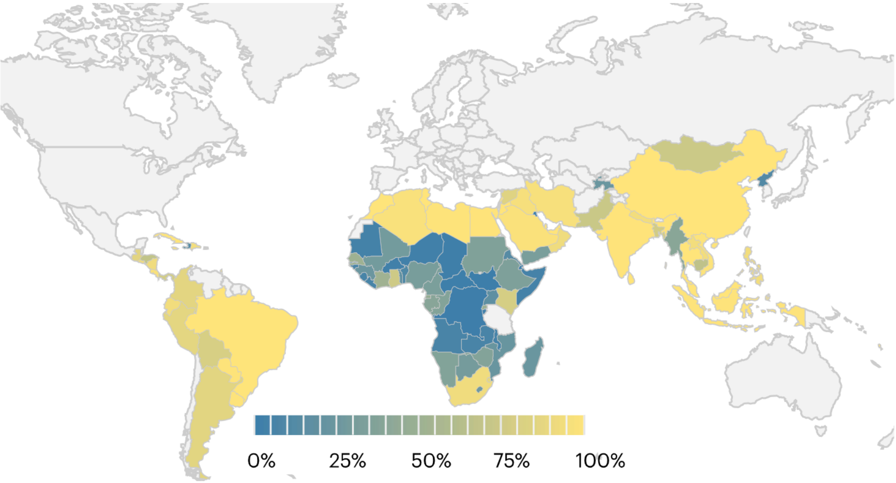

Figure 2.1: Proportion of population with access to electricity [5].

In a macro-economic perspective, electricity access turns out to be necessary to increase productivity, allow industrial development and living standards improvements [6]. An unreliable supply due to insufficient grid infrastructure is a strong barrier to industrial activities [7]. The case of the Indian manufacturing sector is a good illustration as electricity shortage could have reduced its revenue by 5.6% [8]. The relative low price of fossil fuels and their ability to provide electricity continuously explains the choice of the developing countries in their energy mix: 80% of their electricity is produced by coal, oil or gas in Africa and India.

On the other hand, energy production is the main contributor to the global warming. Coal, gas and oil are widely employed and respectively account for 39%, 23% and 3% of the world's electricity production whereas their CO2 emission represents 32.5 MTCO2 [9]. Despite the current carbon footprint of electricity production, 1.3 billion of people still have unsecured access to it and 95% of them live either in sub-Saharan area or in Asia. Between 1890 and 2018, only 2% of GHG was due to activities within the African continent [10]. The coming rise of the African economy could bring millions of people out of poverty, yet, fail to meet the environmental constraint if the same trajectory as the past is taken.

An affordable and reliable energy supply is an absolute necessity to the socio-economic development of billions of people. But the struggle will remain useless if clean solutions are not developed to limit the negative environmental impact as much as possible.

2.1.2 *The role of microgrids for clean electricity supply*

Policies and investments for bringing access to electricity follow two main strategies: grid extension and local energy systems development. Grid extension consists in extending the utility grid by investing in new production units and transmission lines across a country, but this solution requires a lot of capital expenditures. The costs, risks and technical challenges crossing wide desertic areas is a strong barrier to a fully grid-connected future. Local energy systems offer more flexibility to policymakers and investors. They consists in small stand-alone systems such as solar kits or autonomous grids with proper control which are called micro-grid or mini-grid [11].

The microgrid definition of the US Department of Energy is "a group of interconnected loads and distributed energy resources within clearly defined electrical boundaries that acts as a single controllable entity with respect to the grid. A microgrid can connect and disconnect from the grid to enable it to operate in both grid-connected and island-mode".

Microgrid can have an interesting capacity of adaptability as they can serve small load such as a few houses to an entire city or industrial facility. Their capacity to operate either disconnected or connected to the grid is also a promising feature, allowing policymakers to create electricity clusters before considering large interconnection. It also allows securing critical parts of existing grids such as hospitals, universities, state services etc.

The IEA 2019 outlook for Africa sees that microgrids will be a key stakeholder for electricity supply and could account for 30% of the electricity access by 2030 [10]. A review of regulatory framework and policies with regards to microgrid development in 8 countries covering 3 continents such as India, Tanzania or Peru can be found in [12].

2.1.3 *General background on microgrids*

One of the main advantages of microgrids is undoubtably their ability to manage renewable energy resource as well as storage and conventional fossil generation to ensure the right trade-off between costs, reliability and sustainability. Microgrid now covers a wide variety of use from grid connected systems able to sell and buy electricity depending on market price, to robust and isolated systems ensuring continuous power for mining or military facilities [13, 14]. This is illustrated in Fig. 2.2 which displays the University of California San Diego's microgrid.

Figure 2.2: University of California San-Diego's microgrid.

Energy expenses represent a substantial share of capital and operational expenditures. Thus, the performance of the power plant must be ensured and optimized with care. Regardless of the size and use of microgrid, the planning and operation share three fundamental objectives with conventional utility grids [15]:

1. Providing the electricity at the lowest cost possible
2. Ensure the safe supply of electricity to deliver all the consumers at the required time
3. Guarantee the quality of supply at delivery point

Finally, microgrids are more and more developed and operated with the aim of reducing the CO2 footprint.

The performance of the microgrid can be defined as the ability of the plant to achieve these goals. The most important goal according to the user's specifications forms the objective function of an optimization problem. The others build the set of constraints that the plant must satisfy while tracking the maximum or minimum value of the objective.

This optimization paradigm is the cornerstone of the microgrid's performance from the early developments to the plant's real-time management. Therefore, it needs to handle phenomemnon that take place at various time-scales:

- The long-term planning (or sizing) of the micro-grid is carried at development steps and aims at finding the optimal architecture in order to optimize the plant in the long run (typically 20 years)
- The energy management aims at balancing energy flux between the producers and the consumers. Different strategies may be used to minimize the costs under constraints of reliability or environmental footprint. This is carried within typical intervals of 10 minutes to several days.
- The control of power ensures a good quality of supply and a safe operation. It shall prevent large fluctuation and instabilities by balancing the power flows in real time. This is generally assessed with a timescale from a few milliseconds to seconds.

Figure 2.3 shows these different time scales for the main actors and phenomenon taking place during the microgrid's lifetime.

Due to the relative small size of hybrid power plants compared to utility grids, their sensitivity to power fluctuations is significantly increased and developers now have to account for power dynamics, flexibility and uncertainties of production.

From an operational point of view, interaction between time-scales and devices clearly appears. The management layer is distinguished from the control layer by the timescale and the hardware connection to devices. The management layer is generally ensured by one or several EMS (Energy Management System) for the whole plant based on communication technologies or even cloud technologies. In the

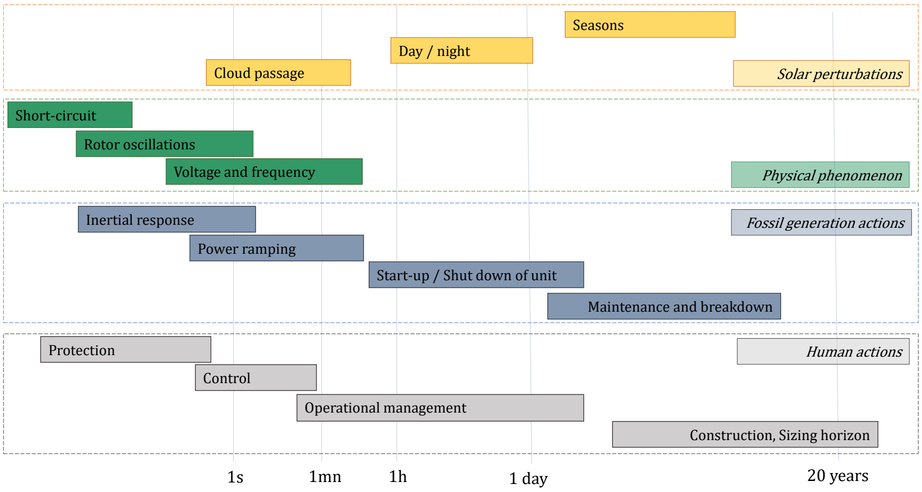

Figure 2.3: Different time-scales for planning and operations.

contrary, the control layer is carried out by the PMS (Power Management System) which adjust the output of each device based on local measurements in order to instantly correct instabilities and protect the equipment [16]. Fig. 2.4 shows an overview of the interreaciton between the control and management layer, additional operational strategies are presented in detail in [13, 14] and will be furtherly reviewed in this chapter.

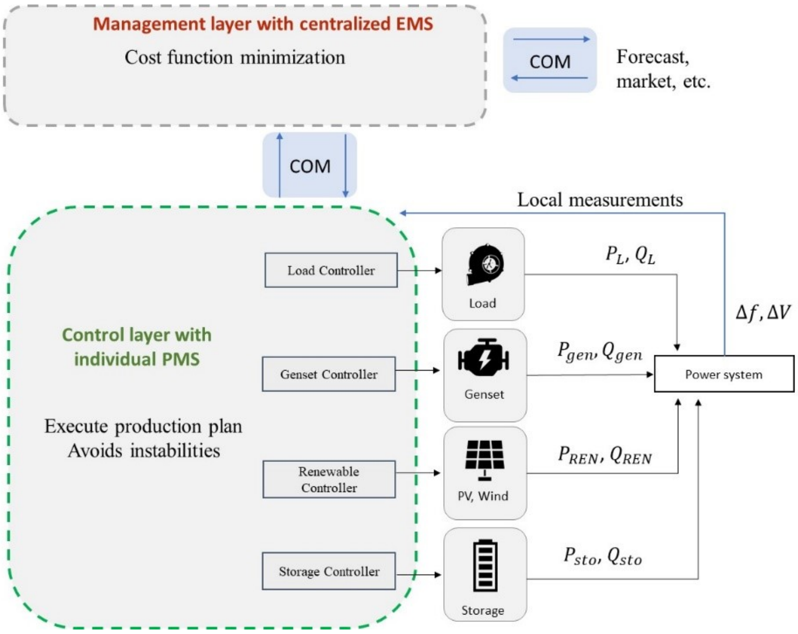

Figure 2.4: Interconnection of management and control layer of an autonomous microgrid.

Lots of running project can be found such as the island of Eigg in Scotland which is an isolated hydro-wind-solar powered grid backed-up by diesel generators [17] or the campus of San Diego's university which smartly interconnects the grid to a portfolio of gas and steam turbines, solar PV and thermal storage [18]. Recent work has also been done on isolated offshore sites for commercial of residential applications [19]. However, lots of research are still carried to optimize the architectures, find the best operational strategies and identify the proper protection schemes depending on needs and constraints [20–22].

Technological choices may differ from one case to another such as commercial, residential, military or industrial plants. In addition, availability of resources (gas, diesel, solar, wind etc.) may vary. Hence, sizing methodologies and operational strategy must adapt to a wide bench of scenarios. Unlike for commercial and residential applications, the literature poorly covers industrial microgrids [20, 21].Therefore, the next part will try to identify the particularities of industrial power system in order to understand the research challenges.

2.1.4 *Industrial microgrids : motivation, definition and examples*

In 2016, the industry sector accounted for 36% of the global CO2 emissions mainly due to its high energy-intensive processes [23]. In order to match with the COP 21's 2° objective, a substantial effort has to be made to improve the energy efficiency and reduce the carbon footprint. As mentioned above, the challenge is not solely to reduce the impact of current activities, but also to prevent the emerging industries from cumulating their emission to the ones that have caused global warming.

From the IEA again, it is highlighted that the industry GHG reduction will be enhanced by three main levers [24]: the minimization of the processes energy demand, powering facilities with low-carbon electricity, and finally the integration of CCS (Carbon Capture and Storage) .

The reduction of energy use by industrial processes is without a doubt, the first action to consider as it enables operational costs and CO2 savings. Consumption monitoring, process optimization and heat and cold recycling are among the most famous solutions as they don't usually require large investment. However, the potential in energy saving always meet thermodynamic, feasibility, and costs limitations. CCS has also shown promising potential to reduce the emissions. Nevertheless, some facilities will not be able to implement it because of the lack of a nearly located CO2 storage capacity or because of insufficient carbon intensity processes.

Process electrification offers an alternative way for achieving the industry's CO2 ambitions. One example consists in converting compressor and pump drivers powered by fossil engines into electric drivers meanwhile powering the facility by a less carbon intensive electricity. But this does not come without challenges.

For most of large-scale industrial plants, reliability is a key factor. The potential penalties resulting from a failure of the power supply are much larger than potential energy savings. Facilities located in developed countries can substantially reduce their GHG emissions using green electricity purchase agreements. The facility will then benefit from the renewable production located sometimes miles away. However, there is numerous applications where the plant is connected either to an unreliable grid or totally isolated from it. In these applications, microgrid will play a key role: GHG reduction thanks to renewables must be handled by on-site autonomous power plants with the highest level of reliability.

2.1.4.1 *A conceptual definition*

It is very hard to find a proper definition of industrial microgrids since needs, size and resources may substantially differ from one case to another. Based on a review of existing projects, studies and industrial surveys, it is possible to propose some general characteristics:

- Size: The installed power capacity or total load served generally excesses several hundreds of kW and often reach several MW

- Type of consumers: Consumers are mainly industrial equipment such as electric drivers for torque production, pumping, compression. The proportion of resistive load is slightly lower than residential microgrid resulting in specific electrical characteristics. The daily profile follows the production schedule and therefore significantly varies from a residential and tertiary load profile (traditionally two peaks in the morning and the evening, high temperature sensitivity due to heating and chilling and high degree of stochasticity).

- Ownership and operation: Generating units and transmission system within the industrial microgrid can be financed, owned and operated by different entities but assets are rarely separated or managed individually. Consuming equipment are considered as a single client. The microgrid management only serve the industrial production schedule, the concept of multi-user decentralized scheme is therefore not fully relevant compared to a centralized decision scheme

An additional key dimension that characterizes industrial microgrids is the need for reliability and a continuous power supply in order to keep the production chain running. If the facility is connected to a

Reference	[25]	[26]	[27]	[28]	[29]	[30]
Application	Mining	Offshore oil	Industry	Industry	Water treatment	Manufacturing
Energy	Electricity	Electricity	Heat Electricity	Electricity	Electricity	Electricity
Power	26MW	40MW	14MW	MW scale	3.2MW	20-40 MW
On grid off grid	Off-grid	Off-grid	On-grid	Not specified	On grid	On grid
Renewable resource	Solar	Wind		Wind – Solar	Wind Solar	Wind Solar
Fossil generation	Diesel	CCGT2	Not specified	Diesel	Diesel	-
Comment	Installed plant	Study	Study	Study	Study	Study

Table 2.1: Examples of studies and projects focusing on industrial microgrids.

stable grid, the continuity of supply is ensured by the transmission system operator. However, both in weak-grid (subject to outages) and off-grid configurations, the continuity of supply relies only on the self-producing capacity of the plant [31, 32].

The reliability challenges of integrating more and more renewable resources into large-scale systems have been covered by island microgrid studies [33] such as those performed for the islands of La Réunion [34, 35]. The stochastic variation of renewable resources endangers the continuity of supply and the power quality and therefore limits the penetration of renewables [36, 37].

This shows that reliability concerns should not be neglected in large industrial off-grid systems. However, the literature only scantly covers this aspect of industrial microgrids, despite the fact that it remains critical for their long-term development [38, 39]. This chapter intends to identify the challenges involved in ensuring reliability in these applications.

2.1.4.2 *Reliability as watchword*

It is needless to that that the continuity of electricity supply is a matter of profitability but it is even more a matter of safety. Industrial facilities (refineries, LNG production plants and terminals, Oil rigs, Chemical units etc.) feature lots of processes where gas and liquid must stay at a defined pressure. Leakage in pipes, tanks or reactors may cause hazardous situations since products may be highly flammable. In the case of a partial loss of the electricity supply, some critical safety equipment may remain connected (fluid recirculation circuits, heating or coolant systems to avoid phase change, etc.) but some products are automatic send to the flaring system, causing air pollution such as SO_2 or H_2S emissions. This is confirmed in lots of accident reports [40], which proves how much the power system must be resilient and carefully designed.

The availability of power system refers to the proportion of the time during which the plant is able to supply its consumers. In a power system, a loss of the electricity supply may be caused by several reasons:

- Generator contingencies : fossil generator breakdown causes a sudden loss of the electricity supply. It is a common practice to operate in "N+1" philosophy, meaning that an additional unit is running to compensate the sudden loss of another unit. In some situations the plant may run in "N" configuration, which means that the system cannot supply the load in case of a loss of a running unit.

- Unplanned load step: if large consumers are suddenly connected to the system, fossil unit will have to rapidly change their power output. This may cause a disconnection of fossil units in the case of large shaft deceleration or turbine over-heating.

- Unplanned load rejection : Load rejection may happen in the case of a consummer breakdown (heater, pump, motor) or sudden disconnection for safety reasons. This causes an acceleration of the generator mechanical shaft. If the speed reaches the upper-limit, the unit can disconnect to prevent over-speed.

- Cascade of generator disconnection : In some severe situations, one of the three above mentioned situations may cause other disconnections of generating units. This can lead to a complete loss of the electricity supply (i.e blackout)

- To prevent a cascade of disconnection, operator may stop some processes to maintain the power balance of the system. These procedures are called "load shedding procedures".

To ensure a power plant's highest availability, the mean time between failures of power suppliers and the mean time to recover normal operation must be evaluated [41]. The availability (Eq. 2.1) of the power system is tracked thanks to the MTBF (mean time between failure) and MTTR (mean time to repair) which are linked to the probability of generators and consumer breakdown, maintenance schedule etc.

$$Availability = \frac{\mathrm{MTBF}}{\mathrm{MTBF} + \mathrm{MTTR}} \tag{2.1}$$

One part of the problem consists in optimizing the maintenance planning of each power device. However, unplanned events, measured by the failure rate of equipment (probability of unexpected loss), need to be minimized. In conventional fossil-based systems, the major risk is fossil generator breakdown, but the integration of PV systems introduces new parameters into the reliability assessment:

- Risk of equipment failure in the PV power plant (PV strings, inverters)

- Loss of transmission system (lines and converters) between the main bus and the PV plant.

Additionally, PV power fluctuations due to cloud passage can cause considerable power quality fluctuations that have the same impact as a loss of equipment. This new aspect in the reliability assessment is related to the site's weather conditions, the installed PV and storage capacities and the fossil generation ramp-rate.

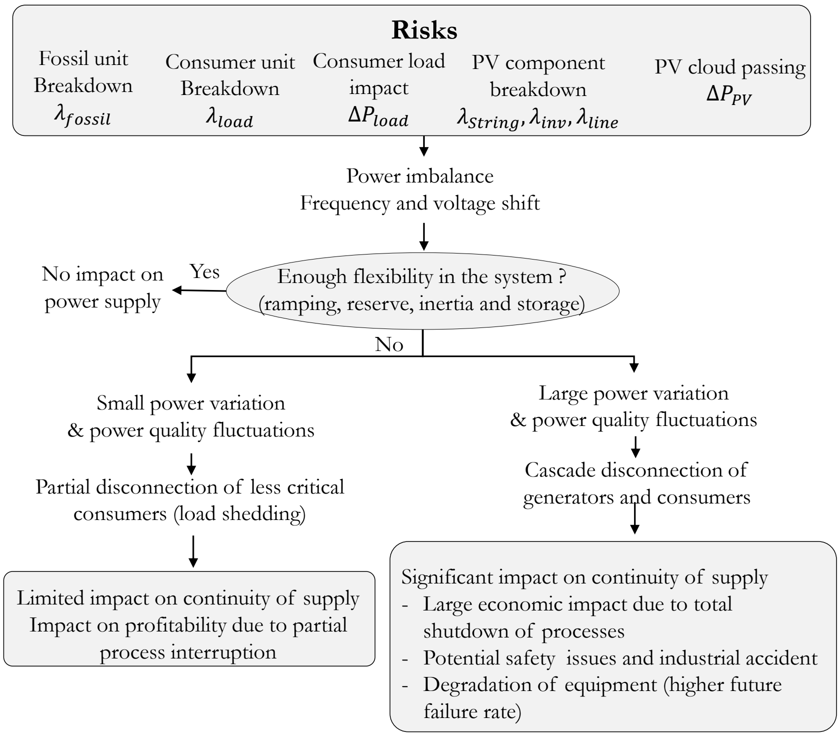

Figure 2.5: Summary of reliability aspects of industrial microgrids from risks to consequences. λ refers to the failure rate (see [42]) and ΔP refers to the probability of power variation in the equipment.

2.1.4.3 *The example of O&G power systems*

A focus on oil and gas applications (O&G) offers a wide variety of examples for industrial microgrids since O&G has used on-site isolated electrical generation for decades. Many operating facilities, studies and future projects can provide useful feedback on experience, operational data, and even methodological insights. Some of the challenges of producing electricity in this sector are shared with numerous other applications, such as hospitals, military facilities, high-tech manufacturing, and even highly sensitive urban areas.

The LNG facility of Ichtys LNG (Austrailia) is an example of a large scale autonomous power plant as it is fully autonomous from the national grid an entirely rely on gas turbines for its electricity generation (about 200MW of installed capacity).

Figure 2.6: The Ichtys LNG terminal (Australia) operated by TotalEnergies.

SPECIFICITIES OF O&G ARCHITECTURES AND OPERATIONS

From internal survey of applications in TotalEnergies main upstream O&G facilities, the following specificities have been identified are are added up to previous industrial characteristics:

- Isolated location: O&G rigs are often located in isolated areas or in developing countries with a poorly reliable grid. The facility can be located either onshore or offshore.
- Low fuel price: As the fuel is available on-site and sometimes not even valued for business (for example natural gas in an oil field), its financial value is very low.
- Proportion of torque, electricity and thermal demand: excepted for refineries which consumes more heat than electricity, O&G facilities almost only uses torque and electricity.
- Reliability and quality specifications: O&G developers have developed dedicated specification for their electrical systems. The production plant needs to be 99.9% available and tight limitation are set for frequency and voltage fluctuations.
- Low load flexibility: For safety and economic reasons, the demand must be met at all time and no shift in load can occur during the day due to unavailability of renewable resources.
- Fossil generation to ensure continuous power: the architecture feature gas turbine or internal combustion engines with a redundancy operational philosophy to prevent generator loss from causing a system failure.

Power quality specification play an important role in the reliability assessment of the power plant. When frequency and voltage limitations are met, operators must trigger load shedding procedures to

Load Acceptance	Minimum frequency ⩾ 90% Fn	Recovery time to more than 97% of Fn ⩾ 3 sec	Minimum voltage % of Un ⩾ 90% Un	Recovery time to more than 97% of Un ⩾ 1.5 sec
Load Rejection	Maximum frequency ⩽ 110% Fn	Recovery time to less than 105% of Fn ⩽ 10 sec	Maximum voltage (% of Un) ⩽ 120% Un	Recovery time to less than 103% of Un ⩽ 2 sec
Steady-state operation	Maximum variation +/- 0.5% Fn	-	Maximum variation +/- 0.5% Un	

Table 2.2: Specifications for Frequency and voltage variation in transient and steady-state operation applied in TotalEnergies industrial facilities.

Frequency range (Hz)	% of Nominal	Duration	Contractual commitment
47 - 47.5	-6% to -5%	1 minute	Once every 5 to 10 years
47.5 – 49	-5% to -2%	3 minutes	Once every 5 to 10 years
49 – 49.5	-2% to -1%	5 hours	100h in total during the customer's installation life
50.5 – 51	1% to 2%	1 hour	15 hours in total during the customer's installation life
51 – 52	2% to 4%	15 minutes	1 to 5 times a year
52 – 55	4% to 10%	1 minute	Exceptionally

Table 2.3: RTE's frequency contractual range [43].

protect the grid from large instabilities. During normal operation, operators must ensure that frequency and voltage do not exceed 0.5 % of the nominal values (see Tab. 2.2). Comparison of industrial standards with french transmission system operator's contractual specifications (Tab. 2.3) shows that similar constraints are set for power system operation. This naturally requires to accurately evaluate the risk of power quality degradation and install mitigation devices if needed.

PATHWAYS FOR RENEWABLE INTEGRATION

Due to the level of reliability necessary and the isolated location of such facilities, fossil generation is generally the only solution to produce electricity which participates in "well-to-wheels" emissions [44]. The increasing pressure of global warming has led the O&G industry to invest in low-carbon R&D (Research and Development) and to consider renewables as a possible solution for its power generation units [45]. Potential plants include onshore and offshore fields, pipeline pumping stations, refineries and, more recently, liquefied natural gas (LNG) terminals.

The Hywind Tampen project is a good example of O&G microgrid. It aims at connecting two offshore platforms in the North Sea (Gullfaks and Snorre) with a floating wind farm of 11 turbines. The construction is planned to start in 2022 and is supported by the Norwegian company Equinor. The two platform's fossil power plants and the wind farm will create a fully autonomous grid isolated from shore. Renewable production is expected to cover 35% of annual power demand and should cut 200 kilotons of Co2 per year.

Figure 2.7: Illustration of hywind tampen hybrid power plant [46].

Table 2.4 gives an overview of studies addressing the problem of hybrid fossil-renewable power for O&G, ranging from large-scale integration potential to highly detailed electrical stability studies. Wind integration and offshore platforms are the most widely covered subjects, while fewer studies have addressed the problem of onshore facilities and solar PV systems from a technical point of view. The studies highlight that electrical instabilities due to renewable resources constitute the main technical limiting factor and that storage is generally necessary to allow large-scale integration. Design optimization, such as carried out in [26], shows the interest of renewable integration for fuel and CO2 reductions. However, no parametric study including storage has been proposed to date and it is expected that the additional capital expenditure would reduce the financial benefits. Furthermore, [47] concludes that renewables will impact the fatigue and lifetime of fossil generation which could be a major issue when reliability is a key factor.

Reference	[48], [49]	[26]	[50]	[47], [51]	[52],[53], [54]
Scope	O&G	Offshore oil	Offshore oil	Offshore oil	Offshore oil
Energy	Electricity, Heat	Electricity	Electricity	Electricity	Electricity
Power range		40MW	40MW	MW	-
Grid Type		Off-grid	Off-grid	Both	Off-grid
Resource	Solar	Wind	Wind	Wind	Wind
Fossil unit	-	CCGT3	CCGT	Gas turbine	Gas turbine
Storage		-	-	Battery	-, -, Battery
Focus area	Large-scale potential for solar	Method for optimizing design	Power quality challenges	Operational & energy optimization	Electrical stability study

Table 2.4: Review of Oil and Gas microgrid studies for renewable integration.

This overview shows the interest of O&G microgrids to identify the challenges and to highlight success stories for other industrial applications in isolated areas. In a research perspective, O&G microgrids provide interesting case studies and make it possible to compare results and validate them in a similar environment before considering their adaptation to other applications.

2.1.5 *Main research challenges*

From the review presented above, the following research challenges are identified:

- Due to their relatively small size compared to large grids, industrial power systems are more vulnerable to electrical instabilities [50]. However, industrial facilities cannot afford unplanned blackouts and electricity shortages. This calls for the development of a method to ensure an equilibrium of active and reactive power with a high degree of reliability.
- Reliability constraints make it necessary to consider unplanned power fluctuations brought about by the integration of PV systems. Notably, the impact of short-term stochastic solar variation on continuity of supply must be addressed.
- Flexibility levers used to compensate renewable power variations are crucial to ensure grid reliability. Storage systems are the subject of increasing investigation, while less attention is being paid to fossil-fuel technologies due to their apparent maturity. But their response to successive ramps remains unknown and may significantly alter their lifetime and fuel consumption. Very few models account for their dynamical behavior or integrate it in a long-term assessment.
- A large number of studies now address the control, management ans sizing of microgrids to smartly interconnect all power devices on the grid. In the context of industrial microgrids, this involves making the right trade-off between economic performance and robustness and therefore requires dedicated strategies.

This chapter intends to contribute to filling these gaps as follows. First, a review of the short-term dynamical assessment of PV systems, fossil generation a storage is presented. Next follows an investigation of real-time control strategies that ensure reliability and power quality within industrial microgrids. Fourthly, sizing procedures are investigated. The final section concludes and presents the scientific method for addressing the problem stated in Chapter 1.

2.2 MAIN POWER GENERATION TECHNOLOGIES

The insights provided by O&G studies enlighten the future for industrial microgrids but often focus on a particular aspect of the system (design, operation, stability). When it comes to supply electricity with high reliability standards and low environmental impact, the big question is to assess the maximum share of renewable and, naturally to find the cost associated to it. In addition, the literature survey shows that less work has been done on solar. However, the decreasing costs and the enormous potential of photovoltaic technologies pushes to integrate it in industrial microgrids. Hence, the technical challenges for the planification and operation industrial microgrids must be identified with regards to the specificities of photovolotaïc generation. Since electrical stability and power quality are crucial aspects, the dynamic behavior of the microgrid have to be understood and modelled carefully. Section 2.2.1 and 2.2.2 presents an overview of the dynamic behavior of fossil and photovolaïc generators. An overview of the relevant storage technologies for intermittency mitigation is therefore provided in Section 2.2.3.

2.2.1 *Conventional fossil generation*

In industrial applications, gas turbines and internal combustion engines are the main technologies used to produce electricity. The choice between these two options depends on the availability of the fuel (diesel, heavy-fuel oil, methane etc.), the costs and the maintenance requirement. Some other consideration may impact the decision such as the need for a heat production, footprint, emissions etc.

With the penetration of variable and uncertain renewable power, fossil generation is about to dramatically change from a steady-state operational paradigm with fixed load and well-known production plan to a constantly changing demand with stochastic perturbation. This forces the manufacturers and users to ensure operational flexibility [55] with an increasing number of start-up, shut-down, fast load change and need for power-quality control. Meanwhile, cost-effectiveness, reliability and emission-regulations compliance needs to be guaranteed.

The main objectives for fossil generation in industrial applications can be summed up as follows:

1. Adapt the power output to match the power needs (provide enough spinning reserve in case of a sudden PV drop or load step).
2. Provide enough primary response to ensure frequency and voltage stability (engine control needs to ensure compliance with the operator's grid code).

3. Maintain the highest level of availability when operated in extended transient mode (prevent the risk of failure or breakdown due to successive load fluctuations).
4. Ensure cost-efficiency in the long run with regards to O&M costs and aging.
5. Guarantee compliance with emission regulations in transient operations.

As performed in [56], numerous commercial studies attempt to compare fossil generation flexibility for hybrid generation purposes. To ensure that such comparisons are creditable and accurate, performance assessment needs shift from steady-state off-design correlations to dynamic modeling at a short time-scale. For project developers, making a choice based on a generator's dynamical performance is not an easy task:

- Ramp-up capacities are rarely provided by manufacturers for small time-scales (seconds).
- Manufacturers usually provide ramp-up capacities for fast start-ups and shut-downs, which are meant to be occasional.
- There is no guarantee that the thermodynamic parameters (pressure, temperature, etc.) will remain within acceptable limits.
- No insights are provided on the machine's performance: fuel consumption, emission, fatigue.

These reasons call for a deeper understanding of fossil generator dynamics and more detailed modeling. The next part presents some theoretical aspects as well as the state-of-the-art on dynamic modeling of fossil assets.

2.2.1.1 *Gas turbines*

WORKING PRINCIPLES

Gas turbine (GT) theory has been widely developed in past decades and detailed in a large number of references [57–59]. GT performance predictions have been one of the main concerns in order to evaluate differences between ISO parameters provided by manufacturers and user's operating conditions. Fig. 2.8 and Fig. 2.9 show the main components of single-shaft and twin-shaft gas turbines.

Gas turbine cycle efficiency is defined by the ratio of total output work over the heat added to the system. The total output work is expressed as the turbine output power minus the compressor power consumption. The overall cycle efficiency η_{cycle} is expressed by 2.2

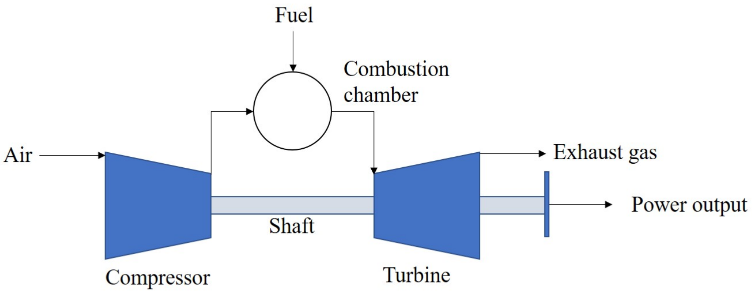

Figure 2.8: Single-shaft gas turbine.

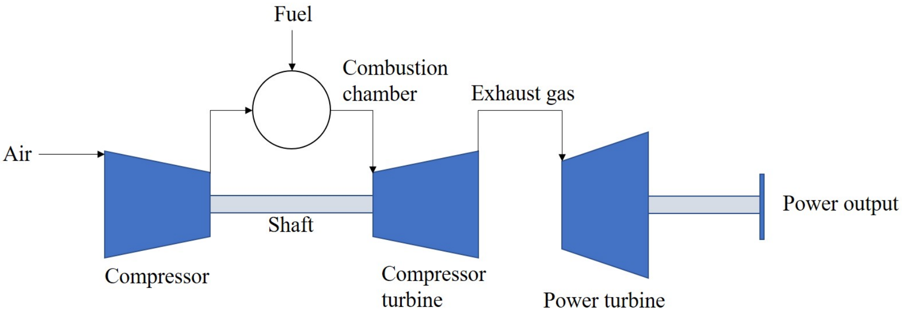

Figure 2.9: Twin-shaft gas turbine.

where W_{total} is the net output power (kJ/s), $\dot{m}_{\text{fuel}}$ is the fuel mass-flow (in kg/s) and LHV_{fuel} the lower heating value of the fuel (in kJ/kg).

$$\eta_{\text{cycle}} = \frac{W_{\text{total}}}{\dot{m}_{\text{fuel}}\text{LHV}_{\text{fuel}}} \tag{2.2}$$

The power plant heat rate is another metric used to characterize the gas turbine performance and defined as the inverse of efficiency (generally expressed in kJ/kWh). Fig. 2.10 compares the heat rate curve of two types of gas turbines and shows that gas turbines have lower performances at part-load.

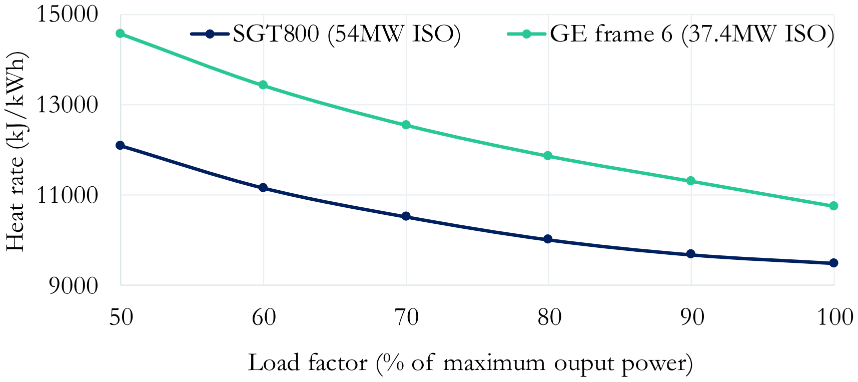

Figure 2.10: Twin-shaft gas turbine.

As shown in Figure 2.11, the compressor crosses iso-efficiency lines during transient operation and increases the turbine's fuel consumption and particle emissions and impacts its mechanical fatigue [58]. Acceleration and deceleration are also constrained by surge and flame-out limits that need to be taken into account to assess the ramping capacity of the turbine.

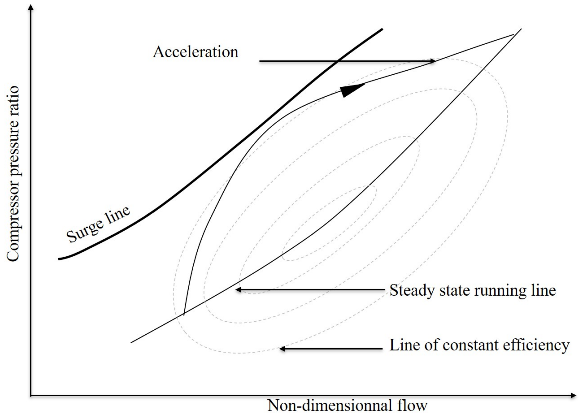

Figure 2.11: Compressor transient running line.

THERMODYNAMIC MODELS

The thermodynamic relationships of the components can be used to simulate the steady state "off-design" points due to part-load operations, special weather conditions, etc. This methodology can be found in the literature and is used by commercial software like ThermoFlow [60] or Proosis [61] but only represents static conditions.

The development of dynamic models for the performance prediction of gas turbines is still the subject of considerable research. Various methodologies with a growing degree of complexity can be used [62]. Some studies propose "black-box" models based on artificial intelligence in order to learn and reproduce the behavior of an asset based on operational data [63]. Computational-Fluid-Dynamics (CFD) models are probably the most accurate, but the level of complexity may go beyond the needs of renewable integration studies. Moreover, these models require large computational resources and perfect knowledge of the components' geometry.

MODELS FOR ELECTRICAL STUDIES

Zero-D modeling appears to be a good trade-off between a comprehensive approach and complex calculations. They consist in describing a component's dynamics using the Laplace's domain with saturation and time constants accounting for each thermodynamic process. Several levels of complexity exist here as detailed in reference [64], which compares different modeling techniques for power quality studies.

The most emplyed models are the GGOV (General Governor, see 7.2) model and the GAST model (in Fig. 2.12).

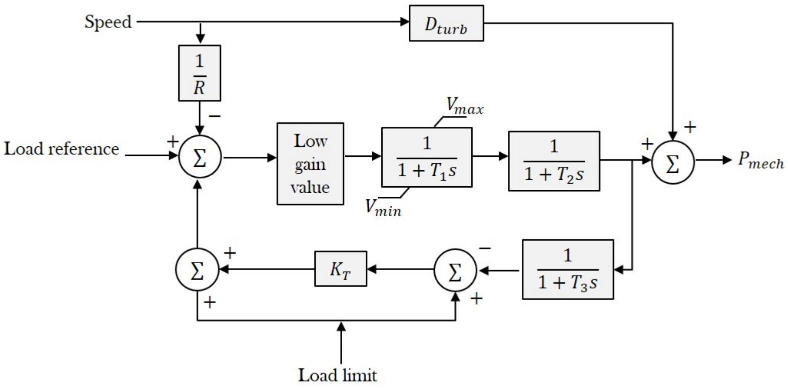

Figure 2.12: The GAST GT Model [64].

Electrical models are focused on the temporal evolution of the gas turbine's mechanical power and do not address fuel consumption or unit degradation. To have a better insight of fuel consumption during electrical transients, a similar 0-D representation is introduced in [65–67] . Blocks are obtained by implementing a Laplace transformation of thermodynamic equations. Reference [65] proposes a MATLAB/Simulink model of a dual-shaft turbine. A 10-second step load is applied, and sensitivity analysis is conducted on the shaft's inertia. This reference provides a control scheme for Gas Turbines (GT) for the evaluation of a wind-GT hybrid power plant and simulates 10 hours of operation. The same modelling technique is applied in [68] to perform a gas turbine diagnostic under transient operation. Reference [66] proposes a dynamic modeling of a single-shaft turbine featuring VIGV (Variable Inlet Guide Vanes). The simulation time is typically 10 minutes.

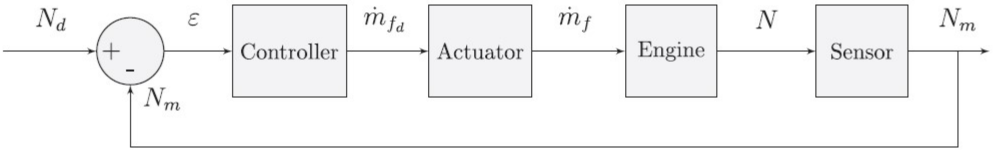

Figure 2.13: Dynamic model of turbine and its regulation system.

Thanks to their hybrid thermodynamic/electrical model, [65] show that hybrid gas/wind power plants can reduce both fuel consumption and NOx emissions by at least 40%. However, NOx reduction is debatable, as pointed out in [69], where an increase in NOx emissions from large-scale gas-fired power plants has been observed for shares of renewables below 30%. Due to increasing pressure from emissions regulations, the question of emissions modeling for transient operations will undoubtably be a key challenge for researchers in the future.

These methodologies may provide tools to represent the behavior of gas turbines but input parameters vary from one turbine to another. In addition, compressor turbine maps are necessary despite the fact that they are not publicly disclosed by manufacturers. This creates a strong barrier to study and compare the performances of gas turbines during transient operation.

2.2.1.2 *Internal combustion engine*

Research on diesel engine modeling has mainly focused on propulsion applications [70] and only a few references study its behavior in power systems [71, 72]. The principle of a diesel generator is basically the same as an automotive diesel engine: combustion within the pistons drives the crank shaft, which provides mechanical torque to the electric generator. This process follows the Carnot thermodynamic cycle.

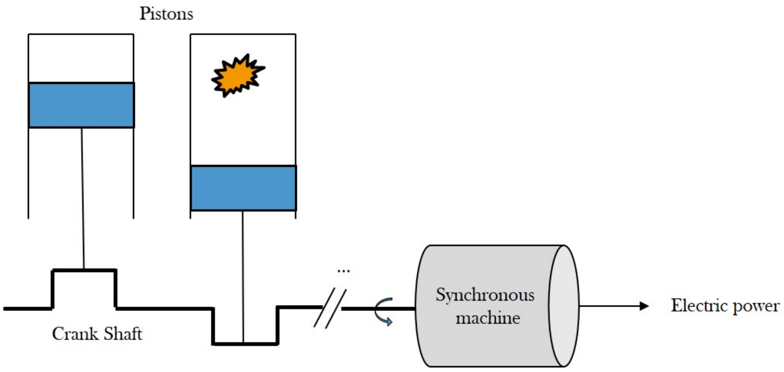

Figure 2.14: Principle of ICE power conversion from combustion to electricity supply.

Unlike for gas turbines, manufacturers tend to provide more insights on the short-term dynamical behavior of their engines since this is a key selling argument. Nevertheless, the impact of a repeated load increase remains unknown and a detailed thermodynamic modeling is necessary.

THERMODYNAMIC MODELS

The thermodynamics of the transient operation of ICE is widely covered in Refs. [74] and [75]. Two main modeling approaches can be used considering either a continuous phenomenon (mean-value model) or discrete events for combustions within the pistons (discrete-event models). Both methods aim at describing the change in the pistons' input parameters (air mass, fuel mass and exhaust gas recirculation) when a torque command is given to the system as described in Fig. 2.16.

In [71, 72], several modeling approaches are described, many of which are based on highly complex fluid mechanics. However, a lack of data on the engine's geometry makes it impossible to imple-

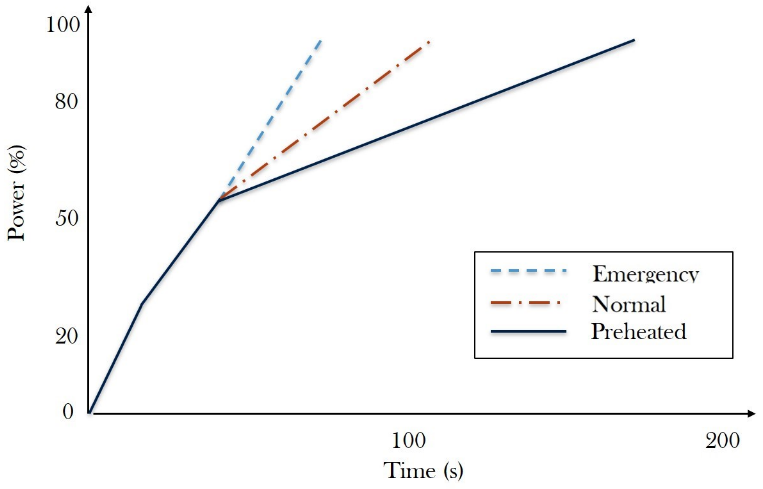

Figure 2.15: Recommended load increase of Wartsila W32 according to the product guide [73].

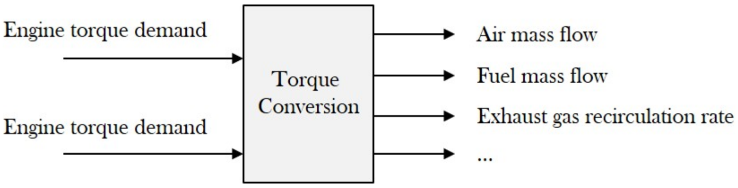

Figure 2.16: Principle of torque regulation.

ment such a model in preliminary study. Reference [76] presents a simple mathematical model of an engine based on thermodynamic expressions, enabling a fairly accurate study of the engine's step load response. The parameters needed for the simulation are generally not available in the literature and the author recommends calibrating the model using experimental data. Finally, reference [77] provides a simple methodology to model the transient behavior of a diesel engine. The model is calibrated with experimental data and requires accurate turbocharger parameters to run.

Due to their high complexity, detailed thermodynamic models cannot cover large time-windows. This is why reduced order models are proposed for electrical studies. On the contrary to gas turbines, no study proposed to link thermodynamic approach with electrical model to have better insight on fuel consumption or degradation during transient operation.

MODELS FOR ELECTRICAL STUDIES

From a control-science perspective, the transient modeling of a diesel engine mainly consists in describing 4 main components: the regulator (controller), the actuator, the engine's combustion, and the synchronous generator. In ref [78, 79] dynamic models are proposed for the frequency control (taking actions on the angular velocity) and therefore represent the short-term transient response of the engine.

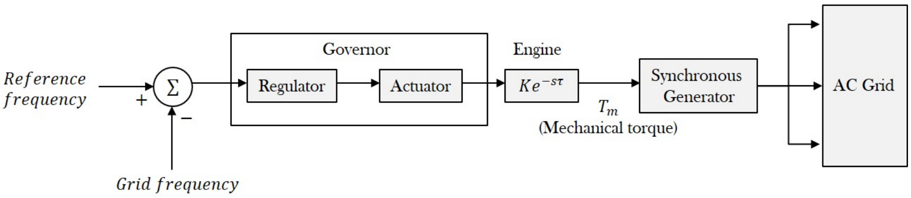

Figure 2.17: Conventional diesel engine representation.

The above-mentioned references are based on a mathematical modeling of the machine's processes and components. Other modeling techniques consist in "learning" the engine's response using neurocomputing. In ref [80], an HIL test bench is combined with a real diesel engine in order to learn the frequency's transient behavior and control. A dynamic model is then built to conduct stability analysis. However, this approach gives a very poor understanding of the machines, which makes it very difficult to adapt to another engines with, for example, a different number of pistons.

In [81], a sensitivity analysis of the engine injection delay is carried out. The results show that a short time-delay significantly improves the grid's frequency stabilization. The study recommends a low injection time-delay (mostly found in high rotational speed engines) in order to improve the penetration rate of renewables.

On the other hand, a good comprehension of the thermodynamical limitation is also a very important factor in renewable integration. In [82–84], it is shown that a high penetration rate can be enhanced by low-loading engines featuring dedicated pre-heating and clutching systems. This calls for further investigations on the link between transient thermodynamic performances and electrical studies.

2.2.1.3 *Ageing and maintenance considerations*

Is has been observed that fossil generators will increasingly be operated in a transient state with rapid variation to smooth out solar variability. The evolution of fatigue and fault probability due to transient operation is still poorly addressed by the scientific community. [85] evaluates the impact of an extended dynamic operation of CCGT, and indicates that the lifetime reduction may be up to 10% greater than in reference steady-state cases. Further analysis would be necessary to evaluate the failure rates of typical fossil technologies in industrial microgrids. Solar variability modeling may once again prove crucial for such an evaluation.

2.2.2 *Large scale solar PV systems*

Solar photovoltaic (PV) power is traditionally assessed with a quasi-static framework as mainly hourly variations are of interest for economic evaluation [86]. As previously mentioned, the vulnerability of large-scale isolated power systems motivates a study of sub-hourly phenomena that might impact electrical stability. Hence, short-term variability is a key element to ensure the balance between production and consumption and therefore a high level of reliability. Eq. 2.3 shows the relationship between the power produced by a PV plant and the solar irradiance [87].

$$P_{PV} = W_{PV}^{installed} * \frac{GHI_{planeofarray}}{1000} * [1 - K_\theta(\theta - 25)] \quad (2.3)$$

Where K_θ is the temperature sensitivity coefficient, $W_{PV}^{installed}$ the rated capacity of the panel in ISO conditions, and $GHI_{planeofarray}$ the Global Horizontal Irradiance calculated in the plane of the panel. The actual amount of energy collected by the panel will depend on additional factors [88] such as the clearness of the sky, the performance of the PV panel (efficiency, temperature sensitivity, aging etc.), shade and fouling due to the surrounding environment, etc.

Accurate modelling of PV system can be a challenging task when temperature data is not available. In addition, the main factors impacting PV performance can be hard to assess (cabling configuration, soiling conditions etc.). An alternative to Eq. 2.3 is to use PV derating factor η_{PV} as used in [86] and expressed in Eq 2.4.

$$P_{PV} = W_{PV}^{installed} * \frac{GHI_{planeofarray}}{1000} \eta_{PV} \quad (2.4)$$

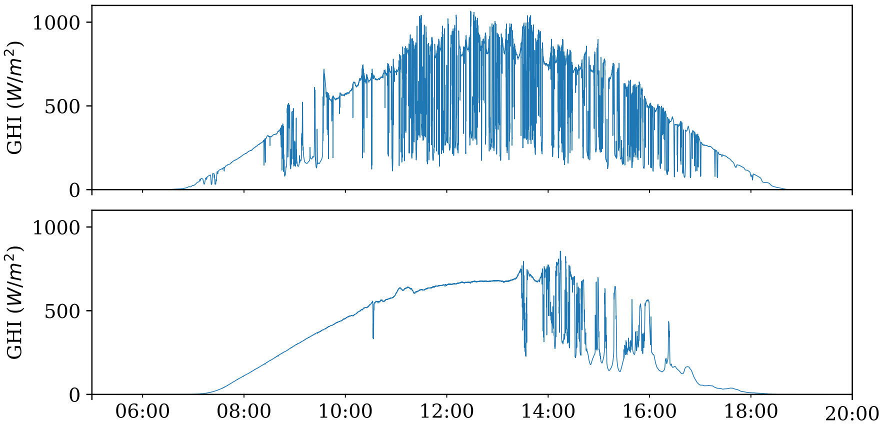

Figure 2.18: Two irradiance profiles captured with 1 second sampling [89].

Cloud passage is the main contributor to short-term variability and needs to be addressed carefully. Fig. 2.18 shows an example of solar irradiance variability over two days with a 1 second time-step.

The following sub-sections will focus on the approaches implemented to explain, measure and forecast short-term solar variability in order to integrate the risk of power imbalance in an industrial microgrid.

2.2.2.1 *Addressing PV variability*

Solar variability affects the irradiance measured by sensors as well as the power produced by one or several PV panels. Two time-scales are important for microgrid operation and planning:

- Solar power range: difference between the minimum and maximum solar power output in a time interval (typically 15 minutes to 1 hour).
- Solar ramps: the change of solar power or irradiance in a short time interval (within the range of the sampling interval: 1 second to 1 min) that dispatchable units will have to instantly compensate

Solar range and solar ramps are necessary to calculate the amount of spinning reserve, the ramping capacity of dispatchable units, and the storage capacity requirements. In high-reliability applications like industrial systems, extreme ramp events are also of interest to make a robust assessment.

VARIABILITY INDICATORS

It is possible to assess the level of variability over an entire day in order to determine the frequency and magnitude of perturbations. The variability index as defined in [90] is the ratio between the length of global irradiance series and the length of clear sky irradiance over a defined time interval (the study proposes to calculate the variability index over 1 day). In [91], 6 metrics are compared to evaluate the solar variability on 31 test days. The study proposes a new indicator based on integrating the cumulative density function of solar increment. According to the study, these metrics can be used to characterize the variability at both high and low frequencies and classify days depending on the perturbations. Variability indicators proposed in the literature are of varying computational complexity. The integrated complementary cumulative distribution function was found to be the best indicator to account for the variability at different magnitude. However, the time-increments used in these two studies were larger than 1 minute which excludes small solar drops that might impact the grid stability. Therefore, it appears necessary to validate the performance of variability indicators in small time-scales (from 1 seconds up to 1 minute).

CLIMATE-DEPENDENT VARIABILITY

Location plays a role in solar variability due to climate type, orography and vegetation (large forests also generate clouds during daylight). A solar variability map of the US drawn up using high-resolution production data [92] shows significant differences between desertic-arid areas and islands like the Lau islands and Hawaii where the highest level of variability is observed. In [93], the author studied the relationship between the clearness index and solar variability for locations in different climate zones. The authors concluded that climate zone and weather-driven clouds may have less impact on variability that the orography of a site. It is expected that the small, fast-moving clouds formed by the relief may have a bigger impact on short-term variability.

2.2.2.2 *Modelling PV system variability*

A PV system's short-term variability is different from the irradiance variability observed from a single sensor. In [94] it is concluded that the power profile entirely follows the irradiance profile for time ranges greater than 10 minutes. However, short-term variability is affected by the size, shape and distribution of a plant. For plants of several megawatts, 1-s, 10-s, and 1-min ramps can be approximately 60%, 40%, and 10% smaller, respectively, than those measured by a pyranometer. These results are confirmed in [95, 96].

SMOOTHING IRRADIANCE DATA TO OBTAIN PV POWER

Since PV power transients are smoother than irradiance transients, considerable work has been done to obtain a realistic power output from the data employing a single irradiance sensor. Hoff and Perez introduced the concept of the dispersion factor for a distributed PV fleet, calculated from the plant's layout, the wind speed and the time interval. The dispersion factor is used to characterize different types of layout (crowded or spacious) and the irradiance variability is smoothed to obtain the power in each configurations [97].

A Wavelet Variability Model (WVM) is proposed in [98] to obtain a PV power time-series from irradiance data. The model parameters are the plant footprint and the density of the sensors. The WVM is compared to three other methods: linear scaling, moving average, and averaging on every sensor available. When compared to the 2MW output power, the WVM outperformed the three methods, especially when evaluating the maximum ramp rates. A toolbox has been developed and is freely available in the MATLAB and Python environment [99].

GENERATING SYNTHETIC TIME SERIES

Assessing solar variability is a big challenge if no high-resolution irradiance data is available on site. One solution is to generate an irradiance profile based on numerical weather prediction or satellite predictions. In [100], methodologies based on Markov chains are proposed to generate irradiance and a clear-sky index profile. [101] reproduces high-frequency patterns of historical data to increase the temporal resolution of satellite prediction. However, these methodologies need representative training data set of high-resolution ground measurements which requires to have closely located sensors available. Recently, [102] paved the way for generating 1 min data without ground measurements, but concluded that additional research needs to be carried out in order to obtain finer resolution.

2.2.2.3 *Forecasting solar variability*

Solar forecasting has been a growing topic in recent years since it provides valuable information for microgrid operation and is used for various purposes, such as market trading, reserve scheduling, genset planning, and storage management [103]. Its potential to optimize battery sizing and lower the LCOE of ramp-constrained multimegawatt power plants is highlighted in [104]. Capturing solar variability with forecasts may consist in providing either very short-term production estimations or an indicator of the variability to be expected for a large horizon (15 mn to 1 h) [105, 106]. As an example, [107] proposes a methodology to estimate the largest ramp rate by analyzing cloud shadow velocity and irradiance sensor measurements. Satellite irradiance forecasts and numerical weather predictors are now widely used and can be accessed online [108]. Due to their large time and space resolution, a downscaling approach is necessary to predict the variability at 10 seconds or 1 minute scales. Such solutions are proposed in [109–111] but due to the geographical dependency of the variability, no generic method has been proposed to downscale satellite prediction without high-resolution data at the specific location. Sky imagers have been developed and commercialized in recent years with the intention of giving very short-term prediction for spinning reserve management (diesel load margin, storage capacity etc.) [112, 113]. The development of these techniques will be a key factor of success for the reliable management of industrial microgrids.

2.2.2.4 *Reliability considerations for PV systems*

Integrating PV systems in industrial power plants brings additional risks for the continuity of supply and may therefore reduce the reliability of the power plant. Reference [114] provides an overview of reliability assessment methods for PV inverters, modules, transmission systems, and overall distribution systems based on fault analysis. Insights on the impact of aging and weather conditions on reliability over the lifetime of a plant are provided in [115], showing that high average ambient temperature is likely to increase failure rates (almost 10% after 5 years in the case of a PV system in Arizona against 0% in Denmark). This factor must therefore be considered in reliability analyses. In [114], solar variability is mentioned as one of the main future challenges for distribution systems; however no insights are given on its impact on reliability. This is why a special focus on solar variability assessment is provided in this study.

2.2.3 *Storage systems*

Storage systems may achieve two different objectives in microgrids: energy shifting and system services. System services refers to applications dedicated to enhancing a system's reliability when subject to unplanned events. For example, a storage system can provide power if the renewable output suddenly decreases or if a fossil generator trips (2.19). The storage device is therefore used as a buffer to compensate for the start time and ramp of the replacing unit.

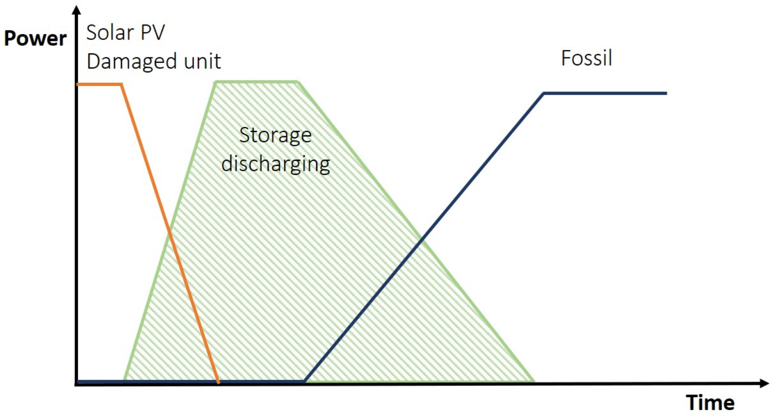

Figure 2.19: Buffer storage system.

Depending on its objectives, a storage system will have specific technical requirements that require carefully choosing the technology. [116] gives an outstanding overview of storage technologies in microgrids and provides examples for the five main types of storage technologies listed in Fig. 2.20.

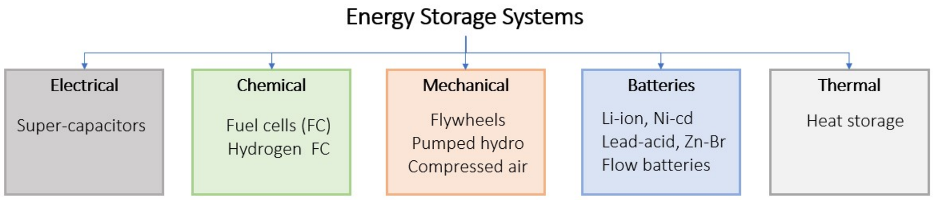

Figure 2.20: Categories of storage technologies.

Thanks to the variety of storage technologies available, numerous applications are covered, from very small uninterruptible power systems to utility scale systems such as pumped hydro. Fig. 2.21 shows the general trends of technologies according to their rating capacities and discharge times (additional features for technology comparison can be found in [117]). Considering the characteristics of industrial microgrids and their production units, storage systems must contain several MWs in order to provide services with reaction times varying from a few seconds to several hours. Li-Ion batteries, flywheels and supercapacitors seem to be the most suitable options for these applications [117, 118].

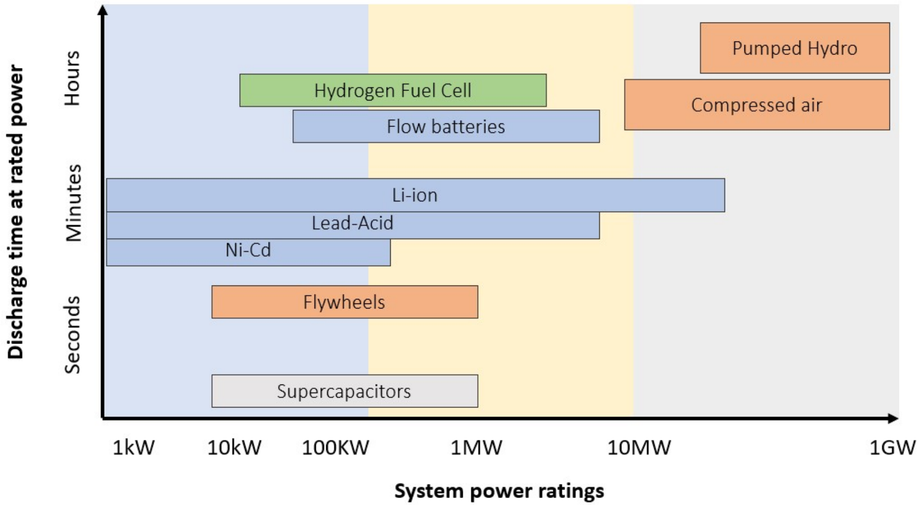

Figure 2.21: Discharge time and power ratings.

Technology	Li-ion Batteries	Fly-wheels	Supercapacitors
Reference	[116, 119, 120]	[121, 122]	[123–125]
Advantages	High energy density, High cycling efficiency Rapid response time, Low self discharge Aplicable to other uses (energy shifting)	Quasi -infinite number of cycles	High power density Long lifetime and limited ageing
Drawbacks	Lifecycle degradation due to cycling and thermal effects	Low energy density High self-discharge rate	High sel discharge rate (up to 40% a day)
Comment	Market leader. Driven by synergies with automotive applications Recent economies of scale	Low maturity, high costs	Suitable only for very short-term applications Low maturity in large-scale applications

Table 2.5: Review of advantages and drawbacks of main storage technologies suitable for industrial microgrids.

2.3 CONTROL AND MANAGEMENT OF MICROGRIDS

Most of studies in microgrid tackle the problem of operation and planning by handling a single aspect of the microgrid (control, energy management or sizing). But due to the specific characteristics of industrial microgrids, careful attention must be taken for each of them. As a matter of fact, the size of the facility emphasizes power quality problems and endangers the continuity of operations. Secondly, operational costs are a part of the product profitability and must be optimized. Finally, as industrial power plant requires huge investment, a reliable sizing is crucial. Control, energy management and sizing are three steps of a single process which aims at finding the best operational scenario for the microgrid.

The operational management of a microgrid consists in adjusting the production units in order to ensure the system reliability and supply the load at the minimum costs an environmental footprint. The term *dispatchable units* refers to devices on which control action can be undertaken to adjust the level of production. These are typically the fossil units and storage systems. As their power output only depends on external phenomenon (wind, sun etc.), renewable resources are considered as non-dispatchable units and only a few control actions can be undertaken to adjust their power output. Loads may be considered either as dispatchable or non-dispatchable depending on their criticality.

2.3.1 *Short term power control*

The performance of a microgrid is highly related to its control scheme since it is supposed to execute de the production plan while protecting the power system and devices when instabilities occur. It ensures a reliable electricity supply by following power quality specification and protects the devices from going out of their operational range. In industrial microgrids, a special attention is paid to the frequency and voltage control. In the next parts, fundamentals of voltage and frequency transients will be presented alongside with the main levers to enhance grid stability. As transient perturbations due to renewable variation or generator contingency mainly impact active power, a special focus will be provided on active power regulation. Then, control strategies for each devices of the microgrid will be presented. Finally, a brief overview of grid modeling technique will be given in order to conduct dynamic studies.

2.3.1.1 *Fundamentals of frequency and voltage regulation*

To properly understand the role of power quality in the continuity of supply, a brief introduction of power system theory is necessary. However, for the sake of simplicity and clarity, this chapter will not develop the theory of power system in details. The ready may refers to specialized work such as [126].

POWER SYSTEM THEORY

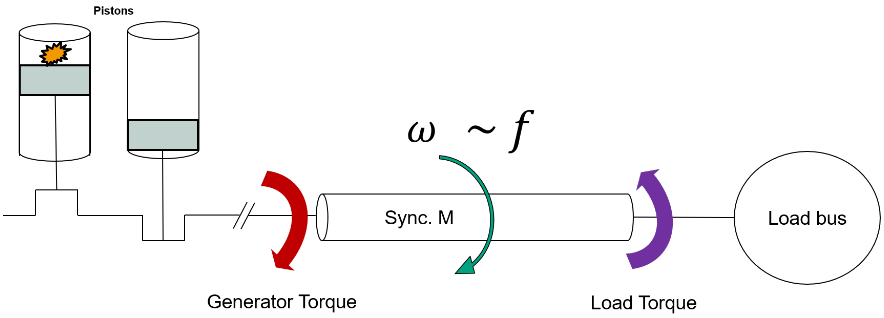

Figure 2.22: Representation of load and generating torque at both sides of a synchronous machine.

The generating torque produces a rotation of the rotor wich induces votalges and currrent thanks to the magnetic fields. This produces sinusoidal voltage and curent signals at each phase characterized by their magnitude and frequency f.

When a torque unbalance between load and generation causes happens, the synchronous machine rotor starts to accelerate or decelerate. This is expressed by the equation of motion derived from Newton's 2nd law (Eq. 2.5). Where J is the moment of inertia of rotating parts of the connected equipments in $kg.m^2$.

$$J\frac{d\omega}{dt} = t_m - t_e \tag{2.5}$$

The frequency f in Hz is related to the voltage and current signal's period ω in $rad.s^{-1}$ which also corresponds to the synchronous machine's shaft rotational speed.

$$\omega = 2 * \pi * f \tag{2.6}$$

On the contrary to frequency stability which can reasonably considered as uniform within the power system (assuming synchronous grid), voltage stability must be evaluate at each node of the power system. This is done by resolving the non linear relationship linking current and voltage at each node k to the injected active and reactive power (Eq. 2.7).

$$I_k = \frac{P_k - jQ_k}{V_k} \tag{2.7}$$

The power flow equations are usually solved in their Jacobean formulation by commercial softwares (Eq. 2.8).

$$\begin{bmatrix} \Delta P \\ \Delta Q \end{bmatrix} = \begin{bmatrix} \frac{\delta P}{\delta \theta} & \frac{\delta P}{\delta V} \\ \frac{\delta Q}{\delta \theta} & \frac{\delta Q}{\delta V} \end{bmatrix} \cdot \begin{bmatrix} \Delta \theta \\ \Delta V \end{bmatrix} \tag{2.8}$$

Voltage stability can be handled at relatively low costs with available commercial technologies. In addition, reactive power compensation capacities (such as capacitors banks) are more affordable than active power compensation capacities (which are new production units such as storage or fast fossil generation). This means that the techno-econoic balance will be less impacted by making adustements on reactive capacities trhough the successive sizing steps. Finally, unlinke for active power, reactive power can be produced by all devices which gives more flexibility to the system. This is why assessing the impact of variable energy ressources penetration on voltage stability can be assigned with a lower priority than assessing frequency stability problems [127, 128]. After the long-term planification, a detailed modeling of voltage control remains necessary in isolated system whenever the grid topology is available. This is generally done in detailed engineering studies and is out of the scope of this study.

The power system's response to a sudden load step (Fig. 2.23) shows that the frequency stabilization is handled by passive and active levers. Passive levers are the first to participate in the frequency regulation and consists in the kinetic energy stored in synchronous machines as well as the frequency dependency of consumers. They are linked to the system's mechanical and electrical characteristics and does not require any human actions. Then, active levers are triggered. These involve power reserves from devices which are activated following a specific order with the aim of recovering from the perturbation.

THE ROLE OF INERTIA IN PASSIVE REGULATION

As seen in Fig. 2.23, the kinetic energy delivered in the first few seconds is much more important than the primary reserve and frequency-dependent load reduction. When a sudden power unbalance happens, mechanical torque as both sides of the alternator shafts causes it to decelerate. The inertia softens the shaft's deceleration by returning the kinetic energy stored in the rotating mass[126]. The inertia constant H (sec) accounts for the kinetic energy stored in the synchronous machine. It is calculated as a function of the angle velocity ω (rad/sec), moment of inertia J (kg/m^2) and power rating of the unit (MVA).

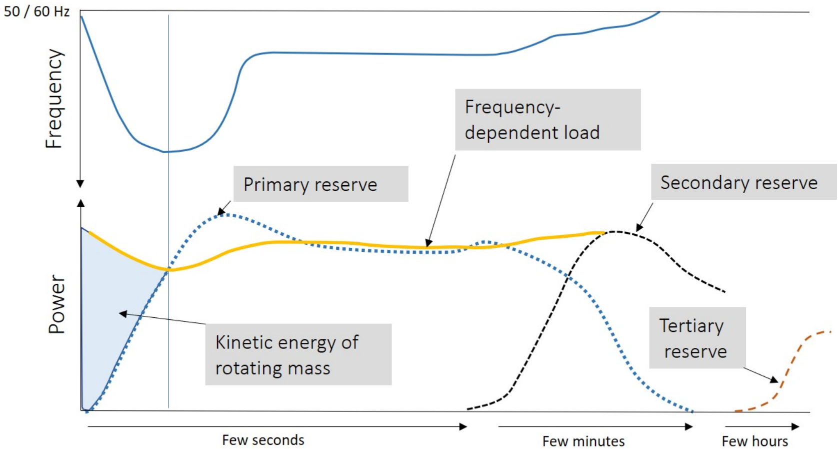

Figure 2.23: Evolution of frequency after a load change [15].

Type of unit	Inertia constant (s)
600 MW steam turbine	13.7
11 MW middle speed diesel engine	3
21 MW middle speed diesel engine	5.2
30 MW gas turbine	2.5
Photovoltaic generator	0

Table 2.6: Value of inertia constant for several production units [129].

$$H = \frac{1}{2} \cdot \frac{J\omega^2 * 10^{-6}}{MVA_{PUratings}} \tag{2.9}$$

The inertia constant of a system is the sum of individual inertia constant H of each generating unit i ($H_{total} = \sum_i H_i$). In the first moments of a perturbation, the frequency shift is only driven by the swing equation and therefore depends on the power difference $\Delta P = P_{gen} - P_{load}$ and the inertia constant H [129]. This means that the frequency drop highly depends on the mass of rotating parts. Hence, moment of inertia of production units are key lever to enhance frequency stability and resiliency of the power system. Due to the increasing penetration rate of renewables, microgrids tends to have less inertia in their system. This is due to the fact the inertia values of diesel generator and gas turbine are smaller than large conventional fossil units (see Tab. 2.6) and also because units may be shut down when renewable power feed the system.

In a microgrid, keeping an enough inertia is crucial to maintain the grid's stability. This aspect must be considered with the same care as active control actions. This is pointed out in [130], where a microgrid's frequency response is evaluated for different inertia constant values. Even though PV systems do not provide inertia to the system, power electronics and fast response storage system may help to synthetize inertia and therefore improve the system's resiliency [131, 132].

2.3.1.2 *Control of dispatchable units*

As soon as a frequency shift is detected, control actions are triggered to prevent the voltage and frequency from exceeding their nominal values. These actions consist in adjusting the power output of the devices to bring, at first, the power unbalance to zero, secondly, to bring the frequency to its nominal value. These actions come after the inertial response due to the time delays of communication systems, fuel injectors, combustors and the limited ramping capacity of fossil units. Typical controls strategies for microgrids under various conditions are detailed in [13, 16] and an outstanding review have been provided by [131]. Fig. 2.23 shows the typical three-layer hierarchical control is used in most of the system to adjust the power and correct the deviations:

- Primary control: immediately adjusts the power output of dispatchable units in order to stop the frequency or voltage shift.
- Secondary control: modifies the output power of dispatchable units to bring the frequency or voltage at its nominal value.
- Tertiary control: re-equilibrates the output power of each generator to make them run at their economical optimum.

These control actions can come from any dispatchable units (fossil units, storage system or even loads) provided that the strategy follows the device's specifications. Their regulation will be detailed in the following parts for each of the microgrid's device. Among all primary controls developed in the literature, the droop-control method is by far the most commonly used and easier to implement. In large power system, it is used to control units involved in the primary regulation [126, 129]. Its use in microgrid is justified and detailed in [133, 134]. Any power imbalance is automatically compensated by the generation proportionally to the frequency deviation. The contribution of each generator is proportional to its droop value R_{gen} giving $\Delta P_{gen} = R_{gen} * \Delta f$ (it must be noticed that the generation remains limited by its ramp-rate). Figure 2.24 illustrates how two units of different droop characteristics can participate to the frequency regulation.

The active power control is a common rule applied by all units which takes place in the primary response. However, controller must embed additional features in order to protect the equipment from going out of their operational range. This will be presented in the next sections.

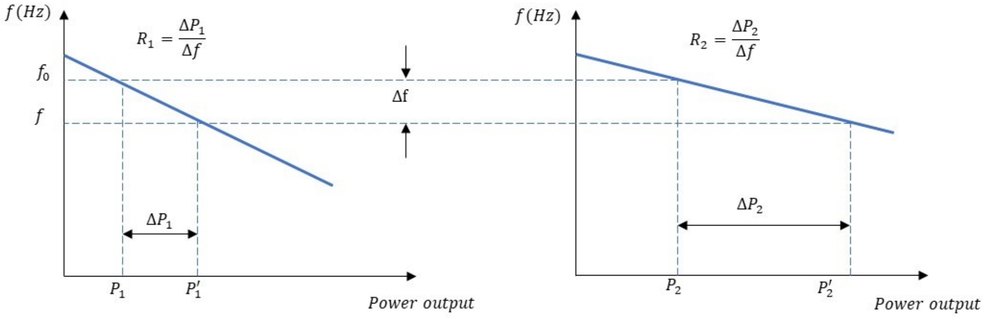

Figure 2.24: Control of two units with different droop characteristics [126].

CONTROL OF FOSSIL UNITS

Fossil engines are naturally the main actors of power quality regulation. In most of stability studies, the regulation potential is solely addressed using the droop R_{gen}. But fossil units remain limited by their flexibility in terms of ramp and load factor (which justifies the study of their dynamical behavior as presented in part 2.2.1). The control of fossil units and its simulation for stability studies will depend on the availability of information regarding the unit's transient behavior and well at its technical limitation (ramping range, power range, maximum fuel mass flow, temperature limits, emissions limits etc.). In most of the cases, the fossil controller is provided by the manufacturer and its information is confidential. In order to model and study the electrical stability, only high level of abstraction is generally possible such as shown in Fig. 2.25.

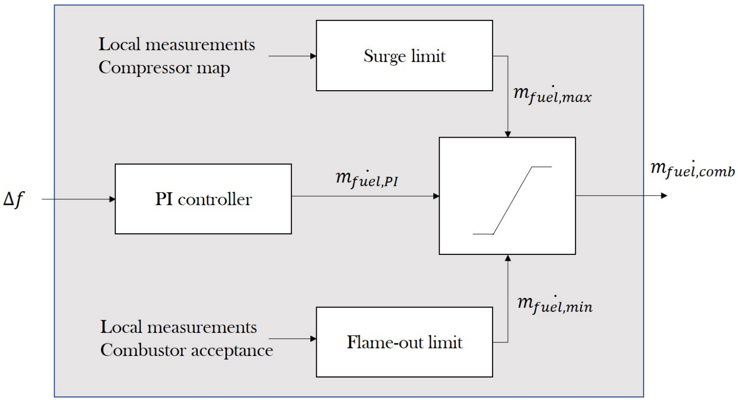

Figure 2.25: Principle of a multi-constrained fossil generation frequency controller.

The control scheme may consist in a succession of saturation and time delay accounting for constraints and transient behavior such as done in the reduced order system frequency response model in [135] and shown in Fig. 2.26. This accounts for either time delays of communication and injectors as well as physical limits of minimum and maximum power.

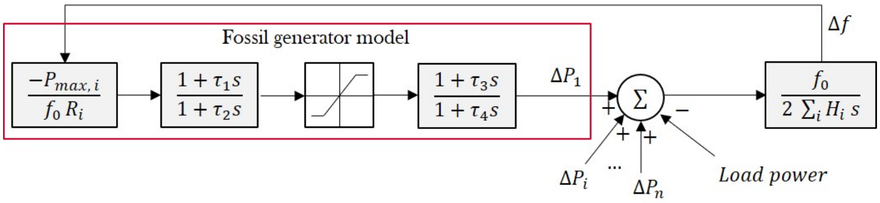

Figure 2.26: Reduced order frequency model accounting for gas turbine constraints and dynamics [135].

In Fig. 2.26 and similarly to the control of conventional large-scale units, the power output is only driven by the droop characteristics and the frequency shift. But in normal operation, the fossil generator needs to supply the power required by the user. The control signals of the load demand and frequency regulation are therefore summed-up to obtain the final power need from the generator [126]).

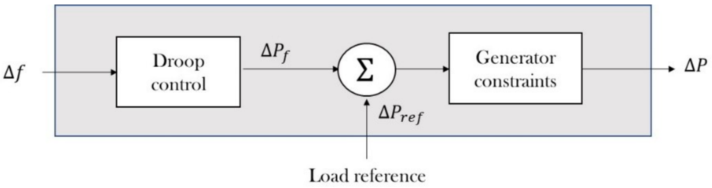

Figure 2.27: Coupled frequency and load reference control.

CONTROL OF GAS TURBINES

In Ref. [58], it is highlighted that gas turbine's control system shall adjust the power output while protecting the engines from exhaust gas temperature excess (turbine's overheating), over speed and over-stress of rotating parts, stalling and surging due to high compressor ratio. Fig. 2.25 gives a direct example for gas turbine: the fuel command depends on the frequency deviation and is then saturated by the surge limit and flame out limit. This is applied in [65] for the control of the mass flow which is a good methodology to include physical limits of components in the power control of gas turbines. However as pointed-out in part 2.2.1, the knowledge required for modelling such control is rarely available and sometime a simplified model has to be implemented (use of maximum and minimum ramp rates for example).

CONTROL OF DIESEL ENGINES

Diesel control strategies and challenges regarding the plant's protection are stated in [136]. Similarly to gas turbines, the power demand of diesel units must take into account its limitation such as the minimum loading factor or its maximum achievable ramp rate.References [78, 79] proposed a diesel engine frequency control and showed how the engine's characteristics may impact the grid stability. In [78], the advantages of a highly flexible control for diesel allowing low loading are presented. The results show an improved stability margin for frequency and highlights the potential of low-load diesel technology to reduce storage capacity investments. As fossil units tend to be flexibility providers more than prime energy suppliers, low-load and highly flexible fossil units' control will probably be a key issue in the future.

CONTROL OF STORAGE SYSTEMS

Fast discharging storage technologies are naturally widely used for short term regulation of power unbalances. An overview of control strategies for storage systems in given in [137]. In [138], an experimental study shows how a droop-controlled storage can be used to regulated the system's frequency. As battery energy systems are now spreading in microgrid applications, the literature covers a wide variety of control strategy. [137] introduced the concept of state-of-charge weighted droop control in order to adapt the regulation to the remaining amount of energy in the battery. Similarly, to fossil engines, battery control system includes protections and saturation to take chemical dynamics and component's electrical limitations into account. A good example of such control is found in [139], where a three-phase battery improves the frequency and regulation using conventional droop and inertia emulation. An ingenious control scheme is proposed by [140] with the aim to coordinate the frequency control of fossil units and storage system. A low pass filter is applied to the frequency deviation so that the generator only corrects low-frequency deviation whether the storage systems correct fast-moving deviation thanks to its high flexibility. Since control scheme must take specificities of each technologies into account, dedicated strategies are developed for flywheels and super-capacitors. In [141], a highly detailed control scheme for a flywheel system is presented. The study proposed to use fuzzy logics in order to improve the integration of wind power into the grid. In [142], a supercapacitor controller is proposed to regulate electrical transient caused by wind power ramps.

CONTROL OF LOADS

In high-reliability industrial application, the continuity of supply is a priority. This lets a small potential for taking actions on load in order to correct instabilities. Underfrequency load shedding procedures must be used only in emergency situations in order to protect the grid from blackout [126]. It is however important to carefully design the load shedding as significant stability improvement [143]. If a significant share of load is considered as non-critical, it is possible to use it as a flexibility potential and regulate the frequency and voltage deviations [47, 144]. However, accurate load models are necessary to accurately assess the potential of flexibility and stability improvements [145].

This solution is one of the most advantageous since no additional investment in necessary to integrate large share of renewables.

CONTROL OF PV SYSTEMS

Unlike for wind generators, which have higher inertia and regulation capabilities for frequency and voltage, PV generator are more limited when no storage is associated [146]. Depending on inverter technology, the power factor can be adjusted and therefore participate to the voltage regulation. Thanks to capacity curtailment, it is also possible to regulate overfrequency events by lowering the power output of the inverter. This is detailed in [147], which presents an overview of the active power control of PV systems. The potential of PV plant curtailment has also been pointed out in [148] to lower the risks of short-term drops due to solar variability. By reducing the number of connected panels and therefore the available production, the potential solar drop is also reduced. This is however subject to high uncertainties related to the forecast of short-term variations. In addition, a significant part of the solar production is lost, which reduces the environmental and economic performance of the plant. This solution must therefore be put into perspective with other mitigation levers, such as storage systems, and should be evaluated at the sizing step.

When associated to a sufficient energy buffer with very fast response time, grid forming inverters can enhance the grid's stability with synthetic inertia. It also allow black start capability when large share of renewables feed the system. An overview of grid forming PV inverters from operator, manufacturer and research perspective is provided in [149].

2.3.1.3 *Electrical modelling and simulation*

Modeling the short-term power control is mandatory to accurately assess a system's potential for renewable integration. Using voltage and frequency response modeling, the authors of [37] proved that the maximum renewable penetration limit to ensure grid reliability in Indonesia was 31%. In [150], a transient stability method is used to determine the maximum intermittent power penetration in an isolated system. Using swing equation equal area criteria, the ability of a system to properly control active power during transient events is studied in [151]. Numerous commercial software applications now allow stability studies featuring renewable technologies (ETAP, MATLAB, PSCAD, OPEN-DSS) and are widely used in both academic and industrial environments. Finally, research programs increasingly work on simulating systems in real time using hardware-in-the loop techniques [152]. By running simulations over a long period of time, it is possible to assess the performance of the microgrid in terms of quality of supply through reliability indicators [28] such as EENS, CAIDI, ASAI, and ASUI. This study gives an example of how to assess

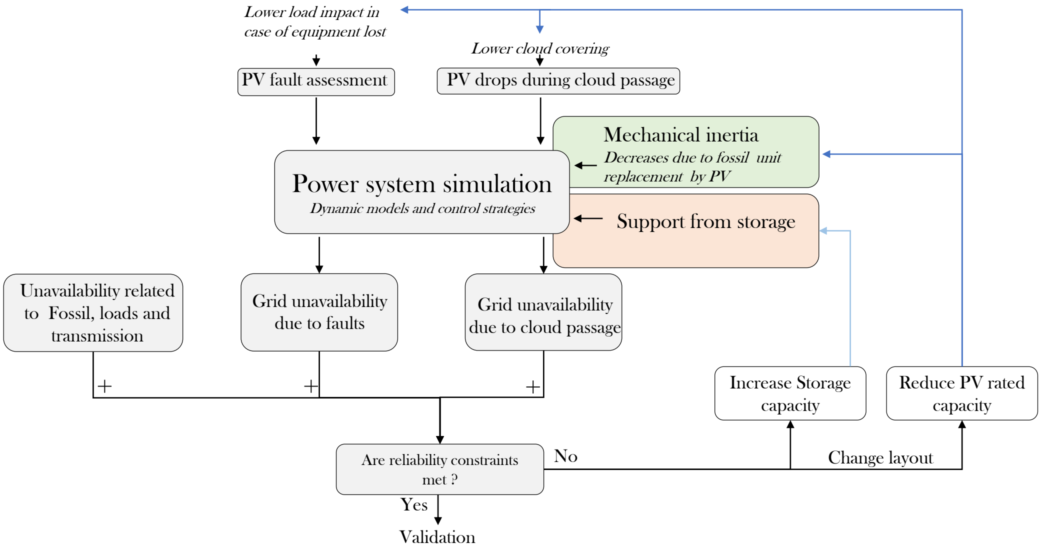

Figure 2.28: Example of a procedure for reliability assessment over a microgrid layout (where decisions are made on PV and storage capacities).

the reliability level in several plant configurations (islanded vs grid-connected, various sizes of PV systems and storage). Thanks to power quality simulation, probabilities of electricity outages (underfrequency load-shedding or grid blackouts) can be identified and thus integrated in the reliability assessment. This issue has been partly addressed in a previous work based on the duration of overfrequency and underfrequency regimes over one day [153]. Deeper investigations need to be carried out to propose a methodology to evaluate the reliability indicators related to power quality problems. Fig. 2.28 proposes such a procedure for the reliability assessment of an industrial microgrid with renewable integration.

2.3.2 *The energy management approach*

Although power control is very important for grid stability and robustness, it does not deal with economic objectives or handle forecasts of load and renewable resources. This is dealt by the energy management layer, which ensures the global equilibrium of production and consumption while minimizing the overall costs. The Energy Management System (EMS) ensures the proper allocation of production units by monitoring data and collecting forecasts. Considering industrial microgrid characteristics, centralized EMS generally seems more convenient [14]. The efficient performance of EMS lies in its ability to allocate the resources of each device at a minimal cost, which means that its dispatch algorithm is of paramount importance. In [154, 155], detailed surveys of energy management methods are proposed.

Linear programming (LP) and multi-layer optimization techniques turn out to be very relevant to address reliability and power quality in industrial energy management problems. This is why a special focus is proposed in this chapter.

2.3.2.1 *Deterministic, robust and stochastic optimization*

Examples of linear programming techniques for energy management are given in Tab 2.7. In most of the cases, a deterministic approach is used which means that uncertainties of renewable forecasts and load forecasts are neglected. However, when dealing with unit commitment, storage charging cycle or reliability constraints, the risk of discrepancies between forecasts and real-time production shall be addressed with more accuracy

A stochastic approach can deal with probabilistic forecasts and is therefore suitable to address renewable's prediction uncertainties [156]. However, the complexity of the problem is significantly increased, and this approach does not guarantee a fully reliable solution. A stochastic approach is more relevant when a trade-off can be made between reliability penalties and operational savings.

A robust approach is useful when reliability constraints play an important role in the operation. It avoids the use of probabilistic forecasts thanks to an efficient selection of uncertainty scenarios [157] (in general, worst-case scenarios are selected). Uncertainty is addressed from a conservative point of view involving a study of the historical performance of the forecast system.

Optimization family	**Principle**	**References**	**Advantages**	**Drawbacks**
Rule-based & dynamic programming	Logical decisions & flow diagrams	[158, 159]	Comprehensive framework Close description of expert knowledge	Lack of flexibility and reproducibility Hard to implement for complex systems
Artificial intelligence	Machine learning based on large datasets	[**wang_neural_2019** , 160]	Large number of situations handled	No comprehensive description Lack of reliability certification
Meta-heuristics	Optimization using bee-colony, genetic algorithms, etc.	[161–163]	Comprehensive optimization framework with non-linear modeling capabilities	No guarantee of optimality
Linear programming	Optimization based on linear description of objective functions and constraints	[**behnke_microgrid_2013**, 135, 157, 164–168]	Guarantee of optimality Easy implementation Fast-running commercial solvers	Requires relatively high level of abstraction Lower performance of non-linear and non-convex description
Multi-layer optimization	Predictive control model	[51, 169–174]	Ability to enable different levels of abstraction with high fidelity model High modularity and flexibility to describe the problem	Need to build a specific framework for each application

Table 2.7: Comparative review of energy management optimization techniques.

2.3.2.2 *Reliability constrained unit commitment*

Thanks to adequate constraints, EMS can protect the grid from unexpected events (generator contingency, sudden load increase, etc.) by implementing the concept of spinning reserve, the N+1 rule, or even an aggregated indicator for a frequency shift.

Reliability constrained unit commitment are proposed in [175] and [176] to address generator contingencies thanks to the "N+1" rule which allocates an additional fossil generator to cover the loss the largest unit. These formulations only handle the power balances before and after and contingencies but do not take the grid dynamics into account.

The resiliency of the grid and its ability to maintain grid frequency within satisfying limits during a unplanned event (generator contingency) can be handle by frequency constrained unit commitment (FCUC). This is proposed in [177] where the equation of motion is used to integrate frequency deviation constraints in the optimization problem. The authors in [168] propose a two-stage stochastic MILP formulation to calculate both unit commitment and reserve scheduling with 0-Hz and +/- 10 mHz of tolerance for frequency deviation. In [165], the frequency control is integrated into the EMS, but this significantly increases the complexity of the problem. A Benders decomposition is therefore used to solve the problem. In reference [135], the challenges of a frequency-constrained model are developed. The possible options to directly integrate frequency shift mitigation lead to either a non-linear problem or a sub-optimal solution (use of minimum ramping capacity, minimum value of inertia, etc.).

The risk of frequency shift due to a loss of renewable production must also be addressed to ensure grid reliability. This is discussed in [178] where the wind production uncertainty is handled thanks to the same constraints as generator contingencies. In [179], several frequency constrained unit commitment formulation are proposed to handle wind power variations and properly allocate the compensation from the storage system. From this survey, it appears that the identification of renewable variability scenario is crucial and even more challenging than the constraint's mathematical formulation itself. In [178, 179] worst cases wind drops have been chosen and considered as sudden variation from an optimization time-step to another. In the case of solar power, production drops may appear in a few seconds which is lower than the optimization granularity. In addition, fossil units have maximum ramp-rates that limit the flexibility of the grid. The specificities of PV based industrial micro-grids have not been addressed in previous work on FCUC which calls for deeper investigations.

2.3.2.3 *Model predictive control for EMS*

As pointed out in [169], a fully-integrated MILP model problem accounting for uncertainties and reliability can be very hard to solve due to the number of variables and constraints. This justifies the use of model-predictive control (or a multi-layer approach) to address both control and management of the microgrid. As presented in [172], model predictive control for energy management consists of a predictive model that plans optimal energy exchanges based on forecasts, and a system model that performs the dispatch and controls the power flux. The predictive model can be based on various management techniques such as presented above. The level of accuracy of the system model can be adapted to available information and may embed a very detailed control scheme. Finally, MPC reproduces the hierarchical relationship of the energy and power management system in real-life conditions.

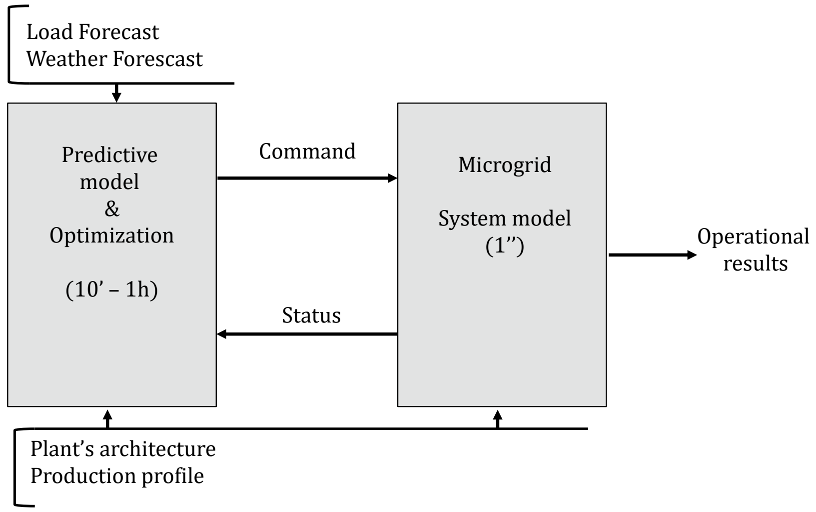

Figure 2.29: Architecture of model predictive control for energy management.

In [51], a two-layer model predictive control is used to simulated an off-grid O&G platform fed by a wind farm, two gas turbines and battery storage. In [169, 170, 173], the high level optimization problem is addressed using linear programming and therefore reproduces the decision of an LP-based energy management system. The results show that the method is able to handle forecast uncertainties, simulate dynamic behavior with accuracy, and improve both renewable penetration and operational savings.

2.4 SIZING OF INDUSTRIAL MICROGRIDS

The previous part (2.3) have shown that the performance and reliability of engine highly depends on the real-time control strategy and the commitment of each device of the microgrid. However, the management of the plant is constrained by the units available on site.

At the sizing step, investment decisions are made for fossil units, storage and PV systems while tracking one or several objectives (costs, emissions) and satisfying a set of constrain (load, reliability, emissions etc.). Several tools are available to help designing the microgrid architecture. HOMER is one of the main sizing tools dedicated to microgrid. It allows evaluating multiple architecture thanks to a simulation of operation over 1 year. Architectures are ranked by lifecycle costs taking into account discount rate, derating factor of units, emission penalties etc [86]. A MILP-based is integrated in the DER-CAM software which therefore guarantee an optimal solution [180].

Numerous studies dealing with sizing optimization are available on the literature and several reviews have been recently published [181–183]. In [184], the design of an offshore O&G hybrid power plant is performed by successive runs of high-level models and detailed models. The methodology uses genetic algorithm to converge to an optimal solution. This approach allows using complex model that directly addres power quality. However, they cannot guarantee a global equilibrium and require running detailed simulation at each step of the process.

From these reviews, linear programming formulation again appears as a good way to optimize the sizing of industrial microgrid.

- Linear programming formulations allow a comprehensive and flexible modelling of the microgrid
- Linear and mixed integer linear problems can be solved by commercial solvers giving guaranty of optimality of the solution and gap to the optimal solution.
- The process of reliability constraints have already been developped in similar problem and the use of endogeneous indicators and constraints for the small time-scale reliability seems adapted to industrial microgrids.

In [180, 185] , the proposed MILP sizing formulations consists in coupling operational management and investment optimization (see Fig. 2.30). The energy management model reproduces the behaviour of the power plant thanks to typical time-indexed operational variables and constraints. It is evaluated over a given time-horizon to reproduce the plant's lifetime. Operational variable are used in the objective function to evaluate the overall OPEX. Meanwhile, sizing variable

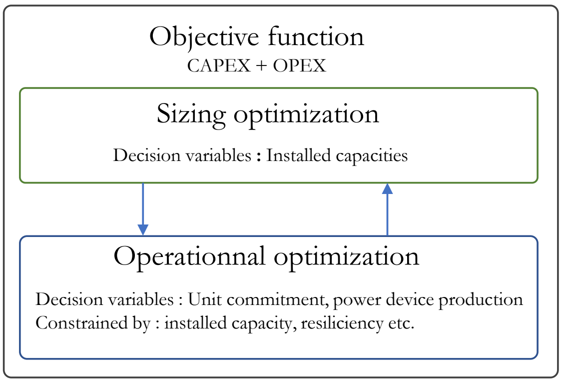

Figure 2.30: Principle of integrated sizing optimization [185].

account for the installed capacities of power units are are therefore not time-indexed. They are associated to installation costs in the objective function to calculate the plant's CAPEX. Therefore, one of the main challenge of MILP formulation for sizing lies in a proper formulation of the management problem. On the other hand, the formulation of both sizing and management problem forces to make assumptions on the control strategy which can reduce the accuary of the method. Such problem has been pointed out in [186] which pushes to carefully track the feasibility of the final solution obtained at the sizing optimization step.

2.4.1 *Reliability-constrained sizing*

To ensure the reliability of the system, the mathematical formulation of the management problem needs to include reliability constraints for contingencies or renewable variations.

Optimal sizing of micro-grid with redundancy constraints have been proposed in [187, 188]. In [189, 190] kinetic indicator are used to guarantee the system reliability while carrying the long-time planning of the French electric grid.

In [191], spinning reserve constraints are used to ensure the load balance in case of solar drops. The study uses probability of solar drops based on historical data with a 15-minutes resolution. The formulation is integrated in the DER-CAM tool which also integrated redundancy constraints. In [192], the resiliency to sub-hourly solar and load variability is addressed thanks to the gaps observed between hourly averaged data and higher resolution timeseries.

In the studies mentioned above, the resiliency of the grid to power unbalances (generator contingency or renewable power variations) is handled thanks to spinning reserve constraints. They ensure that fossil units and storage systems have enough power margin to compensate power drops but do not address the problem of frequency variations. To integrate these aspects, the energy management's sub-problem must integrate FCUC constraints such as detailed in part 2.3.2.2. Such approach has not been proposed in a MILP framework for short-term solar drops resiliency.

2.4.2 *Sizing under uncertainties*

The long-term planning of microgrid is also subject to uncertainties which are mainly related to generator losses, load profile, renewable production and site's yield.

Robust optimization is used in lots of references as it provides much more guarantee on the system' reliability. In [193], robust planning of microgrid is carried with a two-stage optimization of investments and operation under worst-case scenario. The formulation of a robust optimization for a standalone system is well detailed in [194] in order to tackle the risk of insufficient renewable production. The results pointed out the advantages of dynamic programming technique instead of linear programming for improving computational time. In [195], a robust sizing of multi-energy system using MILP is proposed. The authors addressed the load and renewable uncertainty with either worst-cases scenarios (ensuring energy supply 100% of the time) and robust scenario (allow small lacks of energy supply). The result show that worst case scenario lead to high installation costs and sub-optimal solutions whereas robust scenarios allow better performing solution whilst keeping a good level of resiliency. This pushes to consider a certain level of tolerance in reliability constraints to avoid high installation costs.

An alternative to robust sizing is the formulation of a stochastic optimization problem. In the context of industrial microgrid, such approach are less relevant since they require a trade-off between reliability and economic performance. Regardless of the strategy to address uncertainties (stochastic or robust), a deep investigation of load and resources profiles must be carried to generate representative scenarios. This means collecting at least one year of data to suitably address daily and seasonal variations.

2.5 FORMULATION OF THE SCIENTIFIC APPROACH

2.5.1 *Highlights of literature review*

This chapter details the concept of industrial microgrids along with some key characteristics. Industry brings a new field of application for microgrids to add to those previously detailed in [14, 20, 21]. Additionally, a review of renewable integration studies in O&G systems illustrates the main challenges of industrial microgrids, which is a topic that has not been addressed in existing review papers.

The need for continuous operation of industrial power plants requires high availability of electrical generation. On the other hand, the electrical system is more vulnerable due to its low inertia and low flexibility compared to large grids or residential systems with electrical loads that are likely to be shed or delayed. The integration of highly variable and stochastic solar power challenges the performance and reliability of power plants as the rapid power losses involved can cause considerable electrical instabilities.

A particular feature of large-scale microgrids is their use of fossil generators. The integration of renewable energy sources therefore requires a change in the operational approach. Consequently, conventional modeling and optimization tools that were designed for static operations need to evolve, as fuel consumption, fatigue and emissions could significantly diverge from historic benchmarks.

The need for reliability calls for a more extensive understanding of the short-term behavior of renewable systems to anticipate extreme events. Variability analysis techniques have been developed to quantify solar ramps and can be coupled with a geographic smoothing model in order to assess the power fluctuation of the overall solar plant.

Control and management schemes must be chosen in order to correspond to this highly constrained framework. The large number of non-linearities (solar ramps, electrical instabilities, fuel consumption, etc.) as well as the role of the power quality call for the integration of a detailed description of the electrical system in future techno-economic studies. Optimization and simulation techniques should integrate these phenomena to better address the relationship between power control and energy management.

Finally, reliability of power system are the focus of lots of sizing methodologies. Linear formulations show promising capabilities but only provide constraints for the resiliency to generator contingency. On the other hand, non-linear formulation and meta-heuristics allow a more accurate description of electrical stability problem. However, no study were found to address both solar variability and electrical stability.

2.5.2 *Knowledge gaps*

Thanks to this literature review, the knowledge gaps for the performance evaluation and sizing optimization of industrial microgrids can be identified with a brighter vision.

Industrial power systems can be considered as low inertia systems which make them more sensitive to power fluctuations. Meanwhile, their tolerance to power quality disturbances is very low due to the level of reliability expected from operators. The impact of solar power variations on the quality of electricity supply in a system featuring large-scale fossil generators have not been addressed in the literature.

Solar short-term variability is characterized by its low temporal granularity (from a few seconds to one minute) which forces to perform grid simulation with a small temporal resolution. Commercial software and studies have proposed to integrate variable solar profiles but the computational time limit was not addressed. Consequently, available tools and models require large computational resources and are not fitted to the needs of a preliminary assessment study.

Since expensive mitigation technologies can be purchased for managing the solar variability, an accurate evaluation of PV power drops is necessary. The power ratings of industrial power systems leads to consider additional factors in the power PV profile generation such as geographical smoothing. Such aspect have been rarely addressed in the process of power quality evaluation of microgrids.

The operational strategy plays a important role in the economic and environmental performance of the power plant which pushes to adopt optimization techniques. However, this challenges the integration of electrical assessment. Consequently, most of studies addressing the performance evaluation of microgrid only cover a single aspect of the problem (power quality control or operational optimization).

A large number of studies have addressed the optimal sizing of microgrids while ensuring their resiliency to unplanned events such as renewable variations or fossil generation breakdown. However, the lack of dedicated frequency constraints for solar variability management prevents a reliable investment planning.

Existing work on frequency constraint sizing and unit commitment have highlighted the high computational complexity of models due to the non-linearity of power system equations. Additionally, recent work pointed out the risk of suboptimal solutions when using linearized formulation for frequency constraints. The use of optimization technique can be bypassed by performing a large number of grid simulations but the computational time of such method remains a limit for their use in the present application. This suggests taking advantage of both methods and combine them to provide optimal and robust sizing in a limited time.

2.5.3 *Research method*

The objective of this thesis is to provide methods helping industrial developers with the preliminary decision-making process of microgrids. The first problem is to accurately assess the electrical stability as well as economic and environmental performances. The second problem is to develop a sizing methodology for providing project engineers with reliable and optimal investment decisions on PV and storage installed capacities.

Thus, the main scientific objective of this thesis is to integrate the relationship between short term solar variability and electrical stability in the simulation of the optimal operational management of the plant as well as in the power plant's sizing optimization process. This involves developing a set of simulation and optimization models being able address the specificities of large-scale power generators and to consider the different time-scales where operational management and power control take place. The computational burden of the methods should be kept minimal to ensure that they match the needs of preliminary assessment phases. To reach this scientific objective, the following method is proposed and developed throughout the thesis:

Step 1 : Generation of solar variability scenarios (Chapter 3)

First, the identification of solar input scenarios taking irradiance variability into account is investigated. The main objective is to provide operational simulation and sizing with representative time series to properly evaluate electrical perturbations. To cope with the lack of available data, the use of worst-case irradiance dataset coupled with WVM smoothing is preferred to the synthetic generation of solar time series. Given the fact that solar ramps occur at low time-scales (several seconds), high-resolution time series must be used which is computationally demanding. The proposed approach aims at reducing the number of input solar time series for grid simulation. Additionally, the identification of a set of worst-case solar ramps is explored to integrate solar variability into energy-level optimization problems.

Step 2: Impact of solar variability on reliability (Chapter 4)

The impact of solar variability on the reliability of the power system was found to be one of the main research question. This second step aims at developing the proper model for the simulation of power quality under solar variability scenarios. Despite the fact that thermodynamic models can accurately evaluate fuel consumption and potential fatigue due to transient operation, their complexity of development, adaptation and computation puts them out of the scope for the present method. Instead, dynamic electrical model formulated in the Laplace domain are used.

Step 3 : Economic and environmental assessment (Chapter 4)

Economical and environmental performances are driven by EMS layers which take scheduling and dispatch decisions to minimize the fuel consumption or CO_2 emissions. This third step aims at reproducing the management strategy of an industrial microgrid. An EMS optimization problem is formulated based on MILP and decomposed into two layers : A schedule optimization is performed once a day for fossil unit commitment, and a dispatch layer recalculates optimal setpoints without changing the units operating status. This hierarchical structure allows keeping a close similarity to currently operated plants in TotalEnergies.

Step 4 : Integrated operational simulation (Chapter 4)

The electrical model and the energy management model are coupled together to perform the technical, economic and environmental assessment simultaneously. This allows considering the interconnections between energy management and power quality control layers. To reduce the computational burden, a scenario aggregation method is employed: A worst-case scenario provides conservative evaluation of electrical perturbations whereas days of varying variability and irradiance are used for calculating yearly performance indicators.

Step 5 : Sizing optimization (Chapter 5)

Since operational simulation is computationally demanding, a sizing optimization model is developed to find the best performing set of installed capacities for PV and storage systems. A MILP approach is used due to its many advantages in terms of formulation, solving capabilities and guarantee of optimality. Linear frequency constraints are formulated to ensure the system's resiliency against short-term solar drop. Worst-case solar ramp scenarios identified at step 1 are integrated to fit the hourly time-decomposition.

Step 6 : Full sizing procedure (Chapter 5)

As highlighted in the literature, linear formulation of frequency constraint lead to sub-optimal solution and potentially a poor evaluation of electrical perturbations. Thus the sizing optimization is coupled with the operational simulation to provide optimal and robust solutions.

3

SOLAR INPUT SCENARIOS AND SHORT-TERM VARIABILITY

This chapter proposes a set of tools to characterize the short-term variability of Global Horizontal Irradiance (GHI) profiles, simulate the geographical smoothing effect of photovoltaic power plants and extract representative scenarios that will be taken as input in grid simulation and sizing. This work is based on the conference paper presented at ICAE 2020 [196] and the study published in the associated journal Applied Energy [197].

Ce chapitre propose un ensemble de méthodes pour caractériser la variabilité à court terme des profils d'irradiation (GHI), simuler l'effet de lissage géographique des centrales photovoltaïques et extraire des scénarios représentatifs. Ces scénarios seront utilisés comme données d'entrée pour la simulation et le dimensionnement du micro-réseau. Ce travail est basé sur un article de conférence présenté à ICAE 2020 : [196] et un article publié dans la revue scientifique associée Applied Energy [197].

1 PRE-PROCESSING OF IRRADIANCE TIMESERIES

1.2. Quantifying solar variability

Identify and validate variability mertrics for short times scales

Contribution:
Proposed gradient based ramp detection algorithm

1.2. Reproduce the behavior of MW scale power plants

Apply Sandia Lab's Wavelet Variability method to reproduce MW-scale equivalent irradiance profile.

2 VARIABILITY SCENARIO IDENTIFICATION

2.2. Day long scenarios

Typical days choosen thanks to global indicators:
- Worst case scenario to represent the most variable day in the dataset
- Clustered set to evaluate the power plant in various situations

Contribution:
K-means clustering techniques based on global irradiance potential, mid-term variability and short-term variability.

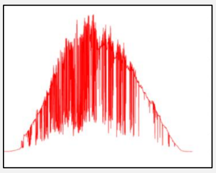

2.3. Isolated ramp scenarios

Set of isolated solar ramp extracted thanks to ramp-detection algotithm. expressed as irradiance drop (in KW/m²) over time period (in seconds).

Contributions:
- Worst-case scenario identification from ramp statistics
- Convex hull representation

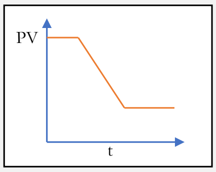

Contents

NOMENCLATURE OF CHAPTER 3

INDICES

Symbol	Description
t	Timestamp of irradiance timeseries
d	Day of year
σ	Cluster number
j	Clustering feature
r	Ramp event within a set of ramps

SETS

Symbol	Description
$\mathcal{R}$	Set of detected ramps
$\mathcal{R}^{\Delta T}$	Set of ramps of duration ΔT
$\mathcal{R}^{max}$	Set of ramps with highest irradiance drop
$\mathcal{H}^{max}$	Convex hull of detected ramps

VARIABLES

Symbol	Description
GHI_t	Global Horizontal Irradiance at t
GHI_t	Clear sky Irradiance at t
VI^{stein}	Variability index proposed in [90]
VI	Proposed variability index
L_{GHI}	Length of GHI curve
$\overline{GHI}_h$	Hourly average irradiance
N_{ramp}	Number of ramp detected in a daily timeseries
ΔI	Irradiance drop during cloud passage
ΔT	Duration of cloud passage
$GHI^{sim}_{plant}(t)$	GHI timeseries after WVM smoothing
GHI_{norm}	Normalized irradiance
$\omega_{\bar{t}}(k)$	Wavelet transform of GHI timeseries

$\bar{t}$	Equivalent frequency
ϕ	Top hat wavelet object
$D_{m,n}$	Distance between WVM sites
A	WVM correlation factor
N_{σ}	Number of elements in cluster
$\rho(d_{m,n}$	Variability dependency of WVM sites
$VR(\bar{t})$	WVM Variability reduction
E_{I_d}	Daily cumulative irradiance
$\overline{R}_{I_h d}$	Mid-term variability indicator for clustering
P_L	Electrical load power
P_{gen}	Fossil generation power
P_{bat}	Battery power
P_{PV}	PV system output power
K_{θ}	PV Temperature derating factor
η	PV global derating factor
Q_{PV}	PV installed capacity
P_{gen}^{max}	Maximum power output of fossil generation
P_{bat}^{max}	Maximum Battery power output
R_{PV_h}	PV spinning reserve margin
M	Mechanical inertia constant
$N^{cluster}$	Number of cluster for Kmeans
G_j^k	Coordinate of center of gravity in dimension j
N_k	Number of element in cluster k
x^k	Element within cluster k
D_i^k	Euclidean distance to center of gravity of cluster k
$\overline{X_j}^{kmeans}$	Weighted average value of kmeans feature j
$P_{unmetload}$	Power unbalance during cloud passage
rr_{gen}	Fossil generation ramp-rate
Υ	Maximum power unbalance during cloud passage

3.1 INTRODUCTION

Integrating large scale PV system in industrial microgrids is a challenging task due to the level of reliability required by electrical consumers. As stated in part 2.1.4, power plant developers must carry a detailed assessment of each factor that may cause a loss of electricity supply. In conventional systems, equipment faults and maintenance are the main risk of electrical perturbations but hybrid systems now faces new perturbations related to the short-term variability of renewable resources. Due to cloud passage, MW-scale PV power plants may loose almost all their production in several seconds. This power drop must therefore be rapidly compensated to avoid large electrical instabilities which requires either fast-response from fossil generation or storage devices. To properly evaluate the economical performances of the system and guarantee its safe operation, solar variability must be deeply investigated.

In the process of sizing and simulating microgrids, solar input scenarios are necessary to provide an approximation of the system in real-life conditions. Hourly-averaged irradiance profiles are generally used by developers thanks to meteorological data. But this overlooks the short-time behaviour of the PV plant and does not allows evaluating the risk of electrical perturbation in case of cloud passage. Hence, new types of scenarios must be identified to take solar variability into account when carrying the performance assessment of industrial microgrids. One of the main challenge is that only high-resolution time-series are able to capture short-term solar variability. For practical reasons related to simulation time and computational complexity, it is not possible to simulate one year of 1-second irradiance data. This calls for a selection of typical scenarios among the dataset.

This chapter presents a methodology to identify two types of solar input scenarios taking solar variability into account: day-long scenarios and isolated ramp scenarios.

First, a pre-treatment procedure is proposed which consists in quantifying the level of variability of a 1-second GHI time series and applying the Wavelet Variability Model (WVM) to reproduce the short term behaviour of MW-scale power plants. Then, day-long scenarios are extracted from the dataset thanks to timeseries clustering. Finally, a set of isolated ramp event is extracted to allow quicker grid simulations and integrate solar variability in microgrid's preliminary assessment procedures.

3.2 PRE-TREATMENT OF GLOBAL HORIZONTAL IRRADIANCE TIME-SERIES

3.2.1 *Variability metrics to characterize daily time series*

To simulate the PV power plant under different levels of variability, quantifiers are necessary to identify and classify solar input scenarios. Lots of indicators already exist to evaluate the solar variability and provide an insight on the solar perturbation that the grid will face (see 2.2.2). However, the sub-minute variability is rarely addressed in the literature. Due to the low inertia of industrial microgrids, sharp drops with a short duration may have a significant impact on the grid stability. Thus, it is necessary to identify a variability indicator adapted to small time scales. In this chapter, the Variability Index (VI) proposed by Stein et. al [90] is used due to its simplicity of calculation and its adaptability to time increments. A limitation of such global indicator is that cloud passage is overlooked and that it does not provide a decomposition of all the ramp events causing solar variability. A second methodology is therefore proposed, which consists in detecting each PV ramp-down thank to a gradient based sliding window algorithm. The resulting daily number of ramps gives a new global indicator that will be compared to the VI. This detection approach also allows building useful ramp statistics that will be used later in this chapter for isolated scenario identification.

3.2.1.1 *The Variability Index*

In their study, Stein et. al proposed a variability index calculated as the ratio of the pyranometer global horizontal irradiance (GHI) measurement curve length over the clear-sky irradiance (CSI) curve length [90]. Clear sky irradiance can be computed thanks to clear-sky model such as the Ineichen model [198]. For the sake of simplicity, hourly averaged irradiance values are used in this work instead of clear-sky irradiance. This avoids the use of clear-sky irradiance models and simplifies the data preparation process for further use in preliminary studies.

The original VI formualtion is expressed in Eq. 3.1 where GHI_t is the measured irradiance and CSI_t is the clear sky irradiance.

$$VI^{stein} = \frac{\sum_{t=t_0}^{t_f} \sqrt{(GHI_{t+1} - GHI_t)^2 + \Delta t^2}}{\sum_{t=t_0}^{t_f} \sqrt{(CSI_{t+1} - CSI_t)^2 + \Delta t^2}} \tag{3.1}$$

The VI calculation based on hourly averaged irradiance is expressed in Eq. 3.2 where L_{GHI} and $L_{\overline{GHI}}$ are the curve lengths of the pyranometer measurements and hourly averaged irradiance respectively. Curve lengths calculations are expressed in Eq. 3.3 and 3.4 with $\overline{GHI}_h$ being the hourly averaged irradiance between h and $h+1$.

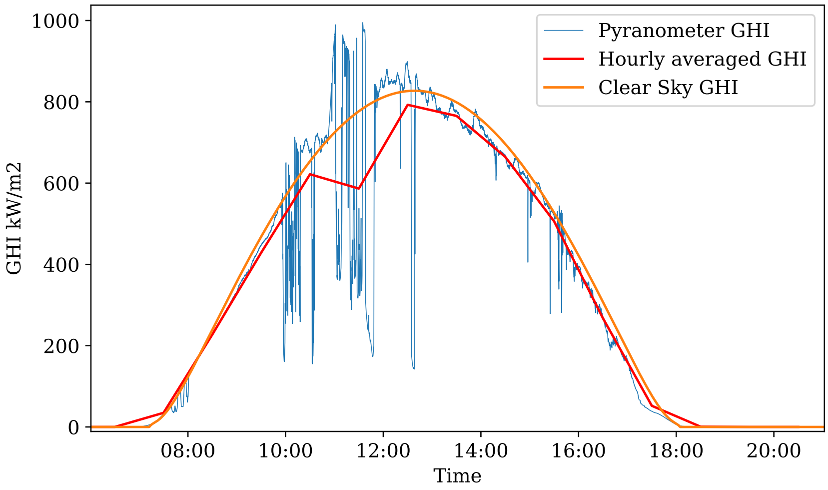

Figure 3.1: Pyranometer measurements, clear-sky irradiance and hourly averaged irradiance of a typical day in Hawaii.

$$VI = \frac{L_{GHI}}{L_{\overline{GHI}}} \tag{3.2}$$

$$L_{GHI} = \sum_{t=t_0}^{t_f} \sqrt{(GHI_{t+1} - GHI_t)^2 + \Delta t^2} \tag{3.3}$$

$$L_{\overline{GHI}} = \sum_{h=h_0}^{h_f} \sqrt{(\overline{GHI}_{h+1} - \overline{GHI}_h)^2 + 3600^2} \tag{3.4}$$

3.2.1.2 *The Ramp Detection Algorithm*

Thanks to the VI, the level of variability can be easily evaluated and quantified with a global indicator. However, this method overlooks the cloud-passage phenomenon by calculating global ratios of curve length. In hybrid systems, only fast ramp-rates (exceeding storage and fossil response capacity) will impact the stability of the system. Thus, a more comprehensive quantification method is useful to decompose solar drop events individually.

Numerous methods can be implemented to extract solar drops with varying levels of complexity. In [95], the solar profile 1-second derivative is used to evaluate the ramp rate. This method can be extended to a larger fixed-time window, but this leads to neglect irradiance changes occurring within the time interval. In this case, such a method cannot be implemented because the time scale of the solar ramp is expected to vary between raw pyranometer data and

PV production data (up to 60% of irradiance change reduction is expected for 1-second resolution data due to geographical smoothing [94]). In [199], a recognition method for irradiance transition was proposed based on moving averaged variations but the algorithm was not provided in the study. This pushed to propose a similar method in this work to detect solar ramps.

Algorithm 1 Ramp detection algorithm.

```
$A \leftarrow 0.009$                                          ▷ Initialization
$N_{ramp} \leftarrow 0$
while $i < N_{TS}$ do
    $P' \leftarrow I(i) - I(i-1)$
    $k \leftarrow 0$
    if $P' < A$ then
        $n_{ramp} \leftarrow n_{ramp} + 1$
        $I'_2 \leftarrow I'$
        while $i + k < N_{TS}$ & $I' * I'_2 > 0$ do
            $I'_2 \leftarrow I(i+k) - I(i+k-1)$
            $k \leftarrow k + 1$
        $T_R(n_{ramp}) \leftarrow k$
        $\Delta I(n_{ramp}) \leftarrow I(i-1) - I(i+k-1)$
    if $k = 0$ then
        $i \leftarrow i + 1$
    else
        $i \leftarrow i + k$
$N_{ramp} \leftarrow n_{ramp}$
```

The algorithm's pseudo-code is presented in Alg. 1. The RDA starts detecting an irradiance ramp if its gradient is higher than the trigger value A (in $W.m^{-2}.s^{-1}$) [1]. The duration of the ramp k starts at 1 second and increases until the irradiance curve's derivative changes its sign or if the last element of the timeseries is reached ($i + k = N_{TS}$). When the end of the ramp is reached, the ramp duration k is stored in $T_R(n_{ramp})$ and the irradiance change is stored in $\Delta I_R(n_{ramp})$. n_{ramp} is the ramp number counter variable which gives the total number ramps at the end of the iterations. The time increments of the methods (denoted as i in Alg. 1) corresponds to the sampling time of the timeseries (1 second in this work). The length of the timeseries N_{TS} corresponds to the number of samples in the timeseries (54000 in this work).

Figure 3.2 shows an example of RDA application on a 100 second time-window. As shown in the figure, only ramp-down events are tracked. This is justified by the fact that fossil generation have higher

---

[1] This value was tested graphically to capture the beginning and end of ramps. The results are naturally sensitive to this value : if A is too low, a ramp could be detected too late which would underestimate its final slope.

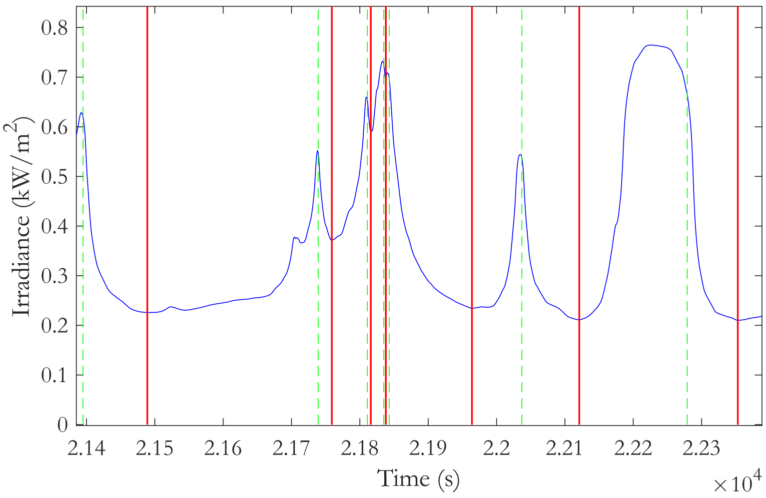

Figure 3.2: Solar drops detected thanks to the detailed algorithm. Green dashed line show the beginning of the solar drop, red lines show the end of the solar drop.

ramp-down capabilities than ramp-up. The total number of ramps obtained N_{ramp} provides another quantifier for the daily level of variability. This quantifier will be compared to the VI in the following part.

Finally, as shown in Fig 3.3, the RDA can characterize isolated events by storing the pairs ΔI_i and T_i. This allows extracting worst-case isolated ramp scenarios and simulate an equivalent perturbation of the system which will be investigated in part 3.3.2.

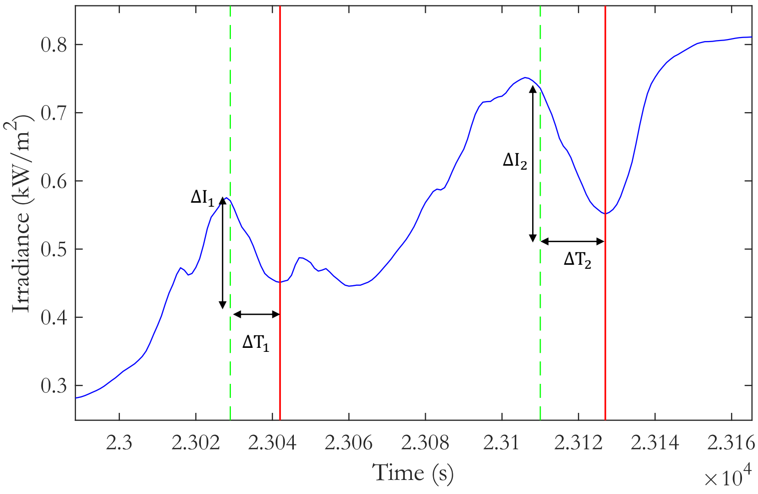

Figure 3.3: Evaluation of each ramp feature : ΔI_i the irradiance lost within the interval T_i.

3.2.1.3 *Application on daily time series and comparison of indicators*

VI and N_{ramps} are compared by calculating daily values on the data collected by NREL [2] in Oahu [89]. Thanks to the work carried out in [92], where solar variability zones were evaluated from a set of measurements of nine power plants, the area of Hawaii was found to be one of the most variable in the world in terms of solar irradiance. This is also confirmed by the results presented in [200]. Hence, the analysis carried using this dataset can also be considered as a worst-case benchmark for future studies. The dataset is composed of 365 daily time series covering 5 am to 8 pm with a 1-second sampling time [3].

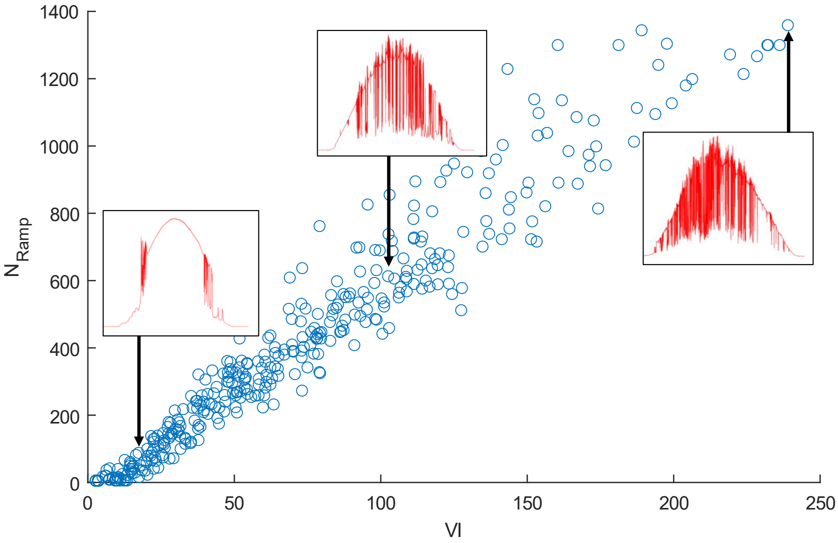

Figure 3.4: VI and Nramp index for 3 days in the Hawaii data-set.

VI and N_{ramp} have been evaluated on each day of the data-set between 2011-10-01 and 2011-09-30 [4]. Figure 3.4 shows as example of three irradiance profiles and Tab. 3.1 reports their corresponding VI and N_{ramps}. The 19th of January shows a smooth irradiance profile which is consistent with low variability metrics ($VI = 14.3$ and $N_{ramp} = 111$). On the right side of the figure, the 16th of march shows the highest variability metrics ($VI = 223.8$ and $N_{ramp} = 1214$) which is consistent with its highly variable profile. The trends of variability metrics are therefore visually confirmed by the shapes of irradiance profiles.

---

[2] National Renewable Energy Laboratory

[3] Uncertainties in the measurement of solar irradiance have been neglected since the information was not made available by NREL

[4] The range value of the VI are different from the indexes processed by Stein et. al. in [90], which range from 0 to 15. This is because 1-min resolution data are used in [90], whereas 1-second data are used in this study, which gives a longer GHI curve

Date	VI	N_{ramps}
2011-01-09	14.3	111
2011-03-28	104.6	606
2011-03-16	223.8	1214

Table 3.1: VI and N_{ramp} for the 3 days shown in Fig. 3.4.

In Fig 3.5, VI is plotted against N_{ramp}. The figure shows that the two metrics are similarly distributed. A correlation factor of 0.96 is found between VI and N_{ramp}. From these results, it appears that the VI is consistent with ramp statistics processed at sub-minute levels. Thus, VI and N_{ramp} seems to equally success at describing the daily level of variability.

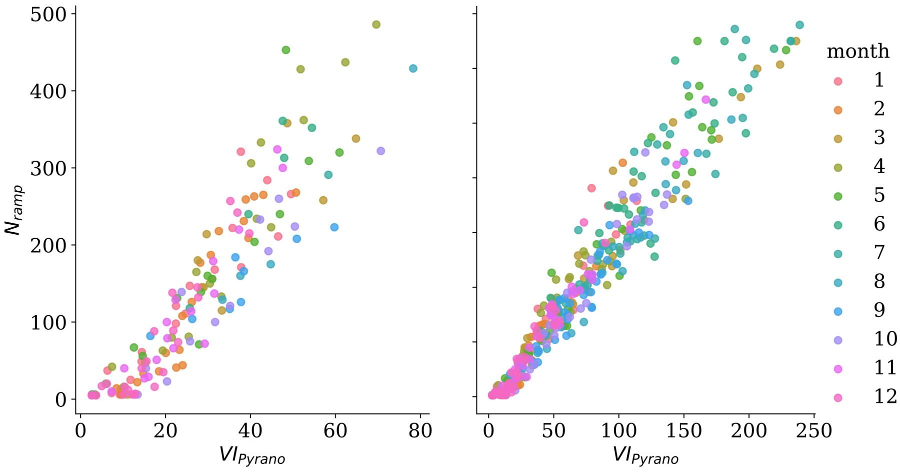

Figure 3.5: Repartition of VI and N_{ramp} with colors depending on the month. A zoom for low variability index is shown in the right-hand side figure.

The main advantage of the VI is its straightforward mathematical formulation, allowing fast calculation and easy comparison between independent datasets. On the other hand, the ramp detection is sensitive to the gradient trigger value A. This means that a parameter calibration could be necessary before applying the ramp detection over another dataset. The VI seems more suited to assess the global level of variability of a timeseries.

On the other hand, running the RDA provides more quantitative results such as the number of ramp exceeding a certain limit of irradiance drop, PV ramp-rate etc. Thanks to the decomposition of the timeseries into isolated events, the RDA is able to extract variability scenarios for use is dynamic simulation. This will be investigated in the next parts of this chapter.

3.2.2 *PV plant geographical variability smoothing*

In the assessment process of microgrids, only irradiance timeseries measured by sensors are available. But as highlighted in Chapter 2, the irradiance variations captured by pyranometers or solar cells are significantly higher than the power changes observed at the output of a large scale PV plant. This effect is called "geographical smoothing" and is explained by the fact that large scale power plants experience partial shadings of clouds due to their large surface (see Fig 3.6). During the cloud passage, irradiance sensors will capture the effect of the cloud at their specific locations whereas the output power behaviour is the result of all irradiance changes over the surface.

If the irradiance sensor's variability is considered in the dynamic assessment of microgrids, electrical perturbations will be over-estimated. This will result in a costly over-sizing of the battery or even a PV plant reduction to limit electrical perturbation. Therefore, the modelling of the geographical smoothing effect is a crucial step before performing the dynamic analysis.

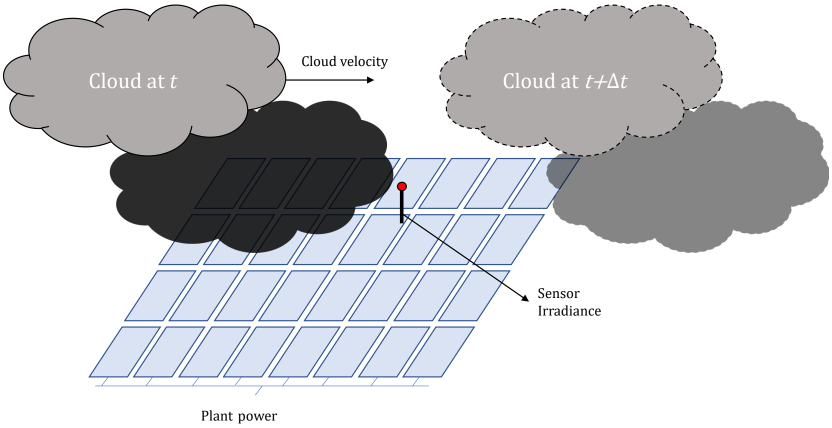

Figure 3.6: Partial shading of PV plant is responsible for the geographical smoothing effect of solar variability.

A methodology based on the wavelet control signal theory has been developed by Lave and Kleissl [98] to simulate the equivalent irradiance profile of a MW-scale power plant and therefore smooth out the single-sensor irradiance. A strong advantage of this method is that the temporal resolution of the simulated power output is the same as the measured irradiance. The WVM has been implemented in Matlab and Python and its libraries are freely available on Sandia National Lab website [99]. The following parts briefly introduce the main steps of the WVM and show how the model will be integrated for the generation of solar input scenarios.

3.2.2.1 *The wavelet variability model*

The main steps of the WVM are summarized in this paragraph but the reader may refer to reference [201] for an extended description of the methodology. The objective of the method is to convert single sensor irradiance timerseries $GHI(t)$ into the equivalent plant's irradiance timeseries $GHI_{plant}^{sim}(t)$.

First, a wavelet transform is applied to a normalized series GHI_{norm} computed using clear sky irradiance and GHI profiles. Wavelet transform $\omega_{\bar{t}}(k)$ consists in describing a signal using a series of wavelet objects ϕ (see Fig 3.7) varying in scale $\bar{t}$ (equivalent frequency) and time-shifts k. Eq. 3.5 expressed the GHI signal's wavelet transform.

$$\omega_{\bar{t}}(k) = \int_{t_{start}}^{t_{end}} GHI_{norm}(t') \frac{1}{\sqrt{\bar{t}}} \phi(\frac{t'-k}{\bar{t}}) dt' \tag{3.5}$$

Where t_{start} ,t_{end} denote the starting and ending times of the timeseries and t' the time-integration variable.

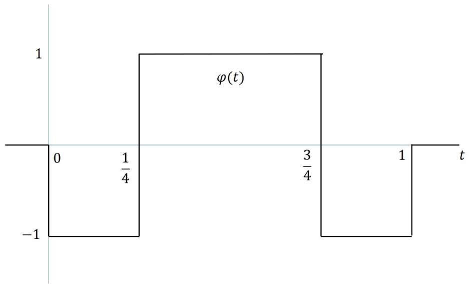

Figure 3.7: Top hat transform used in the WVM.

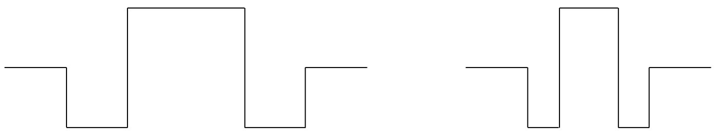

$\bar{t} > 1$
Large scale factor, Small frequency

$0 < \bar{t} < 1$
Small scale factor, high frequency

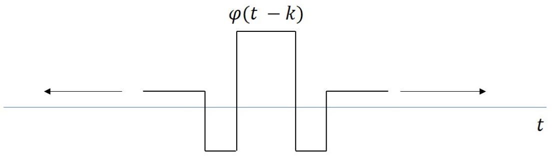

Shift in time by k

Figure 3.8: Effect of scale $\bar{t}$ and shift k on wavelet objects.

The WVM method decomposes the GHI_{norm} signal into 12 wavelet modes in order to account for dynamics at different timescales (from 2^1 seconds to $2^{12} = 4096$ seconds, where $j = 12$ was found to be the limit above which the smoothing effect in insignificant). Eq. 3.6

expresses the property stating that the sum of wavelet modes is equal to the original input signal.

$$\sum_{j=1}^{12} \omega_{\bar{t}=2^j}(t) = GHI_{norm}(t) \tag{3.6}$$

The PV power plant is discretized into N "sites" representing a small amount of PV modules. Then, distances between sites are calculated.

The correlation ρ expresses the strength of the variability dependency between two sites is and calculated as a function of the distance $D_{m,n}$ between sites n and m and timescale $\bar{t}$.

$$\rho(D_{m,n}, \bar{t}) = \exp(-\frac{d_{m,n}}{A.\bar{t}}) \tag{3.7}$$

Where A is a correlation factor that mostly depend on the cloud dynamics and therefore changes with meteorological conditions and locations. More details on the calculation of A are provided in [98]. It is important to notice that cloud dynamics effect is assumed to be isotropic which means that the effect of the plant size and shape is independent from the direction of the clouds.

Variability reduction VR is defined as the ratio of variance of point sensor irradiance by variance of the entire PV power plant at each timescale (Eq. 3.8). If $VR = N$, sites and entirely independent from each other whereas they are fully dependant if $VR = 1$.

$$VR(\bar{t}) = \frac{N^2}{\sum_{m=1}^{N} \sum_{n=1}^{N} \rho(D_{m,n}, \bar{t})} \tag{3.8}$$

The calculation of the variability reduction allows evaluating the PV plant equivalent wavelet modes $\omega_{\bar{t}}^{sim}$ by dividing original wavelet modes $\omega_{\bar{t}(t)}$ by the VR. Eq. 3.9 shows that the more independent the sites are, the lower the impact on the variability reduction will become.

$$\omega_{\bar{t}}^{sim} = \frac{\omega_{\bar{t}(t)}}{\sqrt{VR(t)}} \tag{3.9}$$

Then, an inverse wavelet transform is used to build the averaged irradiance over the PV plant $\langle GHI_{norm}^{sim} \rangle_{plant}$.

$$\langle GHI_{norm}^{sim} \rangle_{plant}(t) = \sum_{j=1}^{12} \omega_{\bar{t}=2^j}^{sim}(t) \tag{3.10}$$

The equivalent GHI values of the plant are finally scaled back to obtain the final equivalent irradiance GHI_{plant}^{sim}.

3.2.2.2 *Application on daily time series*

To validate the interest of pre-treating irradiance timeseries by the WVM, the procedure is applied on the Oahu's dataset. As recommended in [99], a conservative cloud speed of 20 $m.s^{-1}$ is considered.

Figure 3.9 compares the equivalent GHI timeseries of a 50MW power plant GHI^{sim}_{50MW}, a 0.5MW power plant $GHI^{sim}_{0.5kW}$ and the raw profile GHI. The figure suggest that the geographical smoothing effect may be neglected for small PV power plant since small differences are observed between $GHI^{sim}_{0.5kW}$ and GHI. However, significant differences are obtained for a large scale power plant with an irradiance change of less than 100 $W.m^{-2}$ at 12:57 for the 50 MW power plant against more than 500 $W.m^{-2}$ for the raw profile. The duration of the ramp is also impacted with a ramp duration of 1 minute for the 50MW PV plant against 25 seconds for the raw profile.

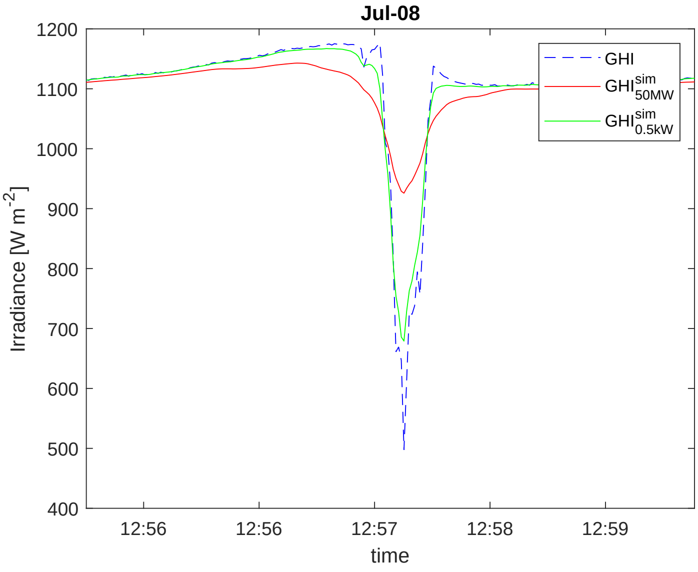

Figure 3.9: Impact of power plant size on short-term behaviour of GHI timeseries.

The VI and N_{ramps} of GHI^{sim}_{50MW} and GHI are calculated for each day of the dataset and reported in Fig 3.10. For the raw timeseries, a maximum N_{ramp} of 1359 and a maximum VI of 238 are observed. On the other had, the maximum values for N_{ramp} and VI after WVM smoothing are 74 and 257 respectively. These results highlight that the WVM has a strong impact on variability metrics.

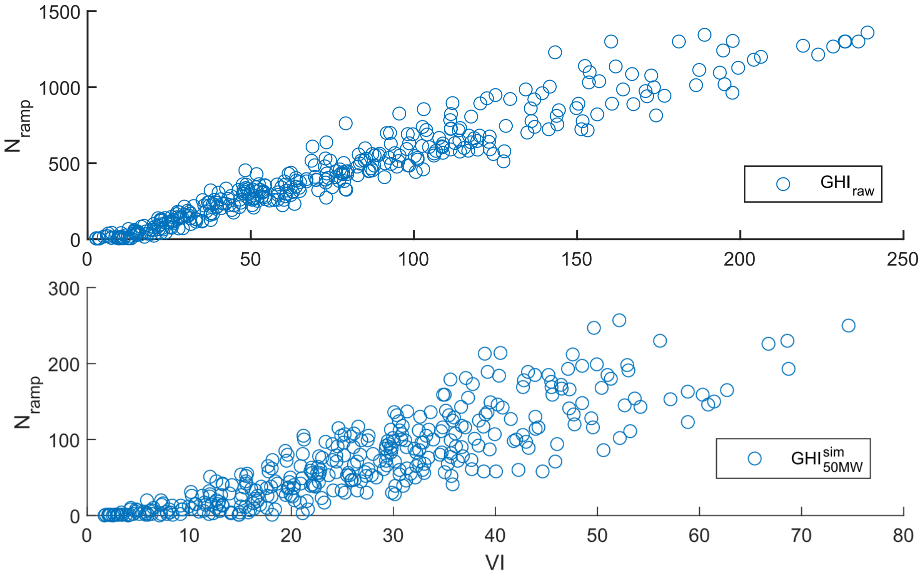

Figure 3.10: N_{ramp} and VI for each day of the dataset. Upper figure shows raw pyranometer values and lower figure shows 50MW WVM filtered values.

Finally, Fig 3.11 shows that the model is also sensitive to the cloud speed parameter which is difficult to evaluate. Hence, the conservative value of 20 $\mathrm{m.s}^{-1}$ will be used when applying the WVM in the next part of this work.

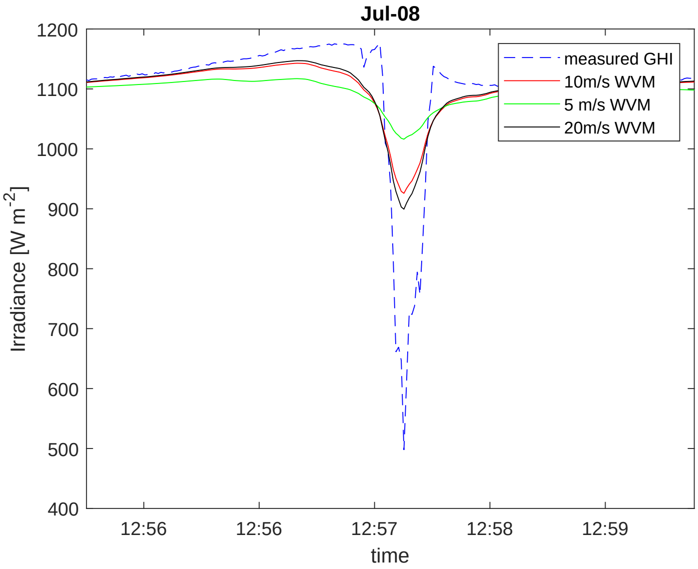

Figure 3.11: Impact of cloud speed on short-term behaviour of GHI timeseries (for a PV power plant of 50 MW).

By significantly modifying the dynamic behaviour of the timeseries at short-time scales, the WVM reveals that MW-scale power plant will experience smoother solar drops than the ones captured by sensors.

Since the WVM provides timeseries with the same temporal granularity as the input data, the simulated irradiance profile can be easily integrated in the simulation process of the power plant. Therefore, solar variability will be addressed with more accuracy which will avoid the over-estimation of electrical perturbations during cloud passage.

3.3 IDENTIFICATION OF REPRESENTATIVE SCENARIOS EVENTS THANKS TO RAMP DETECTION AND VARIABILITY METRICS

The previous section developed two quantifiers for sub-minute solar variability; Then, WVM has been employed to simulate the geographical smoothing effect and obtain the equivalent irradiance timeseries of a MW-scale PV power plant.

In this section, two types of scenario will be identified to address sub-minute variability in grid simulations (Fig 3.12, 3.13) : day-long scenario and isolated scenarios.

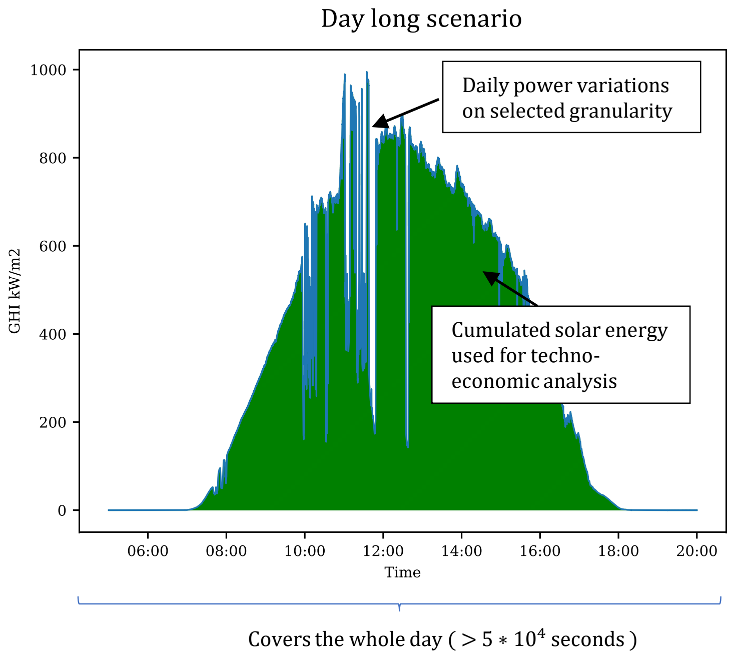
Day long scenario

Daily power variations on selected granularity

Cumulated solar energy used for techno-economic analysis

Covers the whole day ($> 5 * 10^4$ seconds)

Figure 3.12: Day-long scenarios characteristics.

Day-long scenarios are widely employed in microgrid studies. They consist in using a daily timeseries of a given granularity (generally hourly averaged profile are used as presented in [86, 180] to reproduce the PV power plant behaviour and calculate global performances such as the total injected solar energy or CO2 reduction. In the context of this work, grid dynamics must be accurately taken into account which forces to use high-resolution input data and dynamic electrical model. Consequently, computational time is increased as compared to hourly models and does allow simulating the 365 days of the year. If only power quality is of interest, worst-case day-long scenario can be used to account for the highest level of perturbation. The identification of worst-case daily scenario thanks to the VI will be covered in part 3.3.1.1. On the other hand, to fulfil the need of lifetime equivalent indicators such as renewable penetration rate and CO2 emission, worst-case scenario is not sufficient. Part 3.3.1.2 will present the identification process of a set of representative days.

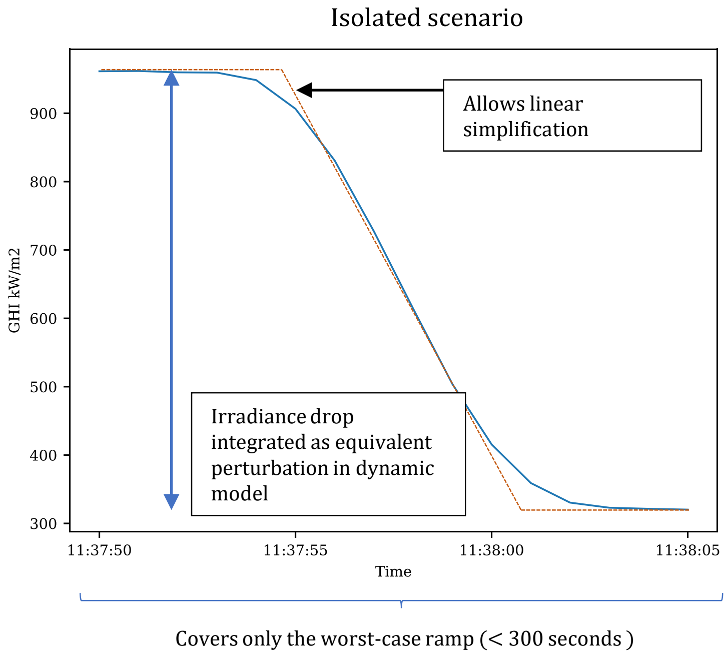

Figure 3.13: Isolated scenarios characteristics.

An alternative to day-long scenarios consists in using isolated ramp event accounting for the largest PV perturbation. This significantly reduces the computation time since the duration of a short-term solar drop does not exceeds 3 minutes. This is particularly useful when dynamic models are too complex to be simulated over a day-long timeseries or for the fast evaluation of mitigation needs such as done in [95]. Another advantage of this approach is that it aggregates the short-term variability and allows its integration in high-level formulation with larger temporal granularity. Such approach is used for generator contingency simulation where the loss of a generator is reduced to a load step. The identification of isolated ramp as input variability scenario will be covered in part 3.3.2.

3.3.1 *Day-long time-series as scenarios*

3.3.1.1 *The worst-case approach*

The worst-case approach consists in identifying the day during which the operation of the microgrid is likely to be the most difficult. Since this work focuses on reliability against cloud passage, worst-case identification is based on variability metrics (VI and N_{ramp}). Tab. 3.2 shows the highest N_{ramp} and VI of the Hawaii dataset before and after applying the WVM procedure for a 50MW power plant.

N_{ramp} and VI point at the same worst-case day for the raw data (2011-07-08). Two different days are obtained for the wvm-filtered dataset (2011-03-16 and 2011-07-08). The timeseries of 2011-03-16 shows larger VI than 2011-07-08 (74.6 against 52) whereas only a small differences are reported for N_{ramp} (250 against 257) which suggests higher short-term variability for 2011-03-16.

From these results, the worst-case scenarios in terms of short-term variability appears to be 2011-07-08 for raw pyranometer timeseries and 2011-03-16 for MW-scale simulated timeseries.

Data type	**/ Qualification method**	**Ramp Detection**	**Variability Index**
Pyranometer data	Date of worst case	2011-07-08	
	VI	238.97	
	Number of ramps	1359	
WVM filtered data	Date of worst case	2011-07-08	2011-03-16
	VI	52.13	74.60
	Number of ramps	257	250

Table 3.2: Solar variability indexes of the worst cases for pyranometer data and WVM-smoothed data.

3.3.1.2 *A clustering technique to identify representative time-series based on variability characteristics*

Worst-case approaches allow a robust sizing but may also lead to costly architectures. The optimization process for architecture sizing benefits from considering more than one worst-case scenarios and account for various situation such as cloudy days with low solar penetration.

As highlighted in [202], identifying a set of typical days of irradiance allow increasing the level of accuracy of the results while keeping the computation time to a reasonable value. The authors proposed to aggregate representative days to capture solar and load seasonal variations. Artificial intelligence (AI) clustering techniques were used. They aimed at forming a group of data called “cluster” in which all the elements share similar characteristics called “features”. In their analysis, the authors used the hourly averaged PV profile to generate input scenarios. However, in the present analysis, short-term characteristics are expected to have a large impact on architectures. This leads to add new criteria into the aggregation process. In [203], a scenario reduction method has been proposed to account for solar profile stochastic behaviour. The authors used the clearness index (ratio between measured irradiance and clear-sky irradiance) to qualify daily profiles and applied the K-means clustering method to generate representative scenarios. However, the clearness index does not fully represent the short-term variability because it does not address the sharpness of the solar drops. Hence, the variability index detailed in the previous section will be used as a feature for scenario generation.

This will allow considering short-term variability in the clustering process.

The first step of the process is to identify daily indicators by analysing how solar timeseries characteristics impact the objectives and constraints of the power plant :

1. The daily cumulated irradiance is used to calculate and maximize fuel savings in most sizing and operational management formulation [86, 167]

2. The variations of irradiance within hourly interval is used to calculate the spinning reserve requirement. Due to minimum and maximum power ratings of engines, spinning reserve requirement force to limit the PV penetration which reduce the profitability of the system. [204]

3. The magnitude and gradient of solar drops impact the real-time system's stability by adding electrical perturbation within the power system's equation of motion [126]. The sizing of mitigation technologies (storage, fast-responding fossil units, load sheddings etc.) directly depends on frequency deviations.

Table 3.3 sums up the selected indicators.

System objective/constraint	Time series characteristic	Indicator
Minimization of fuel consumption	Daily cumulative irradiance	E_{I_d}
Spinning reserve requirement	Maximum gap between hourly averaged irradiance and real irradiance value	$\overline{R_{I_h}}_d$
Frequency deviation	Sharpness of the timeseries	VI_d

Table 3.3: System constraints and daily indicators.

CUMULATIVE IRRADIANCE

In sizing and operational management formulations, fossil units, storage system and renewable resources must balance the hourly electrical load demand P_{L_h} (Eq. 3.11). From, 3.12, we can see that the higher is the irradiance, the lower is the fuel consumption and battery requirement.

$$\forall h \quad P_{L_h} = P_{gen_h} + P_{bat_h} + P_{PV_h} \tag{3.11}$$

$$P_{PV_h} = W_{PV} * \overline{GHI_{d,h}} * [1 - K_\theta(\theta - 25)] \tag{3.12}$$

In the objective function, the fossil generation fuel costs are calculated as the sum of hourly fuel cost $\sum_h FC_h$. At a first order the cumulative irradiance can be considered as the main factor for fuel cost reduction. Thus, the daily cumulative irradiance E_{I_d} (expressed in Eq. 3.14) provides a first indicator for the timeseries clustering where $\overline{GHI_{d,h}}$ denotes the mean value (in kW/m^2) between h and $h+1$ for a day d.

$$E_{I_d} = \sum_{h=0}^{24} \overline{GHI_{d,h}} \tag{3.13}$$

$$\overline{GHI_{d,h}} = \frac{\sum_{t=1}^{3600} GHI_{d,h,t}}{3600} \tag{3.14}$$

MID-TERM VARIABILITY

When performing the power plant schedule, operators must allocate sufficient power margin to cover the difference between hourly PV forecast P_{PV_h} and the real-time PV production P_{PV_t}. If PV power variations are larger than the total operational margin of fossil units and storage system, the stability of the system and the continuity of electricity supply cannot be guaranteed. Eq. 3.15 shows the spinning reserve requirement calculation[5]. Where R_{PV_h} accounts for the risk of PV variation within the hourly time interval h[6].

$$\sum_{gen} P_{gen}^{max} - P_{gen_h} + P_{bat}^{max} - P_{bat_h} \geqslant R_{PV_h} \tag{3.15}$$

R_{PV} can be evaluated by estimating the highest difference between the forecast value and the real value P_{PV_t} at each timestep t (Eq. 3.16). In a deterministic approach, the PV forecast is assumed to be known and corresponds to the hourly averaged PV production P_{PVh}.

$$R_{PV_h} = \max_t (P_{PVh} - P_{PV_t}) \tag{3.16}$$

Consequently, the spinning reserve requirement dedicated to the PV mid-term variability can be expressed as a function of irradiance variations (Eq. 3.17) as illustrated in Fig. 3.14.

$$R_{I_{d,h}} = \max_{t \in [h, h+3600]} (\overline{GHI_{d,h}} - GHI_{d,t}) \tag{3.17}$$

The daily mean value of $R_{I_{d,h}}$ is selected for mid-term variability indicator and expressed in Eq. 3.18. h^0 and h^f are the daylight starting and ending time (5am and 8pm in this case).

---

[5] Note that a second equation ensures similar margin between generators power output and minimum power ratings. This equation is not detailed for the sake of conciseness

[6] In this work, the uncertainties related to a prediction tool are not directly taken into account. The problem is deterministic in the sense that the hourly production is considered known (average value). The uncertainty interval is also known since it is calculated from a historical irradiance data set.

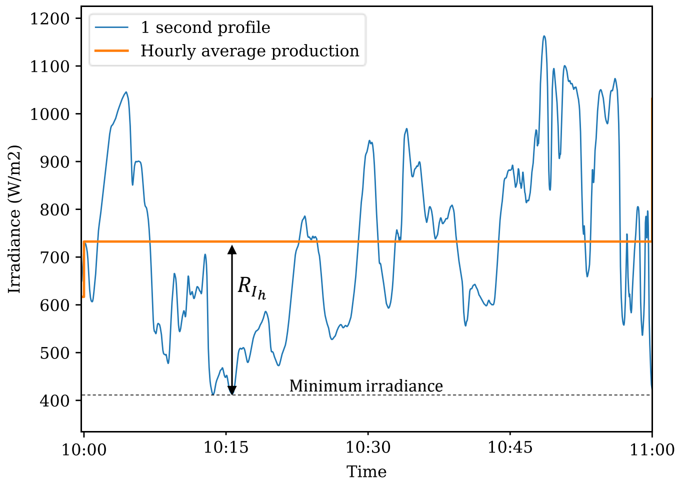

Figure 3.14: Calculation of R_{I_h} in an hourly interval.

$$\overline{R_{I_h d}} = \frac{\sum_{h0}^{hf} R_{I_{d,h}}}{h_f - h_0} \tag{3.18}$$

RISK OF POWER QUALITY DEGRADATION

Finally, the relationship between power quality degradation and irradiance variability must be investigated. Equation 3.19 expresses the frequency shift as a function of incremental power variation ΔP where M is the inertia constant of the system (defined in chapter 2). From this equation, we can see that the variation ΔP_{PV} over a short period dt will have an impact on the power quality.

$$\frac{d\Delta f}{dt} = \frac{\sum_{gen} \Delta P_{gen} + \Delta P_{PV} + \Delta P_{bat} - \Delta P_L}{M} \tag{3.19}$$

In the previous section, a clear correlation between daily VI and solar ramps have been observed. Therefore, the VI will be used as daily indicator to characterise the level of sub-minute variability.

APPLICATION OF KMEANS CLUSTERING

Daily indicators have been calculated and reported in Fig 3.15. Since no clear separation appear in the data, AI technique can be used to generate clusters and extract representative scenarios. In [202, 205], Kmeans algorithm was used to aggregate yearly demand data for microgrid optimization with good performances in representing the full dataset. This motivates the use of the same technique for PV input data reduction. The Kmeans algorithms relies on a minimization of the distances between the element of a group and the center of gravity of the group.

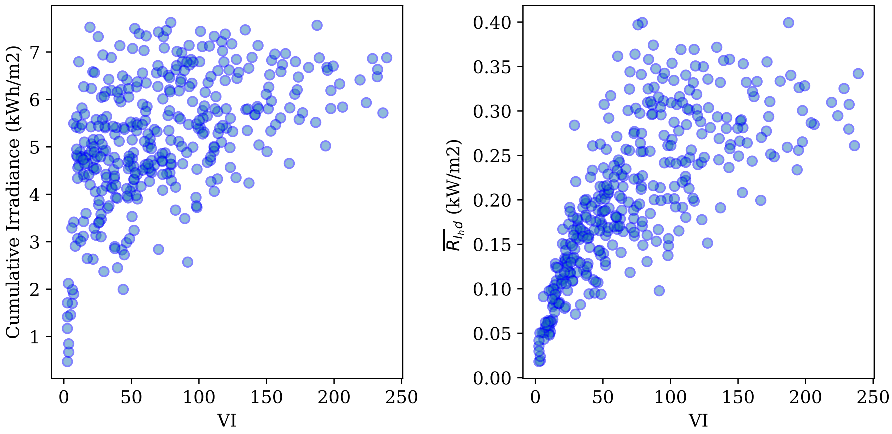

Figure 3.15: Repartitions of each day of the dataset over the selected features.

The first step is to normalize the feature so that distances in each dimension are in the same order of magnitude. The normalized indicator value X_d^{norm} of a day d is calculated as follow:

$$X_d^{norm} = \frac{X_d}{X_d^{max}} \tag{3.20}$$

Kmeans method divides the dataset in a defined number of clusters $N^{cluster}$. Fig. 3.16 shows an example with $N^{cluster} = 5$.

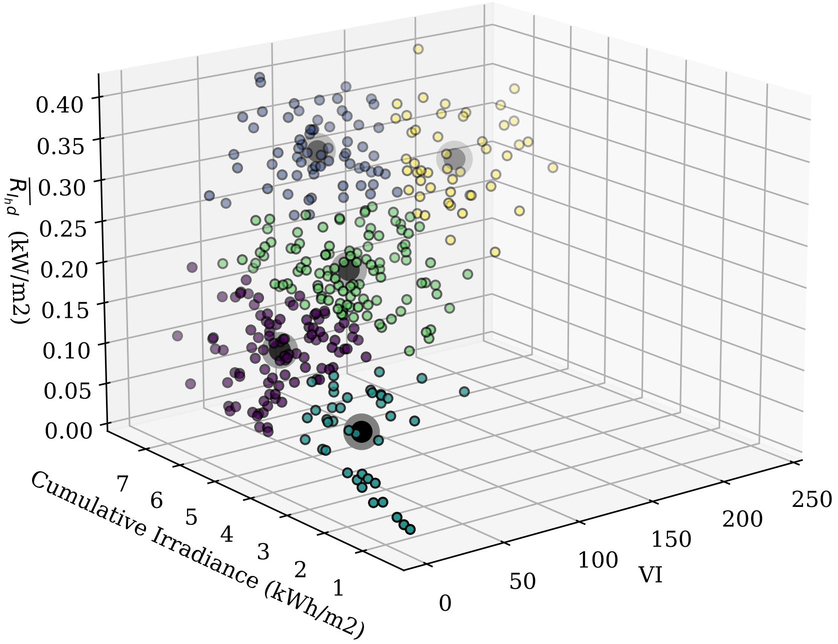

Figure 3.16: Five clusters categorized by Kmeans. Black dots highlight the centers of gravity.

In this work, the reduced set of scenario is built by the closest elements to centers of gravity. Eq. 3.22 defines the representative scenario y^{σ} of cluster σ as the timeseries with the minimal distance D_i^{σ} to its center of gravity.

$$D_i^{\sigma} = \sqrt{\sum_j \left(x_{i,j}^{\sigma} - G_j^{\sigma}\right)} \tag{3.21}$$

$$D_y^{\sigma} = \min_i D_i^{\sigma} \tag{3.22}$$

G_j^{σ} denotes the coordinates of the center of gravity in dimension j and is epressed by Eq. 3.23. N^{σ} denotes the number of elements in the cluster k and $x_{i,j}^{\sigma}$ the coordinate of the element i in the dimension j. Fig. 3.17 illustrates the centers of gravity of 5 clusters as well as their closest elements labelled by their dates.

$$G_j^{\sigma} = \frac{\sum_{i=1}^{N^{\sigma}} x_{i,j}^{\sigma}}{N^{\sigma}} \tag{3.23}$$

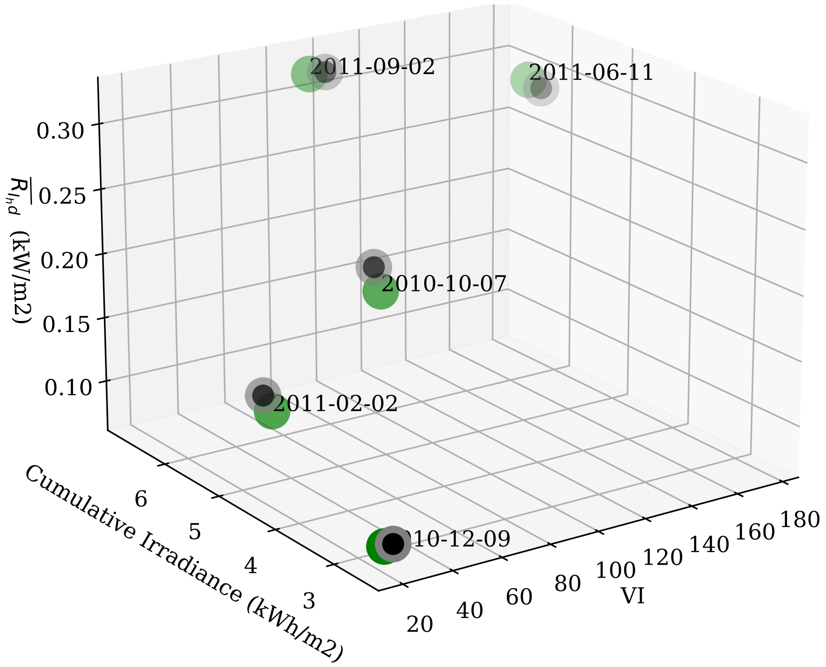

Figure 3.17: Five clusters categorized by Kmeans. Black dots highlight centers of gravity and green dots show the clostest elements of the cluster which are chosen as representative scenario.

SELECTION OF BEST PERFORMING SETUP

The process of Kmeans clustering requires a user defined number of clusters $N^{cluster}$ that should be chosen according to the simulation needs (here a small number of cluster is more suitable to limit the computation time of future simulations) and in best compliance with the behaviour of the whole dataset.

Feature Unit	Cumulative irradiance kWh/m^2	VI -	Mid-term variability indicator kW/m^2
4 clusters	5.06	73.09	0.20
5 clusters	5.17	73.37	0.19
6 clusters	5.18	76.71	0.20
7 clusters	5.21	75.40	0.20
Average value of 365 days	**5.19**	**74.54**	**0.20**

Table 3.4: Comparison of weighted average values $\overline{X_j}^{kmeans}$ for number of clusters varying from 4 to 7 against average values of the whole dataset.

Tab. 3.4 reports the weighted average values $\overline{X_j}^{kmeans}$(defined by Eq. 3.24) for a number of clusters varying from 4 to 7 and compares it to the averaged indicators value over 365 days. All results show good compliance with less than 1% of error apart from the 4-cluster setup which reports an error of $0.14kWh/m^2$ for the cumulative irradiance.

$$\overline{X_j}^{kmeans} = \frac{\sum_{\sigma} x_j^{\sigma} N^{\sigma}}{365} \tag{3.24}$$

Fig. 3.18 shows the repartition of clusters as function of normalized VI_d and $\overline{RI_{I_h}}_d$. In configurations with 6 and 7 clusters, areas of low irradiance and low spinning reserve are mixed up which means that the corresponding representative scenarios will be equivalent in terms of variability. In this case, the kmeans setup with 5 clusters shows the best compromise and will be used in the next parts.

3.3.1.3 *Discussion on day-long scenario identification*

By selecting the highest VI among the dataset, a worst case scenario has been identified. Then, 5 representative days were selected thanks to Kmeans clustering. Tab. 4.11 reports the characteristics of each day of the set alongside with a brief description. Fig. 3.19 shows the irradiance profile of all selected day-long scenarios.

Thanks to the worst-case scenario, robust approach may be undertaken to evaluate the risk of power quality degradation. However this scenario does not represent days with lower irradiance and results will not be representative in terms of fuel savings.

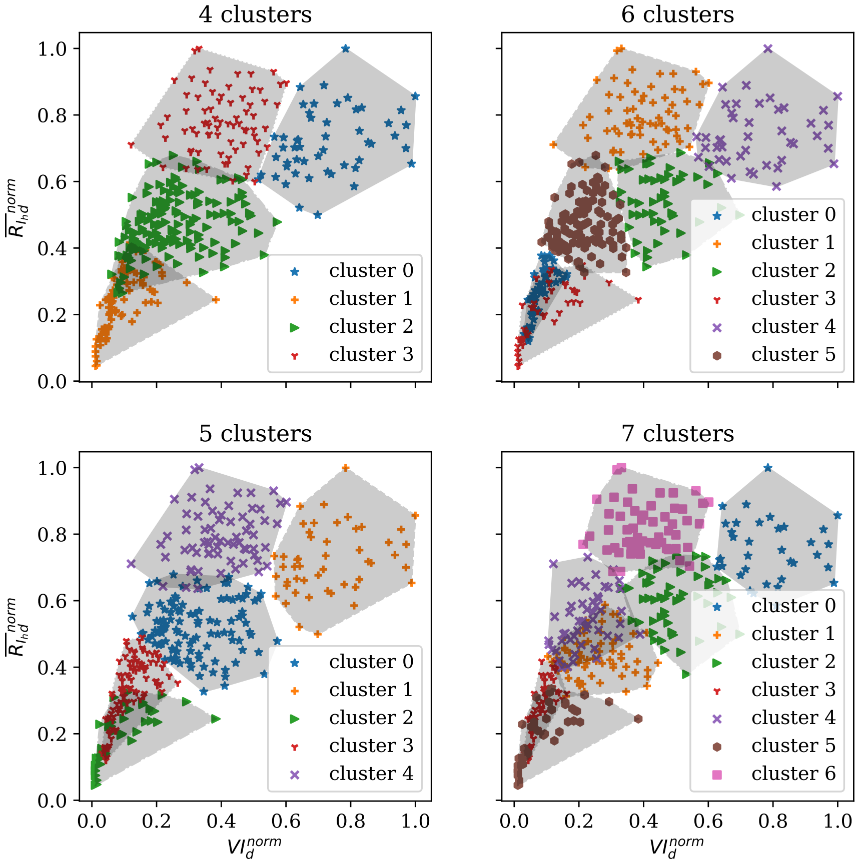

Figure 3.18: Group repartition for cluster numbers varying from 4 to 7.

	Date	Description	N°	VI	Cumulative irradiance (kWh/m2)
1	2010-12-09	Overcast	40	21.31	2.63
2	2011-02-02	Medium production, low variability	98	30.90	4.92
3	2010-10-07	Medium production and variability	111	74.97	4.87
4	2011-09-02	High production, high variability Medium sharpness	67	91.10	6.78
5	2011-06-11	High production and variability	49	172.71	6.20
wc	2011-03-16	Worst case variability	n.a	238.97	5 .92

Table 3.5: Solar input scenarios resulting from the clustering and worst-case identification of the Hawaii dataset.

On the other hand, the 5 days identified thanks to Kmeans provide varying situations from overcast weather ($VI = 21.31$, $E_{I_d} = 2.63$) to high production and variability ($VI = 171.72$, $E_{I_d} = 6.20$). The occurrence associated to each scenario allows aggregating the result of grid simulations to reconstruct yearly indicators.

Combining worst-case identification and Kmeans allows reducing the number of day-long scenarios from 365 to 6 timeseries which significantly reduces the number of grid simulation to be performed.

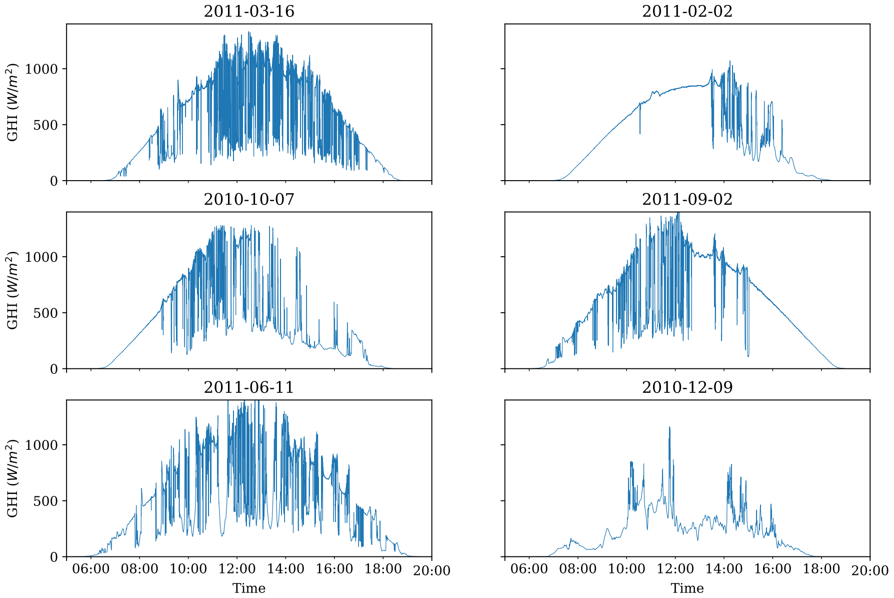

Figure 3.19: Days long scenarios: worst-case scenario and 5 days resulting from Kmeans clustering.

3.3.2 *Isolated ramp events as scenarios*

As presented in section 3.2.1.2, the ramp-detection algorithm is able to extract solar drop scenarios and provides two features : irradiance drop ΔI and duration T. The solar perturbation $I(t)$ is modelled by a linear reduction of irradiation over T as expressed in Eq. 3.25 and shown in Fig. 3.20. If the linear drop represents the worst-case irradiance drop over a given time-windows, it can be used to evaluate the maximum electrical perturbation related to cloud passage. This isolated scenarios can be of great interest to study electrical stability using very short grid simulations.

$$I(t) = \begin{cases} I_0 - \frac{\Delta I}{T} t & \text{if } 0 \leqslant t \leqslant T \\ I_0 - \Delta I & \text{otherwise} \end{cases} \tag{3.25}$$

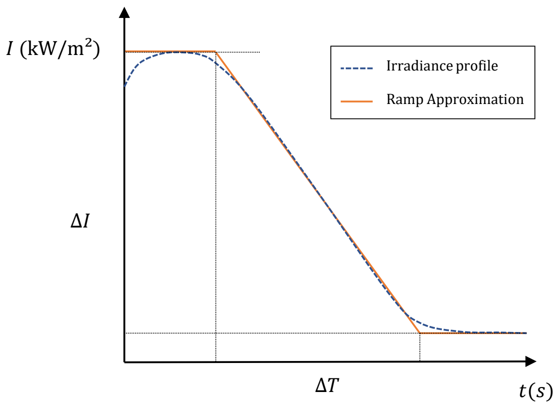

Figure 3.20: Linear ramp approximation to model isolated solar drop scenario.

The PV output power is calculated thanks to the rated installed capacity W_{PV} and PV plant efficiency η_{PV} as expressed in 3.26.

$$P_{PV}(t) = GHI(t)W_{PV}\eta_{PV} \tag{3.26}$$

One example of isolated scenario application is the evaluation of the maximum power unbalance during a solar drop between fossil generation, PV power and load. Eq. 3.32 shows how the maximum power unbalance is calculated while respecting the ramping constraint expressed by Eq. 3.34. By assuming a constant load power during a cloud passage event, Eq. 3.29 expresses the maximum power unbalance Υ. This provides a straightforward relationship between the electrical perturbation and an isolated ramp scenario r=(T, ΔI).

$$P_{unmetload}(t) = P_L - P_{gen}(t) - P_{PV}(t) \tag{3.27}$$

$$P_{gen}(t+1) - P_{gen}(t) \leqslant rr_{gen} \tag{3.28}$$

$$\Upsilon = \max(P_{unmetload}) = \Delta I.\eta_{PV}.W_{PV} - T.rr_{gen} \tag{3.29}$$

The electrical perturbation must now be evaluated with the proper isolated scenarios. The set of solar drop $\mathcal{R}$ detected by RDA over the full dataset is shown in Fig. 3.21. The envelope corresponding to 99% of all events shows that extreme events are missing ($\geqslant 1.1kW/m^2$). To ensure a robust approach, the following analysis will be based the worst-case ensemble gathering 100% of all detected ramp.

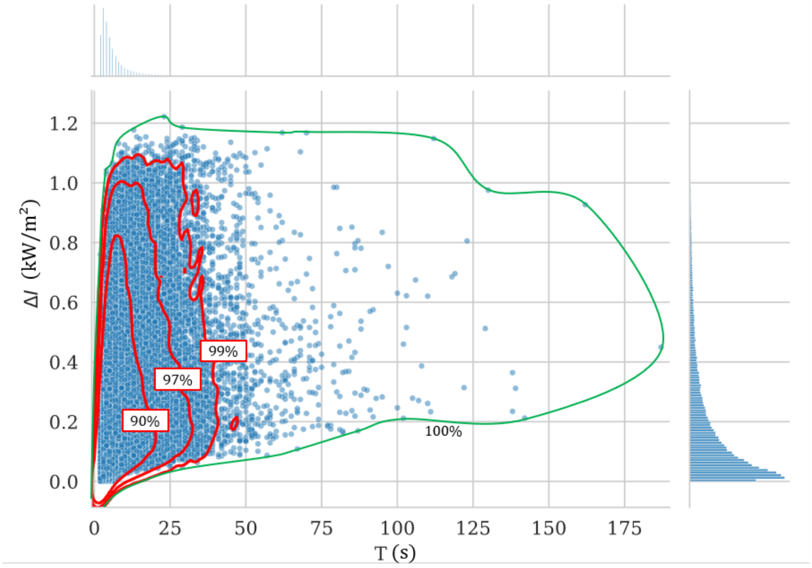

Figure 3.21: Set of ramps, single dimension probability functions and envelopes gathering 90%, 97%, 99% and 100% of detected ramps.

3.3.2.1 *Worst case ramp events*

Due to the expression of power unbalance (Eq. 3.29), it is not possible to consider a single event as worst-case isolated scenario. Tab. 3.6 shows an example with $W_{PV} = 50$ MW. With a total ramp-rate of 0.433 MW/s, the worst ramp rate is r_2 with 47.6 MW of power unbalance. However, with $rr_{gen} = 1.33$ MW/s, the worst ramp is r_1 with 42.2 of power unbalance. Hence, a set of isolated must be used for grid simulations instead of a single ramp event.

Name	r_1	r_2
Ramp features	$\Delta I = 0.95 kWm^2$, $T = 4s$	$\Delta I = 1.06 kWm^2$, $T = 14s$
$rr_{gen} = 0.433 MW/s$	45.8 MW	**47.6 MW**
$rr_{gen} = 1.33 MW/s$	**42.2 MW**	40.4 MW

Table 3.6: Comparison of maximum power unbalance for two ramp events and two fossil ramp rates with a PV installed capacity of 50 MW.

The set $\mathcal{R}^T$ gathers all ramps of duration T and is defined following Eq. 3.30. Fig. 3.22 shows an example with $\mathcal{R}^{30}$.

$$\mathcal{R}^T = \{(\Delta I, T) \in \mathcal{R}\} \tag{3.30}$$

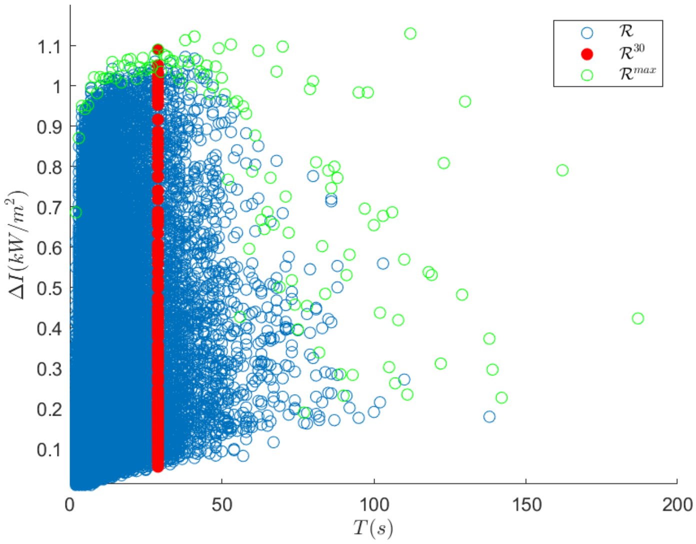

Figure 3.22: $\mathcal{R}$, $\mathcal{R}^{30}$ and $\mathcal{R}^{max}$ for the Hawaii dataset.

Following Eq. 3.29, the power unbalance of every element within $\mathcal{R}^T$ will be lower or equal than the power unbalance resulting from the element of highest irradiance drop within $\mathcal{R}^T$.

Hence, the maximum ramp set $\mathcal{R}^{max}$ can be defined to reduce the number of simulations (see Eq. 3.31)

$$\mathcal{R}^{max} = \bigcup_{T} \left\{ (\Delta I, T) \in \mathcal{R}^T \mid \Delta I = \max_{r \in \mathbf{R}^T} (\Delta I)_r \right\} \tag{3.31}$$

Thanks to the identification of $\mathcal{R}^{max}$, the number of scenarios has been significantly reduced (more than 120.10^3 ramps in $\mathcal{R}$ against 178 in $\mathcal{R}^{max}$). However, Fig. 3.22 suggests that some points within $\mathcal{R}^{max}$ may be equivalent or even useless in the calculation of the maximum power unbalance (for example when the irradiance drop of a ramp is lower than the irradiance drop of both neighbours).

3.3.2.2 *Convex hull reduction*

The convex envelope of $\mathcal{R}^{max}$ allows reducing the set of events to consider. The Carathéodory's theorem [206] defines $\mathcal{H}^{max} = conv(\mathcal{R}^{max})$ as follows :

All elements $p \in \mathcal{H}^{max}$ can be written as a convex combination of k points in $\mathcal{R}^{max}$ with $k \leqslant 1 + dim(\mathcal{R}^{max})$.

Since $dim(\mathcal{R}^{max}) = 2$, this gives $p = r_1 t_1 + ... r_k t_k$ with $\sum_{k=1}^{3} t_k = 1$ and $r_k \in \mathcal{R}^{max}$

$\mathcal{H}^{max}$ provides two interesting properties leading to reduce the number of elements necessary for grid simulations (see Fig. 3.23 for graphical interpretation and Annex 7.1 for proofs of P1 and P2).

Let u_1, u_2 be two consecutive elements of $\mathcal{H}^{max}$ and $u' \in [u_1, u_2]$ such as $u' = \tau u_1 + (1-\tau)u_2$ with $\tau \in [0,1]$

Property 1 (P1) : The power imbalance $\Upsilon(u')$ of each point in the segment $[u_1, u_2]$ is higher or equal than the power imbalance $\Upsilon(r)$ calculated from every element r of lower irradiance drop .
$\forall r = (T_{u'}, \Delta I_r) \quad | \quad \Delta I_r \leqslant \Delta I_{u'}$
$\Upsilon(r) \leqslant \Upsilon(u')$

Property 2 (P2) : The power imbalance of each point of the segment $[u_1, u_2]$ is lower or equal than one of the two closely located point of the convex hull (u_1 or u_2)
$\Upsilon(u') \leqslant \Upsilon(u_1)$ or $\Upsilon(u') \leqslant \Upsilon(u_2)$

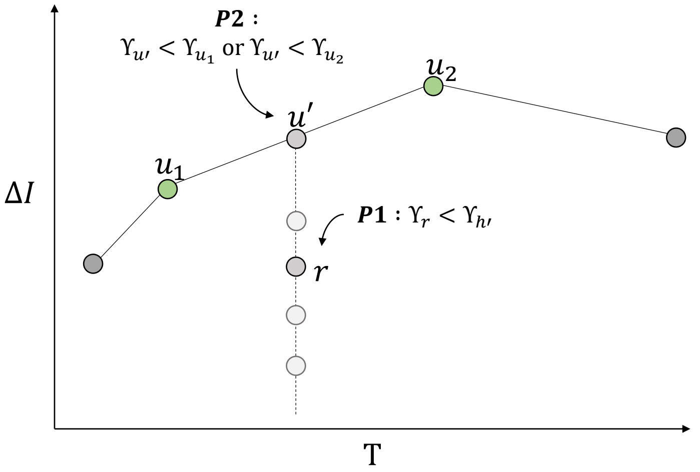

Figure 3.23: Graphical interpretation of P1 and P2.

P1 and P2 demonstrate that grid simulations performed using elements of the convex envelope $\mathcal{H}^{max}$ are more conservative than grid simulation performed with $\mathcal{R}^{max}$. More importantly, the number of elements in $\mathcal{R}^{max}$ is significantly reduced such as highlighted in Fig. 3.24 (9 elements against 178).

Finally, the same process can be done for WVM-smoothed irradiance to account for the variability smoothing effect of the power plant. In Fig. 3.25, the convex hull of 50MW equivalent irradiance ramps is compared to the convex hull obtained from pyranometer measurements [7]. The figure highlights that the worst-case ramps have lower

---

[7] In practice, the convex envelope is computed by a standard Matlab function (https://fr.mathworks.com/help/matlab/ref/convhull.html)

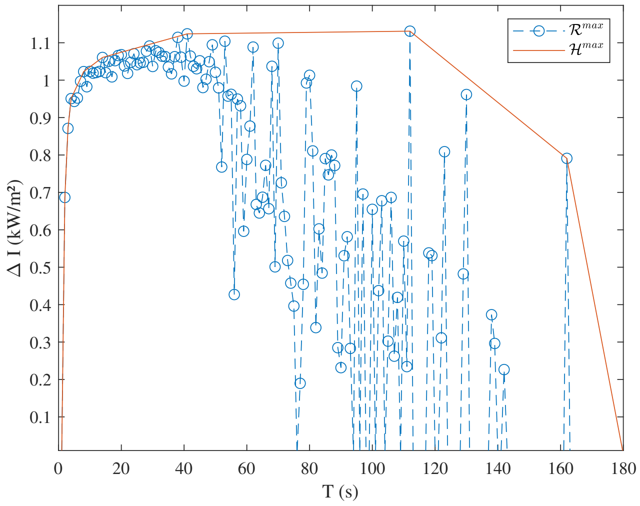

Figure 3.24: $\mathcal{R}^{max}$ and convex hull $\mathcal{H}^{max}$ (pyranometer data).

gradients and lower irradiance drops. Consequently, the WVM convex hull avoids over-estimating the grid's electrical perturbations.

To evaluate the worst-case electrical perturbations, the set $\mathcal{H}^{max}$ will be used in the next chapters and discussed in detail in Chapter 5.

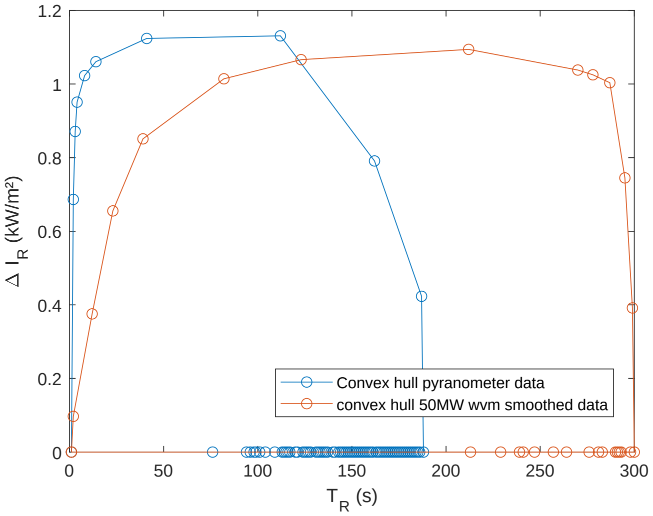

Figure 3.25: Convex hulls of worst case ensembles for pyranometer and 50-MW wvm-smoothed data.

3.3.3 *Comparison between day-long and isolated scenarios*

Now that several methodologies for scenarios generation have been presented, their relevance for electrical stability and techno-economic evaluation must be discussed. Only day-long time series can be used for techno-economic analysis since Isolated scenarios do not give any information on cumulative irradiance and therefore do not allow calculating the fuel savings over the lifetime. However, the relevance of performing electrical simulations over large time windows such as day-long time series can be challenged since they require large computational resources. Isolated scenarios are an opportunity to perform quicker and more comprehensive electrical and power balance analysis.

To ensure that isolated scenarios are a good alternative to day-long time-series, a primary support storage system will be sized using both types of scenarios. The resulting battery capacity will be compared.

3.3.3.1 *Power adequacy for battery capacity sizing*

A comprehensive and effective methodology for determining battery capacity consists in detecting the maximum power gap between the load and the generators. This method is based on the hypothesis that a perfect adequacy between power production and consumption. This method has been implemented in [207] where the power adequacy methodology is used to compensate solar ramps when generators have insufficient ramping capacity. More complex methods requiring dynamic electrical simulation can be implemented such as proposed in [47]. Following the analysis performed in this thesis, a comparison between dynamic electrical modeling and power adequacy have been proposed an published in [197].

Eq. 3.32 and 3.33 show how the capacity is calculated while respecting the ramping constraint expressed by 3.34.

$$P_{unmetload}(t) = P_L - P_{fossil}(t) - P_{PV}(t) \tag{3.32}$$

$$W_{bat} = \max_t(P_{unmetload}(t)) \tag{3.33}$$

$$P_{fossil}(t+1) - P_{fossil}(t) \leqslant rr_{fossil} \tag{3.34}$$

Where P_{PV} is the PV power, P_{fossil} is the power generated by fossil units, P_L is the load demand and $P_{unmetload}$ is the amount of power that cannot be satisfied by the generating units. W_{bat} is the battery power capacity obtained by filling the power gap $P_{unmetload}$ during the PV power loss. The PV power P_{PV} is calculated from the PV plant's rated capacity and GHI value. A large number of advanced models exist to estimate PV plant performance based on optical and thermal simulation, such as presented in [208], but require a detailed description of the power plant (module types, electrical layout, etc.). In the context of variability analysis, the precise estimation of power absolute value is less important than the power dynamics. Hence, a linear model is used in this study as shown in Eq. 3.35 (a constant value of 0.8 is set for η_{PV}).

$$P_{PV}(t) = \frac{GHI}{(1000W/m^2)} P_{PV}^{inst} \eta_{PV} \tag{3.35}$$

3.3.3.2 *Application of variability scenarios*

To compare the impact of variability scenario on the battery power capacity sizing, the power adequacy method is used with the worst-case day long scenario (2011-03-16) and the convex hull defined in the previous section (Fig. 3.25). I^{wvm} and I^{pyrano} respectively denotes raw pyranometer and wvm-filtered isolated scenarios while D^{wvm} and D^{pyrano} respectively denotes raw pyranometer and wvm-filtered day-long scenarios. Tab. 3.7 displays the parameters used for the simulation.

Symbol	Name	Unit	Value
P_{PV}^{inst}	PV capacity	MW	50
η_{PV}	PV efficiency	%	80
P_L	Electrical load	MW	100
rr_{fossil}	Fossil generation ramp rate	MW/sec	0.433

Table 3.7: Parameters for power adequacy sizing.

Figure 3.26 highlights the battery capacities associated to each scenarios. Battery capacities are very similar between isolated scenarios and day-long scenarios. This shows that the ramp-detection method is able to extract the worst event among the whole data-set and therefore aggregate the risk of variability for a whole year of data. Moreover, the difference in battery capacities between wvm-filtered scenarios and pyranometer scenarios shows that the geographical smoothing has a significant impact on the battery power requirements (43% of battery reduction for both isolated and day-long scenarios) This shows the interest of taking the geographical smoothing to avoid over-investment in primary support storage.

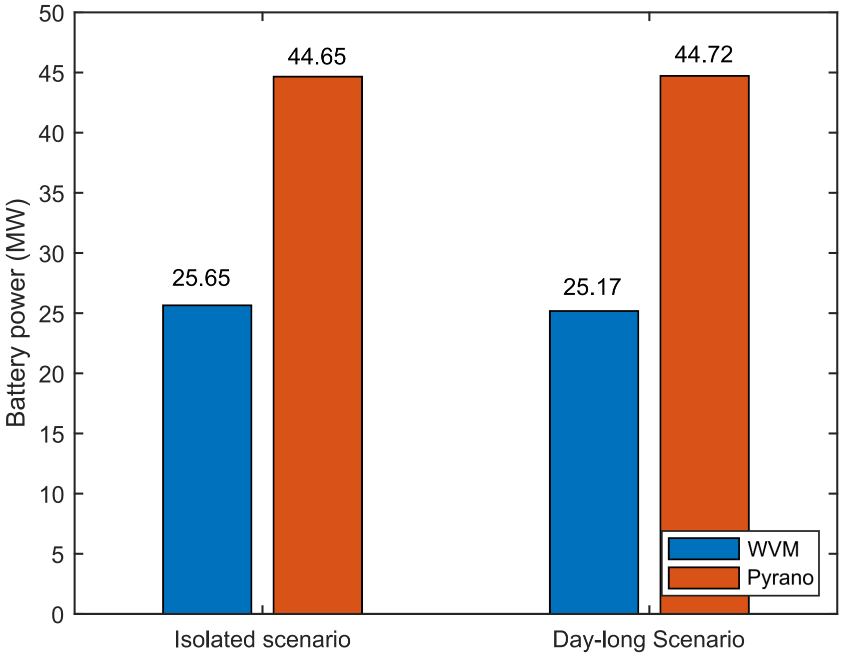

Figure 3.26: Battery capacities resulting from power adequacy simulation.

The choice of isolated or day-long scenarios will depend on the needs of the simulation. In one hand, isolated scenarios are fast to simulate and results do not require complex post treatment. On the other side, day-long scenario are longer to simulate but also provide insight of the cumulative irradiance and therefore the potential of fuel savings. In preliminary study, isolated scenarios are a good way to quickly evaluate the grid perturbation and assess the needs in battery support or fast response generator.

3.4 CONCLUSION

This chapter provides a set of tools to pre-process a high-resolution irradiance dataset and provide solar input scenarios accounting for the sub-minute variability.

In the first part, variability indicators were investigated to qualify daily GHI profiles. The Variability Index has been compared to the number of detected solar ramps and was found to be well suited for quantifying short term variability. The WVM was applied to evaluate the equivalent variability of a MW-scale power plant. Results showed that the plant size significantly reduces the variability of the power plant (variability index is reduced from 238 down to 74 in the worst-case scenario).

Then, methodologies for solar input scenario generation were proposed. First, a K-means time series clustering procedure was proposed to identify a set of representative day-long scenarios. When associated to a worst-case, this set can be used to evaluate both electrical perturbations and yearly averaged performances.

Then, a methodology to extract isolated solar drop events based on the ramp detection procedure has been proposed. A convex hull representation is used to gather a minimum number of worst-case ramps (9 events selected among 120 10^3 ramps detected by the RDA). These isolated ramp scenarios can be used for quick electrical analysis since their durations vary between 15 to 200 seconds (instead of 5.4 10^5 for a day-long timeseries).

The performance of isolated scenarios and day-long scenarios has been compared by evaluating the battery capacity needs for an isolated microgrid. Results showed that isolated scenarios provide similar battery capacity while significantly reducing the calculation and interpretation complexity. Finally, it was found that the geographical smoothing effect of the MW-scale power plant can reduce the battery capacity needs by 43%.

Thanks to the scenario identification, grid simulations can be performed with less computational resources. Simulation tools must now be developed to evaluate the impact of such scenarios on the performance of hybrid architectures.

4

A MULTI LAYER APPROACH FOR THE OPERATIONAL SIMULATION OF AN INDUSTRIAL MICROGRID

This chapter presents a novel methodology for the operational simulation of industrial microgrids. The environmental, economic and electrical performances are assessed thanks to combinations of energy-level optimizations and short-term electrical simulations. The set of Day-long scenarios identified in chapter 3 is used to construct yearly indicators and limit the computation time. A patent claim covering the multi-layer simulation method and the input data reduction has been submitted thanks to this work.

Ce chapitre présente une nouvelle méthode pour la simulation opérationnelle de micro-réseaux industriels. Les performances du systèmes sont évaluées grâce au couplage d'optimisations énergétiques et de simulations électriques détaillées. Les scénarios journaliers identifiés dans le chapitre 3 sont utilisés pour construire des indicateurs annuels et limiter le temps de calcul. Une demande de brevet couvrant la méthode de simulation multicouche et la réduction des données d'entrée a été déposée grâce à ce travail.

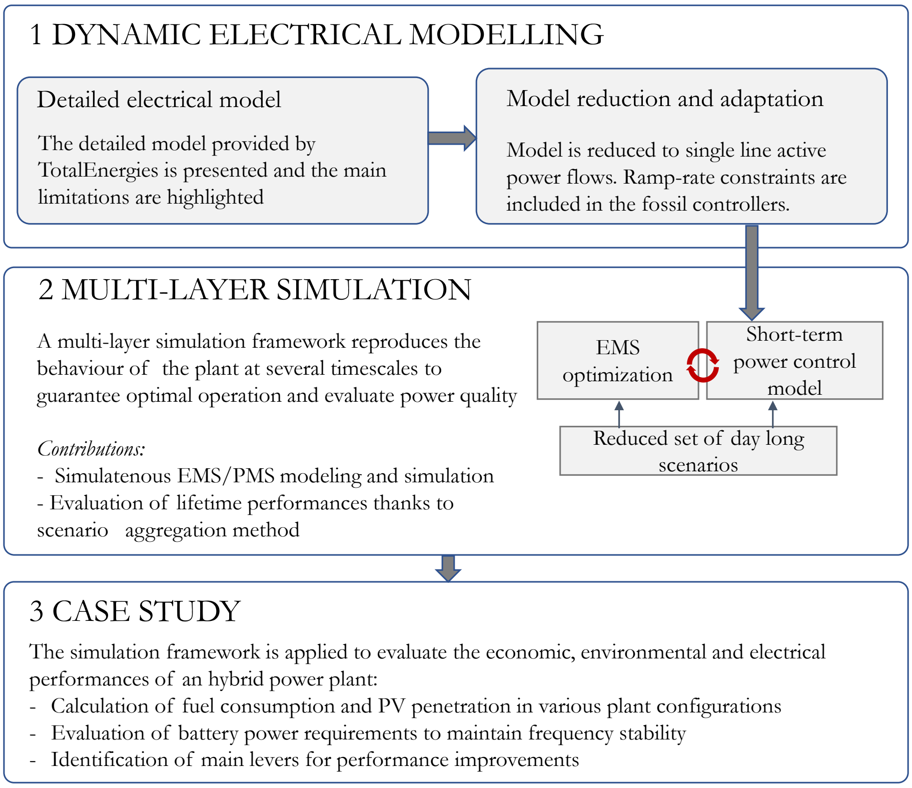

The detailed model provided by TotalEnergies is presented and the main limitations are highlighted

Model is reduced to single line active power flows. Ramp-rate constraints are included in the fossil controllers.

A multi-layer simulation framework reproduces the behaviour of the plant at several timescales to guarantee optimal operation and evaluate power quality

Contributions:

- Simulatenous EMS/PMS modeling and simulation
- Evaluation of lifetime performances thanks to scenario aggregation method

The simulation framework is applied to evaluate the economic, environmental and electrical performances of an hybrid power plant:

- Calculation of fuel consumption and PV penetration in various plant configurations
- Evaluation of battery power requirements to maintain frequency stability
- Identification of main levers for performance improvements

Contents

NOMENCLATURE OF CHAPTER 4

Temporal indices

Symbol	Description
h	Hourly timeslice
k	Secondary optimization timeslice (10 minute)
t	short-term timeslice (1 second)

Other indices

Symbol	Description
m	Machine technology
i	instance of machine of technology m
σ	Day-long irradiance scenario

Sets

Symbol	Description
$\mathcal{M}^{UC}$	Available units for the schedule optimization
$\mathcal{M}^{Dispatch}$	Available units for the dispatch optimization
$\mathcal{K}_{\sigma}$	set of day-long irradiance scenarios

Optimization decision variables

Symbol	Description
FC	Fuel consumption
u, v	Start-up and shut-down binary variable
ω	Fossil unit binary operating status
P_{PV}^{inj}	Averaged injected PV power
W_{PV}^{used}	Available PV power capacity after curtailment
$P^{lst,max}$	Maximum power lost during contingency
ΔP^{cont}	Fossil unit power variation after contingency
$\Delta P_{m,i,h}^{avg}$	Fossil unit power variation during PV variations

Optimization parameters

Symbol	Description
W_{PV}^{inst}	PV installed power capacity
W_{bat}^{inst}	Battery installed power capacity
η_{PV}	PV derating factor (%)
N_m	Number of available fossil machines
c_f	Fuel price
c_{CO_2}	Equivalent CO_2 emission penalty
c_u, c_v	Start-up and shut-down costs
P_m^{min}, P_m^{max}	Fossil unit minimum and maximum power
Pl	Load power
$\overline{I_h^{wvm}}$	Hourly averaged wvm-filtered irradiance
c_m^{inst}	installation cost of fossil unit
K	Large scale constant
ΔI_h^{avg}	Max PV power variation within hourly interval
M_{dn}, M_{up}	Minimum up and down time
P^{lst}	Power lost due to generator contingency
P_{bat}^{N+1}	Storage power capacity for N+1 redundancy

Power system variables and parameters

Name	Description
f	Grid frequency
f_0	Grid nominal frequency
Δf	Grid frequency shift
θ	Rotor angle
$\dot{\theta}$	Rotor angle velocity
τ_m	Mechanial Torque
τ_e	Electrical Torque
M	Inertia constant
K_p	PID proportional parameters
K_d, T_d	PID derivative parameters
K_i	PID integral parameters
K_s	Fossil setpoint controller proportional parameter
P_{PV}	PV active power
Q_{PV}	PV reactive power
P_{bat}	Battery active power

Power system variables and parameters

Q_{bat}	Battery reactive power
$r(f)$	Battery frequency-dependant droop
P_k	fossil generation setpoint from EMS
$P^*_{setpoint}$	Fossil setpoint controller output
P^*_{Θ}	Fossil frequency controller output
P^*_{mech}	Fossil controller output
rr_{up}	fossil generation ramp rate
n_{turb}	Number of operating turbines
$\overline{I^{wvm}_k}$	10 minute averaged WVM filtered irradiance
I^{wvm}_t	WVM filtered irradiance
W^{ss}_{bat}	Battery power capacity to maintain steady-state frequency
W^{limit}_{bat}	Battery power capacity to maintain transient frequency

4.1 INTRODUCTION

In the previous chapter, solar irradiance scenarios have been identified to properly address solar variability in grid simulations. In this chapter, solar scenarios will be taken as input to evaluate their impact on the performance of an hybrid architecture composed of gas generators, PV power plant and primary support storage system. The main performance indicators are the CO_2 annual emissions, operating costs and net present costs, maximum frequency deviation and cumulated time of frequency disturbances. Such evaluation raises challenges in the preliminary assessment of the power system:

First, the management strategy of the power plant must be taken into account to represent its economical and environmental performance. As a matter of fact, scheduling decisions are made to allow the integration of PV power and reduce the fuel consumption of fossil units. As highlighted in Chapter 2, the operational optimization is handled by the EMS[1] during operations and is based on an high level energy modelling with 15-minute to 1h time intervals. Due to these time-scales, the impact on electrical stability cannot be addressed.

On the other hand, the quality of supply is a key aspect due to the need of reliable and continuous electricity supply. If maximum frequency and voltage deviations are met, architecture should be considered as unreliable and should be eliminated from the screening process. This leads to build dynamic model capable of evaluating several architectures in a limited amount of time. Additionally, technical input necessary for electrical stability are not always available, leading to limit the model complexity.

In the first part of this chapter, the problem of power quality evaluation is addressed. A detailed electrical model is reduced into a single-line active power flow model to allow faster simulation of daily time series. The second part introduces a multi-layer simulation framework to link the electrical model with an energy management optimization. By aggregating results from the set of day-long scenarios previously identified, yearly performance indicators are calculated. A worst-case scenario is used to ensure electrical stability and evaluate the minimum required battery capacity. The operational simulation is applied on a case study in the third part. The role of fossil generators characteristics, redundancy constraints and PV installed capacity on the electrical stability and profitability of the plant are investigated.

---

[1] Energy Management System

4.2 POWER QUALITY EVALUATION IN HYBRID INDUSTRIAL MICROGRID

Dynamic simulation aims at tracking the quality of supply thanks to two main electrical variables: grid frequency and voltage. The objective of such simulation is to ensure the grid stability during cloud passage and evaluate the need in primary storage support associated with the PV penetration scenarios. The steady state and transient operational limits of frequency and voltage have been formulated in TotalEnergies internal specifications handbook [2]. Following clarifications meeting with TotalEnergies electrical experts, grids codes for PV cloud passage have been defined and are compared to unplanned events grid codes in Tab. 4.1 and Tab. 4.2.

Following these specifications, an architecture can be qualified as :

- *Fully reliable*: No transient or unauthorized disturbance are observed during cloud passage
- *Acceptable with limited risks*: Transient disturbances are observed but remain below maximum transient limits
- *Unstable*: At least one unauthorized disturbance is observed due to a PV variation.

	Steady-state	Transient disturbance	Unauthorized disturbance
Grid code following unplanned event (Generator contingency loss of load load picking etc.)	$\Delta f < 0.5\%$	$\Delta f \geqslant 5\% f_n$ and recovery to $3\% f_n$ within 3 seconds	$\Delta f \geqslant 3\% f_n$ after 3 second following the event
Grid code for PV cloud passing)	$\Delta f < 1\% f_n$	$1\% f_n \leqslant \Delta f \leqslant 5\% f_n$	$\Delta f \geqslant 5\% f_n$

Table 4.1: Grid code for frequency variations, with $f_n = 50\text{Hz}$.

	Steady-state	Transient disturbance	Unauthorized disturbance
Grid code following unplanned event (Generator contingency loss of load load picking etc.)	$\Delta f < 0.5\%$	$\Delta V \geqslant 10\% V_n$ and recovery to $3\% V_n$ within 1.5 seconds	$\Delta f \geqslant 3\% V_n$ after 1.5 second following the event
Grid code for PV cloud passing)	$\Delta V < 1\% V_n$	$1\% V_n \leqslant \Delta V \leqslant 10\% V_n$	$\Delta V \geqslant 10\% V_n$

Table 4.2: Grid code for voltage variations, with $V_n = 11\text{kV}$ at generator and load buses.

---

[2] TotalEnergies. Exploration Production, "Electrical requirements for generating units , General Specification, GS_EP_ELE_013".

4.2.1 *3-phase electrical model of an industrial microgrid*

An electrical model has been provided by TotalEnergies and describes active and reactive power dynamics within a 3-phase network. All components (fossil generators, PV system, battery system and load) are connected to a single bus and ideal transmission lines are used. Figure 4.1 shows the main blocks of the detailed electrical model as provided. Table 4.3 shows the main grid characteristics.

Parameter Name	Unit	Value
Line to line voltage	kV	11
Grid frequency	Hz	50
Constant Load active power	MW	140 - 170
Constant Load active power	MVAR	28 - 34
Gas turbine maximum output power	MW	48

Table 4.3: Summary of grid characteristics.

4.2.1.1 *Model description*

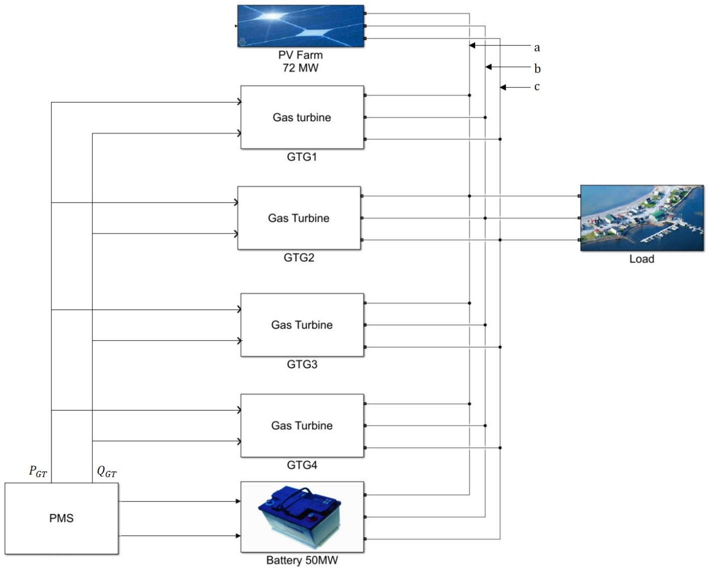

Figure 4.1: Overall view of the 3-phase industrial microgrid model.

SYNCHRONOUS MACHINES AND FOSSIL GENERATORS

In AC microgrids, synchronous machine play a role of paramount importance since they allow the conversion of mechanical power into electrical power but also provide a reference for the grid frequency. In the three-phase model, the synchronous machine is described thanks to a Matlab Simulink standard block taken from the simscape specialized power system library [209] [3].

Under the assumption of synchronous system, all synchronous machine and fossil engine's shaft share the same angular velocity $\dot{\theta}$. Consequently, current and voltage signal $x(t)$ of the three lines a, b, c also share the same phase $\dot{\theta}$ (see Eq. 4.1).

$$\begin{bmatrix} x_a(t) \\ x_b(t) \\ x_c(t) \end{bmatrix} = A \begin{bmatrix} \sin(\delta_0 + \dot{\theta}t) \\ \sin(\delta_0 - \frac{2}{3}\pi\dot{\theta}t) \\ \sin(\delta_0 + \frac{2}{3}\pi\dot{\theta}t) \end{bmatrix} \tag{4.1}$$

$$\frac{d\theta}{dt} = \dot{\theta} \tag{4.2}$$

The variation of angular velocity depends on the equilibrium between the electrical torque τ_e and mechanical torque τ_m at both sides of the synchronous machines as expressed by the mechanical swing equation (Eq. 4.3). D an J respectively denote the load damping parameters and the moment of inertia of the shaft (in $kg.m^2$).

$$J\frac{d\dot{\theta}}{dt} = -D\dot{\theta} + \tau_m - \tau_e \tag{4.3}$$

Eq. 4.4 expresses the inertia constant M (provided in the parameter list in Annex 7.3) as a function of the moment of inertia J, nominal rotor velocity $\dot{\theta}_0$ and nominal unit real power MVA^{pu}.

$$M = \frac{J\dot{\theta}_0^2 10^{-6}}{MVA^{pu}} \tag{4.4}$$

---

[3] For the sake of conciseness, the model is not described in this work but the reader may refer to the user guide provided in the reference.

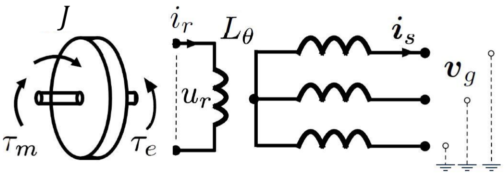

Figure 4.2: Principle of synchronous machine. i_r and u_r denotes the rotor current and voltage; i_s denotes the stator current and v_g the grid voltage; L_θ refers to the inductance matrix

One key consideration of synchronous machine operation is the control of field winding's voltage and current. This is done thanks to excitation systems called Automatic Voltage Regulators (AVR) which adjusts the field current and voltage magnitude to maintain the grid voltage within acceptable limits. A wide range of synchronous machine and AVR models can be found in the IEEE standards library. The IEEE's standardized AC7B excitation system has been chosen by the manufacturers of the gas turbine which explains its use in this three-phase model.

The mechanical torque generation is one of the most important part of the fossil generation power conversion chain. Electrical models aim at reproducing the reaction of fuel actuation and combustion chamber to control signals. Here again, wide range of standardized models can be found in the literature [64] among which the IEEE GGOV model have been chosen (Fig. 4.3). In this three-phase representation, the mechanical power is calculated instead of the mechanical torque. Eq. 4.5 expresses the relationship between power and torque [4].

$$P_m = \tau_m \dot{\theta} \tag{4.5}$$

---

[4] Note that the swing equation can also be expressed as a function of the difference between electrical power and mechanical power.

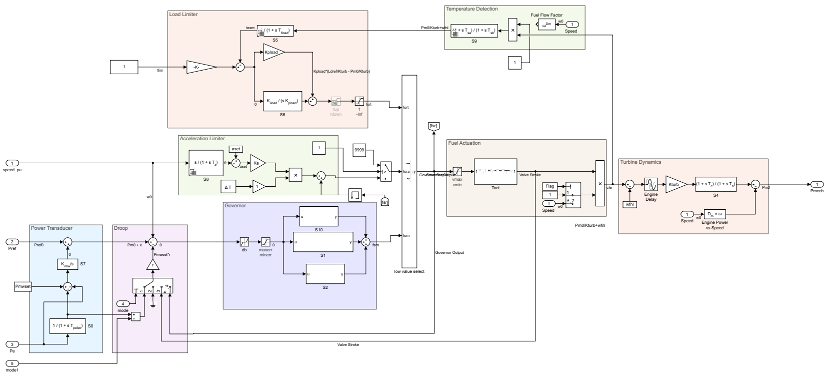

Figure 4.3: The GGOV fossil generator model as implemented in Matlab/Simulink (see annex 7.2 for wider picture).

The GGOV reproduces a conventional control scheme for fossil generation which consists in regulating the rotor velocity and reference power using an PID-based controller. A low-value select block allows considering mechanical and thermal limitations of the gas generator to limit the control signal. On the other hand, a time-constant representation reproduces the fuel actuation and combustion dynamics. Figure 4.4 shows the overall fossil generation model composed of synchronous machine model , automatic voltage regulation and turbine blocks. Equation 4.6 expresses the power control setpoint y as a function of the input signal u (calculated from rotor velocity).

$$y = K_p u + K_d \frac{du}{dt} \frac{1}{T_d} e^{-\frac{t}{T_d}} + K_i \int_0^t u dt \tag{4.6}$$

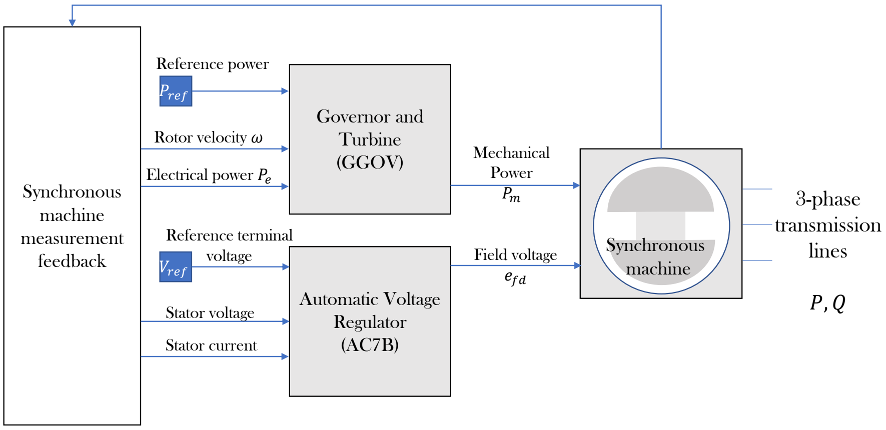

Figure 4.4: AVR, GGOV and synchronous generator form the fossil generation block.

PV SYSTEM MODEL

The PV plant model assumes a balanced three-phase system with a constant unity power factor (no reactive power production). The DC to AC conversion is assumed to be ideal (no losses due to inverter). These assumptions allow expressing the 3 phase line voltage and current following Eq. 4.7 and 4.8.

$$\begin{bmatrix} V_a \\ V_b \\ V_c \end{bmatrix} = \begin{bmatrix} V_{a1} \\ \alpha^2 V_{a1} \\ \alpha V_{a1} \end{bmatrix} \tag{4.7}$$

$$\begin{bmatrix} I_a \\ I_b \\ I_c \end{bmatrix} = \begin{bmatrix} I_{a1} \\ \alpha^2 I_{a1} \\ \alpha I_{a1} \end{bmatrix} \tag{4.8}$$

$$\alpha = e^{\frac{2}{3}\Pi j} \tag{4.9}$$

With V_{a1}, I_{a1} being the positive sequence component of phase a, and α the phasor rotation operator[5]. From the measurement of line-to-line voltage V_{ab} and V_{bc}, the phase voltage are processed as follows:

$$V_a = \frac{1}{3}(V_{ab} - \alpha^2 V_{bc}) \tag{4.10}$$

By assuming a constant unity power factor, the apparent power S_{PV} the active power P_{PV} and reactive power Q_{PV} can be expressed following Eq. 4.11.

$$S_{PV} = P_{PV} + jQ_{PV} = P_{PV} = \frac{3}{2} V_a I_a \tag{4.11}$$

The PV power P_{PV} is calculated thanks to the global horizontal irradiance Irr, the PV rated capacity W_{PV}^{inst} and the PV derating factor η_{PV}.

$$P_{PV} = Irr \times W_{PV}^{inst} \times \eta_{PV} \tag{4.12}$$

---

[5] In this model, the method of symmetrical components was originally employed to allow fault analysis. This will not be of use in this part since only solar irradiance simulation will be covered.

BATTERY MODEL

The battery electrical model is the same as the PV electrical model (Eq 4.7 to 4.11). The battery active power is controlled thanks to the frequency droop. In this model, the battery does not provide voltage support thanks to reactive power supply. The voltage regulation is solely handled by the gas generator thanks to AVR. Table 4.4 shows the battery model parameters [6]. Eq. 4.13 expresses the grid frequency f from the angular velocity $\dot{\theta}$ whereas Eq. 4.14 expresses the power control thanks to the frequency-dependant droop $r(f)$.

$$f = \frac{\dot{\theta}}{2\Pi} \tag{4.13}$$

$$S_{bat} = P_{bat} + jQ_{bat} = P_{bat}^{max} r(f) f \tag{4.14}$$

The principle of the frequency-dependant droop $r(f)$ is shown in Fig. 4.5.

$$|r(f)| = |\frac{\Delta P}{\Delta f}| = \begin{cases} 0 & \text{if} \quad |f - f_0| < f_{min}^{droop} \\ r_1 & \text{if} \quad f_{min}^{droop} \leqslant |f - f_0| < f_1^{droop} \\ r_2 & \text{if} \quad |f - f_0| \geqslant f_1^{droop} \end{cases} \tag{4.15}$$

$$P_{max}^{min} \leqslant P_{bat} \leqslant P_{bat}^{max} \tag{4.16}$$

Parameter Name	Symbol	Unit	Value
Battery maximal charging power	P_{bat}^{max}	MW	50
Battery maximal discharging power	P_{bat}^{min}	MW	50
Freuqency reference value	f_0	Hz	50
Frequency dead-band trigger value	f_{min}^{droop}	Hz	0.1
Frequency droop zone trigger value	f_1^{droop}	Hz	0.25
Frequency droop zone 1	r_1	%	1
Frequency droop zone 2	r_2	%	1

Table 4.4: Battery model parameter.

---

[6] The table reports a synthetic case initially developed with TotalEnergies to test the dynamic models. The battery sizing is here voluntarily overestimated and will be furtherly refined

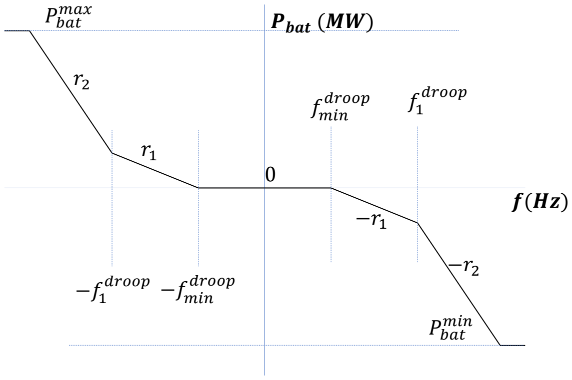

Figure 4.5: Principle of dual-zone droop control of battery active power.

4.2.1.2 *Simulation of worst-case irradiance time series*

To evaluate the impact of PV integration on the quality of supply, an industrial microgrid composed of 4 gas turbines is taken as example with two PV penetration rate scenarios (see Tab. 4.5). In case 1, the maximum PV penetration rate reaches 50% against 80% for case 2. These two scenario are simulated using the worst-case solar variability timeseries identified in Chapter 3[7] and filtered using the WVM[8].

Case	Active Load Power (MW)	Reactive Load Power (MVAR)	PV (MW)
1	140	28	70
2	170	38	140

Table 4.5: Characteristics of two cases used for worst-case simulation using the three-phase model.

Figure 4.6 and 4.7 report the results for case 1 and case 2 respectively. The frequency fluctuations are larger for case 2 (-0.35Hz for case 2 against -0.20Hz for case 1) which shows higher PV penetration rates increase electrical perturbation. The voltage specification limit ΔV^{spec} (0.5% of nominal value) is not reached in both cases which shows the ability of the AVR system and gas generator to maintain voltage fluctuation without external support.

Fig. 4.8 compares the battery active power supply for both cases. In case 1, no power support from the battery is necessary which means that the four GTs can solely handle the frequency control and maintain frequency within the specifications. However, in case 2, PV fluctuation become too large and the battery is used to compensate active power unbalance and maintain the frequency within its limits. In case 2, the battery active power reaches 3.51 MW. Bearing in mind that the simulated time series constitutes a worst-case scenario in terms of

---

[7] 2011-03-06 in the dataset obtained from [89]

[8] Wavelet Variability Model; Irradiance data which is filtered with installed PV power parameters of 70MW for case 1 and 140MW for case 2

variability, the maximum battery power supply gives the required storage capacity for this architecture.

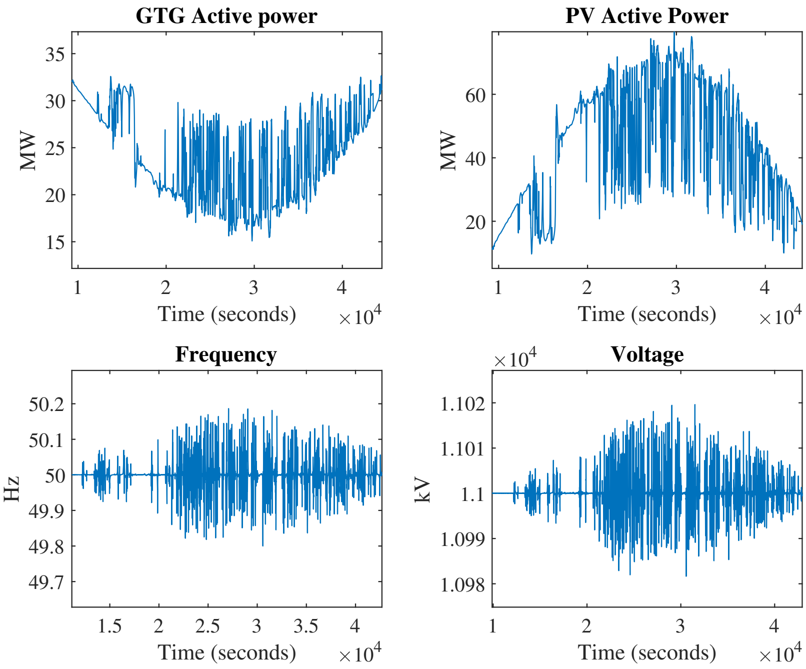

Figure 4.6: Simulation results for case 1 (140 load, 70MW of installed PV capacity).

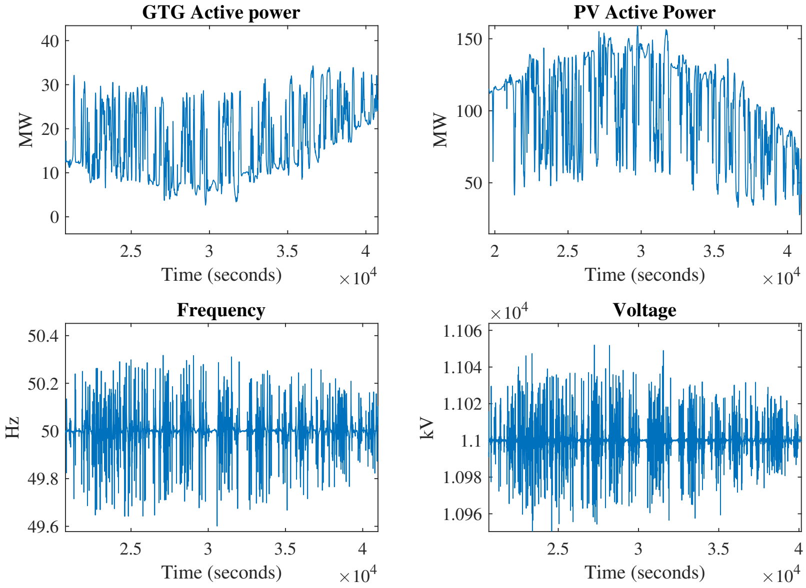

Figure 4.7: Simulation results for case 2 (170MW load, 140MW of installed PV capacity) with a focus on high production time-window.

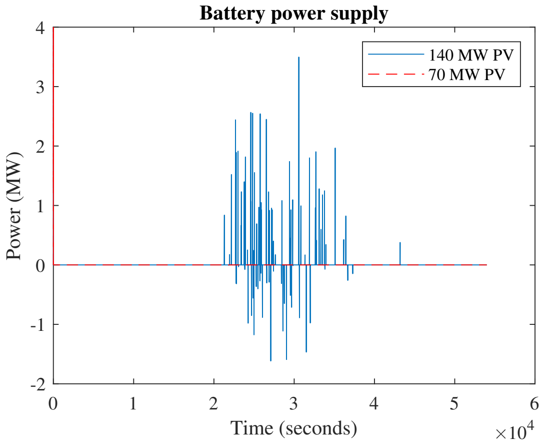

Figure 4.8: Comparison of battery active power supply for case 1 and 2.

4.2.1.3 *Limitations of three-phase modelling approaches*

The three-phase electrical model provided by TotalEnergies showed its ability to simulate the hybrid power plant under solar variability conditions. The results show that an active power supply from the battery is necessary to ensure the frequency stability for high PV penetration rates.

However, the three-phase electrical modelling showed several limitations. First , the level of complexity of electrical model require large computational resources. To simulate 15 hours of operation with a 1 second resolution PV profile, the computation time varies from 1 hour to 3.8 hours [9]. Secondly, GGOV, AVR and Synchronous machines models require lots of input parameters (list is provided in annex 7.3) that are rarely available at preliminary assessment phases. Similarly, line voltage and grid topology are rarely know at preliminary steps. Such level of uncertainties challenges the interest of performing detailed simulation (especially for line voltage[10]). Finally, the GGOV model is designed to simulate emergency procedure such as load step compensation. Hence, the physical limitation corresponding to the normal load following operation are not considered. As a matter of fact, ramp-rate limitation are often provided by manufacturer to limit the ageing of the turbine. This is not considered in the GGOV modelling although it might substantially alter the dynamical performance of the system.

A reduced model will be proposed in the next part to simplify the simulation process and better account for ramp-rate constraints.

---

[9] 3 hour using a 4cores 8go RAM Intel i5 CPU, 1h using an 20 core 128Go Ram Intel Xeon CPU

[10] As a matter of fact, proper voltage analysis require to solve the power flow equation. To do so, accurate data on cabling configurations, transformers and inverters are necessary. This explains why detailed electrical studies and power flow analysis are not carried at preliminary phases

4.2.2 *The single-line active power model*

4.2.2.1 *Single-line simplification*

The 3-phase detailed model presented in part 4.2.1 showed its ability to provide accurate evaluation of frequency, voltage as well as power supply from all devices. But its limitations in terms of complexity, calculation time and accuracy pushes to adapt it.

The model adaptation consists in reducing the grid description to a single line diagram accounting for active power flows only. The cross dependencies between reactive power versus frequency stability on one side, and active power balance versus voltage stability are ignored ($\frac{\delta V}{\delta P} = 0$ and $\frac{\delta f}{\delta Q} = 0$). This is motivated by the fact that no large voltage drops have been observed during cloud passage even for high penetration rates (see Fig. 4.7 where voltage fluctations remained above 10.95kV).

By neglecting voltage fluctuations, the individual synchronous machine models can be replaced by the equivalent mechanical equation presented in Eq 4.17 (second-order approximation of the swing equation [126]).

$$\frac{d\Delta\dot{\theta}}{dt} = \frac{\Delta P_{mech} + \Delta P_{PV} + \Delta P_{bat} - \Delta P_{load} - D\Delta\dot{\theta}}{M_{eq}} \tag{4.17}$$

The equivalent mechanical equation uses the equivalent inertia of the system M_{eq} expressed in Eq. 4.18. Where M_i is the inertia constant of the machine i expressed in the machine's per-unit system (see 7.3) and MVA_i^{pu} is the per-unit normalization factor (typically the nominal real power of the unit). The load damping parameter D is assumed to be zero since no data were provided by TotalEnergies regarding the sensitivity of the load with regards to the frequency variations.

$$M_{eq} = \sum_i MVA_i^{pu} M_i \tag{4.18}$$

The GGOV is used to model the gas turbine's mechanical power and control system. Since the electrical power is not computed by the synchronous machine model anymore, is is assumed to be equal to the mechanical power at the GGOV input.

PV system is considered as an active power source following Eq. 4.12. The battery systems follows the same equation as in the three-phase model (Eq. 4.14 and 4.15). In order to account for the energy balance of the storage system throughout the day, state-of-charge equations are integrated (Eq. 4.19 and 4.20).

$$E_{bat}(t+1) = E_{bat}(t) + \eta_{bat} P_{bat} \frac{\Delta t}{3600} \tag{4.19}$$

$$E_{bat}^{max} Soc^{min} \leqslant E_{bat}(t) \leqslant E_{bat}^{max} Soc^{max} \tag{4.20}$$

Where E_{bat} is the energy stored in the battery in MWh, Soc is the battery state of charge in % and Δt is the time step used for the simulation in seconds. η_{bat} denote the battery discharging efficiency in % due to DC-AC conversion losses.

Fig. 4.9 shows the single-line model of the power system as implemented in Matlab/Simulink where the 3-phase line representation is replaced by single line active power flows.

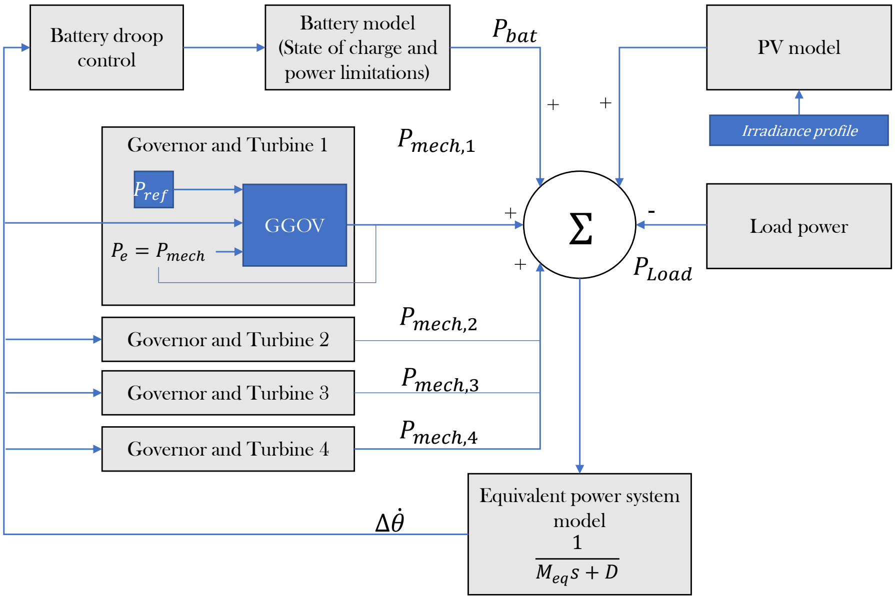

Figure 4.9: Single line model of the power system as implemented with GGOV model for fossil power generation.

The three-phase and monoline models are compared in Fig. 4.10 with a PV ramp of 70% over 50 seconds and a constant load power of 140MW. The monoline model shows a satisfying match with the three-phase model. In this case, the battery supply reaches 2.4MW and the frequency drops down to 49.88Hz with less than. The relatively low battery power supply is explained by the fact that the system stability is mainly ensured by the gas turbines and that no ramp-rate constraints are considered. The computation time is substantially reduced (51 seconds for the three-phase model against 2 seconds for the simplified model).

RAMP-RATE CONTROLLED FOSSIL GENERATION

The single line simplification significantly reduces the computational time. By removing the AVR and synchronous machine model, fewer input parameters are now necessary. In the three-phase model, three sets of parameters are necessary for GGOV (37 parameters), AVR (38

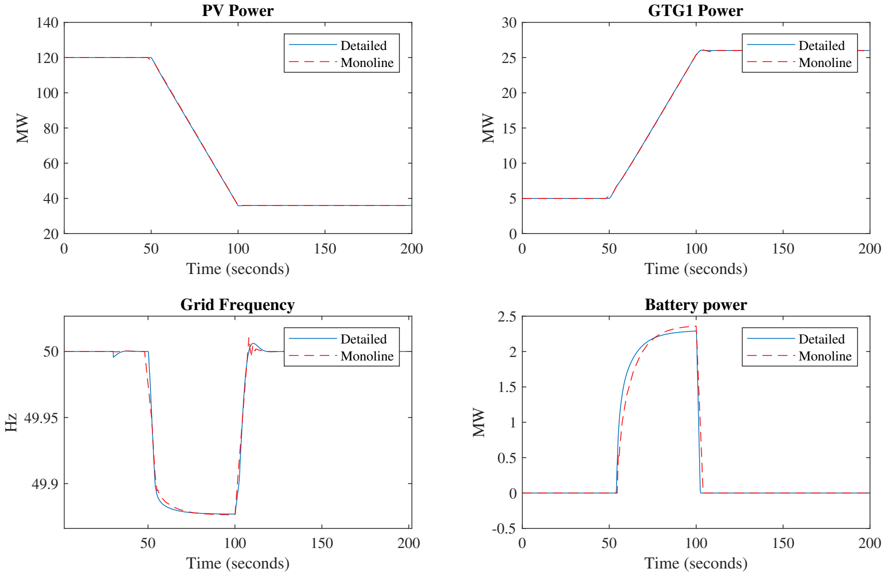

Figure 4.10: Comparison between simulation results of three-phase and simplified electrical model using GGOV model for fossil generation.

parameters) and synchronous machine (17). On the other hand, the monoline model replaces AVR and synchronous machine block by the swing equation and therefore only uses the inertia M and damping constant D. However, the use of the GGOV model remains a challenge if data are not available.

In most cases, only ramp-rates are publicly disclosed by manufacturers which leads to develop a dedicated ramp-constrained model. In addition, the GGOV model was initially developed to simulate large load picking which rarely occurs. Therefore, the response time of the GGOV can be considered as an emergency response (see Tab. 4.6). Since solar drops frequently occur due to cloud passage, fossil units should be operated in emergency mode as less as possible and follow the normal ramp-rate (also called load-following ramp-rate).

Name	Nominal Power (MW)	Mode	Time to achieve 100% of load increase (s)	Ramp rates (MW/sec)
Industrial GT	54	Emergency	11	10
		Normal	260	0.208
Gas ICE	9.3	Emergency	40	0.232
		Normal	60	0.155

Table 4.6: Time to achieve 100% of load increase and corresponding ramp rates for gas turbine and internal combustion engine in emergency and normal modes.

The ramp rate control consists in replacing the fuel actuation and turbine dynamics block by a slew rate saturation (Eq 4.21 and 4.22).

$$\frac{du}{dt} = \frac{P^*_{mech}(i) - P^*_{mech}(i-1)}{t(i) - t(i-1)} \tag{4.21}$$

$$P_{mech}(t(i)) = \begin{cases} \Delta t.rr_{up} & \text{if} \quad \frac{du}{dt} > rr_{up} \\ P^*_{mech}(t(i)) & \text{if} \quad rr_{down} \leqslant \frac{du}{dt} \leqslant rr_{up} \\ \Delta t.rr_{down} & \text{if} \quad \frac{du}{dt} < rr_{down} \end{cases} \tag{4.22}$$

$$P_{min} \leqslant P_{mech} \leqslant P_{max} \tag{4.23}$$

Where P^* is the controller power output, P is the ramp rate limiter output, $t(i)$ the time corresponding to the simulation step i and rr_{down}, rr_{up} the manufacturer's ramp rate parameters.

To ensure the stability of the system during ramp event, the PID control implemented in the GGOV is replaced tuned back (Eq. 4.24 and Tab. 4.7). In addition, the unit power setpoint P_k obtained from the EMS is tracked using proportional control (Eq. 4.25). The mechanical control signal before ramp saturation P^*_{mech} is given by Eq. 4.26. The calculation steps of the final mechanical power output P_{mech} are displayed in Fig. 4.11.

$$P^*_{\theta}(t) = K_p \Delta\dot{\theta} + K_i \int_0^t \Delta\dot{\theta} dt + K_d \frac{d\Delta\dot{\theta}}{dt} \tag{4.24}$$

$$P^*_{setpoint} = K_s \left(P_k - P(i-1)\right) \tag{4.25}$$

$$P^*_{mech} = P^*_{\theta} + P^*_{setpoint} \tag{4.26}$$

Parameter	GGOV	Ramp saturated (Emergency)	Ramp saturated (Normal)
K_p	5.3	-0.5	-0.12
Ki	1.9	-0.016	-0.0315
K_d	4.9	-0.01	-0.01

Table 4.7: PID parameters for GGOV and ramp-saturated models.

Figure 4.12 displays the response of the GGOV model and ramp-saturated model both in emergency (600MW/min) and normal operation (12.5MW/min) mode. The response rate of GGOV and ramp

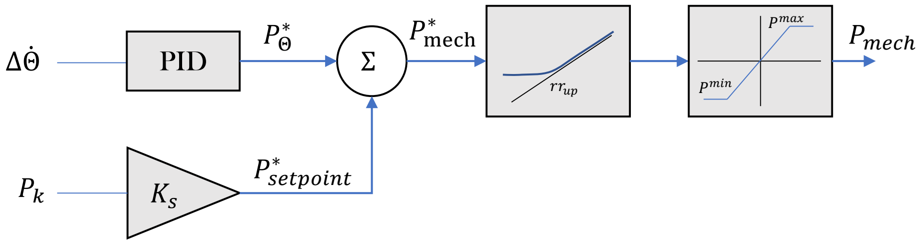

Figure 4.11: Ramp saturated model replacing the GGOV block in the Monoline model.

saturated model in emergency model are very similar thanks to the PID tuning. The simulation time of the ramp-saturation model sightly increases (10 seconds for a 150 seconds time-window). In normal mode, the impact of the frequency become significant which forces the battery to supply more than 20MW. This shows that considering ramp saturation may substantially modify the electrical stability of the system and the power quality. The similar response rate between GGOV and emergency mode shows that the ramp-saturated model remains accurate to evaluate the power quality.

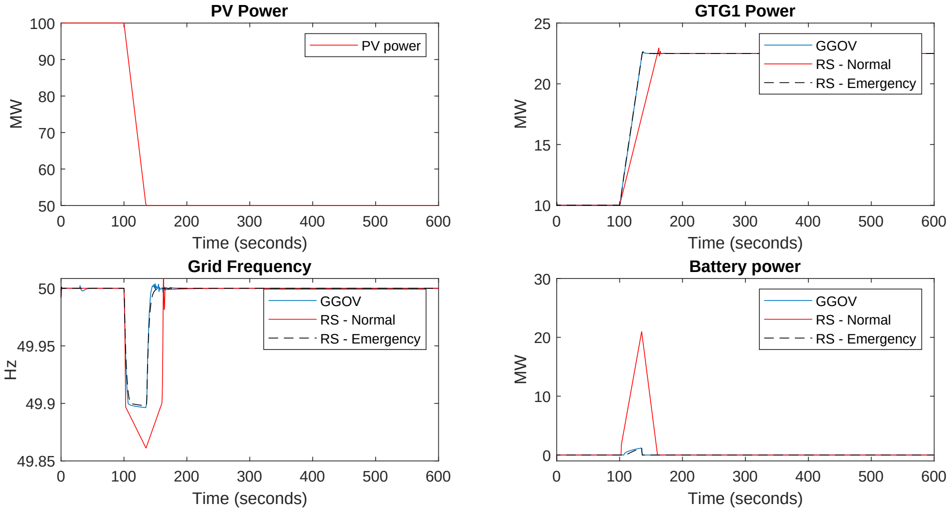

Figure 4.12: Comparison of system response to a PV drop of 50% over 35 seconds for GGOV model and ramp-saturated (RS) model in emergency and normal operation mode using the simplified model.

4.2.2.2 *Simulation of daily irradiance timeseries and comparison with 3 - phase model*

The simplified model with and without ramp rate control is compared to the three-phase model presented in section 4.2.1. The day-long timeseries ($5.4\ 10^4$ seconds) is simulated in 1 hour with the three-phase model, against less than 3 seconds for the simplified model [11]. The two cases proposed in Tab. 4.5 are simulated and results are presented in Tab. 4.8 and 4.9. For both cases, similar results are obtained for three-phase model and simplified model without ramp-saturation. In case 1, there is no battery power supply and the minimum frequency is around 49.80 Hz. In case 2, the maximum battery power output reach 3.51 MW and 3.71 MW for the three-phase and simplified model respectively. This shows the consistency of the model simplification. On the other hand, the simplified model with ramp saturation requires much more battery power : 20.76 MW in case 1 and 32.3 MW in case 2. Thanks to the battery supply, frequency is kept close to the steady-state frequency variations (49.5 Hz). The impact of the ramp-rate control on battery capacity requirement appears to be significant (0 MW without ramp rate control against 20.76 MW with normal ramp-rate control in case 1). This shows that if ramp-rate limitations are imposed by manufacturers, a primary support storage system is necessary.

Parameter Unit	Max. Battery power MW	Frequency MAE Hz	Minimum Frequency Hz
3-phase model	0	0.01	49.85
Monoline model	0	0.05	49.80
Monoline model + ramp saturation	20.76	0.20	49.48

Table 4.8: Comparison of simulation results for 3-phase and simplified model in case 1 (140 MW load + 70 MW PV)
12

Parameter Unit	Max. Battery power MW	Frequency MAE Hz	Minimum Frequency Hz
3-phase model	3.51	0.02	49.75
Monoline model	3.62	0.06	49.69
Monoline model + ramp saturation	32.3	0.49	49.47

Table 4.9: Comparison of simulation results for three-phase and simplified model in case 2 (170 MW load + 120 MW PV).

4.2.3 *Impact of schedule decisions on power quality*

Thanks to power plant electrical modelling and simulation using high-resolution timeserie, the impact of PV integration on power quality can be assessed. However, several aspects of fossil generators management are ignored in this approach. First of all, the minimal power of gas generator is not taken into account in the GGOV models. As a result, GTs operate bellow their minimal power rating in both cases shown in Fig. 4.6 and 4.7. In real life conditions, a part of the PV capacity should be curtailed to keep generators within their operating range. Additionally, GTs have a lower efficiency at low load

---

[11] Computer performances : 8 core and 64 Go Ram Intel Xeon CPU

factors. This pushes to reduces the number of running turbines to increase their power ratings and reduces their fuel consumption. These considerations are at the center of planning optimization techniques aiming at finding the best set of fossil units at each hour of the day. In simple systems composed of a single type of generator, the planning constraints can be expressed by Eq. 4.27 and 4.28 (for the sake of simplicity, more complex constraints such as spinning reserve or redundancy are ignored at this step and will be detailed in the next sections of this chapter).

$$\sum_m P_m + \overline{P_{PV}} = P_L \tag{4.27}$$

$$P_m^{min} \leqslant P_m \leqslant P_m^{max} \tag{4.28}$$

The number of operating turbines can be expressed following Eq. 4.29 depending on the load demand P_L. By considering $\overline{P_{PV}}$ as the averaged PV power in an hourly interval, the required number of turbines for case 1 and 2 is calculated in Tab. 4.10.

Due to the high PV penetration, the number of turbine can vary from 1 to 4. This will lead to a reduction of mechanical inertia in the system (Eq. 4.18) and ramping capabilities (Eq. 4.30) from the gas turbines which affects the stability of the system and therefore the battery requirements.

$$n_{turb} = E\left(\frac{P_L - \overline{P_{PV}}}{P_m^{max}}\right) + 1 \tag{4.29}$$

$$rr_{max} = \sum_{i=1}^{n_{turb}} rr_i \tag{4.30}$$

	Hour	5	6	7	8	9	10	11	12	13	14	15	16	17	18
Case 1	$\overline{P_{PV}}$	0	0,2	11,6	29,0	35,9	65,0	58,8	64,9	70,0	63,0	45,6	35,9	14,1	0,0
	n_{turb}	4	4	3	3	3	2	2	2	2	2	3	3	3	4
Case 2	$\overline{P_{PV}}$	0,0	0,5	23,2	57,9	71,9	130,1	117,5	129,8	140,1	126,0	91,2	71,8	28,1	0,0
	n_{turb}	4	4	4	3	3	1	2	1	1	1	2	3	4	4

Table 4.10: PV power and number of turbine for case 1 and 2 under 2011-03-16 irradiance conditions.

ELECTRICAL SIMULATION OF CLOUD PASSAGE

To evaluate the impact of planning decisions on power quality, PV plants of various sizes are simulated for all isolated solar ramp scenarios of the convex hull defined in Chapter 3. Figure 4.13 shows the grid frequency profile with the largest deviations among all ramp events of the convex hull (observed for a ramp of 0.4 kW/m2 over 15 seconds). Thanks to the battery support, the frequency is maintained within the specified limitations (49.5Hz).

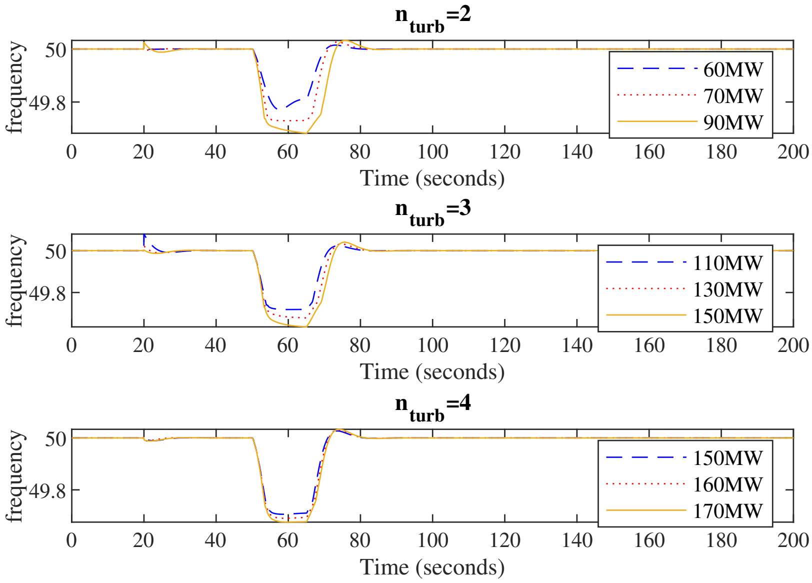

Figure 4.13: Frequency simulation during the worst cloud passage of several PV power plants (0.4 kW/m2 over 15 seconds) without ramp-rate control.

Fig. 4.14 displays the required battery capacity to maintain the frequency stability for several installed PV capacity. In Fig. 4.14 (A), the maximum PV capacity at which no battery support is needed depends on the number of connected turbines : 60 MW of installed capacity for 2 turbines against 100 MW with 4 turbines connected. This figure also highlights that for a given PV installed capacity, large battery capacities are required to maintain frequency stability if a small number of turbines are running : No battery supply for 4 turbines, 3.5 MW for 3 turbines and more than 11 MW for 2 turbines in the case of a 100 MW PV plant. These observations are even more striking in the case of ramp controlled turbines (In Fig. 4.14 (B)) with much larger battery power supply : for a 70 MW PV plant, the battery support raises from 16.22 MW with 4 turbines up to 21.5 MW with 2 turbines.

These results illustrate that battery size can be underestimated if a fixed number of turbines is considered (for example 4 turbines along the day). In practice, the power system would face high risks of electrical instability when shutting down fossil units. Hence, to size the battery system and meet the power quality constraints, hourly schedule decisions should be considered as they impact the resiliency of the system.

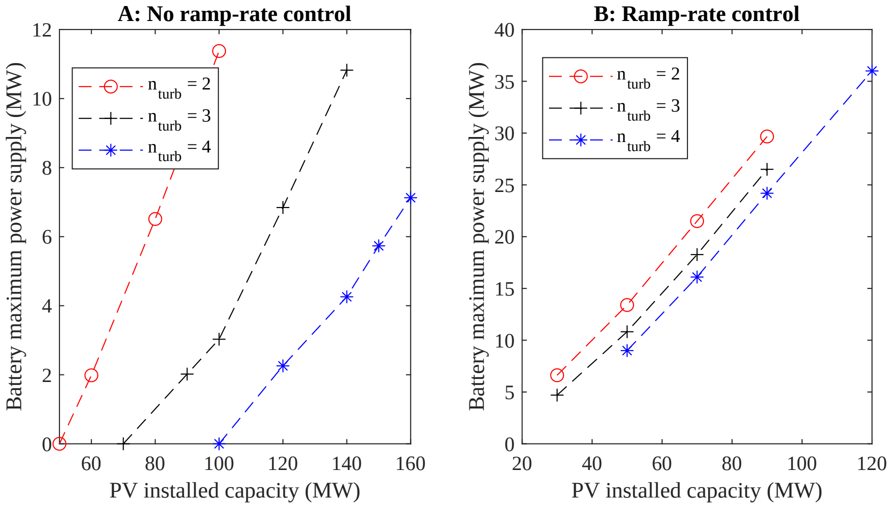

Figure 4.14: Battery power support required to maintain frequency stability for several power plant under their worst cloud passage (0.4kW/m2 over 15 seconds). A : No ramp rate control on gas turbines; B : ramp rate control at 12.5MW/min.

It can be concluded that detailed electrical modelling cannot solely address the problem of power quality in hybrid systems. To maximize the PV penetration, reduce the fuel consumption and keep the fossil generator within their operational limits, schedule decisions need to be made to reduce the number of running generator along the day.

This gives a wide range of configuration that depends on the load profile and PV power production during the planning interval as well as the performances of the generators. These planning decisions reduce the resiliency of the grid to electrical perturbation. To accurately evaluate the performances of the power plant, the coupling effect between energy management optimization and power quality simulation needs to be addressed.

4.3 MULTI LAYER SIMULATION OF HYBRID POWER PLANT

Now that dynamic models for the evaluation of power quality and storage capacity evaluation have been proposed, economic and environmental performances must be integrated to perform an overall preliminary assessment of the hybrid power plant.

To that end, an energy management model must be constructed to reproduce the decision process as it would be conducted in real-life applications. This consists in taking decisions on fossil generators status and power output as well as PV curtailment. These decisions are made to minimize the system's fuel consumption (or a composite function taking additional operational costs) and respect operational constraints on fossil generators as well as resiliency constraints (PV loss or generator failure).

As shown in part 4.2.3 the energy optimization may impact the power plant's configuration between each decision (number of connected generators, proportion of connected PV array etc.). To ensure a reliable evaluation of battery needs and plant's performances, electrical simulations must be carried alongside energy management optimization.

In this section, a novel methodological framework is formulated to evaluate economic, environmental and electrical performance simultaneously. The principle of the method is to simulate the power plant thanks to the simplified dynamic model after each decision of the energy management. Such methods respects the industrial constraints on calculation time thanks to fast-solving models (both for planning decisions and dynamic simulation) and the use of scenario reduction method presented in Chapter 3. In the present work, the energy management model is formulated as a Mixed Integer Linear Programming (MILP) model.

In part 4.3.1, the principle of the simulation framework is detailed and compared to the state-of-the art methods for hybrid power plant simulations. In part 4.3.2, an energy management formulation including resiliency constraints for cloud passage and generator outages is detailed. The coupling process with the short term layer is then presented in part 4.3.3. Finally, the strategy for scenario reduction and aggregation is presented in part 4.3.4.

4.3.1 *Approach*

The reconciliation of energy management strategy at hourly time scales and power quality control at short time scale is a challenge that is still being investigated by the scientific community. The main challenges of such reconciliation are summed up in Fig. 4.15 and may be briefly listed as follows :

- Different time-scales: Energy optimization aim at managing generator schedule on a 10 min to 1 hour timescale which corresponds to the time required to start of shut-down a generator. On the contrary, frequency and voltage shift occur at low timescales (few seconds).
- Calculation methods : As stated in part 2.3, Energy management problems are formulated and solved thanks to optimization techniques (heuristics, non linear or linear optimization) whilst electrical simulation requires to solve differential power flow equations (thanks to time-domain simulation and representation in the Laplace domain).
- Opposite incentives : The energy management layer pushes to integrate as much PV as possible to reduce the fuel consumption whereas electrical analysis will tend to reduce the instability by lowering PV penetration or increasing the number of running generators.

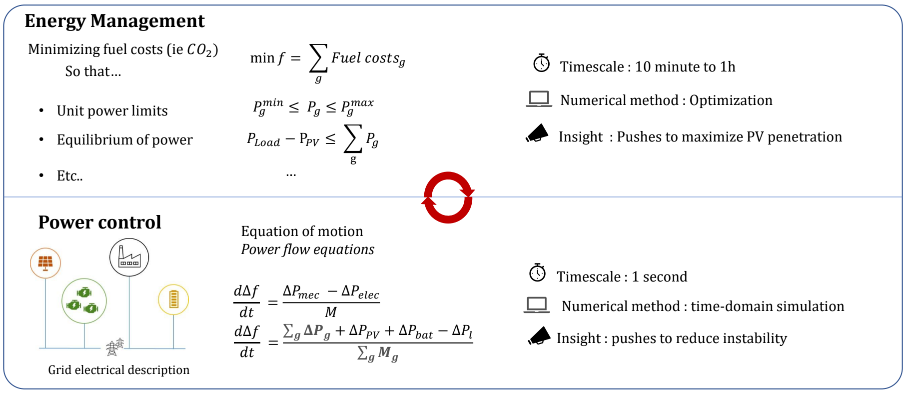

Figure 4.15: Main differences between energy management and control layers.

One solution is to integrate the power control problem within the high level energy management optimization framework. This is investigated in [135, 165, 168, 210] where various strategies are implemented to ensure the frequency stability thanks to linear or non-linear constraints. However, the size of the optimization problem forces to reduce the level of accuracy of the short term representation to keep the solving time reasonable. In addition, the use of integrated indicators and constraints at hourly steps does not allow providing metrics on the power quality and the occurrence of the disturbances observed. Finally, as highlighted in [135], the aggregation of frequency stability in linear constraints leads to suboptimal solution which reduces the fuel savings.

The challenge of fully-integrated optimization problem justifies the use of a multi-layer approach to reduce computational burden and provide more tangible power quality metrics. As shown in Fig. 4.16, the energy management simulation will be handled in an hourly interval thanks to a linear programming framework. This allows developing a flexible and comprehensive optimization framework whilst providing the guaranty of optimality of the proposed dispatch. On the other side, the short term power control is simulated thanks to the single-line model proposed in part 4.2.2.

Simultaneously taking into account energy management and power control allows reproducing the operational decision scheme of the power plant. For an industrial power plant, the day-ahead management is expected to be conducted as follows[13]:

1. The schedule of the fossil generators is processed depending of needs, availability and costs. Since large scale engine have a quite long start-up time and non-negligible start-up costs, the schedule covers several hours of operation. In this work, we consider it done at the beginning of the day and for the next 24 hours. The decision made on start-up and shut down procedures are only made at this step and cannot be modified during the day (excepted emergency procedures related to equipment contingency).

2. As the PV production and load demand vary over the day, the commitment of each machines must be reprocessed with updated values. These values are sent as new power setpoints to the fossil generators.

3. The power output is finally re-adjusted in real time to ensure adequacy between electrical generation and demand and keep frequency and voltage within acceptable limits following the primary, secondary and tertiary control. At this step, a battery storage system is integrated to provide primary reserve support in case of power unbalance.

To reproduce this process, two steps of optimization are implemented and are interfaced with the short-term power control layer. This is shown in Fig 4.16. The principle of each steps are the following:

1. The hourly forecast (or hourly mean irradiance value) of a day is used to calculate the optimized schedule of the fossil generators (block 1).

---

[13] This process has been identified thanks to meetings with operators and power plants experts in TotalEnergies and represents the current operational philosophy. The main reason for not updating start-up ad shut-down decisions throughout the day is that these procedure require complex preparation and potentially put the continuity of supply at risk in case of failures. It could be argued that this operational strategy is suboptimal when integrating PV power (for example, forecasts updates allow recalculating the power balances with better economical performances). The potential of more advanced strategies (such as model predictive control) should be evaluated in the future and put into perspective with the implications in terms of reliability and feasibility of implementation at sites.

2. At every step of 10 minutes, a dispatch optimization is carried out by considering the updated PV output power (block 2).
3. The schedule and new optimal dispatch are sent to a model-based simulator that will simulate the plant with a 1 second resolution during the 10 minute time-window (block 3). A 1-second resolution irradiance profile is used to take PV cloud passing into account. The power control model can adjust the fossil generator and the battery power output.
4. Step 2 and 3 are repeated until the end of the day.

The optimization layers are modelled using the python-based *Pyomo* library and solved thanks to *Gurobi 9.1*. As previously detailed, the control layer is modelled thanks to *Matlab/Simulink*.

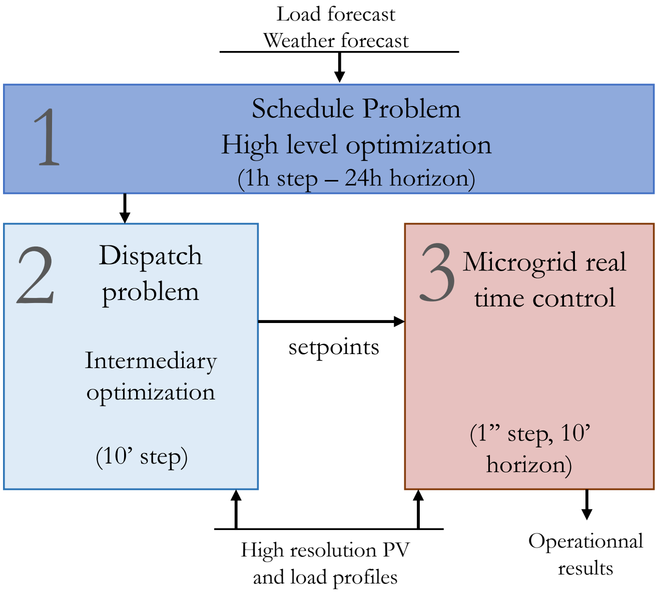

Figure 4.16: Three layers of the simulation framework.

4.3.2 *The generic energy management model*

4.3.2.1 *Objective function and decision variables*

The aim of the energy management optimization is to minimize the fuel consumption costs and the operational costs related to start-up and shut-down procedures of fossil units (Eq. 4.31). The main decision variables are the fossil generator status $\omega_{h,m,i}$, the fossil generator output power $P_{h,m,i}$ and the PV plant injected power $P^{inj}_{PV_h}$. At this step the primary support storage system is not considered since its role is only to provide power support if instabilities occur. It is assumed that (1) the cumulated energy supplied by the storage system can be neglected compared to the consumption of the electrical load and (2) that its energy capacity is high enough to neglect the charging strategy during the day.

$$\min \sum_{h=1}^{H} \sum_{m,i} (FC_{m,i,h}(c_f + c_{CO_2}) + u_{m,i,h}c_{u_m} + v_{m,i,h}c_{v_m}) \quad (4.31)$$

4.3.2.2 *Constraints*

Linear constraints of the management problem are detailed in this section following formulation proposed in [167] . The contingency constraints have been adapted from [188] to match with a single-bus case and to a pool of generators of various technologies.

LOAD BALANCE

The load balance equation (Eq 5.6) ensures the equilibrium of power during each time-step between PV, fossil generation and electrical load.

$$\forall h, \quad \sum_{m,i} P_{m,i,h} + P^{inj}_{PV_h} - Pl_h \geqslant 0 \tag{4.32}$$

FOSSIL GENERATION OPERATIONAL CONSTRAINTS

Eq. 5.8 and 5.9 ensure that minimum and maximum power output of fossil generators are not violated.

$$\forall h, m, i \quad P_{m,i,h} \leqslant P^{max}_{m} \omega_{m,i,h} \tag{4.33}$$

$$\forall h, m, i \quad P_{m,i,h} \geqslant P^{min}_{m} \omega_{m,i,h} \tag{4.34}$$

Start-up and shut-down procedures are integrated using previous state of the fossil generator $\omega_{m,h-1}$ (Eq. 4.35). Equation 4.36 ensures that a unit is not started and shut-down at the same time.

$$\forall h, mi \quad u_{m,i,h} - v_{m,h} \geqslant \omega_{m,i,h} - \omega_{m,h-1} \tag{4.35}$$

$$\forall h, mi \quad u_{m,i,h} + v_{m,i,h} \leqslant 1 \tag{4.36}$$

Minimum up and down time constraints express the minimum amount of time during which a unit must stay on after being turned-on (Eq. 4.37) or stay off after being turned off (Eq. 4.38).

$$\forall m, \quad \forall h \geqslant M_{up_m} \quad , \sum_{k=h-M_{up_m}}^{h-1} \omega_{m,k} - M_{up_m} * v_{m,h} \geqslant 0 \tag{4.37}$$

$$\forall m, \quad \forall h \geqslant M_{dn_m}, \quad M_{dn_m} * (1 - u_{m,h}) - \sum_{k=h-M_{dn_m}}^{h-1} \omega_{m,k} \geqslant 0 \tag{4.38}$$

Eq. 4.39 and 4.40 ensure that all machines of same types are equally loaded (also called load sharing). The element p is defined by the pair (m,i) which which refers to the i^{th} engine of type m. Hence, $p = (m, i)$ belongs to the ensemble of available units M^{UC}.

$\forall$ h, $\forall \quad p = (m, i), \quad p' = (m', i') \quad \in M^{UC} \mid i \neq i' \quad$ and $\quad m = m'$:

$$P_p - P_{p'} \leqslant K(2 - (w_p + w_{p'})) \tag{4.39}$$

$$P_p - P_{p'} \geqslant K(2 - (w_p + w_{p'})) \tag{4.40}$$

CONTINGENCY CONSTRAINTS

A key aspect in the reliability of the power system is the ability to provide power even in case of a loss of fossil generator. This is ensured thanks to redundancy constraints which allocate enough spinning reserve to cover the loss of the largest generator. In conventional systems, this results in running the system with an additional generator (called "N+1 configuration") and leads to higher fuel consumption because of lower part load efficiencies of GTs. Alternatively, a storage system can ensure this spinning reserve to turn off the N+1 generator. This configuration is called "N". The power capacity of such storage system is denoted P_{bat}^{N+1} and is considered as fixed since it is not a decision variable of the problem.

Figure 4.17 illustrates how spinning reserve allocation and N+1 storage can cover the lost of the largest generator.

The operational margin of each unit is denoted $\Delta P_{m,i,h}^{cont}$ and is defined by Eq. 4.41.

$$\forall h, m, i \quad \Delta P_{m,i,h}^{cont} \leqslant P_m^{max} - P_{m,i,h} \tag{4.41}$$

Eq. 4.42 ensures that $P_{m,i,h}^{cont}$ is zero if the unit (m,i) is turned off.

$$\forall h, m, i \quad \Delta P_{m,i,h}^{cont} \leqslant K \cdot \omega_{m,i,h} \tag{4.42}$$

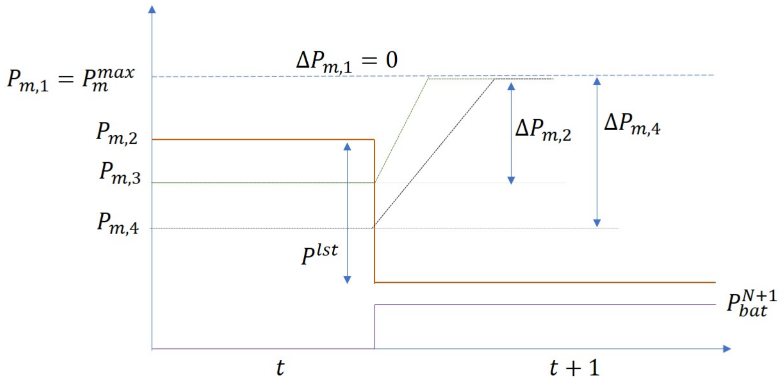

Figure 4.17: Contribution of units and storage to the post contingency state.

P^{lst} refers to the power lost during the contingency and corresponds to the largest power contribution following Eq. 4.43.

$$\forall h, m, i \quad P_h^{lst} \geqslant P_{m,i,h} \tag{4.43}$$

$P_m^{max,lst}$ denotes the maximum output power of the lost unit following Eq. 4.44, 4.45 and 4.46. ΔP_h^{lst} refers to the potential contribution of the lost unit.

$$P_h^{lst} + \Delta P_h^{lst} = P_m^{max,lst} \tag{4.44}$$

$$\forall h, m, i \quad P_h^{lst,max} \leqslant \sum_{m,i} \Delta P_{m,i,h}^{cont} \tag{4.45}$$

$$\forall h, m, i \quad P_h^{lst,max} \geqslant P_m^{max} \cdot \omega_{m,i,h} \tag{4.46}$$

Finally, Eq. 4.47 ensures the load balance at post-contingency state thanks to the cumulated participation of each unit and the potential N+1 storage system. This formulation slightly differs from [188] since the lost unit can be a partially operating unit. Note that the ramp-rate of the fossil units during contingency events is considered as large enough to neglect the grid dynamics.

$$\forall h \quad P_h^{lst} \leqslant \sum_{m,i} \Delta P_{m,i,h}^{cont} - \Delta P_h^{lst} + P_{bat}^{N+1} \tag{4.47}$$

PV INTEGRATION AND CURTAILMENT

The PV system output power depends on I_h and η_{PV} which accounts for the global horizontal irradiance profile as well as optical and thermal effects affecting the system performance. The injected power $P_{PV_h}^{inj}$

therefore depends on the available capacity after potential curtailment $W_{PV_h}^{used}$. This lets a possibility of reducing the availble capacity if reserve requirement becomes too large or if the minimum load of fossil units is reached.

$$\forall h, W_{PV_h}^{used} \leqslant W_{PV}^{inst} \tag{4.48}$$

$$\forall h, P_{PV_h}^{inj} \leqslant W_{PV_h}^{used} * \overline{I_h^{wvm}} * \eta_{PV} \tag{4.49}$$

FUEL CONSUMPTION LINEAR INTERPOLATION

The fossil unit's fuel consumption is calculated thanks to a linear relationship (see fig 4.18). a_m and b_m denotes the coefficient of the fuel curve for the machine of type m.

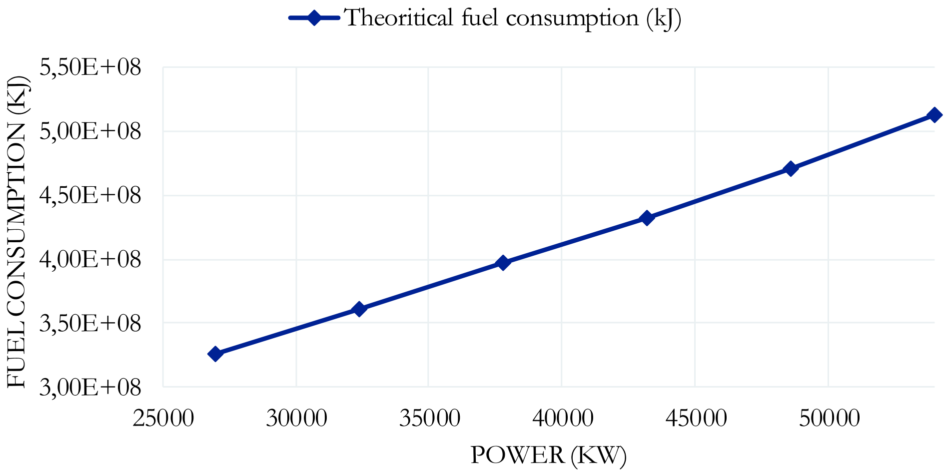

Figure 4.18: Siemens SGT800 fuel consumption for 1h of operation at load.

$$\forall h, m, i$$

$$FC_{h,m,i} = a_m P_{h,m,i} + b_m \tag{4.50}$$

CLOUD PASSING SPINNING RESERVE

The spinning reserve constraint (Eq. 4.51) ensures that the operational margin of all units can cover the PV variation.

$$\forall h \quad \Delta I_h^{avg} W_{PV_h}^{used} \leqslant \sum_{m,i} \Delta P_{m,i,h}^{avg} \tag{4.51}$$

$\Delta P_{m,i,h}^{avg}$ refers to the contribution of each engine to the PV spinning reserve and is defined following Eq. 4.52. Eq. 4.53 ensures that this contribution is zero if the unit is turned off.

$$\forall h, m, i \quad \Delta P^{avg}_{m,i,h} \leqslant P^{max}_{m} - P_{m,i,h} \tag{4.52}$$

$$\forall h, m, i \quad \Delta P^{avg}_{m,i,h} \leqslant K \cdot \omega_{m,i,h} \tag{4.53}$$

4.3.2.3 *Implementation of energy optimization for the schedule and dispatch problem*

At the schedule step, decision are made on the status of fossil units which is not possible at the dispatch step.

In the schedule problem, the optimization is processed over 24 hourly time-step. The ensemble of generators $\mathcal{M}^{UC}$ is composed of all available units.

In the dispatch optimization, the status variables $\omega_{k,m,i}$ become parameters of the problem. The optimization adjusts the power output of generators within the ensembles $\mathcal{M}^{Dispatch}_{h} = \{(m,i) \mid \omega_{h,m,i} = 1\}$. All constraint of the schedule optimization problem are applied excepted Eqs. 4.36, 4.37 and 4.38 since no start-up and shut down decisions are made.

The dispatch optimization is done over a single time step k (a single independent optimization at each 10 minute time-slice $k \in [1, .., 6]$).

The load profile is considered constant within each hourly interval for the schedule optimization and is interpolated at each 10 min time-slice for the dispatch optimization.

$$P_L(h,k) = P_{L_h} + k\frac{P_{L_{h+1}} - P_{L_h}}{6} \tag{4.54}$$

4.3.3 *Short term control layer*

The short term simulation layer simulates the behaviour of the power plant by tracking optimal setpoints of fossil generators $P_{m,i,k}$ obtained from the upper optimization layer and adjusts the production of generating devices to keep the power quality within the specifications. The model proposed in part 4.2.2 implemented in *Matlab/Simulink* is interfaced with the optimization layers.

Figure 4.19 shows the inputs and outputs of the control layer. The PV production is calculated thanks to the 1 second irradiance profile I^{WVM}_t and the available capacity after curtailment $W^{used}_{PV_h}$. Equation 4.12 becomes:

$$P_{PV}(t) = W^{used}_{PV_h} * I^{WVM}_t * \eta_{PV} \tag{4.55}$$

The status decisions of fossil generator $\omega_{h,m,i}$, $u_{h,m,i}$, $v_{h,m,i}$ are sent as parameters to the control layer to force the shut-down and start-up of units as planned by the first optimization layer. The fossil generation setpoint $P_{k,m,i}$ processed by the 2nd optimization layer feeds the unit's setpoint in Eq.4.25.

The load profile is interpolated thanks to the values of the upper optimization layer:

$$P_L(t) = P_{L_k} + t * \frac{P_{L_{k+1}} - P_{L_k}}{600} \tag{4.56}$$

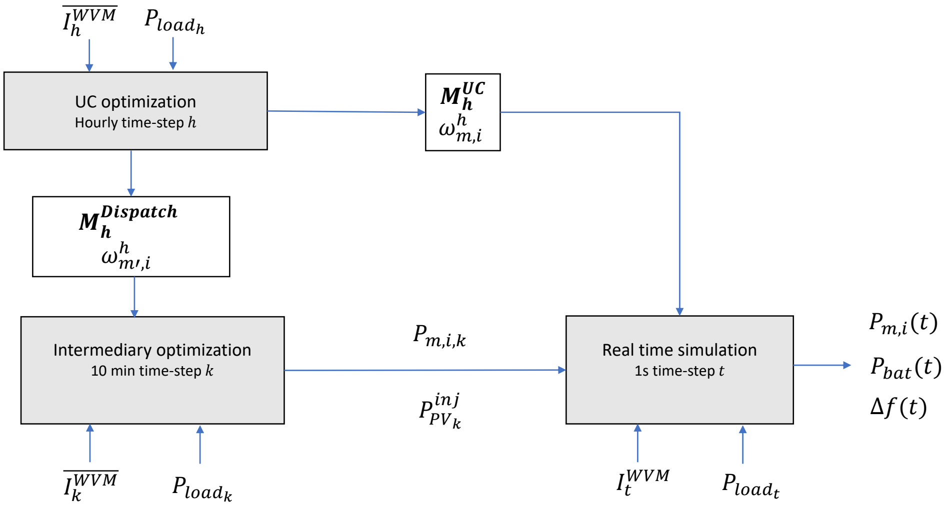

Figure 4.19: Inputs and outputs of the short-term layer. The real time simulation block refers to the single-line electrical model previously detailed (see Fig. 4.9)

4.3.4 *Scenario aggregation for performance evaluation*

4.3.4.1 *Aggregation method*

As presented in the previous part, energy management optimisation (implemented using python's *Pyomo* library) is interfaced with the power control layer modelled thanks to *Matlab/Simulink*. Due to the time required by the optimization solver, API[14] and data management, the simulation of an entire daily timeseries from 7:00am to 8:00pm requires approximately 40 minutes (regardless of the computer's performances). An evaluation using 365 daily timeseries does not match the objective of fast calculation stated in the introduction since it would require more than 240h to simulate a single architecture. Therefore, the scenario reduction method proposed in Chapter 3 is used. This provides representative results in terms of global solar yield and solar variability. To ensure the robustness of the results, a

---

[14] Application Programming Interface

worst case scenario is also simulated and verifies the operability of the system. This gives a set of 6 scenarios : 5 clusters + 1 worst case (in the case of Hawaii solar data). By implementing a parallel computing method, the 6 scenario can be simulated simultaneously in 40 minutes by a standard computer [15].

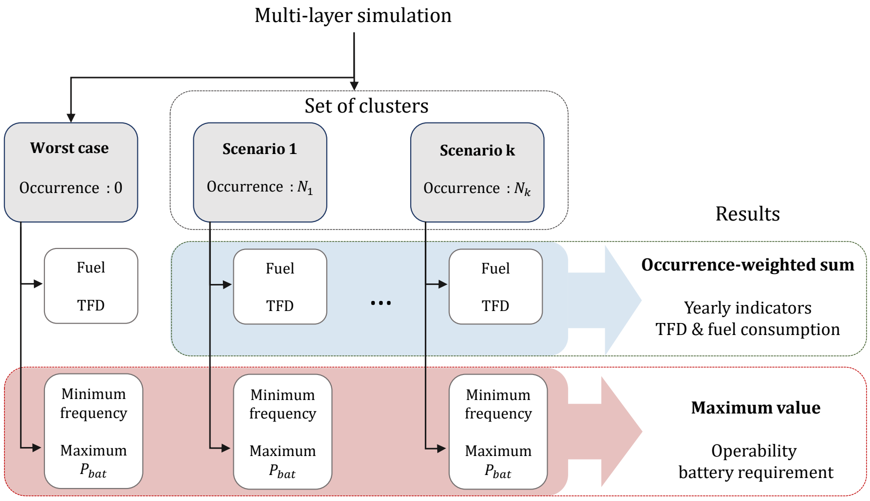

Figure 4.20: Procedure for scenario aggregation.

The scenario aggregation procedure is presented in Fig. 4.20. The fuel consumption, grid frequency and battery power output of each scenario are collected at the end of the simulation and are respectively denoted as $P_{m,i}(t)$, $f(t)$ and $P_{bat}(t)$ with m, i referring to the ith generator of type m . The ensemble of scenario $\mathcal{K}_\sigma$ is defined as $\mathcal{K}_\sigma = \{1, ..., n_\sigma\} \cup \{wc\}$ where $\{1, ...\sigma\}$ are the clustered scenario and wc refers to the worst case scenario. Table 4.11 presents the ensemble obtained from worst-case identification and scenario clustering of the Hawaii dataset [89]. It should be noticed that the number of cluster is not a fixed parameter and should be adapted to have the better match between results from cluster scenarios and 365 days aggregation. It should also be kept in mind that to fully take advantage of the parallel computing, the number of cluster should be lower than the number of cores of the computer. This allows performing a full analysis of an architecture in 40 minutes.

---

[15] Note that the computation time of a single irradiance scenario does not significantly changes with a more powerful computer. However, having more cores available allows running multiple scenarios in parallel

Scenario	Date	Description	Occurence	VI	Cumulative irradiance (kWh)
1	2010-12-09	Very Cloudy	40	21.31	2.63
2	2011-02-02	Medium production, low variability	98	30.90	4.92
3	2010-10-07	Medium production and variability	111	74.97	4.87
4	2011-09-02	High production, high variability Medium sharpness	67	91.10	6.78
5	2011-06-11	High production and variability	49	172.71	6.20
wc	2011-03-16	Worst case variability	0	238.97	5 .92

Table 4.11: Solar input scenarios resulting from the clustering and worst-case identification of the Hawaii dataset.

4.3.4.2 *Indicators calculation*

YEARLY PERFORMANCE INDICATORS

Thanks to the numbers occurrences corresponding to each scenario, yearly performance indicators can be calculated. The global fuel consumption (in kJ) and $CO2$ emission (in tons) are calculated according to Eq. 4.57 and 4.58 with a_m, b_m being the coefficients of the fuel curve and f_{CO2} the $CO2$ emission factor ($tCO2/kJ$). In the following equations, $P^{\sigma}_{m,i}(t)$ and $f^{\sigma}(t)$ denote the short-term simulation results corresponding to scenario σ

$$FC^{global} = \sum_{\sigma \in \mathcal{K}_\sigma} N^{\sigma} \sum_{(m,i)\in M} \sum_{t=0}^{t_f} P^{\sigma}_{m,i}(t) a_m + b_m \tag{4.57}$$

$$CO_2^{global} = FC^{global} * f_{CO_2} \tag{4.58}$$

The overall operating costs OC (\$/year) of the system are expressed in Eq. 4.59 with c_{fuel} the fuel costs (\$/kJ) and c_{CO_2} the $CO2$ emission tax (\$/tons).

$$OC = FC^{global} c_{fuel} + CO_2^{global} c_{CO_2} \tag{4.59}$$

In addition to these economic and environmental indicators, yearly reliability indicators are calculated. The TFD (Time of Frequency Disturbances in sec/year) refers to the cumulated time during which transient disturbances have been observed ($|\Delta f| > \Delta f_{ss}$ with $\Delta f_{ss} = 0.5\% f_0$ according to Tab. 4.1). The calculation of TFD is expressed in Eq. 4.60 and 4.61.

$$TFD^{global} = \sum_{\sigma \in \mathcal{K}_\sigma} N^{\sigma} \sum_{t=0}^{t_f} \mu_f^{\sigma}(t) \delta t \tag{4.60}$$

$$\mu_f(t) = \begin{cases} 1 & \text{if} \quad |\Delta f| > \Delta f_{ss} \\ 0 & \text{if} \quad |\Delta f| < \Delta f_{ss} \end{cases}$$

(4.61)

To evaluate the risk of generator degradation due to ramping exceeding the normal ramp-rates (in case of simulations considering emergency ramp-rates in the fossil generation model), the TONRR (Time Over Normal Ramp Rate, in sec/year) is proposed and refers to the cumulated time during which the unit have been operated above its normal-operation ramp-rate ($\frac{\Delta P_{m,i}}{\Delta t} > rr_{up}^{normal}$). This is expressed in Eq. 4.62, 4.63 and 4.64. As shown in Fig. 4.20, the worst case is not considered in the calculation of yearly indicators which is why its occurrence is set to zero in Tab. 4.11.

$$TONRR_{m,i} = \sum_{t=0}^{t_f} \mu_{rr}(t)\delta t \tag{4.62}$$

$$\mu_{rr}(t) = \begin{cases} 1 & \text{if} \quad \frac{\Delta P_{m,i}(t)}{\Delta t} > rr_{up}^{normal} \\ \\ 0 & \text{if} \quad \frac{\Delta P_{m,i}(t)}{\Delta t} < rr_{up}^{normal} \end{cases}$$

(4.63)

$$TONRR_m^{global} = \sum_{\sigma \in \mathcal{K}_\sigma} TONRR_m^{\sigma} N^{\sigma} \tag{4.64}$$

MACRO SCALE SIZING-RELATED INDICATORS

The indicators listed above are able to quantify the performance of the power plant thanks to the aggregation of "close-up" shots of the plant behaviour. But macro scale indicator are also necessary to qualify the feasibility of an architecture. These indicators consider both cluster scenarios and the worst-case scenario to provide a robust evaluation. In this work, two type of macro-scale indicators are proposed :

- Architecture stability : True if no unauthorized disturbance due to PV cloud passing are observed (if $\forall t, \quad |\Delta f(t)| < \Delta f_{max}$ with $\Delta f_{max} = 5\% f_0$ according to Tab. 4.1)
- Battery Saturation : True if the maximum battery output power observed during the set of scenario K_σ is equal to the maximum capacity of the storage system.

These qualifiers are useful in the primary storage capacity evaluation process. For a given architecture, the minimum required capacity leading to a stable architecture is denoted as W_{bat}^{limit}. In these configuration the battery is saturated and a frequency disturbance appears due to the gap between battery support, generator ramp-up and PV production.

When the battery is not saturated, the grid frequency will be maintained within the steady-state limits thanks to the frequency droop controller. The maximum output power of the battery observed throughout all scenarios is therefore the minimum battery capacity to maintain the grid frequency within steady-state limits W_{bat}^{ss}.

In practice, W_{bat}^{ss} can be obtained by simulating an architecture with a very big storage capacity (for instance the same value as the PV rated capacity). W_{bat}^{limit} is obtained by carrying a sensitivity analysis on the storage capacity and evaluating the architecture stability from Δf.

4.3.4.3 *Input profiles*

SOLAR INPUT PROFILE

Thanks to the scenario identification developed in the previous chapter, a few scenarios are taken as input in the simulator (5 clusters + 1 worst-case). The WVM filtered 1-second irradiance GHI [16] timeseries of each scenario is pre-process according to the needs of each of the 3 layers. In this work, a deterministic approach is used to handle solar data. This means that both averaged production and minimum production within the hourly interval is assumed to be known by the EMS system. The analysis could be enriched by the integration of uncertainties resulting from forecast systems which requires a deep investigation of their performances and a stochastic or robust MILP formulation.

Since the first layer performs a day-ahead hourly schedule, an hourly forecast is generated by calculating the hourly averaged irradiance $\overline{I_h^{wvm}}$. To evaluate the need in spinning reserve requirement (see eq 4.51, the maximum difference between the averaged value and the 1 second profile is calculated following 4.65.

$$\Delta I^{avg} = \max_t(\overline{I_h^{wvm}} - I_t^{wvm}) \tag{4.65}$$

The secondary layer, which adjusts the power rating of fossil generators every 10 minutes, is based on the 10 minute averaged irradiation $\overline{I_k^{wvm}}$ (Eq. 4.66).

$$\overline{I_k^{wvm}} = \frac{1}{600}\sum_{t=0}^{600} I_t^{wvm} \tag{4.66}$$

The control layer includes the PV profiles calculated from 10 minutes slices of 1 second wvm filtered data. Figure 4.22 shows the solar input data for the three layers.

---

[16] Global Horizontal Irradiance

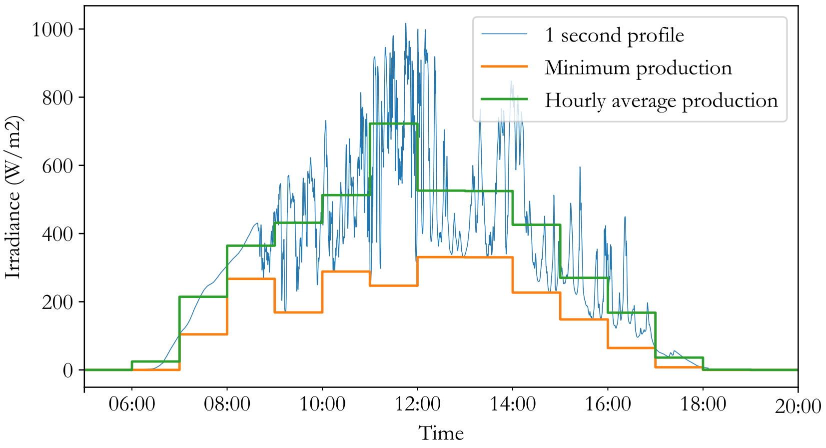

Figure 4.21: Example of deterministic spinning reserve generation.

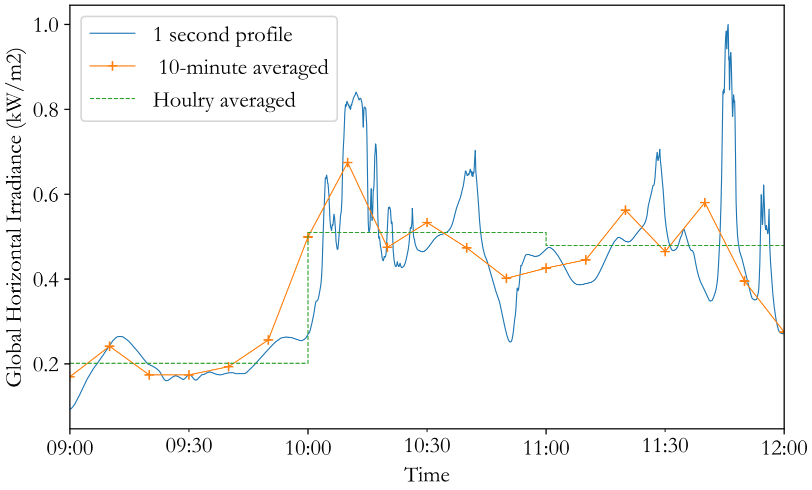

Figure 4.22: Example of GHI input profiles.

LOAD INPUT PROFILE

Intra-hourly load variation are neglected due to the stability of the processes. Figure 4.23 shows the ensemble of daily load profile for an LNG processing plant. The hourly averaged load profile of each daily profile is used in the schedule layer. 10 minutes interpolation is used for the secondary dispatch layer and 1 second interpolation is used and the power control layer. Table 4.12 sums up the solar and load input profiles used by the three layers of the simulator.

	Schedule	**Dispatch**	**Real-time control**
Load	Hourly averaged (raw data)	10-minute interpolation	1-second interpolation
GHI	Hourly averaged	10 minute averaged	1-second profile (raw data)

Table 4.12: Summary of input data profiles for each step of the simulation.

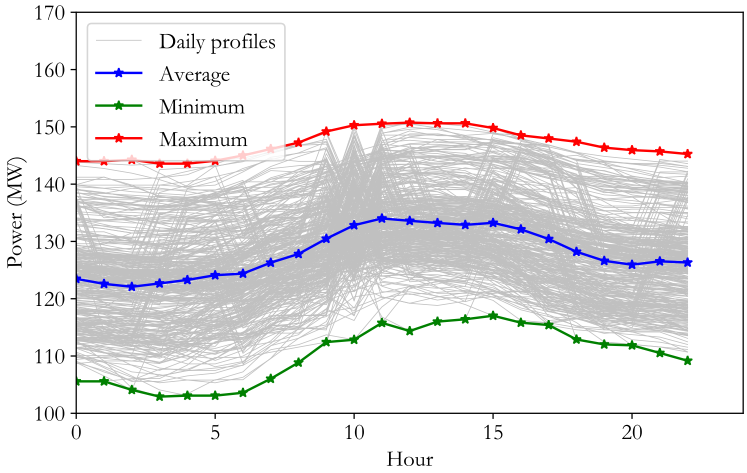

Figure 4.23: Load profiles of the LNG facility. Grey lines show all daily load profiles registered, colored lines show the maximum, minimum and averaged demand profiles.

Now that the theoretical framework of the multi-layer operational simulation has been developed, the next section will present an application on an industrial case study. This will give an example of the simulation capabilities and discuss the interests of this tool for preliminary assessment of hybrid architectures.

4.4 HYBRID POWER SIMULATION FOR AN LNG PROCESSING PLANT

The simulation framework proposed in the previous section has been designed to evaluate the performance and battery requirements of an hybrid architecture. The simulator should provide representative results regarding:

- The economical and environmental performances of the system such as the global fuel consumption, the total CO_2 emission and the total operating costs.
- The reliability of system : a guarantee of operability by ensuring that no unauthorized disturbances where observed and the cumulated time of frequency disturbances TFD^{global}.
- The optimal size of the storage system to maintain the frequency within steady-state limits W^{ss}_{bat} and the minimal size of the storage to guarantee stability with authorized transient disturbances W^{limit}_{bat}

In the first part of this section, a base case will be simulated. To test the relevance of the aggregation method, results will be compared with a full year simulation resulting from the 365 daily scenarios.

Then, the question of the impact of operating philosophy of industrial microgrid will be addressed. Operating choices mainly consists in imposing the redundancy constraint on fossil generation and in considering GT manufacturer's normal operation ramp-rate. The impact of such choices on the performance of the hybrid power plant will be studied.

Finally, the architectural levers to reduce the carbon footprint and improve economical performance of hybrid power plant will be studied. This consists in running a sensitivity analysis on the installed PV capacity, installed primary system storage and fossil power plant.

The case study represents an LNG facility where solar PV must be integrated to an existing fossil power plant. Several size of PV and ESS[17] will be studied to investigate the electrical and economical performance of the system. Table 4.13 shows the different configurations of the system. The load profile of the system is displayed in Fig. 4.23. The averaged power demand profile is used as input to the simulator. The five clusters and the worst case scenario identified in Chapter 3 are used as input (see previous section for more details on solar input management). Tab. 4.15 reports the main parameters related to fossil generators.

---

[17] Energy Storage System

-	Base case	Range studied
Number of gas turbines	5	[0 - 5]
Number of gas engines	0	[0- 16]
PV installed capacity (MW)	70	[50 - 100]
ESS installed capacity (MW)	20	[0 - 25]

Table 4.13: System configurations.

Parameter	Unit	Value
PV CAPEX	€/kW	600
Storage CAPEX	€/kW	400
CO_2 Tax	€/tCO_2	40
CO_2 emission factor	tCO_2/tfuel	2.7
Fuel Costs	€/mmbtu	10
PCI fuel	MJ/mmbtu	38.1
Project lifetime	years	20
Discount rate	%	0

Table 4.14: Parameters for costs analysis and optimization.

Parameter	Symbol	Unit	GT	ICE
Power range	P_m^{min}, P_m^{max}	MW	22.5 - 45	2.7 - 9.3
Fuel curve coef.	a_m	kJ/kWh	6.8 10^3	7.2 10^3
Fuel curve intercept	b_m	kJ	139 10^6	7.3 10^6
Start-up & shut down cost	c_{u_m}, c_{v_m}	$	979	165
Minimum up time	M^{up}	h	6	1
Minimum down time	M^{dn}	h	6	1
Inertia constant	M	s	5.51	0.5

Table 4.15: Fossil generation parameters for gas turbine SGT800 (GT) and gas engine W20V34SG (ICE).

4.4.1 *Base case*

4.4.1.1 *Results with scenario aggregation method*

The base architecture in the GT-PV-ESS configuration consists in 5 gas turbines and a PV installed capacity of 70 MW. Redundancy constrainst are not considered which means that the plant is operated in "N" configuration. The size of ESS is to be defined thanks to the power quality analysis. Therefore, infinite power and energy capacity are set. The maximum battery power supply over the 6 daily scenarios will be considered as the required storage for the architecture. The gas turbine maximum ramp rate corresponds to the normal operation ramp rate of 12.5 MW/min.

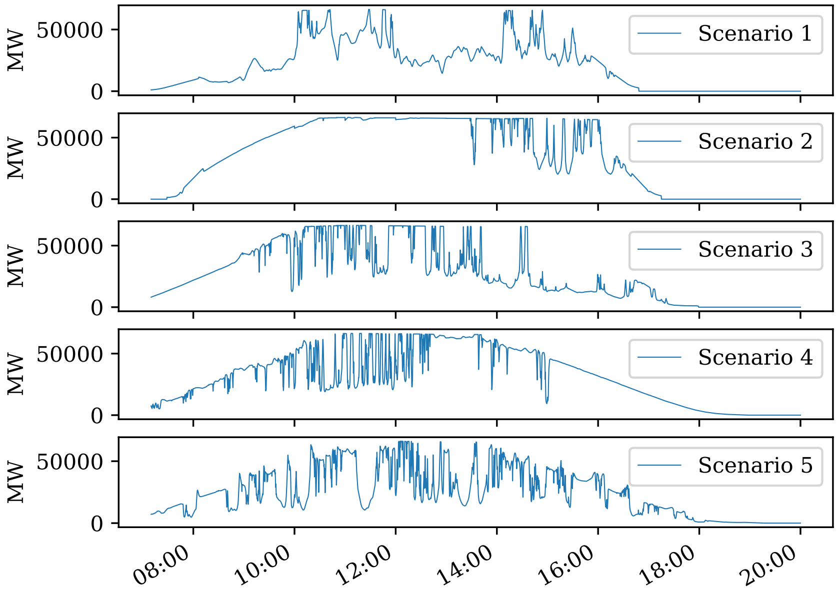

Figure 4.24: Daily PV plant output power profiles.

Figure 4.24 displays the PV plant output power. Due to the gas turbine minimum load factor of 50%, the PV output power is curtailed which limits the renewable penetration (especially during scenarios 2 and 3). The frequency shift is maintained within +/- 0.5% of the nominal frequency as shown in Fig. 4.25. This shows the ability of gas turbine and storage system to compensate for the cloud passage.

In Fig. 4.26, the gas turbine and battery output power are displayed. It can be seen that only 3 gas turbine are operating thanks to the fuel consumption optimization which is the minimum achievable considering spinning reserve constraints. Throughout the 6 days, the battery output power reaches a maximum of 20.5 MW. TONRR is zero because the normal operation ramp rate is set in the rate limiter of the fossil generation block. The TFD is also zero because because the battery is large enough to cover every cloud passage.

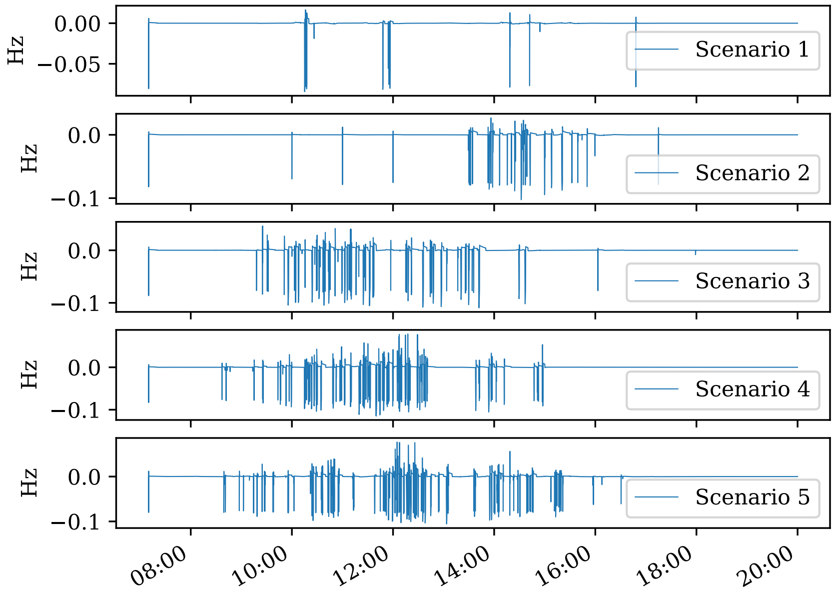

Figure 4.25: Daily frequency profiles.

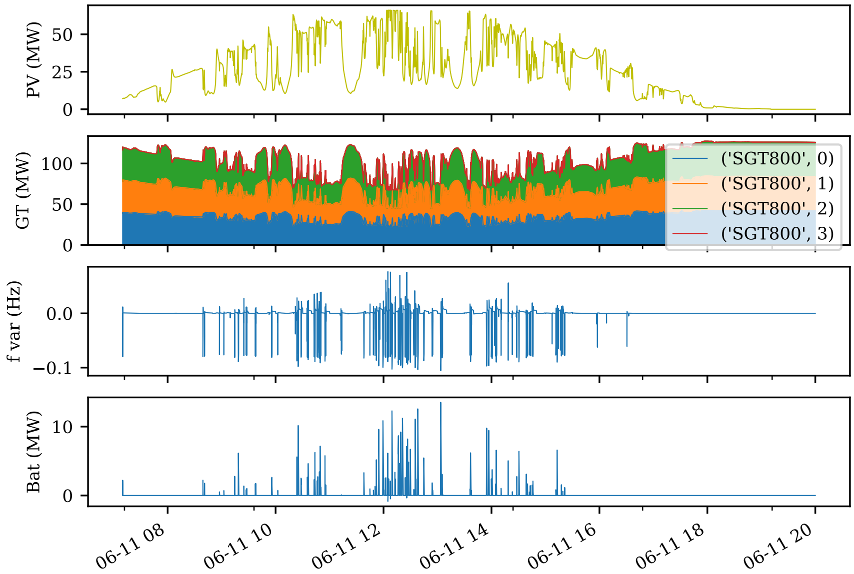

Figure 4.26: Simulation results of scenario 5 for the base case. "GT" denotes Gas turbines power output.

Scenario	Max. battery power	TFD	Fuel consumption	Battery energy supply
-	MW	sec	kJ	MWh
1	19.9	0	$11.58\ 10^6$	0.05
2	18.3	0	$12.47\ 10^6$	0.34
3	3.70	0	$13.40\ 10^6$	2.17
4	18.0	0	$12.80\ 10^6$	2.5
5	14.2	0	$13.01\ 10^6$	1.6
wc	20.5	0	$12.10\ 10^6$	7.6

Table 4.16: Summary of main metrics resulting from base case simulation.

One of the main assumption for building the energy optimization model was to neglect the battery energy flows in the hourly power balance (see part. 4.3.2.1). The energy supplied by the battery over each daily scenarios is reported in Tab. 4.16. The maximum energy is supplied during the *wc* scenario with 7.6 MWh. This represents 0.8% of the 852 MWh supplied during the time-window (7:00am - 8:00pm) and confirms that battery energy flows can be neglected in hourly load balance.

Most of battery systems are characterized by their ratio of maximum power delivery capacity over energy capacity at full charge (denoted as C-rate). The worst-case scenario shows that a battery with a C-rate of 2.9 would be sufficient to cover the whole day without needing intermediary charging.

4.4.1.2 *Comparison with full year simulation*

To validate the use of the reduced set of day-long scenarios, the aggregated indicators are compared with values resulting from the simulation of the whole year (365 solar irradiance scenarios). Table 4.17 compares indicators obtained from the aggregation of clusters scenarios and worst case (Clusters + worst case) and indicators obtained by running the simulator over the whole dataset (Full year). Results show very similar results for lifetime OPEX (-0.3%). This shows that the set of scenarios is representative in terms of fuel savings. Since no battery power limitation were considered, both configuration gives a TFD of zero and a minimum frequency of -0.25Hz. However, the maximum battery power is higher for the full year configuration (25.2 MW against 20.5 MW) which shows that the worst-case scenario is not fully conservative and that more extreme events happen throughout the year.

Simulation	Clusters + worst case	Full year
Maximum battery power (MW)	20.5	25.2
TDF (s)	0	0
Lifetime OPEX (€)	$3.09\ 10^9$	$3.08\ 10^9$
PV curtailment (%)	3.4	4.3
Minimum frequency (Hz)	-0.025	-0.025

Table 4.17: Comparison of aggregated indicators for cluster + worst case and full year simulation with infinite battery power capacity.

The difference in battery sizing between full year and cluster simulations suggest that an inadequate battery sizing could be obtained leading to instabilities when facing extreme solar drops. When simulating the full year with a maximum battery capacity of 20.5 MW, a TFD of 74 seconds have been observed (0.0002% of the total time of operation). Therefore, this can be taken as an opportunity to reduce the costs of the sizing by neglecting most extreme events while ensuring the reliability of the system in more than 99.99% of the time.

The aggregation of cluster scenarios and worst case significantly reduces the simulation time (7.3 hour for the full year against 40 minutes for cluster + worst case aggregation) while successfully providing performance indicators regarding economics, power quality and battery sizing.

4.4.2 *Impact of operational philosophy on performances*

4.4.2.1 *Redundancy constraints*

To ensure the continuity of supply in case of generator contigency, redudancy constraints can be activated in the schedule optimization formulation (see Eq. 4.41, 4.42, 4.45). These constraints ensure that enough spinning reserve is available to supply the lost of the largest contribution form fossil generation. This spinning reserve can be ensured by all connected fossil units which generally leads to start an additional unit (N+1 operating philosophy) but also causes higher fuel consumption since the load factor is reduced. An alternative is to use a dedicated storage system to ensure the spinning reserve, keeps a minimal number of connected fossil units and improves the overall efficiency of the fossil generation (N operating philosophy).

In part 4.4.1.1, the power plant is operated in N philosophy whereas in this part, redundancy constraints are activated to investigate their impact on the plant's performances.

Fig. 4.29 displays the fossil dispatch over irradiance scenario n°2 (2011-02-02). As expected, an additional unit is turned-on which forces the system to operate with 3 running GTs. This lets a smaller margin for PV integration due to the minimum load factor of 50%.

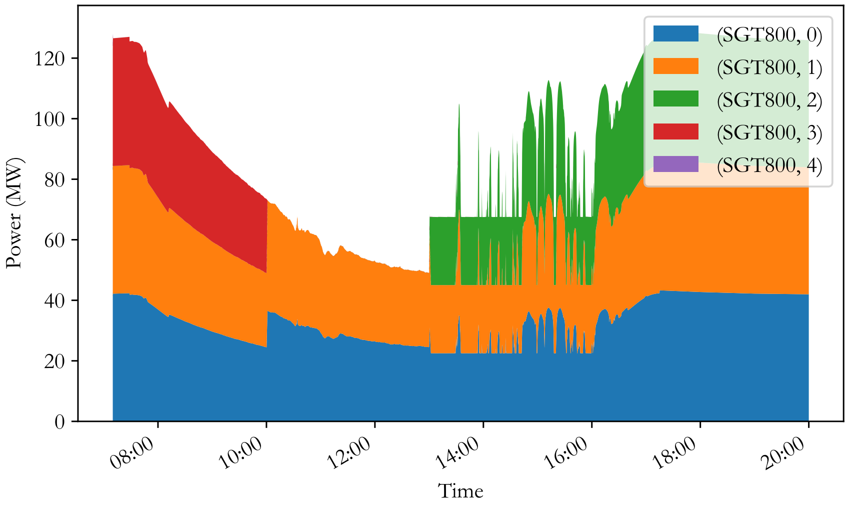

Figure 4.27: Fossil generation output for base case in N philosophy.

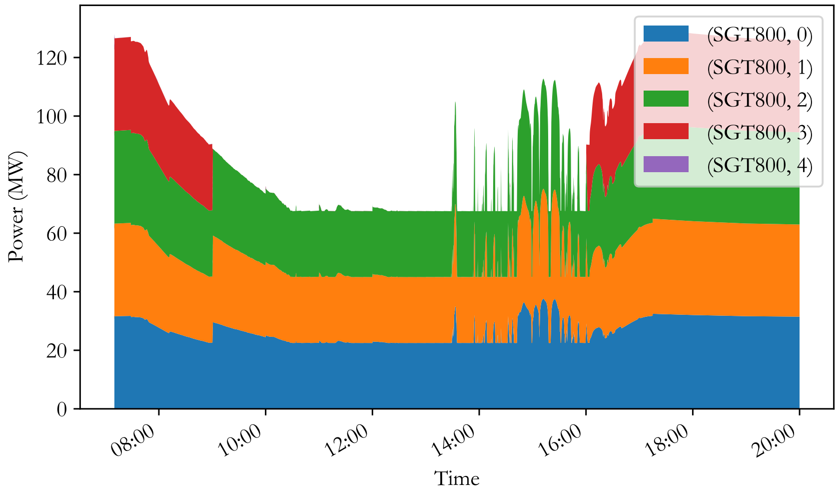

Figure 4.28: Fossil generation output for base case in N+1 philosophy.

Fig. 4.29 shows the PV injected power over the 5 clustered scenarios. In the 2nd scenario, PV capacity is curtailed from 10am to 4pm in N+1 against 1pm to 4pm in the N philosophy leading to an overall curtailment of 8.23% (+4.4% as compared to N). On the other hand, the additional N+1 units increases the ramping capability of the power plant which leads to a reduction of storage requirement (14.67 MW against 20.5 MW).

The costs difference between N and N+1 reaches 12.81 m€ (10.81 m€ from fuel savings and 2 m€ from battery capacity reduction, following costs hypothesis detailed in 4.14). However, switching from N+1 to N configuration shall require the investment of a storage system dedicated to redundancy. Therefore , these costs reductions should be put into perspective with the investment costs of the N+1 storage system. This will be further investigated in the new chapter.

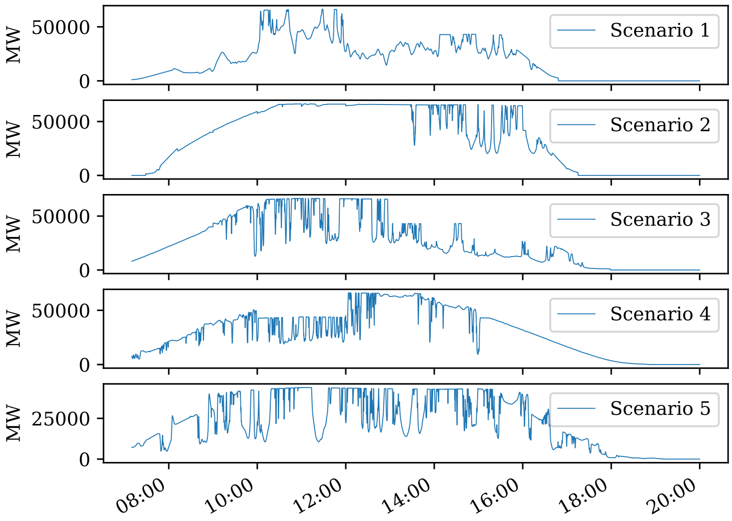

Figure 4.29: Injected PV power for base case in N+1 philosophy.

4.4.2.2 *Fossil units operated in emergency ramp-rate*

Fossil generation ramp-rate plays a major role in PV drop compensation. In most of the cases, manufacturers force to operate in normal ramp-rate conditions. In this section, the fossil generation ramp rate is set to 600 MW/min (against 12.5 MW/min in normal load mode).

Figure 4.30 shows the operation of the power plant with 70 MW installed PV capacity. It appears that no battery support is necessary to maintain the grid frequency within the specification limits thanks to the high flexibility of gas turbines. The TONRR is evaluated at 56.62 hour/year (0.64% of the year).

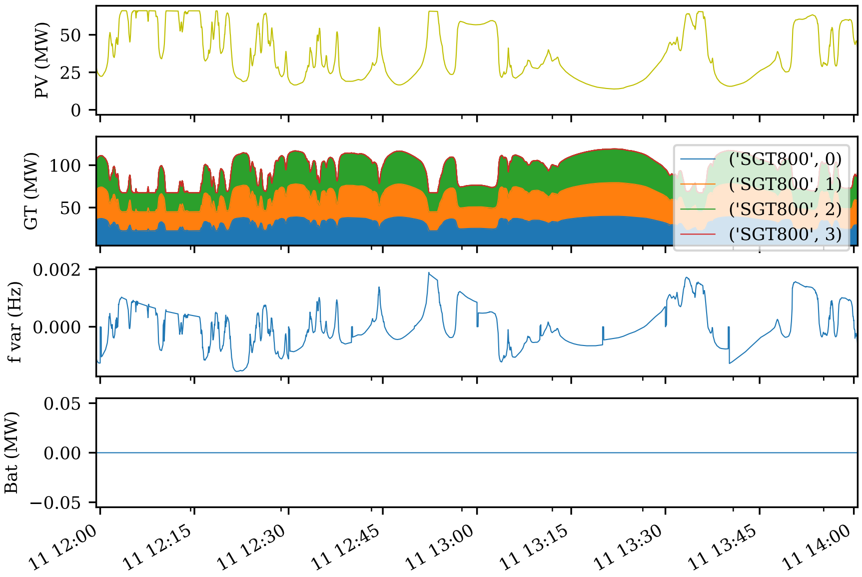

Figure 4.30: GT power operated with emergency ramp-rate (scenario 2).

Unfortunately, it is not possible to draw conclusions on the impact of this scenario of operation on ageing and maintenance effect due to the lack of knowledge on transient operation of gas turbines. However, this could bring some useful piece of information for technical discussion with manufacturers in order to settle on a suitable ramp-rate that will guarantee safe operation of the gas turbine.

4.4.3 *Levers for power plant performance improvements*

In this section, the impact of PV installed capacity and fossil generation technology on costs and fuel savings will be investigated.

4.4.3.1 *Sensitivity over PV and storage capacity*

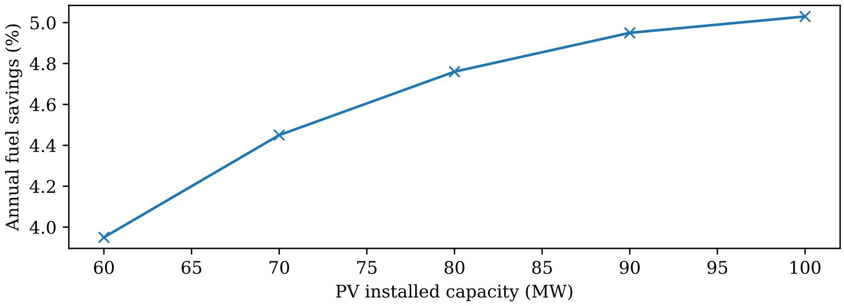

Figure 4.31: Relative fuel savings (compared to no PV penetration).

The impact of battery and PV installed capacities on relative fuel savings is displayed in In Fig. 4.31 whereas its impact on net present costs (NPC) is highlighted in Fig. 4.32. It appears that architectures with low battery capacities and high PV power have better economical performances but the reliability must be considered.

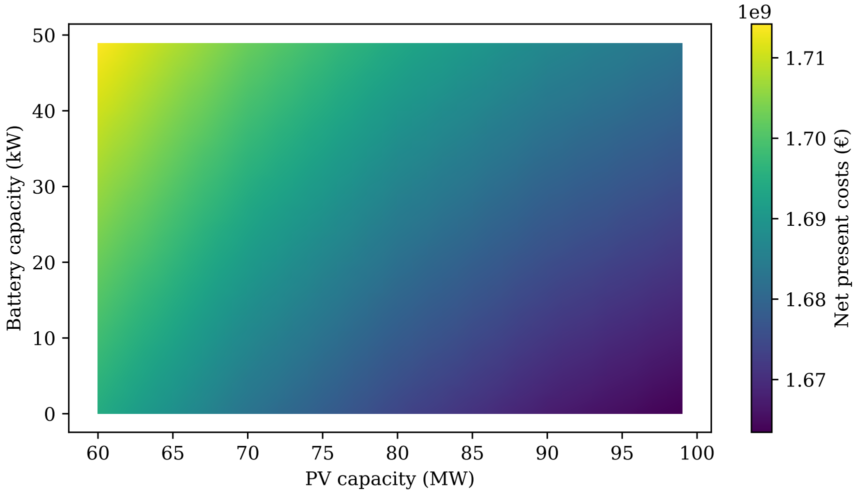

Figure 4.32: Net present costs of architecture with varying PV and Battery capacities (PV costs : 600$/kW, Battery costs : 400$/kWh).

The simulator has been ran for PV capacities varying from 60 MW to 100 MW and battery capacities varying from 14 to 30 MW. In Fig. 4.33, the TFD highlights the degradation of power quality for low installed battery capacities (yellow area). This reports an inverse trend as compared to 4.32 : best economics lead to poor electrical performances.

The green area shows configurations that ensure TFD $= 0$ which means the frequency shift is kept above 49.5Hz. On the contrary, red area shows that in some configuration, the frequency reaches 47.5Hz which is unacceptable with regards to power quality constraints. The red area can be understood as a feasibility limitation for architecture sizing whereas green area reports architectures with oversized battery.

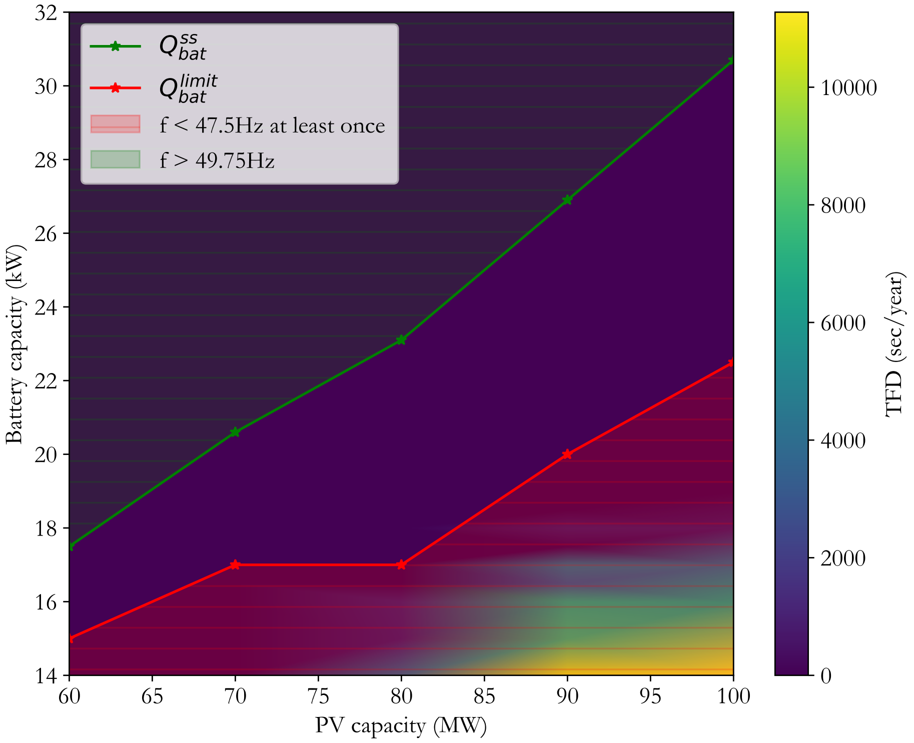

Figure 4.33: Time of frequency disturbances (TFD) and stability zones for varying architectures. W_{bat}^{ss} can be read at the lower border of the green zone and W_{bat}^{limit} can be read at the higher border of the red zone.

Taking the case of a 70 MW PV plant as example, the lower boundary W_{bat}^{ss} for battery power to ensure a fully reliable architecture is 20.5MW (lower bound of green area). By allowing small disturbances (0.25Hz $< |\Delta f| <$ 2.5Hz), the storage capacity can be reduced down to 18MW (upper bound of red area) which provides a value for W_{bat}^{limit}. Table 4.18 summarizes these results for all architecture considered in N and N+1 configurations.

The evaluation of W^{ss}_{bat} allows calculating the economical performances of a fully reliable power plant. When considering larger frequency deviations tolerances, the battery power can be refined and reduced (-2.5 MW with 60 MW of PV, -8.7 MW with 100 MW of PV). Thus, the best economical performances can be evaluated thanks to the simulator by minimizing the battery investment costs for a given PV installed capacity.

	PV installed capacity (MW)	60	70	80	90	100
	Available PV energy (MWh)	1.25E+05	1.46E+05	1.66E+05	1.87E+05	2.08E+05
N	**Used PV energy (MWh)**	1.23E+05	1.40E+05	1.55E+05	1.67E+05	1.76E+05
	PV energy curtailment (%)	1.44	3.83	7.12	10.70	15.23
	Fuel savings (%)	4.02	4.62	5.10	5.46	5.65
	W^{ss}_{bat} **(MW)**	17.5	20.6	23.1	26.9	30.7
	W^{limit}_{bat} **(MW)**	15	18	18	20	22
N+1	**Used PV energy (MWh)**	1.20E+05	1.34E+05	1.50E+05	1.59E+05	1.69E+05
	PV energy curtailment (%)	3.68	8.23	9.71	14.86	18.62
	Fuel savings (%)	3.86	4.27	4.87	5.06	5.27
	W^{ss}_{bat} **(MW)**	14.88	14.67	19.08	20.19	20.91

Table 4.18: Summary of power plant performances for 5GT architecture.

4.4.3.2 *Smaller generators to improve the PV integration*

In Tab. 4.18, the performances of GT-PV-ESS architecture are reported under N and N+1 operational philosophy. Due to the PV power curtailment imposed by minimum power output and spinning reserve constraints, CO_2 savings and injected PV energy are not increasing proportionally to the installed PV capacity. The PV curtailment is higher in N+1 philosophy since an additional generator is connected which reduces even more the potential of PV integration. The required storage capacity for cloud passing management is slightly lower in N+1 philosophy since the cumulated ramping capacity is increased by the redundancy.

The limitation of using such types of generator in hybrid power plant appears. First, the insufficient difference between minimum and maximum power output as well as long minimum down times limits the integration of PV power. This results in PV power curtailment at hours of high irradiance (see 2nd scenario in Fig. 4.24). This significantly limits the optimization potential of the energy management layer and pushes to use a higher number of fossil generator with better operational margin and lower minimum down time constraints.

In Fig. 4.34, the efficiencies of the 45 MW gas turbine and a 9.3 MW gas engine (GE) are compared. Gas engines outperform large turbines for every load factor which will improve the fuel savings. According to Tab. 4.19, the dynamics of gas engines may also give more flexibility to the system thanks to lower minimum up and down time and better ramp-rates. In this section, the performance of a GE-PV-ESS system will be simulated and compared with GT-PV-ESS architectures.

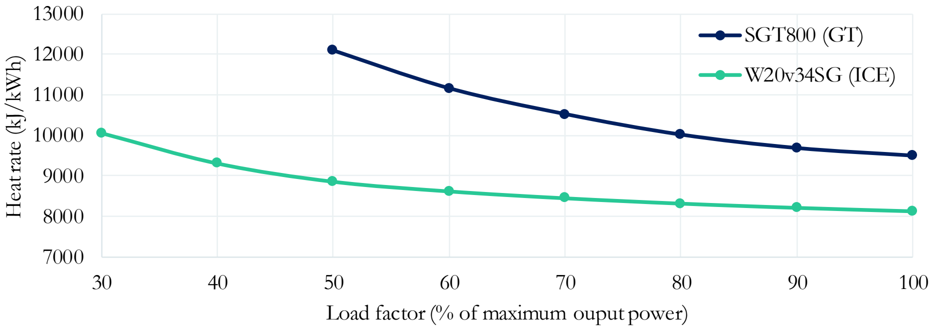

Figure 4.34: Comparison of fossil generators heat-rate as function of load factor.

	Rated power MW	Range of operation %max	Ramp-rate %max/sec	Min. up-time h	Min. Down time h
GT	45	50	0.39	6	6
GE	9.3	70	1.67	1	1

Table 4.19: Comparison of GT and GE characteristics.

Table 4.20 reports the results of the simulation with 16 gas engines and a PV capacity varying from 60 to 100WM both in configurations N and N+1. Thanks to the lower minimum load factor, a higher proportion of solar energy is used as compared to the GT case. For a 100 MW power plant with GE, only 3.11% of PV energy is lost due to curtailment against 15.23% for the GT case. This naturally results in higher fuel savings (11.16% against 5.65%).

	PV installed capacity (MW)	60	70	80	90	100
	Available PV energy (MWh)	1,25E+05	1,46E+05	1,66E+05	1,87E+05	2,08E+05
N	**Used PV energy (MWh)**	1,25E+05	1,45E+05	1,66E+05	1,84E+05	2,01E+05
	PV energy curtailment (%)	0,21	0,21	0,38	1,60	3,11
	Fuel savings (%)	6,14	7,43	8,82	9,85	11,16
	W_{bat}^{ss} **(MW)**	3.99	7.50	8.97	12.2	13.0
	W_{bat}^{limit} **(MW)**	0	5	5.5	8	8.5
N+1	**Used PV energy (MWh)**	1,25E+05	1,45E+05	1,66E+05	1,84E+05	2,02E+05
	PV energy curtailment (%)	0,21	0,21	0,32	1,55	3,01
	Fuel savings (%)	6,09	7,37	8,65	9,77	10,84
	W_{bat}^{ss} **(MW)**	2,77	3,53	5,17	7,81	11,46

Table 4.20: Summary of power plant performances for 16 engine configuration.

The smaller size of gas generator also reduces the spinning reserve for contingency (9.3 MW against 45 MW). The additional engine ensuring the redundancy has less impact on the fuel consumption (GE have better performance at low load factor). This results in a lower gap between the PV production curtailment in N and N+1 configuration : +0.1% for GE against +3.39% for GT.

Finally, the stability map in Fig. 4.35 shows that storage requirements are much smaller for GE configurations (W_{bat}^{ss} =13 MW for 100 MW of PV against 30.7MW with GT). With small transient disturbances tolerance (between 0.5% and 5% of the nominal frequency), no storage is required for a 60 MW PV plant (W_{bat}^{limit}=0). For all installed PV capacity, the TDF is less than 25000 sec/year which represents 0.007% of the year.

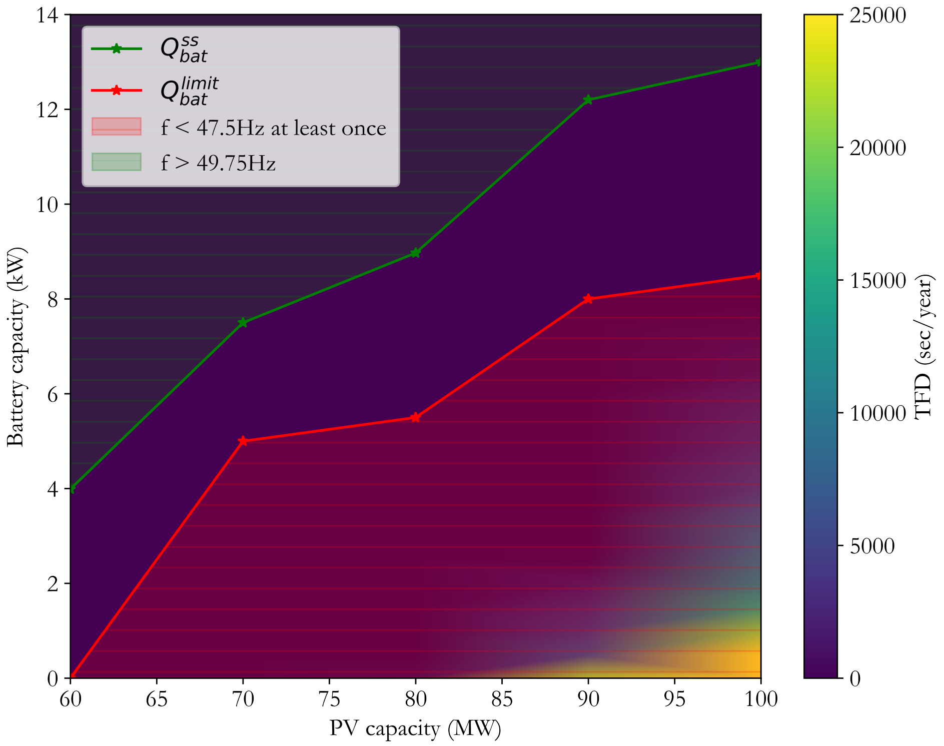

Figure 4.35: TFD and stability zones over varying PV and Battery capacity for a GE-PV-ESS architecture. W_{bat}^{ss} can be read at the lower border of the green zone and W_{bat}^{limit} can be read at the higher border of the red zone.

4.4.4 *Discussion*

A sensitivity analysis on operational philosophy (N+1 rule and rap-rate), PV and battery installed capacity and fossil generation technology allowed to evaluate their costs and technical impacts.

Switching from gas turbines to internal combustion engines reduces CO_2 emissions by 30% regardless of the share of PV power (see Fig. 4.36 and 4.37). This incentives to choose smaller engines with better part-load performances. However, the costs of this solution is difficult to evaluate since a higher number of engines leads to higher shipment and maintenance costs.

In case of gas turbines, the integration of PV system reduces CO_2 emission by 4% with a 60 MW power plant an 5.65% for a 100MW

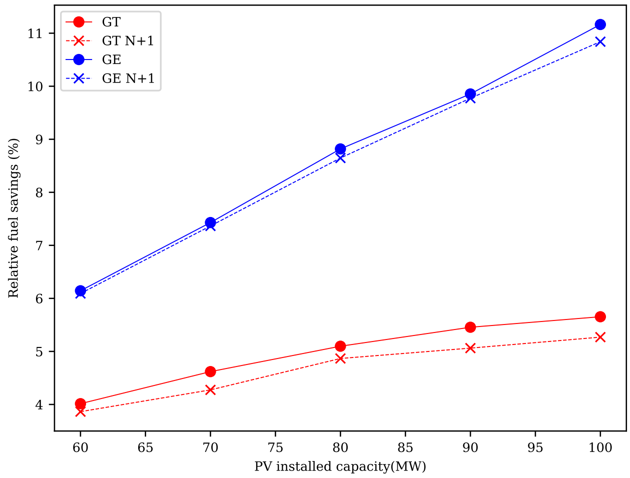

Figure 4.36: Relative fuel savings.

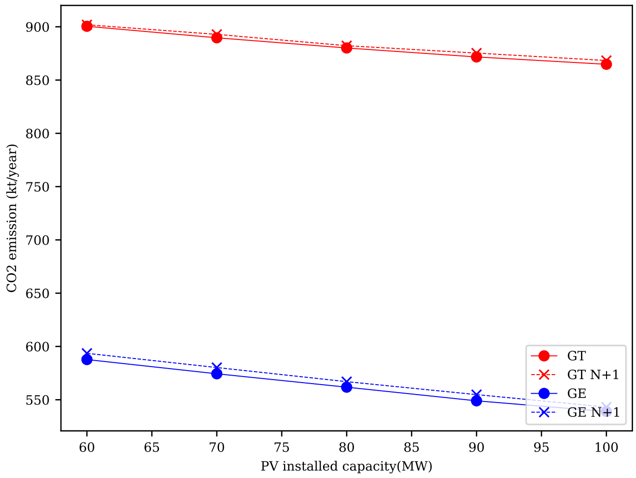

Figure 4.37: CO_2 emissions.

power plant which gives an average of 0.04% of CO_2 reduction per MWp installed. In case of gas engines, CO_2 reduction raises from 6% for a 60 MW PV plant up to 11% for a 100 MW power plant, giving an average 0.125% of CO_2 reduction MWp installed (see Fig. 4.37). The better performance of gas engines at reducing CO_2 emission is due to the higher share of injected PV electricity thanks to higher flexibility of start-up procedure and operational margin (see Fig. 4.38)

The requirements in storage capacity to maintain the frequency within specification limits are evaluated thanks to the grid simulation. GE architecture require less storage (2.5 MW against 15 MW for a 60 MW power plant) thanks to their higher ramping capabilities. However, the storage requirement are less sensitive to the PV capacity

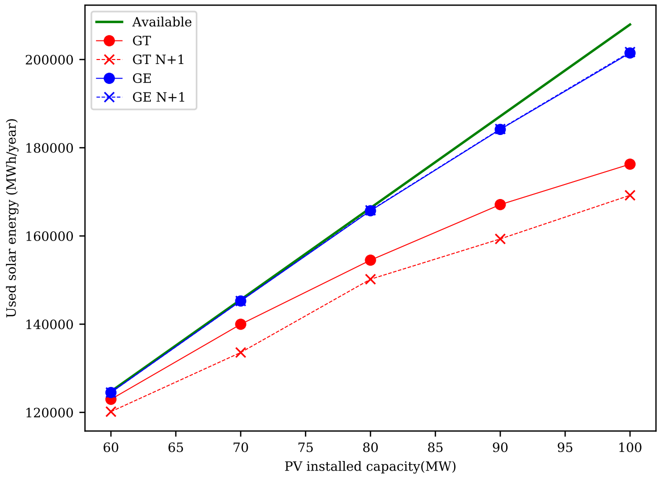

Figure 4.38: Used solar energy.

for GT architecture than for GE architecture. This is due to the lower mechanical inertia of GE which makes the grid more sensitive to PV fluctuations.

Thanks to the evaluation of TFD and minimum frequency, a potential for capex reduction is introduced by allowing transient frequency variation between 1% and 5%. The storage capacity can be reduced from 30.7 MW down to 22 MW for GT and from 13 MW down to 8.5 for GE (with 100 MW of PV capacity). According to the TFD, transient variation represent 0.003% and 0.007% of the total time of operation respectively for GT and GE. Such results give confidence that $W_{\mathtt{bat}}^{\mathtt{limit}}$ can be used without putting the grid stability in danger.

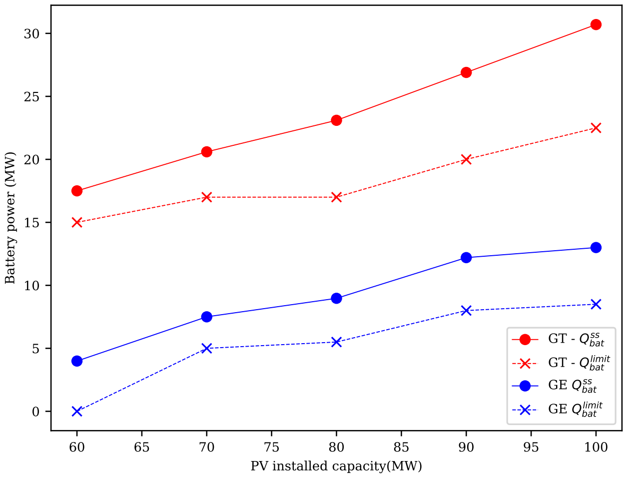

Figure 4.39: required power for cloud passing.

4.5 CONCLUSION

In this chapter, a methodology for the evaluation of economical, environmental and technical performances of an industrial hybrid power plant has been proposed.

At first, electrical modelling of industrial microgrid was investigated to allow irradiance time series simulations. State of the art techniques for GT and grid modelling [64] showed limitations for the preliminary assessment of the system: (1) a high number of input parameters are required, (2) computational time reach 3 hours for a daily irradiance timeseries, (3) the ramping constraints of fossil generation are not considered. In the same philosophy as in [47], a simplified single-line model is been proposed in this chapter and an equivalent ramp-constrained model is designed to account for ramping constraints. This allows simulating timeseries 200 times faster, reducing the number of inputs to the minimum possible (from 92 down to 10) and taking into account larger frequency deviations due to limited ramping capabilities of gas turbines.

In the second part, the electrical model is coupled with a two-layer energy optimization to reproduce the operational strategy of the power system and the coupling effect of EMS and PMS layers. To handle the differences between day-ahead hourly forecasts and real-time power data, a two-layer optimization is implemented as proposed in [170]. The simulation framework is able to simulate the power plant under high-resolution irradiance timeseries, reproduce optimal decision as they would be made by operators, and evaluate the impact on the reliability of the system. This aspect has been covered for real-time applications using hardware in the loop [211] but never in a generic framework allowing preliminary assessment of hybrid architecture.

To allow a fast and representative assessment of the power plant performance over its lifetime, the scenario reduction procedure detailed in chapter 3 was used. Thanks to 5 days resulting from the timeseries clustering, fuel consumption, CO_2 savings and cumulated time of frequency disturbances are evaluated and aggregated to reconstruct yearly performance indicators. Additionally, the worst-case scenario ensures that the system is stable under highly variable irradiance conditions and provides a conservative assessment of the battery requirements. This reduces the number of simulation for a given architecture by 60. Using parallel computing, the simultaneous simulation of the 6 scenarios requires 40 minutes with a standard personal computer [18].

An hybrid power plant powering an LNG facility is used as a case study in the third part of this chapter. first, the simulation framework

---

[18] 8 cores and 64 Go Ram Intel CPU

is used to evaluate the performance of a 70 MW PV power plant with 5 gas turbines. Grid simulations highlight the need of 20.5 MW of storage capacity to maintain the frequency deviation bellow 0.25 Hz. The aggregation of reduced irradiance scenario is compared to a full year simulation for validation. Similar results are obtained in terms of environmental and economic performances. The battery capacity provided by the aggregation method was proven to be reliable more than 99.99% of the time.

The simulation framework is used to screen several configurations of hybrid power plants with varying installed PV capacities and two types of fossil generators (gas turbines and gas engines). A stability map is drawn to evaluate the reliability of a system for a given pair of PV and battery installed capacity. The stability map shows that increasing the PV installed capacity forces to install more and more storage capacity which modifies the techno-economic equilibrium (+5.1 MW of storage for a 100 MW PV system as compared to a 70 PV system). Considering frequency deviations tolerances can reduce the battery requirements up to 26%.

Lifetime CO_2 emission and battery requirements show that that architectures with a large number of small-size generator are better performing at integrating PV electricity (-30% of CO_2 emissions).

In the EMS optimization, a deterministic approach is used for the integration of PV production profile and spinning reserves. This may lead to an over-estimation of the power plant performance. Integrating forecast system data and prediction uncertainties may represent the power plant behaviour with more accuracy. An adaptation of the proposed MILP formulation using robust and stochastic approaches is promising perspectives for this work.

In the last part of this chapter, the simulation framework was used in a preliminary sizing philosophy. The methodology allows sooner integrating reliability considerations and therefore increases the confidence of developers in the sizing process. Despite the fact that simulation time of a given architecture have been significantly reduced, the screening potential remain limited when a large number of scenarios must be studied (a stability map like Fig. 4.33 takes more than 15 hours of simulation using a 40 cores computer). This is mainly due to the short-term power control layer and its API. To allow a faster preliminary sizing, high level optimization approaches are necessary. One option is to endogenize grid reliability constraints instead of using time-domain simulations. In the next chapter, a MILP formulation for sizing optimization will be proposed and combined to the simulation framework detailed in this chapter.

5

OPTIMAL AND ROBUST SIZING OF INDUSTRIAL MICROGRIDS

This chapter presents a procedure for the study of PV integration in industrial power plants. This procedure embeds the contributions of chapters 3 and 4 as well as a preliminary optimization based on Mixed Integer Linear Programming ensuring the resiliency to fast cloud passage. The formulation of frequency-constrained optimization problem results from the collaboration with NTNU's Department of Electric Power Engineering and more specifically Erick Alves to whom I am very grateful. This work has been submitted to Elsevier's Applied Energy Journal in March 2022 and presented at the ROADEF 2022 conference.

Ce chapitre présente une procédure pour l'étude de l'intégration de génétareurs photovoltaïques dans les centrales électriques industrielles. Cette procédure intègre les contributions des chapitres 3 et 4 ainsi qu'une optimisation préliminaire basée sur la programmation linéaire en nombres entiers assurant la résilience aux passages nuageux. La formulation du problème d'optimisation sous contrainte de fréquence résulte d'une collaboration avec le département d'ingénierie électrique de NTNU et plus particulièrement Erick Alves. Ce travail a été présenté à la conférence ROADEF 2022 et soumis au journal IEEE Access.

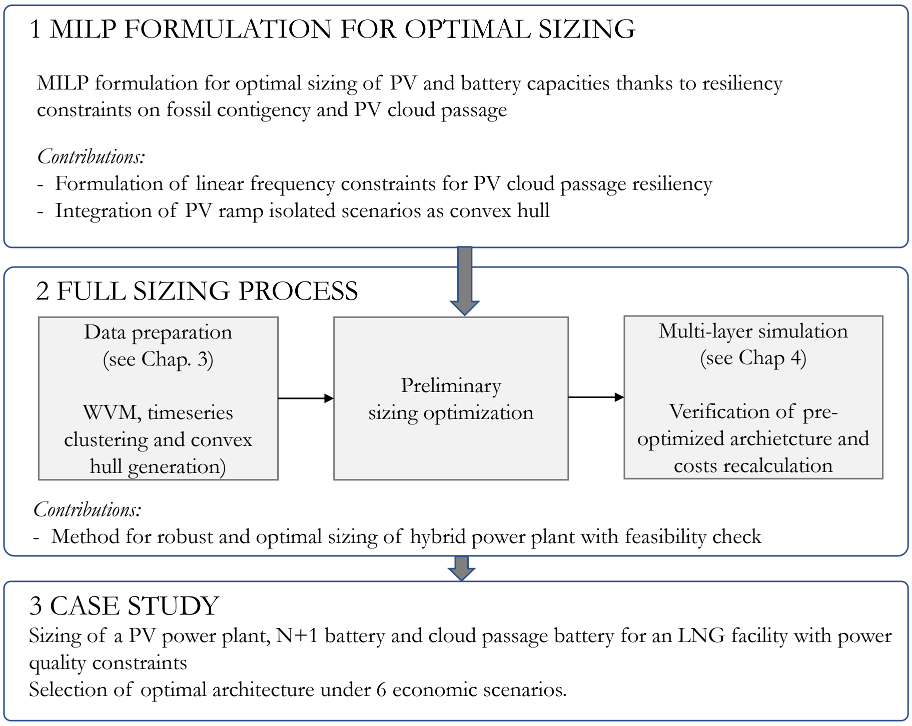

Contents

NOMENCLATURE OF CHAPTER 5

Indices

Symbol	Description
h	Hourly optimization time-slice
y	Year
σ	Day-long irradiance scenario
m	Fossil unit type
i	ith installed fossil unit of type m
r	Ramp event

sets

Symbol	Description
$\mathcal{R}^{max}$	Ensemble of worst detected ramps
$\mathcal{H}^{max}$	Worst-case convex hull of detected ramps

Electrical and power system Variables

Symbol	Description
Δf	Frequency shift
Δf_{min}	Maximum frequency shift
M	Mechanical inertia constant
ΔP_{fossil}	Fossil power variation
ΔP_{bat}	Battery power variation
ΔP_{PV}	PV power variation
ΔP_{L}	Load power variation
D_{L}	Load damping constant
rr_{PV}	PV power ramp rate
rr_{fossil}	Fossil normal power ramp rate
$\Delta P_{fossil}^{setpoint}$	Fossil power variation from setpoint control
$\Delta P_{fossil}^{droop}$	Battery power variation from droop control
k_{fossil}	Fossil droop parameter
r_{bat}	Battery droop parameter
k_{d}	Total system damping
d_{r}	Total system ramp
db_{Hz}	Fossil unit droop deadband
TFD	Time of frequency disturbances

Optimization decision variables

Symbol	Description
O^{CAPEX}	CAPEX part of objective function
O^{OPEX}	OPEX part of objective function
W_{bat}^{inst}	Installed battery power capacity
W_{PV}^{inst}	Installed PV power capacity
$FC_{m,i,h}$	Fuel consumption
$u_{m,i,h}$	Fossil unit startup binary decision
$v_{m,i,h}$	Fossil unit shut down binary decision
$\omega_{m,i,h}$	Fossil unit operating status binary decision
$W_{PV_h}^{used}$	PV used power capacity after curtailment
$P_{bat,h}^{N+1}$	Installed battery power capacity for N+1 resiliency
$P_{m,i,h}$	Fossil unit power
$P_{PV_h}^{inj}$	Injected PV power
$\Delta P_{m,i,h}^{avg}$	Spinning reserve for mid-term solar variations
$\Delta P_{m,i,h}^{cont}$	Spinning reserve for N+1 resiliency
$P_h^{lst,max}$	Maximum lost power in case of contingency
$P_{bat,h,r}^{N+1}$	Battery power required for N+1 resiliency
ΔP_{PV}^{fc}	Fast cloud PV power variation
W_{bat}^{fc}	Installed battery power capacity for cloud passage
P_{bat}^{fc}	Battery power required for cloud passage resiliency
$\Delta P_{h,m,i,r}^{DC}$	Spinning reserve at the end of cloud passage
$\Delta P_{h,m,i,r}^{PC}$	Spinning reserve after recovery to cloud passage

Optimization economic parameters

Symbol	Description
d	Discount rate (%)
Y_{inst}	Project lifetime
c_{PV}	PV installation costs
c_{bat}	Battery installation costs
c_f	Fuel costs
c_{CO_2}	CO_2 penalty
c_{u_m}	Start-up costs
c_{v_m}	Shut down costs

Optimization technical parameters parameters

Symbol	Description	Unit/Set
N^{σ}	Occurence of day-long scenario σ	
η_{PV}	PV derating factor	
I_h	Hourly averaged irradiance	
P_{L_h}	Hourly load demand	
P_m^{max}	Maximum fossil unit power	
P_m^{min}	Minimum fossil unit power	
a_m	Fossil unit fuel curve slope	
b_m	Fossil unit fuel curve intercept	
M_{up_m}	Maximum fossil unit up-time	
M_{dn_m}	Maximum fossil unit down-time	
K	Large scale constant	
ΔI_h^{avg}	Maximum irradiance variation within 1h	
Pl_h	Load power	
ΔT^{fc}	Duration of fast cloud ramp	
ΔI^{fc}	Irradiance drop of fast cloud ramp	

5.1 INTRODUCTION

In the previous chapter, a methodology for the simulation of industrial micro-grids have been proposed. Thanks to the coupling of optimal energy management and power control, technical, economical and environmental performances of hybrid architectures can be evaluated. The results showed that the performances of industrial micro-grids are highly dependant on architectural choices made at the sizing steps. The needs of primary support storage system for cloud passage and contingency resilience can outweigh the benefits of lifetime fuel savings which leads to a non-trivial techno-economic optimization problem. Despite the reduction of simulation time, the use of the simulator for a large screening with several economic scenarios will be undoubtedly too long. This pushes to investigate high-level techno-economic sizing methods for industrial microgrids allowing faster assessment of the power plant's performances.

This chapter will present a methodology for the robust and optimal sizing of industrial microgrid. The methodology is based on two main steps : (1) a preliminary optimization of the sizing with resiliency constraints based on Mixed Integer Linear Programming (MILP) formulation and (2), the operational simulation presented in Chapter 4.

To help power plants architects, the sizing method must identify the best performing hybrid architecture while accurately reproducing the power plant behaviour. The need for reliability must be integrated as constraints in the optimization formulation to ensure electrical stability in case of generator contingency and fast cloud passage. The sizing method should quickly provide solutions to allow a large screening of architecture. Therefore, the computational complexity and calculation time is a key indicator in the performance evaluation of this method.

5.2 A ROBUST SIZING OPTIMIZATION MODEL WITH RESILIENCY CONSTRAINTS

The integration of resiliency constraints brings challenges for the formulation of a MILP problem. Solar variability scenarios must be integrated in a high-level energy formulation despite their low granularity. Then, the relationship between frequency shift and power imbalance must be integrated within a linear constraint which generally leads to suboptimal solutions. Finally, resiliency constraints for contingency events brings additional reserve requirements which needs to be handled by fossil units or storage systems. A cost-effective strategy for reserve allocation must be defined to properly size storage systems.

5.2.1 *Mathematical formulation of the sizing problem*

The optimization model is based on the operational model developed in Chapter 4. Capacity investment variables for PV and storage devices are now integrated in the objective function (Eq. 5.1) to evaluate the CAPEX. This allows making the right trade off between CAPEX and OPEX savings.

The optimization is performed over a fixed time-horizon covering the 5 clustered days identified in chapter 3 following the same aggregation technique as in chapter 4. A continuous time horizon composed of the 5 day-long timeseries is built to generate the irradiance input parameters. $N^{\sigma}(h)$ denotes the occurrence of the timestep h when $h \in [h_o^{\sigma}, h_f^{\sigma}]$ with σ being the day-long irradiance scenario.

Objective function:

$$\min \quad O^{CAPEX} + \sum_{y=0}^{Y_{inst}} \frac{\sum_h N^{\sigma}(h) O_h^{OPEX}}{(1+d)^y} \tag{5.1}$$

$$O^{CAPEX} = W_{PV}^{inst} * c_{PV} + W_{bat}^{inst} * c_{bat} \tag{5.2}$$

$$O_h^{OPEX} = \sum_{m,i} (FC_{m,i,h} * (c_f + c_{CO_2}) + u_{m,i,h} * c_{u_m} + v_{m,i,h} * c_{v_m}) \tag{5.3}$$

Eq. 5.6 to 5.17 express the system operational constraints as formulated and detailed in [167]. Eq. 5.6 ensures that the hourly load demand P_l is satisfied. The injected PV power is calculated in Eq. 5.7 thanks to the hourly averaged irradiance I_h and PV derating factor η_{PV}. Eq. 5.4 ensures that the hourly curtailed PV capacity is lower that the PV installed capacity. Eq. 5.8 to 5.12 express the fossil generators operational constraints where P_m^{max} and P_m^{min} denote the parameters for maximum and minimum power ratings and M_m^{up} and M_m^{dn} denote the parameters for minimum up and down time of the fossil unit. The fuel consumption is evaluated thanks to the fuel curve's linear interpolation parameters a_m and b_m in Eq. 5.10.

$$\forall h, \quad W_{PV_h}^{used} \leqslant W_{PV}^{inst} \tag{5.4}$$

$$\forall h, \quad W_{bat}^{inst} \geqslant P_{bat,h}^{N+1} \tag{5.5}$$

Load balance (equilibrium of power):

$$\forall h, \quad \sum_{m,i} P_{m,i,h} + P^{inj}_{PV_h} - P_{L_h} \geqslant 0 \tag{5.6}$$

$$\forall h, \quad P^{inj}_{PV_h} \leqslant W^{used}_{PV_h} * I_h * \eta_{PV} \tag{5.7}$$

Fossil power limits

$$\forall h, m, i \quad P_{m,i,h} \leqslant P^{max}_{m} \tag{5.8}$$

$$\forall h, m, i \quad P_{m,i,h} \geqslant P^{min}_{m} * \omega_{m,i,h} \tag{5.9}$$

Fuel interpolation

$$\forall h, m, i \quad FC_{h,m,i} = a_m P_{h,m,i} + b_m \tag{5.10}$$

Fossil generator status change

$$\forall h, m, i \quad u_{m,i,h} - v_{m,h} \geqslant \omega_{m,i,h} - \omega_{m,h-1} \tag{5.11}$$

$$\forall h, m, i \quad u_{m,i,h} + v_{m,i,h} \leqslant 1 \tag{5.12}$$

Fossil generator minimum up and down time

$$\forall m\ \forall h \geqslant M_{up_m}, \sum_{k=h-M_{upm}}^{h-1} \omega_{m,k} - M_{up_m} * v_{m,h} \geqslant 0 \tag{5.13}$$

$$\forall m\ \forall h \geqslant M_{dn_m}, M_{dn_m} * (1 - u_{m,h}) - \sum_{k=h-M_{dnm}}^{h-1} \omega_{m,k} \geqslant 0 \tag{5.14}$$

Fossil load sharing
$\forall\ t,\ \forall\ p(m,i), p'(m',i') \in M \mid i \neq i' \text{ and } m = m' :$

$$P_p - P_{p'} \leqslant K(2 - (w_p + w_{p'})) \tag{5.15}$$

$$P_p - P_{p'} \geqslant K(2 - (\omega_p + \omega_{p'})) \tag{5.16}$$

Eq. 5.17 and 5.18 ensure that fossil generators can compensate the maximum variations ΔI^{avg}_{h} between the hourly average PV power and its minimum value over the hourly interval. The decision variable $\Delta P_{h,m}^{avg}$ denotes the generator spinning reserve allocated to cover these variations.

$$\forall h, \quad \Delta I_h^{avg} \eta_{PV} W_{PV_h}^{used} \leqslant \sum_{m,i} \Delta P_{m,i,h}^{avg} \tag{5.17}$$

$$\forall h, m, i, \quad \Delta P_{m,i,h}^{avg} \leqslant P_m^{max} - P_{m,i,h} \tag{5.18}$$

$$\forall h, m, i, \quad \Delta P_{m,i,h}^{avg} \leqslant K \cdot \omega_{m,i,h} \tag{5.19}$$

5.2.2 *Contingency resilience constraints*

In this work, the grids dynamics during generator trip is neglected. It is assumed that ensuring enough spinning reserve to cover the loss of a fossil unit is enough to protect the grid from large instabilities. More advanced constraints can be integrated but require further investigations for handling the non-linearity [212]. Eq. 5.21 to 5.24 express the system constraints for contingency resilience and allow calculating the storage capacity necessary $P_{bat,h}^{N+1}$ to cover the loss of a gas turbine that might happen within the hour h. Figure 5.1 illustrates how generators spinning reserve and N+1 storage unit contribute to the post-contingency power balance.

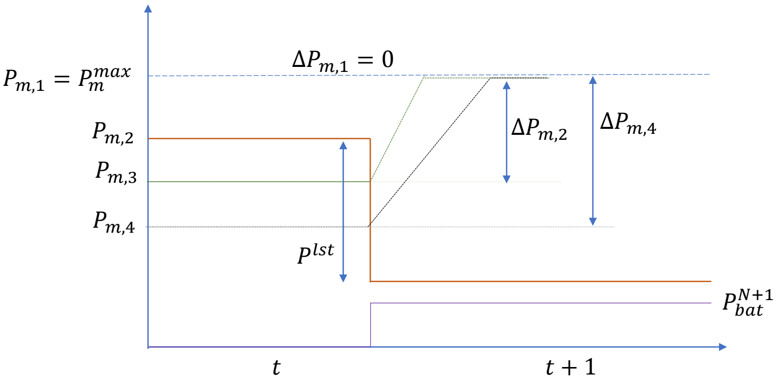

Figure 5.1: Power balance during contingency and post-contingency state

$$\forall h, m, i \quad P_h^{lst} \geqslant P_{m,i,h} \tag{5.20}$$

$$\forall h, m, i \quad \Delta P_{m,i,h}^{cont} \leqslant P_m^{max} - P_{m,i,h} \tag{5.21}$$

$$\forall h, m, i \quad \Delta P^{cont}_{m,i,h} \leqslant K \cdot \omega_{m,i,h} \tag{5.22}$$

$$\forall h, \quad P^{lst,max}_{h} \leqslant \sum_{m,i} \Delta P^{cont}_{m,i,h} + P^{N+1}_{bat,h} \tag{5.23}$$

$$\forall h, m, i \quad P^{lst,max}_{h} \geqslant P^{max}_{m} \cdot \omega_{m,i,h} \tag{5.24}$$

5.2.3 *Cloud passage resiliency constraints*

As seen in chapter 4, hybrid architectures may not meet the power quality constraints during cloud passage above a certain limit of PV penetration without the use of a primary support storage system. The aim of cloud passage stability constraint is to ensure that the power quality constraint ($\Delta f \leqslant \Delta f_{min}$) is respected during a solar power drop. Given the system's equation of motion (Eq. 5.25), frequency drops are expected to happen if PV generation variations are not balanced by dispatchable units (fossil generators and storage system).

$$\frac{d\Delta f}{dt} = \frac{\Delta P_{fossil} + \Delta P_{bat} + \Delta P_{PV} - \Delta P_{L} + D_{L}\Delta f}{M} \tag{5.25}$$

Solar power variations are assumed to be linear drops with two features: duration ΔT^{fc} and power drop ΔP^{fc}_{PV} (see Fig. 5.2). During cloud passage, the PV power supply is expressed by Eq. 5.26.

$$P_{PV}(t) = rr_{PV} t = \frac{\Delta P^{fc}_{PV}}{\Delta T^{fc}} t \tag{5.26}$$

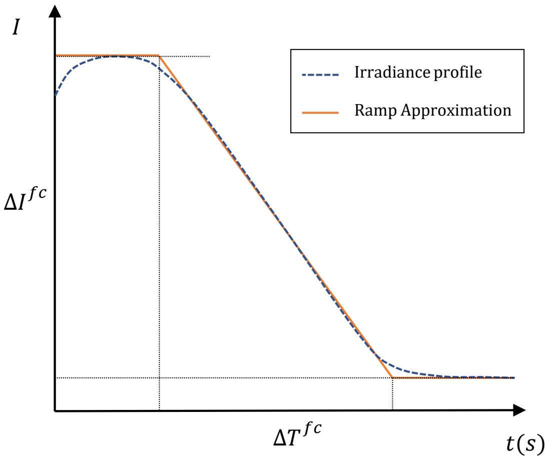

Figure 5.2: Linear approximation of short-term solar drop.

The fossil unit power supply is composed of a frequency droop component and a setpoint component (Eq 5.27). The setpoint component consists in the normal load following response and is limited by the load following ramp-rate (Eq. 5.29).

$$\Delta P_{fossil}(t) = \Delta P_{fossil}^{setpoint}(t) + \Delta P_{fossil}^{droop}(t) \tag{5.27}$$

$$\Delta P_{fossil}^{droop}(t) = -k_{fossil} \Delta f(t) \tag{5.28}$$

$$\Delta P_{fossil}^{setpoint}(t) \leqslant rr_{fossil}(t) \tag{5.29}$$

According to the droop controlled battery model proposed in Chapter 4, the battery power supply is defined by Eq. 5.30. Where r_{bat} denotes the droop coefficient of the battery in % of rated capacity per unit of change of frequency).

$$\Delta P_{bat}(t) = \frac{-W_{bat}^{fc}}{r_{bat}} \Delta f(t) \tag{5.30}$$

As previously sated, industrial loads are expected to have negligible short term variations. During the cloud passage, the load power is considered as constant ($\Delta P_L = 0$). During large frequency variations, the gas turbine is operated using its emergency ramp rate. Therefore, the setpoint component is considered to be saturated ($\Delta P_{fossil}^{setpoint}(t) = rr_{fossil}(t)$). This allows reformulating Eq. 5.25 into Eq. 5.31.

$$\frac{d\Delta f}{dt} = \frac{d_r t - k_d \Delta f}{M} \tag{5.31}$$

With k_d the total system damping:

$$k_d = \frac{W_{bat}^{fc}}{r_{bat}} + k_{fossil} + D_L \tag{5.32}$$

The term d_r denotes the difference between PV and fossil ramp rates :

$$d_r = rr_{fossil} - rr_{pv} \tag{5.33}$$

The solution of this equation with $\Delta f(0) = 0$ is given by Eq. 5.34. This provides a complex and non-linear relationship between Δf and W_{bat}^{fc} which prevents its use within a MILP formulation [1].

$$\Delta f(t) = \frac{d_r t}{k_d} - \frac{M d_r - M d_r e^{-\frac{k_d * t}{M}}}{k_d^2} \tag{5.34}$$

---

[1] Note that in practice d_r and k_d are calculated thanks to manufacturer's data and worst-case solar drop. The influence of these parameters has not been studied since the aim of this paragraph is mainly to justify the linear optimization approach.

The formulation of a non-linear optimization model for the unit commitment with stability condition at the point of minimum frequency has been extensively covered in [135] [2]. The authors highlighted the sub-optimality of linear frequency constraint problems but also pointed out the computational complexity of solving non-linear models (notably using Benders decomposition). In the present work, solutions of the MILP model will be refined by the operational simulator which handles the non linearity of the frequency deviation. Therefore, the use of a linear frequency constraint model is a good solution to quickly evaluate investment decisions related to the PV and primary support storage systems.

5.2.3.1 *Static frequency constraint* ($\Delta f = 0$)

The first approach for frequency constraint consists in considering no frequency drop during the cloud passage. The following assumptions are made :

- Constant load power : $\Delta P_L = 0$
- No power supply from the battery at t=0 : $(P_{bat}^{cloud}(t_0) = 0)$
- No load damping effect : $D\Delta f = 0$
- No initial frequency drop : $\Delta f_0 = 0)$

Additionally, this constraint considers that fossil generators can only supply power according to their ramp rates ($k_{fossil} = 0$).

To ensure that the frequency will remain constant, the battery supply must follow the difference between PV and fossil generation at each time of the cloud passage leading to Eq. 5.35.

$$rr_{fossil}t - rr_{PV}t + P_{bat} = 0 \tag{5.35}$$

The maximum power supply is reached at $t = \Delta T^{fc}$ which gives a lower bound for the battery power capacity W_{bat}^{fc} (Eq. 5.36). This constraint will be referred to as "static" in the following sections.

$$W_{bat}^{fc} \geqslant \Delta P_{PV}^{fc} - \Delta T^{fc} * rr_{fossil} \tag{5.36}$$

This formulation gives a simple and straightforward relationship between the ramp capabilities of the turbines, the solar perturbations and the battery requirement. However, the battery requirement are likely to be over-estimated for two main reasons : (1) the grid operator allows a frequency tolerance Δf_{min} which lets a flexibility for the power unbalances, (2) gas turbines can excess their nominal ramp rate according to their droop characteristics if frequency shift reaches the operator's tolerance.

---

[2] Note that the work was focused on contingency events which are considered as load step whereas is the present study, solar drop are considered as load ramps.

5.2.3.2 *Dynamic frequency constraint ($|\Delta f| \leqslant \Delta f_{min}$) with gas turbine droop response*

To evaluate the storage requirement with more accuracy, a second frequency constraint is introduced.

By setting deadband $db_{Hz} = \Delta f_{min}$ on the fossil droop component (Eq. 5.38) , the unit response exceeds the normal ramp rate only during unauthorized frequency shifts (Eq. 5.37).

$$\Delta P_{fossil,max} = \Delta P_{fossil}^{setpoint} + \Delta P_{fossil}^{droop} \tag{5.37}$$

$$\Delta P_{fossil}^{droop} = \begin{cases} k_{fossil}\Delta f & \text{if} \quad \Delta f \leqslant db_{Hz} \\ 0 \quad \text{if} & \text{if} \quad \Delta f \geqslant db_{Hz} \end{cases} \tag{5.38}$$

$$\Delta P_{fossil}^{setpoint} \leqslant rr_{fossil} \tag{5.39}$$

As soon as the frequency drops below the deadband value, the fossil unit will supply power according to the droop term $k_{fossil} db_{Hz}$ and will re-establish a positive power balance to drive the frequency up to a suitable equilibrium. Thus, $k_{fossil} db_{Hz}$ can be considered as a supplementary power reserve ensuring the frequency stability as soon as Δf_{min} is reached. The total reserve is obtained by subtracting this droop component leading to Eq. 5.40.This constraint will be referred to as "dynamic" in the following sections.

$$W_{bat} \geqslant \Delta P_{PV}^{fc} - \Delta T^{fc} rr_{fossil} - db_{Hz} * D_{fossil} \tag{5.40}$$

$$D_{fossil} = \sum_{m} k_m \tag{5.41}$$

In this case, the ramping capabilities of the turbines are not fully respected, but the battery supply limits the fossil droop response to a small proportion of the ramp event. Therefore, the impact on unit ageing will be limited.

5.2.4 *Cloud passage scenarios*

ROBUST SOLAR VARIABILITY SCENARIOS

In the frequency constraints formulated above, linear ramp events are used to evaluate the storage power that must be available to guarantee the system stability. Robust scenarios for such ramp must now be evaluated. The challenge of this task is to aggregate and extract isolated ramp events from daily timeseries to allow their integration in a high level energy model.

In section 3.3.2, worst-case irradiance drops have been selected among all ramps detected throughout the year. The convex hull shown in Fig. 5.3 gathers the set of worst case events. To provide a robust evaluation of the battery needs, frequency constraints must be evaluated for all elements $r = (\Delta I_r^{fc}, \quad \Delta T_r^{fc})$ of the set as expressed in Eq. 5.42.

$$W_{bat} \geqslant \max_{r \in \mathcal{H}^{max}} P_{bat_r}^{fc} \tag{5.42}$$

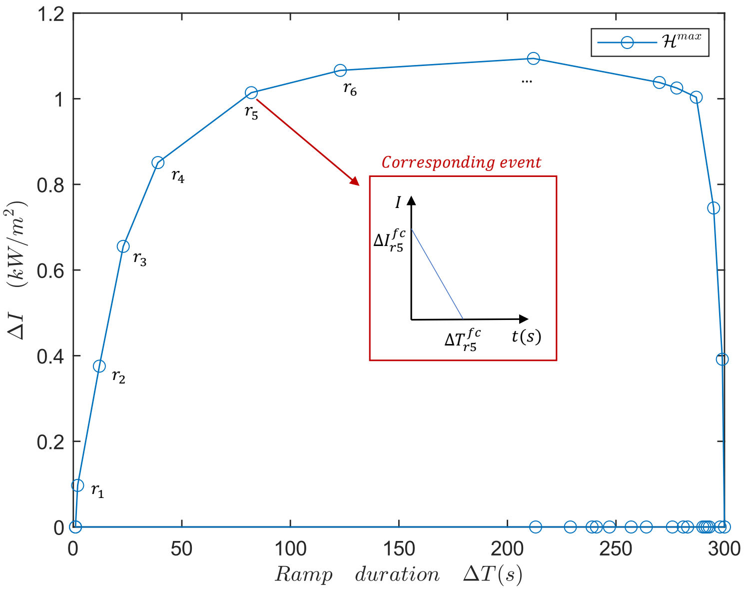

Figure 5.3: Global convex hull $\mathcal{H}^{max}$ of detected ramps among the whole Hawaii dataset with a graphical interpretation of a ramp event r.

As shown in Fig. 5.3, the maximum drop observed reaches $1.09\ \mathrm{kW/m^2}$ which will cause the loss of almost all of the PV power when running at its full power supply capability. Therefore, this situation should only occur during hour of high irradiance. If the frequency constraints are similarly evaluated for each hour of the day using $\mathcal{H}^{max}$, risk of solar drop will be highly overestimated for hours of low irradiance.

An alternative to global convex hull consists in using hourly convex hulls $\mathcal{H}_h^{max}$ (see Fig. 5.4 and 5.5). Eq. 5.43 and 5.44 defines the maximum ramp set $\mathcal{R}_h^{max}$.

$$\mathcal{R}_{h,\delta t} = \{(\Delta I, \delta t) \mid \quad h < t \leqslant h+1\} \tag{5.43}$$

$$\mathcal{R}_h^{max} = \bigcup_{\delta t} \left\{ (\Delta I, \delta t) \mid \Delta I = \max_{r \in \mathcal{R}_{h,\delta t}} (\Delta I)_r \right\} \tag{5.44}$$

The hourly hull $\mathcal{H}_h^{max}$ is defined such as :

$\forall \quad r(\Delta I, \Delta T) \in \mathcal{R}_h^{max} \quad , \forall \quad \epsilon \in [0,1],$

$$\epsilon \Delta T + (1-\epsilon)\Delta I \quad \in \mathcal{H}_h^{max}$$

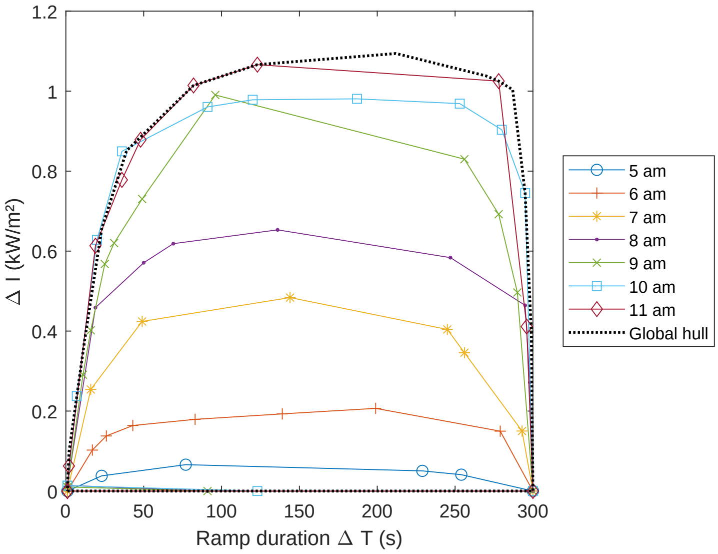

Figure 5.4: Hourly convex hulls $\mathcal{H}_h$ of detected ramps among the whole Hawaii dataset between 7am and 12am and global convex hull $\mathcal{H}_h^{max}$ (in black) gathering all ramp events.

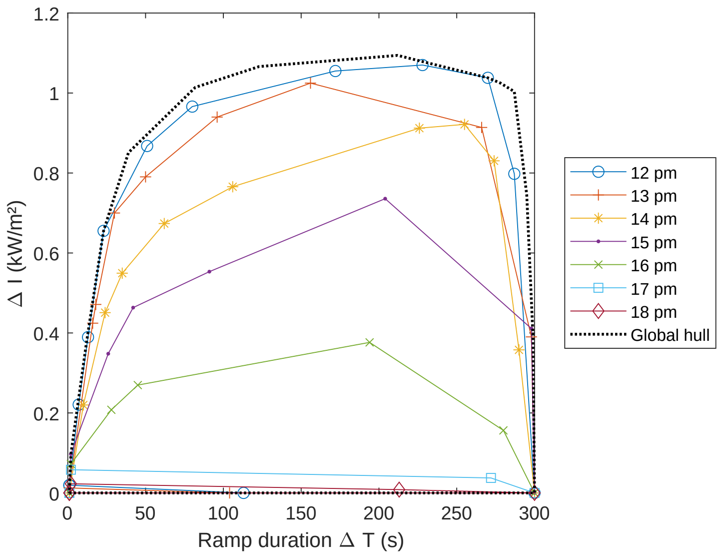

Figure 5.5: Hourly convex hulls $\mathcal{H}_h$ of detected ramps among the whole Hawaii dataset between 12am and 8pm and global convex hull $\mathcal{H}_h^{max}$ (in black) gathering all ramp events.

SOLAR POWER DROP CALCULATION

Now that irradiance drop scenarios have been defined, the corresponding solar power $\Delta P_{PV_r}^{fc}$ drop must be calculated. A first option consists in calculating the power drop thanks to the PV installed capacity . This is expressed in Eq. 5.45 where η_{PV} denotes the PV plant derating factor (in %). This approach is highly conservative since it does not consider the capacity reduction due to curtailment which is expected to reduce the risk of PV drop.

$$\Delta P_{PV}^{fc} = W_{PV}^{inst} \Delta I_{h,r}^{fc} * \eta_{PV} \tag{5.45}$$

An alternative to Eq. 5.45 consists in calculating the power drop thanks to the PV remaining capacity after curtailment $W_{PV_h}^{used}$ (Eq. 5.45). Therefore, when PV power is curtailed, the risk of PV drop is reduced which lets more flexibility to the optimization. The principle of this calculation is shown in Fig. 5.6. Following Eq. 5.45, PV curtailment can be driven by fast cloud passage to protect the grid or avoid large storage investment. This operational rule should be reproduced by the power plant's EMS to avoid discrepancies between pre-sizing and operational simulation.

$$\Delta P_{PV}^{fc} = W_{PV_h}^{used} \Delta I_{h,r}^{fc} * \eta_{PV} \tag{5.46}$$

The power plant sizing will be performed using these two operational strategies which will be referred to as "installed" for sizing following Eq. 5.45 and "curtailed" for sizing following 5.46.

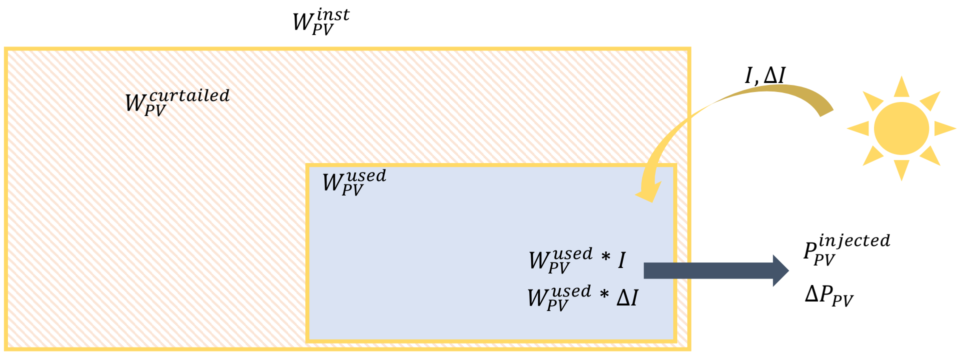

Figure 5.6: Principle of PV curtailment and implications in terms of produced power and solar drops. Note that in practice, the curtailed PV surface would be more homogeneous.

5.2.5 *Integration within MILP formulation*

A static frequency constraint (Eq. 5.36) and a dynamic frequency constraint (Eq. 5.40) have been proposed in the previous section. They must now be integrated in the optimization problem to ensure the system's resiliency to cloud passage. Decision variables are introduced to size the cloud-passage storage system : W^{fc}_{bat} refers to the total storage capacity dedicated to fast-cloud (fc) compensation and $P^{fc}_{bat_h}$ denotes the power that must be available at each hour h to ensure the system's stability. The index r refers to a ramp event within the convex hull's set $\mathcal{H}^{max}$. The duration and solar power drop associated to this ramp events are now denoted $\Delta T^{fc}_{h,r}$ and $\Delta P^{fc}_{PV_{h,r}}$.

To integrate the frequency constraints in the MILP formulation, the cloud passage event is divided in two main steps : the cloud passage (DC) and post-cloud state (PC) as shown in Fig. 5.7.

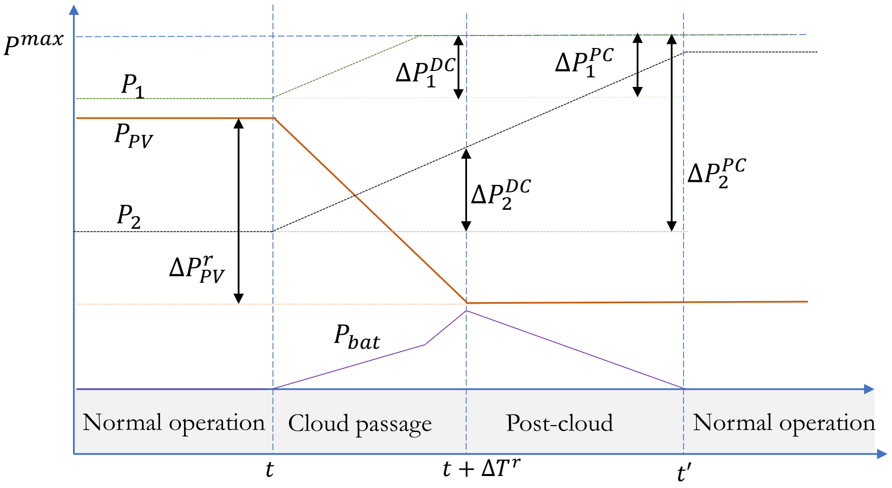

Figure 5.7: Cloud passage decomposition.

CLOUD PASSAGE PHASE

In the cloud passage phase (denoted as DC), the frequency constraint must be satisfied thanks to either static (eq 5.47) or dynamic formulation (eq 5.48). $\Delta P^{DC}_{h,m,i,r}$ denotes the contribution of fossil generator (m, i) at the end of the cloud passage [3].

$$\forall h, r, \quad \Delta P^{fc}_{PV_{h,r}} \leqslant P^{fc}_{bat,h} + \sum_{m,i} \Delta P^{DC}_{h,m,i,r} \tag{5.47}$$

$$\forall h, r, \quad \Delta P^{fc}_{PV_{h,r}} \leqslant P^{fc}_{bat,h} + \sum_{m,i} \Delta P^{DC}_{h,m,i,r} + db_{Hz} D_{fossil} \tag{5.48}$$

In case of dynamic frequency constraint, Eq. 5.49 evaluates the fossil generation damping capacity with $k_{fossil,m,i}$ being the fossil generator's droop parameter.

$$\forall h, \quad D_{fossil} = \sum_{m,i} \omega_{h,m,i} k_{fossil,m,i} \tag{5.49}$$

Eq. 5.50 ensures that fossil generators do not meet their maximum power ratings at the end of the cloud passage whereas Eq. 5.51 ensures that the fossil generation does not violate its maximum ramp-rate.

$$\forall h, m, i, r, \quad \Delta P^{DC}_{h,m,i,r} \leqslant P^{max}_{m} - P_{m,i,h} \tag{5.50}$$

$$\forall h, m, i, r, \quad \Delta P^{DC}_{h,m,i,r} \leqslant \Delta T^{fc}_{r} * rr_{m} \tag{5.51}$$

Eq. 5.52 ensures that a shut-down unit cannot contribute to the cloud passing compensation.

$$\forall h, m, i, r, \quad \Delta P^{DC}_{h,m,i,r} \leqslant K * \omega_{h,m,i} \tag{5.52}$$

POST-CLOUD PASSAGE PHASE

At the end of the post-cloud step, the battery should not provide any support and fossil generator must keep increasing to reach a new equilibrium (secondary frequency support). The PV gap ΔP_{PV} must be solely filled by the fossil generation leading to Eq. 5.53. $\Delta P^{PC}_{m,i,h,r}$ denotes the contribution of the machine to the cloud compensation at the end of the post-cloud state. Eq. 5.54 and 5.55 ensure that enough spinning reserve is available.

---

[3] Note that constraint 5.47 is intended to ensure power balance during a cloudy passage by taking into account the dynamics during the downward ramp. The calculation of the turbine references only takes into account the available margin. Thanks to this process, the margin is involved in the calculation of the gas turbine power setpoint.

$$\forall h, m, i, r \quad \Delta P^{fc}_{PV_{h,r}} \leqslant \sum_{m,i} \Delta P^{PC}_{m,i} \tag{5.53}$$

$$\forall h, m, i, r \quad \Delta P^{PC}_{m,i,h,r} \leqslant P^{max}_{m,i} - P_{m,i,h} \tag{5.54}$$

$$\forall h, m, i, r \quad \Delta P^{PC}_{m,i,h,r} \leqslant K * \omega_{m,i,h} \tag{5.55}$$

STORAGE CAPACITY INVESTMENT VARIABLES

The cost of cloud passage storage is integrated in the objective function thanks to the total storage investment variable W^{inst}_{bat}. According to 5.56, the total storage capacity is higher than the sum of N+1 battery requirement and fast-cloud battery requirement at each optimization timestep h.

$$\forall h \quad W^{inst}_{bat} \geqslant P^{fc}_{bat,h} + P^{N+1}_{bat,h} \tag{5.56}$$

5.2.5.1 *Synthesis*

In section 5.2.3, two frequency constraints have been formulated whereas several possibilities for cloud passage scenarios evaluation have been explored in section 5.2.4. The resulting optimization setups are summarized in Tab. 5.1 before evaluating the proposed formulation with a case study in the following section.

Category	Name	Description	Equation
Frequency constraint	Static	No frequency drop	5.47
	Dynamic	Frequency drop within specification	5.48
Irradiance drop scenario	Global	A single convex ramp hull gives irradiance drop worst-cases for every timestep	$\forall h, \quad r \in \mathcal{H}^{max}$
	Hourly	Hourly convex hulls gathering worst-cases related to the specific timestep	$\forall h, \quad r \in \mathcal{H}^{max}_{h}$
PV drop calculation	Installed	Power drops calculated from the total PV installed capacity	5.45
	Curtailed	Power drops calculated from the hourly remaining PV capacity after curtailment	5.46

Table 5.1: Summary of optimization setups for the sizing.

5.2.6 *Validation and application*

In this section, the robust and optimal pre-sizing procedure will be tested on a case study with two objectives: (1) validate the resiliency of the architecture thanks to dynamic electrical simulations, (2) investigate the impact of the proposed constraints on the resulting architectures. Input parameters used in this section are listed in Tab. 5.2.

Type	**Name**	**Symbol**	**Unit**	**Value**
Project	Lifetime	Y^{inst}	Year	20
Fossil Gen.	Ramp rate	rr_m	$kW.s^{-1}$	208
	Fuel slope	a_m	$m^3.h^{-1}.kW^{-1}$	13782
	Fuel intercept	b_m	m^3	5523
	Fuel price	c_{fuel}	$\$.mbtu^{-1}$	20
PV system	Capex	c_{PV}	$\$.kW^{-1}$	600
	Derating factor	η_{PV}	%	80
Battery system	Capex	c_{bat}	$\$.kW^{-1}$	400

Table 5.2: Input parameters for case study application.

5.2.6.1 *Validation of frequency constraints*

The first step of the validation consists in simulating isolated cloud passage thanks to dynamic models and compare the results with the battery requirements obtained thanks to static and dynamic constraints.

The ramp constrained dynamic model developed in part 4.2.2 is used for this validation with 4 SGT800 gas turbines and a PV installed capacity of 75 MW. Static and dynamic calculation are performed using the convex hull in Fig. 5.3 and reported in Tab. 5.3.

Ramp r -	Duration ΔT_r^{fc} s	Irr. drop ΔI_r^{fc} $kW.m^{-2}$	PV drop $\Delta P_{PV_r}^{fc}$ MW	Static bat. $P_{bat_r}^{stat}$ MW	Dynamic bat. $P_{bat_r}^{dyn}$ MW
r_1	2	0.097	5.82	4.16	0.56
r_2	12	0.37	22.52	12.54	8.94
$\mathbf{r_3}$	**23**	**0.65**	**39.31**	**20.17**	**16.57**
r_4	39	0.85	51.06	18.61	15.01
r_5	82	1.02	60.85	0	0
r_6	123	1.06	63.97	0	0

Table 5.3: Results of static and dynamic battery calculations for the first 6 elements of the global convex hull $\mathcal{H}^{max}$ (see Fig. 5.3).

The maximum power requirements among all events of $\mathcal{H}^{max}$ are found for r_3 with a PV power drop of 39.31 MW over 23 seconds. The resulting battery requirements are 20.17 MW and 16.57 MW according to static and dynamic constraints respectively.

The solar ramp r_3 constitutes the worst-case event in the present configuration and is simulated using the dynamic model. Figure 5.8 shows the resulting battery and fossil generation power as well as grid frequency. Thanks to the battery power support, the frequency drop reaches 49.8 Hz which meets the constraints of 1% of maximum frequency deviation. The maximum battery power supply (14.6 MW) remains below the dynamic and static battery requirements. Since the minimum frequency of 49.5 Hz is not reached, the gas turbine response remains below the nominal ramp rate and the droop response is not used. The gap between linear frequency constraint results and simulation results can mainly be explained by the fact that the role of inertia has been neglected.

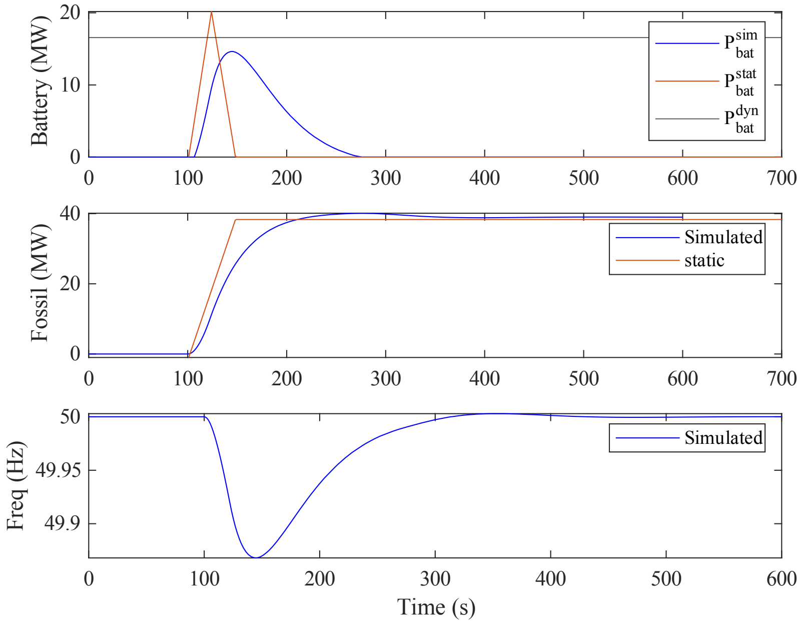

Figure 5.8: Simulation of worst-case solar ramp r_3 with a PV plant of 75 MW.

The second step of validation aims at comparing the battery power supply obtained from the simulation of a real irradiance timeseries against the battery requirements obtained from the convex hulls. The worst-case day long scenario of the Hawaii dataset (2011-03-06, see chapter 3) is taken as an example. Figure 5.9 shows the simulation results between 11am and 12am. As expected, the maximum simulated battery power supply reaches 12.01 MW which is lower than $P^{dyn}_{bat_r}$ (16.57 MW) and $P^{stat}_{bat_r}$ (20.17 MW). These results corroborate the outcome of Fig 5.8 which gives confidence that linear frequency constraints provide conservative battery requirements during a cloud passage event.

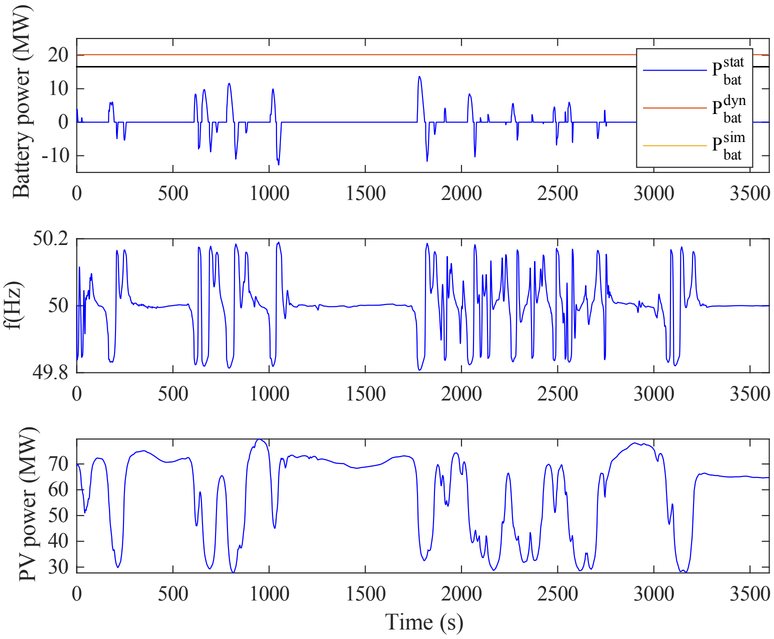

Figure 5.9: Simulation of worst case variability irradiance profile (2011-03-06) between 11am and 12am.

In Fig. 5.10, the hourly power requirements from hourly hulls are reported as well as the maximum power supply observed at each hour of the worst-case day-long timeseries. The simulated battery power is always lower than P_{bat}^{dyn} and P_{bar}^{stat} which shows the ability of the convex hulls to provide conservative scenarios for the battery sizing.

5.2.6.2 *Application and constraint comparison*

The formulation of a frequency-constrained optimization problem has let several possibilities for computing risks of solar drops and ensuring the load balance during cloud passage (see 5.1). PV drops computed from installed capacity, global convex hull and static stability constraints are expected to give more expensive solutions than the ones computed thanks to curtailed PV capacity, hourly convex hulls and dynamic frequency constraints.

Optimal solutions are calculated for each configurations based on economical parameters listed in Tab. 5.2. Table 5.4 reports the results of the optimization [4]. The *base case* denotes the solution of the problem without PV and battery installation whereas in the *No-FC* case, frequency constraints are deactivated.

REFERENCE CASES : BASE AND NO-FC

The highest costs are obtained in the *base case* configuration whereas

---

[4] The optimization were performed using the Gurobi by a 20 intel Xeon Cores computer with 128Go of RAM. A time limit of 1h and an optimality gap of 1% have been set

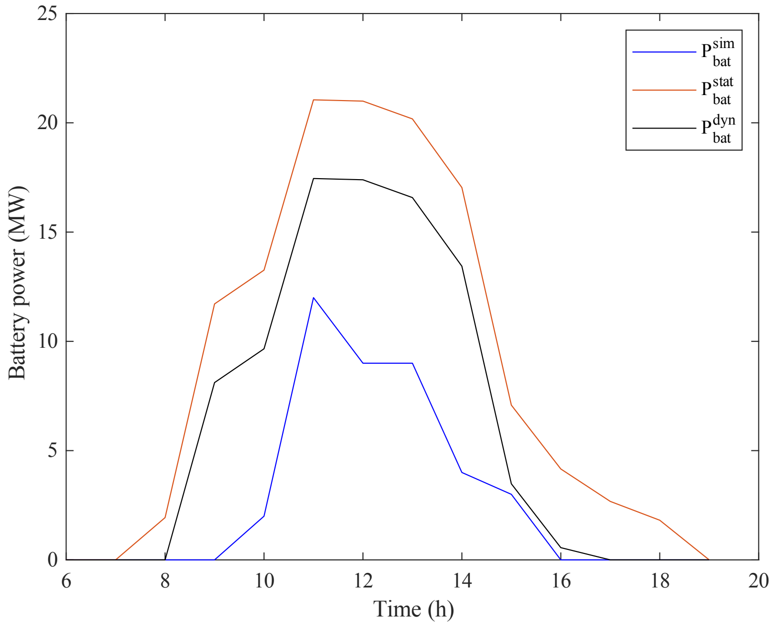

Figure 5.10: Hourly maximum battery power from dynamic simulation of 2011-03-06 and battery requirements (P_{bat}^{dyn}, P_{bat}^{stat}) from hourly hulls $\mathcal{H}_h^{max}$.

the maximum cost and CO_2 savings are achieved by the *NO-FC* case with 196.9 MW of installed PV capacity. Since no frequency constraint are applied, the cloud storage installed capacity is zero. Due to the spinning reserve constraints (Eq. 5.17 and 5.18), a large share of solar energy is curtailed as shown in Fig. 5.11. Between 8am to 4pm, the injected PV power is 62 MW. In this configuration, a solar ramp like r3 (see Tab. 5.3) would cause a power drop of at least 46 MW after 23 seconds and undoubtedly lead to a loss of the grid's stability.

IMPACT OF GLOBAL/HOURLY HULLS AND PV CAPACITY REFERENCE

As reported in Fig 5.12 and Tab. 5.4, computing stability constraints with global convex hull and installed capacity leads to a very small PV penetration and cost savings (-0.30%). This is due to the constantly high risk of cloud passage even at hours of low irradiance. The integration of hourly convex hulls with installed capacity as reference for the PV drop calculation significantly increase the potential for PV integration (67.1 MW) as highlighted in Fig. 5.13. This leads to a costs reduction of 3.8% and CO_2 reduction of 4.81% which is more than half of the reduction obtained by the NO-FC case (which is expected since the PV capacity is much larger in the NO-FC case).

Computing solar drops with PV curtailed capacity increases the PV installed capacity up to 88.3 MW leading to a total cost reduction

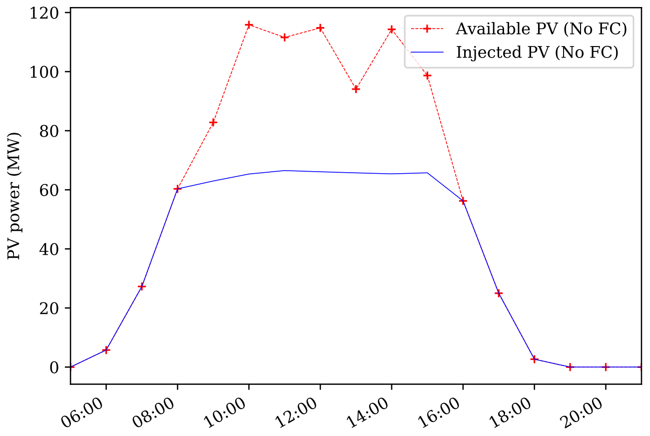

Figure 5.11: Available and injected PV profile for the "NO-FC" case.

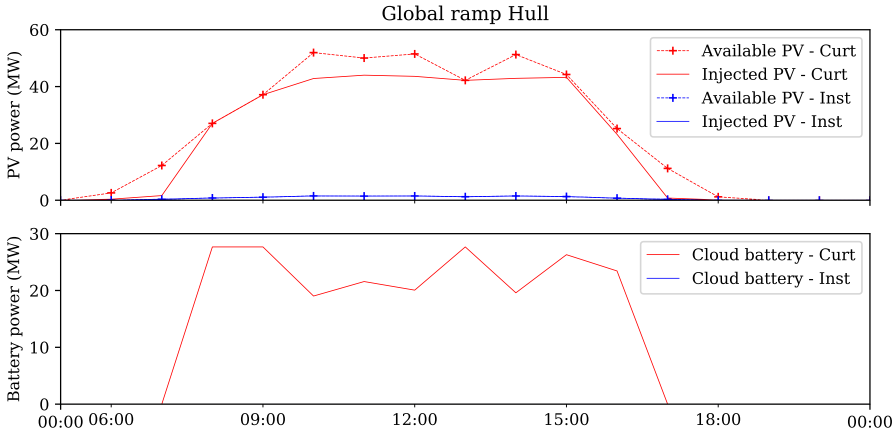

Figure 5.12: Hourly power profiles of available PV, injected PV and battery requirements with global hull.

of 4.18% and CO_2 reduction of 5.5%. As shown in Fig. 5.12 and 5.13, the combination of hourly hulls and curtailed PV capacity as reference increases the potential for PV integration (with PV power at 45 MW from 9am to 4pm against less than 40 MW between 10am and 3pm with installed capacity as reference). A power plant in hourly+curtailed configuration leads to saving 5.9% of overall costs and 7.37% of total CO_2 emissions.

However, calculating PV drop from curtailed PV capacity lets a potential for the optimization to drive the PV curtailment as a function of the PV risk. This means that the PV curtailment decision at each timestep depends both on the solar power forecast and the solar variability scenario. This strategy should be reproduced within the power plant's EMS to ensure consistency with sizing results. In the

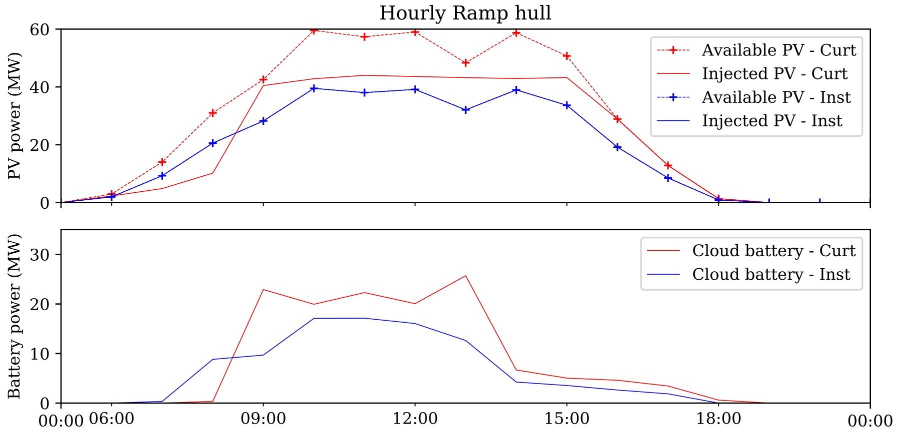

Figure 5.13: Hourly power profiles of available PV, injected PV and battery requirements with hourly hulls.

next section, the simulator's EMS strategy will be modified to include variability-driven curtailment and further evaluate the profitability of such operational strategy.

IMPACT OF STATIC AND DYNAMIC FREQUENCY CONSTRAINTS

The integration of static frequency constraint has shown a clear impact on optimal solution as previously detailed. From the dynamic frequency constraint formulation (Eq. 5.40), the battery requirement are expected to be lower for the same risk of PV drop. This is verified in Fig. 5.14 and 5.15. In the curtailed + hourly hull configuration, 101.2 MW of PV capacity is installed regardless of the type of the frequency constraint. However, Tab. 5.4 reports that the battery requirement is reduced by 2.7 MW (-9.8 % as compared to static constraint). This results in lower CAPEX (-1.2%) for the same CO_2 savings. On the other hand, the impact on overall costs in insignificant since no discount rate have been considered in this case. Integrating discount rate may further highlight the interest of the dynamic formulation as it mostly impacts the capital expenditures.

	Base Case	No FC	Global				hourly			
FC type	-	-	Static		Dynamic		Static		Dynamic	
Risk reference	-	-	Inst.	Curtailed	Inst.	Curt.	Inst.	Curt.	Inst.	Curt.
Total costs (E+09 $)	4.96	4.25	4.95	4.76	4.95	4.75	4.77	4.67	4.77	4.67
CAPEX (E+07$)	1.76	13.4	1.86	8.11	1.86	8.05	6.57	8.79	7.26	8.68
Fuel OPEX (E+08 $)	2.47	2.06	2.46	2.34	2.46	2.34	2.35	2.29	2.35	2.29
CO_2 (E+05 kt)	8.04	6.69	8.01	7.60	8.01	7.59	7.65	7.45	7.64	7.45
Installed PV (MW)	0.0	196.9	2.6	88.3	2.6	89.2	67.1	101.2	76.3	101.2
Cloud battery (MW)	0.0	0.0	0.0	27.7	0.0	24.7	23.2	27.4	26.7	24.7
N+1 Battery (MW)	44.0	40.4	42.7	42.7	42.7	42.7	40.4	40.4	40.4	40.4
Optimality gap (%)	0	0.85	1.88	1.29	1.57	1.22	3.34	1.08	2.87	0.99

Table 5.4: Comparison of optimal solution for several constraints setups.

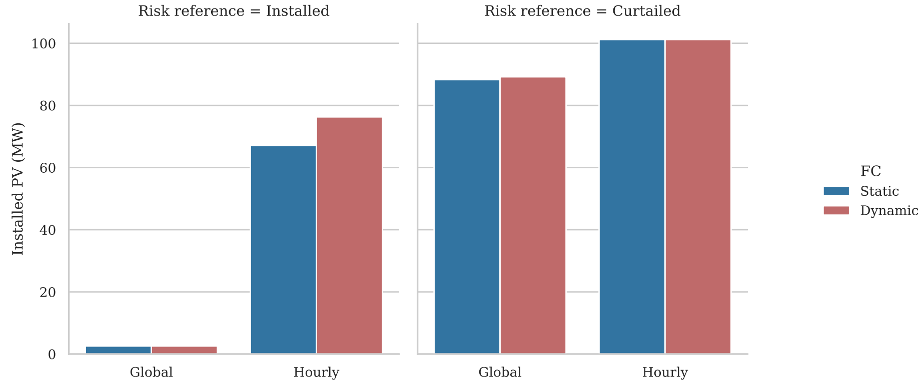

Figure 5.14: Comparison of PV installed capacity for several constraints setup.

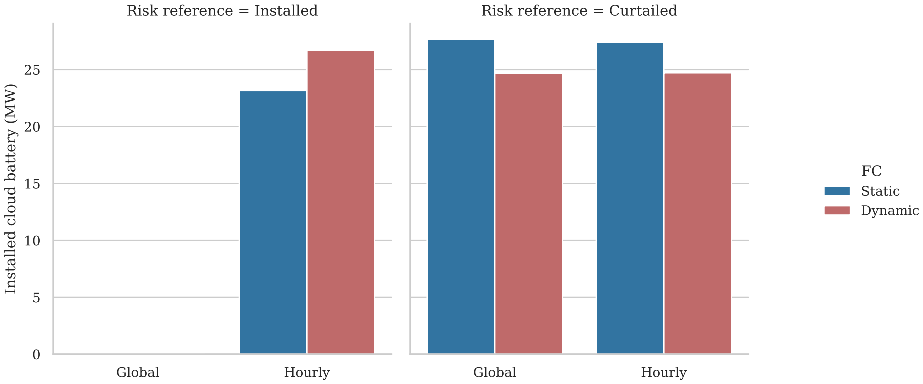

Figure 5.15: Comparison of battery installed capacity for several constraints setup.

5.2.7 *Discussion*

Based on the work of [167], this section proposed an optimal sizing formulation for PV integration in industrial microgrids. The resiliency to fossil generators contingency is ensured thanks to a similar spinning reserve calculation as expressed in [213]. The main contribution of this work was to develop linear frequency constraints for the resiliency to cloud passage. Isolated ramp scenarios extracted from convex hulls are used to evaluate battery requirements. This constitutes a new contribution to the previous work on frequency constraints formulations such as [177] which only covered risks of fossil generator contingency and [179] which included the variability of wind resources but did not addressed short-term solar variability. The impact of short term solar variability on the sizing of microgrids was covered in [191] which included solar drop scenarios from statistical analysis of historical data. The method proposed in this work allows addressing solar ramp event with a smaller temporal granularity and variable duration as opposed to [191] which considered fixed time increments of 15 minutes. Therefore, the short-term grid dynamics leading to frequency variation are addressed by a robust approach and takes place into a linear optimization framework allowing fast calculation of optimal solution.

When compared with dynamic simulation results, static and dynamic frequency constraints appears to over-estimate the need in power compensations. This leads in higher capital expenditure or lower PV penetration. The sub-optimality problem of linear frequency constraints formulations have been highlighted in [135]. To improve the solution and reduce the battery costs, non linear formulation or blenders decomposition were proposed. However, this should be put into perspective with the good performing optimality gaps of the present solution (1% for the dynamic+curtailed+hourly configuration reported in Tab. 5.4). Integrating non linear formulation would certainly improve the accuracy of the solution but also increase the computational burden, leading to higher computational times or higher optimality gaps.

Nevertheless, dynamic simulation results suggest that the optimal solution found by preliminary optimization should be refined to improve the capital expenditures related to the storage system. This justifies the use of the multi-layer simulation of Chapter 4 as an additional step of the sizing process to obtain optimal and robust solution for PV integration in industrial microgrid. The full process of optimization will be developed in the next section.

5.3 PROCEDURE FOR OPTIMAL AND ROBUST SIZING

5.3.1 *Procedure presentation*

Bearing in mind the simulation time of the solution developed in Chapter 4 (approximately 40 minutes per architecture), covering a wide range of PV and storage systems while running a sensitivity analysis on economic parameters would undoubtedly take too long. Therefore, the preliminary optimization presented above is coupled with the simulation framework to refine the architecture and guarantee their operability. Figure 5.16 shows the three main steps of the process.

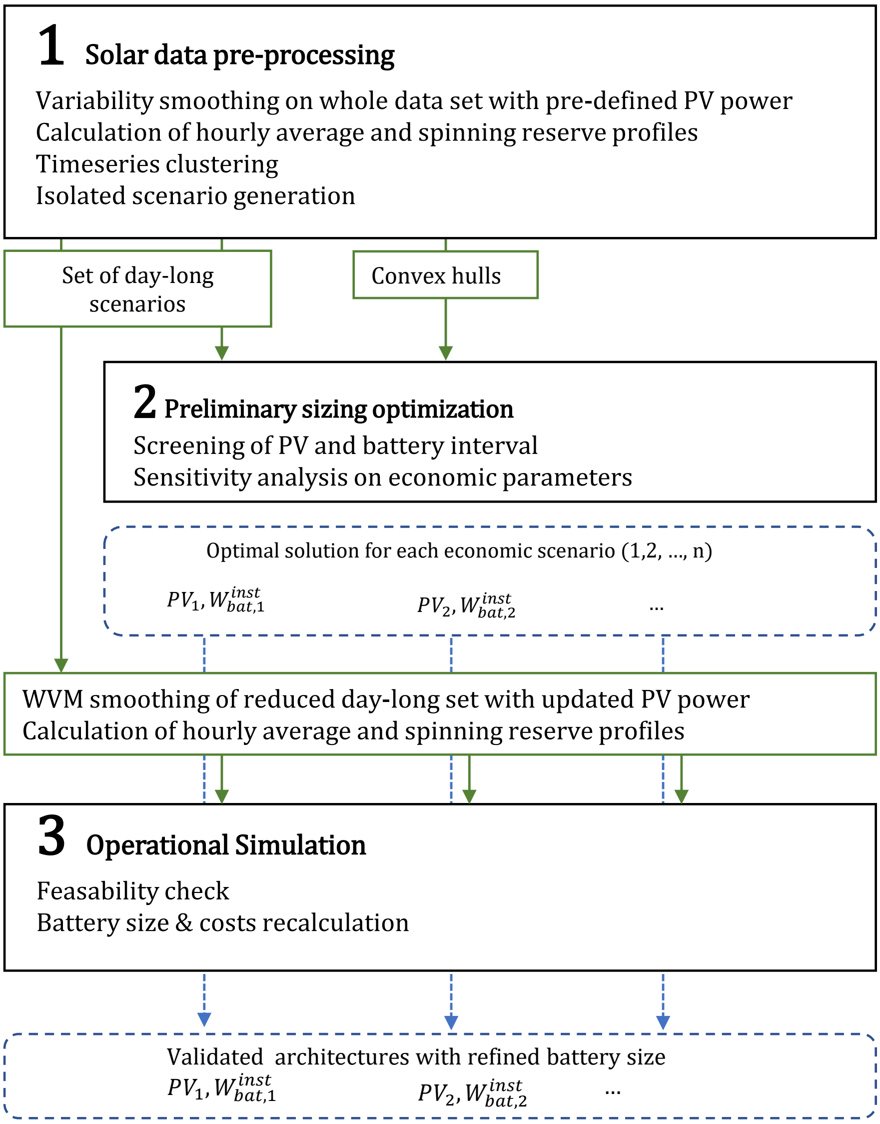

Figure 5.16: Full process of hybrid architecture sizing.

5.3.2 *Solar data-pre-treatment*

At the first step, the equivalent irradiance of a MW-scale PV plant is calculated for each day of the year. Then, hourly convex hulls are calculated thanks to ramp detection. The reduced set of day-long scenarios is also identified thanks to solar timeseries clustering.

The irradiance data pre-processing has been extensively covered in Chapter 3. The main challenge related to irradiance treatment during the sizing process is that the power plant size is unknown before the preliminary optimization. This forces to make an "educated guess" to start the procedure (for example in the next section, a PV power of 50MW is used for the initial WVM irradiance smoothing). The reduced set of day-long scenarios is shown in Tab. 5.5.

Scenario	Date	Description	Occurence	VI	Daily irradiance (kWh)
1	2010-12-09	Very Cloudy	40	21.31	2.63
2	2011-02-02	Medium production, low variability	98	30.90	4.92
3	2010-10-07	Medium production and variability	111	74.97	4.87
4	2011-09-02	High production, high variability Medium sharpness	67	91.10	6.78
5	2011-06-11	High production and variability	49	172.71	6.20
wc	2011-03-16	Worst case variability	0	238.97	5 .92

Table 5.5: Solar input scenarios resulting from the clustering and worst-case identification of the Hawaii dataset.

Figure 5.17 illustrates that the size of the power plant has an impact on short-term solar perturbations. Thus, the irradiance input profiles for the simulation step will be reprocessed by the WVM with the PV power resulting from preliminary optimization. This is expected to correct the potential biais brought by the uncertainty of the initial PV power value.

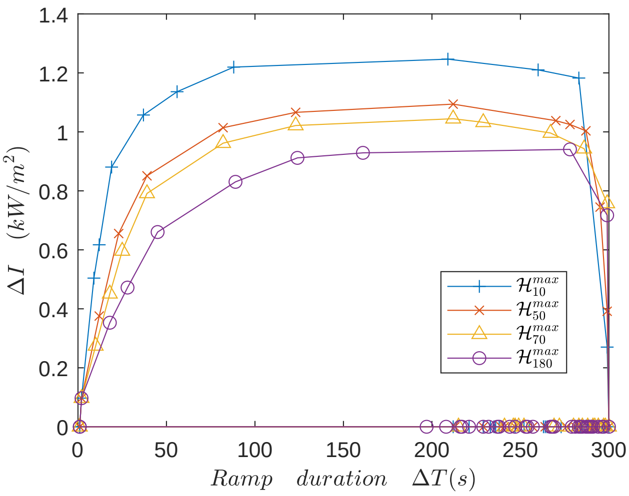

Figure 5.17: Convex ramp hulls after from WVM-smoothed irradiance of several PV power.

5.3.3 *Preliminary sizing optimization*

At the second step, a preliminary optimization is performed thanks to the model developed in section 5.2. The optimization is ran over the lifetime of the plant with a time horizon composed of 5 consecutive timeseries (each day of the reduced day-long set). If several technical setups and economic scenarios are studied, the preliminary sizing provides a set of architectures composed of a PV capacity, a cloud passage battery and a N+1 battery for each economic scenarios.

5.3.4 *Operational simulation*

Finally, architectures found at the preliminary optimization step are simulated over each day of the reduced set of day-long timeseries. Due to the linearization of the frequency constraint and the use of the worst-case convex hull, the cloud battery capacity are expected to be larger than necessary. Thus, the architecture cost is re-processed using the refined battery size and fuel consumption data.

Figure 5.18 describes the principle of architecture validation and battery capacity recalculation thanks to the operational simulator.

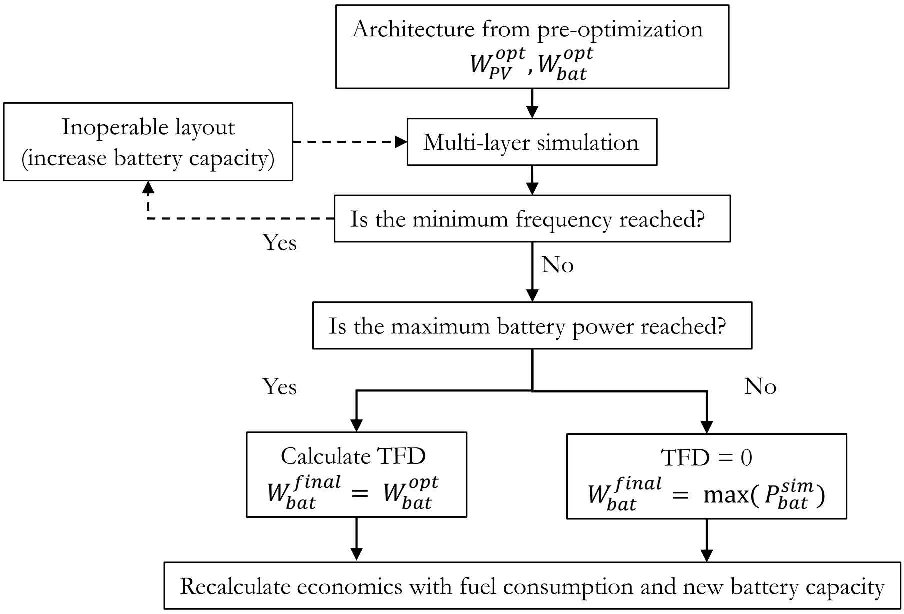

Figure 5.18: Procedure for layout validation and battery capacity calculation at simulation step.

The aim of the simulation step can be summed up as follows:

1. Validate de pre-optimized architecture if no large frequency drop happens over the 6 irradiance timeseries selected
2. Evaluate the actual required power capacity thanks to the maximum battery power supply over the 6 timeseries

3. Recalculate the overall costs of the system thank to refined battery capacity and fuel consumption.

Case of optimization with PV drop based on curtailed capacity

To ensure the consistency between the preliminary optimization sizing results and the operational simulation, the frequency constraint using the curtailed PV capacity must be integrated within the optimization layer (Eq. 5.46 and Eq. 5.49 to 5.52.). Since the battery capacity is not a decision variable in the operational management problem, Eq. 5.48 becomes :

$$\Delta P^{fc}_{PV_{h,r}} \leqslant W^{fc}_{bat} + \sum_{m,i} \Delta P^{DC}_{h,m,i,r} + db_{Hz} D_{fossil} \tag{5.57}$$

Where W^{fc}_{bat} denotes the battery installed capacity determined at the preliminary optimization step.

5.4 SIZING OF HYBRID POWER PLANT FOR AN LNG FACILITY

5.4.1 *Case study description*

In this section, the method for optimal and robust sizing presented in Section 5.3.1 will be applied for the solar-power integration in a Liquefied Natural Gas (LNG) processing plant. The architecture and data were provided by TotalEnergies from a real project carried by the R&D teams.

As illustrated in Fig. 5.19, the LNG processing plant mainly consists in several trains of liquefaction systems consuming both torque and electricity. The total electrical load of the system reaches 150 MW and vary over the day depending on the offloading procedure to LNG cargos. In Fig. 5.20, the daily load profiles provided by TotalEnergies are reported with maximum, minimum and average load profile.

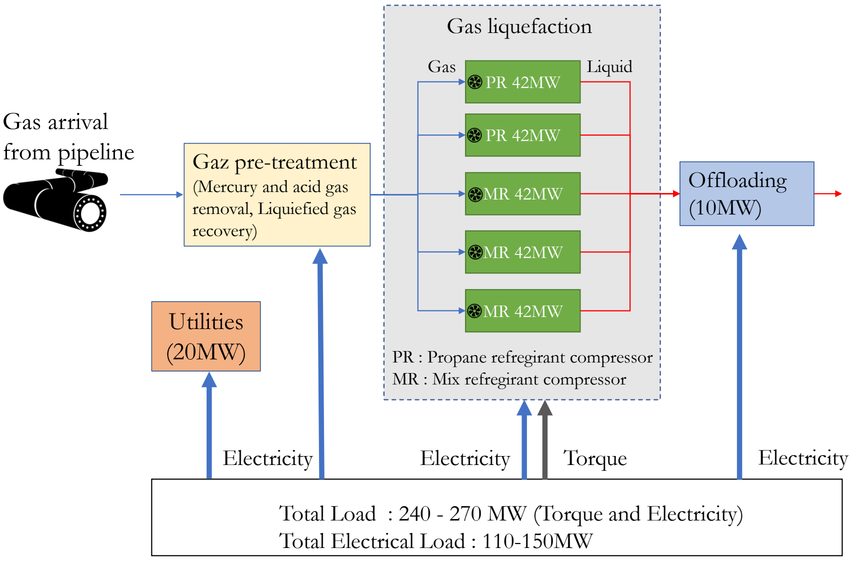

Figure 5.19: Working principle and main energy consumers of an LNG processing plant.

Since leakage may happen at every point of the gas treatment, liquefaction and loading process, safety equipments must be continuously supplied. If a motor is disconnected due to grid instabilities or a loss of electricity supply, the plant's safe operation is endangered. Additionally, economic penalty would result from delaying the loading schedule. Thus, the same frequency and voltage deviations constraints as presented in chapter 4 are applied:

- Steady-state voltage and frequency variation (including variation caused by PV cloud passage) : +/- 1% of nominal value

- Maximum transient deviations : +/- 5% of nominal frequency and +/- 10% of nominal voltage at load bus

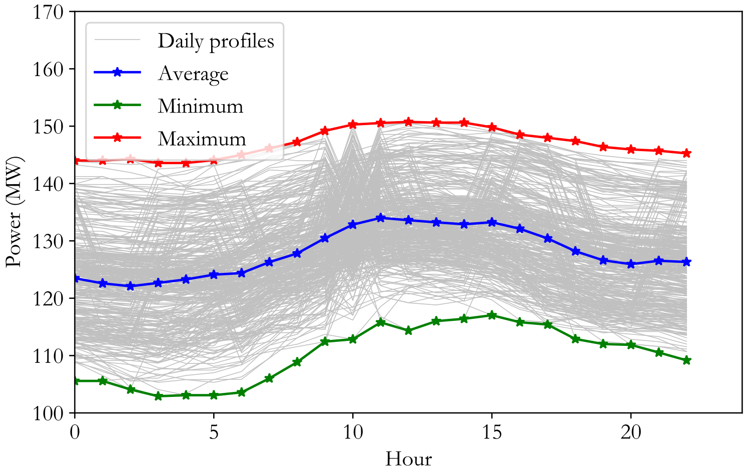

Figure 5.20: Load profiles of the LNG facility.

The power generation consists in an existing set of gas turbines as shown in the left part of Fig. 5.21. In the initial configuration, the plant is operated in "N+1" which means that an additional unit is turned on to cover the loss of a gas turbine. This results in lower load ratio of running turbines and therefore lower thermal efficiencies. The aim of hybrid power plant is to install a PV power plant to reduce the carbon emission and fuel costs of the system. Additionally, the "N+1" GT can be replaced by a storage system to increase the overall efficiency of the system. Since the five gas turbines are already installed, their installation costs will not be considered.

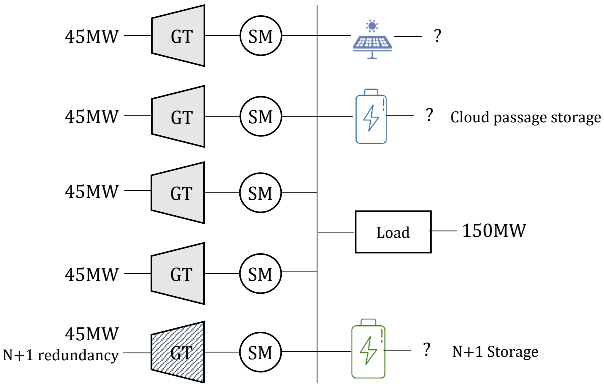

Figure 5.21: Description of electrical power plant.

The costs considered for the project are reported in Tab. 5.6 with references values and variation range. The range of variation for PV and battery are chosen according to market outlooks presented in [214, 215] while ranges for discount rates, fuel costs and CO_2 penalty were provided by TotalEnergies. Aggregated fuel costs (in \$/MJ) are considered to gather the CO_2 penalty and fuel cost.

In section 5.4.2, the sizing procedure will be applied with economic parameters at their reference values. In section 5.4.3, a sensitivity analysis will be carried to investigate the impact of economic parameters on optimal architectures.

-	Unit	Reference value	Range
Fuel cost	\$/mmbtu	20	[5 - 25]
CO_2 Penalty	\$/ton	40	[20 - 80]
PV installation cost	\$/kW	600	[400 - 1000]
Battery installation cost	\$/kW	400	[300 - 600]
Discount rate	%	0	[0 - 6]

Table 5.6: Economic parameters for case study analysis.

5.4.2 *The reference cost scenario*

5.4.2.1 *Sizing optimization*

In this section, the sizing procedure is applied with all economic parameters at their reference values (see Tab. 5.6). Two configurations will be investigated for the integration of PV power in the LNG facility (both setups integrate PV, N+1 storage and cloud passage storage):

1. *PV-dyn-inst*: Dynamic cloud passage constraint based on installed capacity by activating Eq. 5.45.
2. *PV-dyn-curt*: Dynamic cloud passage constraint based on hourly curtailed capacity by activating Eq. 5.46 (this configuration implies modifying the management strategy to account for the stability constraint in the planning decisions).

To compare the economical and environmental benefits of the N+1 storage and PV integration, it is necessary to perform 3 additional optimizations:

1. Base case: Neither PV nor N+1 battery are considered to calculate the system performance before hybrid integration
2. *N1*: No PV considered to evaluate the impact of the N+1 storage system separately.
3. *PV-NC*: No cloud passage constraints are set to evaluate the PV capacity and CO_2 savings in a same manner as a conventional sizing tool.

Scenario/Unit	Total costs B$	CAPEX m$	OPEX m$/year	CO$_2$ kt/year	PV MW	Cloud Battery MW	N+1 Battery MW
Base-case	5.5	0.0	274.1	890.5	0.0	0.0	0.0
PV-NC	4.3	134.3	206.8	672.0	196.9	0.0	40.4
N1	5.0	17.6	247.3	803.8	0.0	0.0	44.0
PV-dyn-inst	4.8	72.6	235.0	763.6	76.3	26.7	40.4
PV-dyn-curt	4.7	86.8	229.1	744.5	101.2	24.7	40.4

Table 5.7: Optimization results for each optimization setups.

Table 5.7 reports the results of the optimization whereas Fig. 5.22 and 5.23 display the additional relative CO$_2$ and costs savings for each of optimization setups as compared to the *base-case*.

As expected, the *base-case* provides the highest costs and the *PV-NC* leads to the highest PV capacity (196.9 MW) which provides an upper bound for the costs and CO$_2$ reduction (highlighted in dashed lines in Fig. 5.22 and 5.23).

Interestingly, the N+1 storage system is the main lever for CO$_2$ reduction since it reduces the emission by 87.5kt/year as compared to the *base-case*. On the other hand, the difference between *PV-dyn-curt* and *N1* is 59kt/year which shows that the PV integration has less impact than the N+1 storage integration.

The comparison between *PV-dyn-inst* and *PV-dyn-curt* highlights the interest of integrating hourly curtailed capacity in the PV drop calculation since it reduces the CO$_2$ emissions by 19.1 kt/year thanks to higher PV capacity. The impact on costs is less significant (-0.1 B$ which represents 1.89% of additional savings as compared to *base case*) since this solution requires more investments on PV system (+25 MW).

Another interest of the *PV-dyn-curt* setup is the significant reduction of the cloud passage battery capacity (-2 MW as compared to *PV-dyn-inst* for +25 MW of PV). However, the feasibility of such operational strategy must be verified by the simulator to ensure the electrical stability.

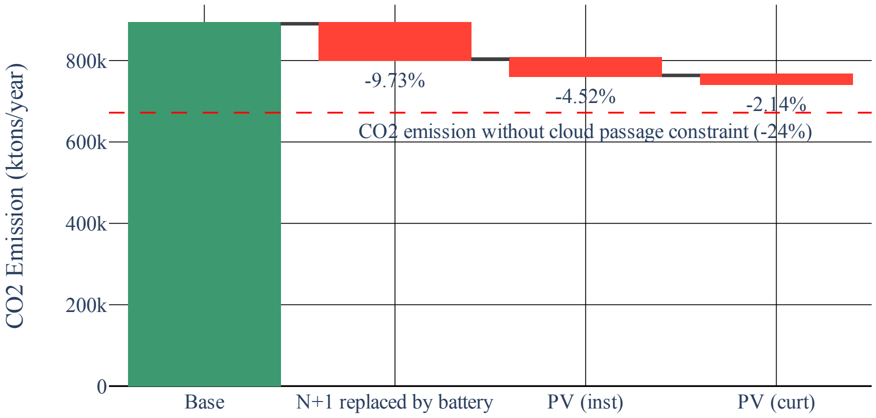

Figure 5.22: Relative CO$_2$ reduction for several optimisation setups.

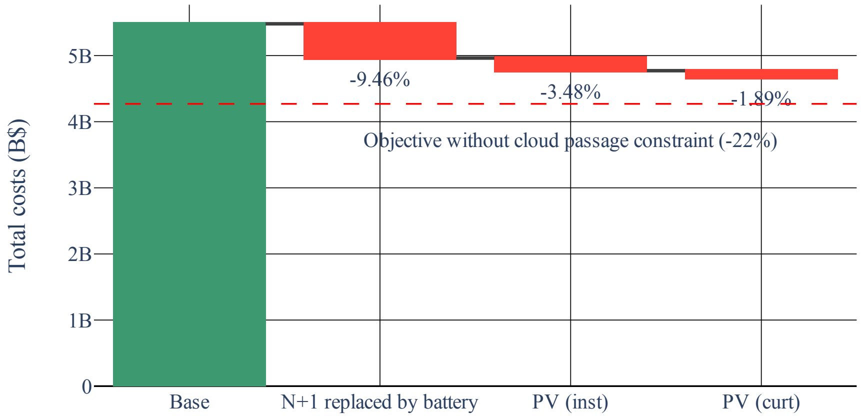

Figure 5.23: Relative costs reduction for several optimization setups.

5.4.2.2 *Operational simulation*

Now that optimal size for PV and battery capacities have been obtained thanks to the preliminary optimization, the operational simulator is used to validate the feasibility and refine the costs. Tab. 5.8 reports the results of the operational simulation for the *PV-dyn-inst* and *PV-dyn-curt* setups.

-	PV	Battery	TFD	Max. Power supply	Min. Frequency
Scenario / Unit	MW	MW	s	MW	Hz
PV-dyn-inst	76.3	26.7	0	19.7	49.88
PV-dyn-curt	101.2	24.7	0	24.7	49.72

Table 5.8: Comparison of grid simulation results between *PV-dyn-inst* and *PV-dyn-curt*.

Both architecture are validated since the minimum frequency is higher that the transient frequency limitation (47.5Hz). In the case of *PV-dyn-inst*, the battery is not saturated and a maximum power of 19.7 MW is supplied. This significantly reduces the size of the storage system (-7 MW). An example of simulation results is displayed in Fig. 5.24 and 5.25

In the case of *PV-dyn-curt*, the simulation results for the PV production highlights that the cloud passage constraint has a very limited impact on the curtailment (the PV power remains limited at 72MW from 10 am to 4 pm). This shows that the cloud passage constraint does not penalize the PV integration and only affects the size of the battery.

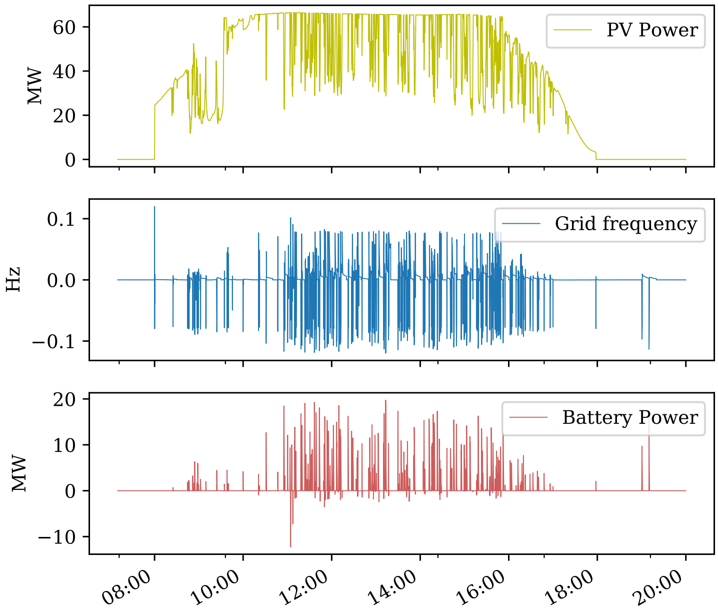

Figure 5.24: PV, frequency and battery profiles during worst-case day (2011-03-16) for the reference costs (RC) scenarios in *PV-dyn-inst* setup.

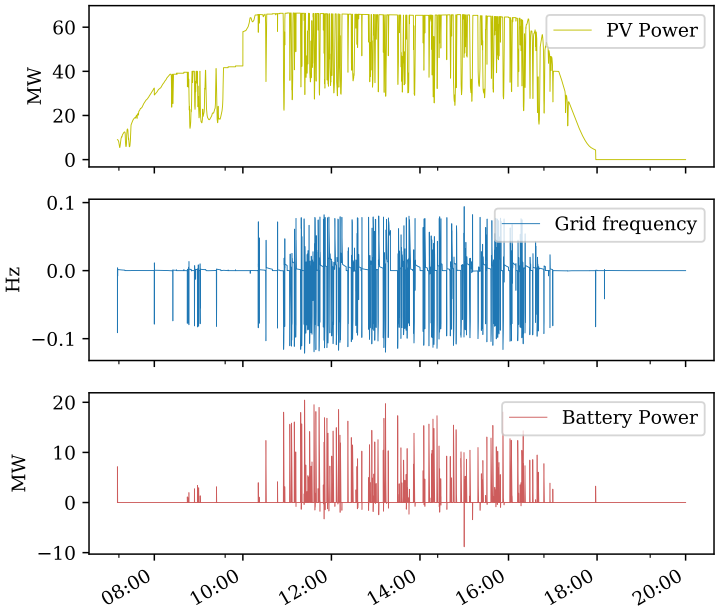

Figure 5.25: PV, frequency and battery profiles during worst-case day (2011-03-16) for the reference costs (RC) scenarios in *PV-dyn-curt* setup.

5.4.2.3 *Final Architecture*

Now that architectures have been validated, the total costs and CO_2 emissions can be refined thanks to the battery maximum power supply provided in Tab. 5.8 and the fuel consumption provided by the simulator.

Table 5.15 reports the final architectures characteristics, costs and emissions both in *PV dyn inst* and *PV dyn curt* configuration.

	PV	Cloud Bat	N1 Bat	CAPEX	OPEX	Total Costs	CO_2
Scenario/Unit	MW	MW	MW	m$	m$/year	B$	kt/year
PV dyn inst	76.3	19.7	40.4	69.8	229.3	4.7	746.3
PV dyn curt	101.2	24.7	40.4	86.8	219.3	4.5	713.8

Table 5.9: Final architecture and economic performances for the reference cost scenario.

Figure 5.26 shows how CO_2 is reduced along the sizing process. As compared to pre-optimization results, the simulation reduces the CO_2 emission by considering smaller time-step (-23.3 kt/year). When compared to the base-case results, this brings additional relative savings of 1.94%. This should be put into perspective with the maximum boundary of -24% for the CO_2 reduction (*PV-NC* setup) and with the 4.52% of relative savings already obtained by PV at the preliminary optimization. A similar trend is observed for the costs reduction as shown in Fig. 5.27 with -2.23% of costs reduction added up to the initial costs reduction of -3.48% obtained by the preliminary optimization. The simulation step significantly improves the performance of this configuration which justifies the additional time spent in simulating the architecture (approximately 40 minutes).

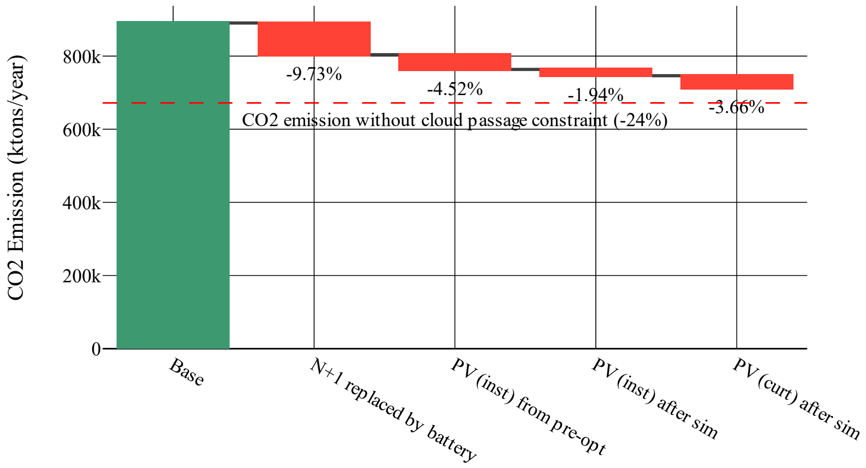

Figure 5.26: Relative CO_2 reductions after each step of the process.

The simulation results report higher gap between *PV-dyn-inst* and *PV-dyn-curt* as compared to the results of the preliminary optimization : -0.2 B$ of costs reduction against -0.1 B$. The total CO_2 reduction allowed by PV integration in *PV-dyn-inst* as compared to the *base-case* is 56.7 kt/year. On the other hand, the change in operational strategy *PV-dyn-curt* accounts for a CO_2 reduction of 32.5kt/year as compared to *PV-dyn-inst*. This results were expected and emphasize the interest of modifying the operational strategy to consider PV curtailed capacity in the power drop calculation.

The total costs and CO_2 savings potential of the hybrid power plant are respectively evaluated at 18.45% and 19.85%. After re-evaluating the system performance thanks to the simulator, the PV integration now account for half of the costs and CO_2 savings. These performances are a considerable improvements as compared to preliminary optimization results with a cost difference of 0.2 B$ and a CO_2 emission difference of 30.7 kt/year for the final architectures in *PV-dyn-curt* configurations.

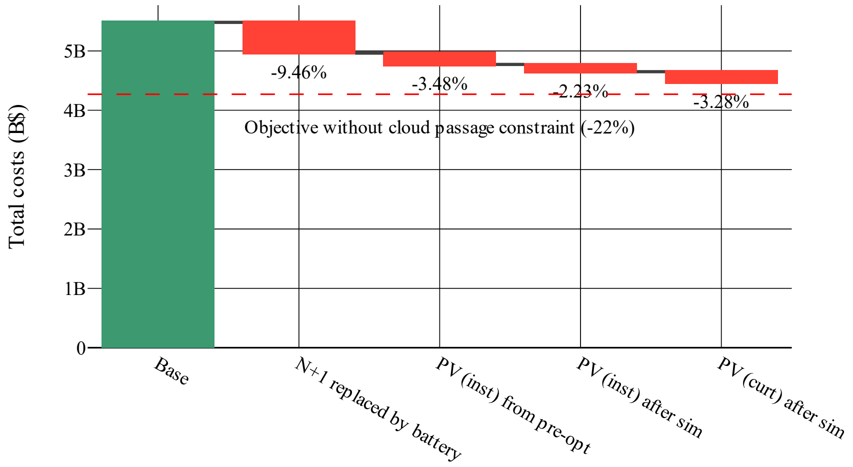

Figure 5.27: Relative costs reductions after each step of the process.

The sizing methodology provided two architectures with with varying operational choices (*PV-dyn-inst* and *PV-dyn-curt*). The preliminary optimization provides a first set of optimal size for PV, N+1 storage and cloud passage storage by screening a large feasibility interval in less than 1 hour. This first step is equivalent as evaluating the economical performance of each configuration in the stability map presented in part 4.4.3 which required 15h of calculation with an advanced computer[5]. Thanks to the reliability constraints of the preliminary optimization, the architecture were found to be operable by the simulator which avoids an iteration on battery capacity for ensuring frequency stability. The simulation reduces the size of the storage system and allows recalculating the system performance with more accuracy thanks to smaller time-step leading to better costs and CO_2 savings. The total computational time of the methodology for evaluating *PV-dyn-inst* or *PV-dyn-curt* is approximately 2 hours with a standard computer[6].

---

[5] advanced computer : 40 cores, 128Go Ram intel Xeon

[6] standard computer : 4 cores 8Go RAM intel i5 CPU

5.4.3 *Sensitivity analysis on economic parameters*

In this part, the size of the PV system, cloud passage battery and N+1 battery will be evaluated under 6 economic scenarios:

1. Reference costs (RC): All economical parameters at reference value (which corresponds to the results presented above).
2. High capital costs scenarios (HCC) : PV and Battery installation at their highest values.
3. High fuel costs (HFC): Aggregated fuel cost at its highest value.
4. High cost (HC) : All parameters at their highest values.
5. Low capital costs (LCC): PV and Battery installation at their lowest values
6. Low costs (LC): All costs at their lowest values

Similarly to part 5.4.2, the performance of the system will be evaluated in *PV-dyn-inst* and *PV-dyn-curt* configurations. To allow comparing the performance of PV integration, the *base-case* is also computed at the preliminary sizing step.

5.4.3.1 *Sizing optimization*

Table 5.10 to 5.12 report the results of the optimization performed with an optimality gap tolerance of 2%.

	Total costs	CAPEX	OPEX	CO$_2$	PV	Cloud Battery	N+1 Battery
Scenario/Unit	B$	m$	m$/year	kt/year	MW	MW	MW
RC	5.5	0.0	274.1	890.5	0.0	0.0	0.0
HCC	5.5	0.0	274.1	890.5	0.0	0.0	0.0
HFC	7.4	0.0	369.3	890.5	0.0	0.0	0.0
HC	0.4	0.0	369.3	890.5	0.0	0.0	0.0
LC	1.5	0.0	77.4	890.5	0.0	0.0	0.0
LCC	5.5	0.0	274.1	890.5	0.0	0.0	0.0

Table 5.10: Optimization results for Base case (no PV considered).

	Total costs	CAPEX	OPEX	CO$_2$	PV	Cloud Battery	N+1 Battery
Scenario/Unit	B$	m$	m$/year	kt/year	MW	MW	MW
RC	4.8	72.6	235.0	763.6	76.3	26.7	40.4
HCC	4.8	97.0	235.7	766.0	62.4	17.2	40.4
HFC	6.4	72.6	316.6	763.6	76.3	26.7	40.4
HC	0.4	26.4	333.9	803.8	0.0	0.0	44.0
LC	1.4	41.2	66.6	766.6	60.6	16.0	40.4
LCC	4.7	50.6	235.0	763.6	76.3	26.7	40.4

Table 5.11: Optimization results for PV-dyn-inst (Dynamic cloud constraint based on installed capacity).

	Total costs	CAPEX	OPEX	CO_2	PV	Cloud Battery	N+1 Battery
Scenario/Unit	B$	m$	m$/year	kt/year	MW	MW	MW
RC	4.7	86.8	229.1	744.5	101.2	24.7	40.4
HCC	4.7	129.2	229.6	746.1	91.4	22.6	40.4
HFC	6.3	97.1	308.1	743.1	118.5	24.7	40.4
HC	0.4	26.4	333.9	803.8	0.0	0.0	44.0
LC	1.4	52.9	65.0	747.3	86.3	20.8	40.4
LCC	4.6	67.5	228.7	743.3	120.0	24.7	40.4

Table 5.12: Optimization results for PV-dyn-curt (Dynamic cloud constraint based on curtailed capacity).

Figure 5.28 displays the PV and cloud battery installed capacities for the *PV-dyn-inst* configuration. Interestingly, the preliminary optimization provide equivalent solutions for RC, HFC and LCC scenarios with a PV installed capacity around 80WM. In the *PV-dyn-curt* configuration (displayed in Fig. 5.29), the installed capacities for LCC and HFC are larger than in the RC scenario (120MW instead of 100MW). Therefore, the optimization takes more advantage of the cost difference when PV drop constraint is integrated in the management layer.

In both configurations, the HC scenario leads to installing an N+1 storage system without PV. This most probably comes from the discount rate of 6% which highly penalises the OPEX savings and supports architectures with limited capital investments.

In both configurations, the optimal solutions for HCC and LC are equivalent (around 60 MW for *PV-dyn-inst* and 90MW for *PV-dyn-curt*. This shows that low fuel costs associated to low capital costs (LC scenarios) have the same impact as high capital costs. The difference between LC and HFC scenarios highlights the role of the fuel costs in the optimization results.

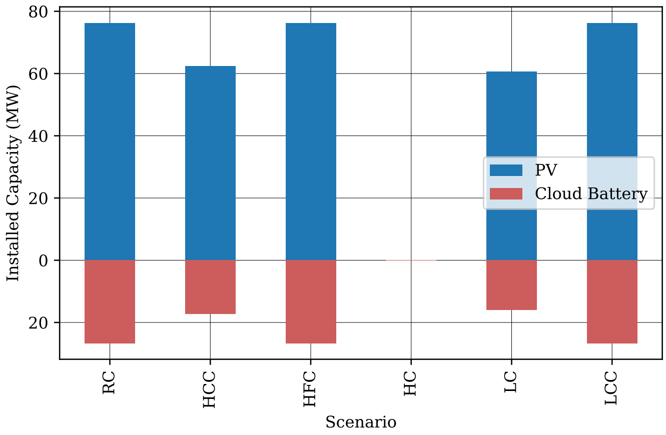

Figure 5.28: PV and cloud battery resulting from optimization for the 6 economic scenarios in *PV-dyn-inst*.

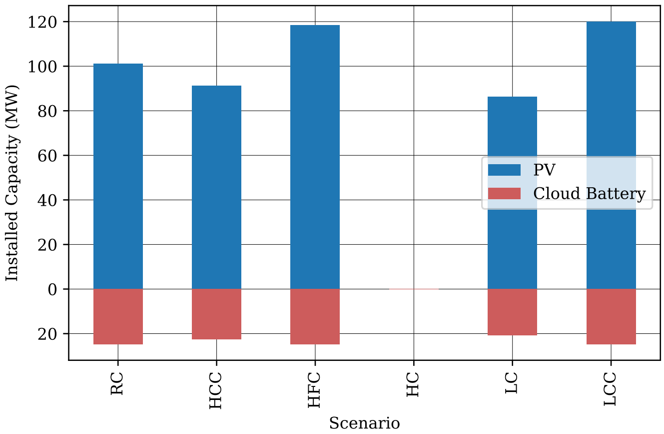

Figure 5.29: PV and cloud battery resulting from optimization for the 6 economic scenarios in *PV-dyn-curt*.

5.4.3.2 *Operational simulation*

The simulation results are displayed in Tab. 5.13 for *PV-dyn-inst* configurations and Tab. 5.14 for *PV-dyn-curt* configurations. Similarly to the reference cost scenario analysis, all architectures were validated in the first round of simulation with no TFD and a frequency being kept above the minimum transient limit.

-	PV	Battery	TFD	Max. Power supply	Min. Frequency
Scenario / Unit	MW	MW	s	MW	Hz
RC	76.3	26.7	0	19.7	49.88
HCC	62.4	17.2	0	17.2	48.75
HFC	76.3	26.7	0	19.7	49.88
HC	0	0	0	0	50.00
LC	60.6	16	0	16	47.87
LCC	76.3	26.7	0	19.7	49.88

Table 5.13: Results of grid simulation for each economic scenario in the *PV-dyn-inst* setup .

-	PV	Battery	TFD	Max. Power supply	Min. Frequency
Scenario / Unit	MW	MW	s	MW	Hz
RC	101.2	24.7	0	24.7	49.72
HCC	91.4	22.6	0	22.6	49.20
HFC	118.5	24.7	0	20.43	49.87
HC	0	0	0	0	50.00
LC	86.3	20.8	0	19.74	49.88
LCC	120	24.7	0	20.43	49.87

Table 5.14: Results of grid simulation for each economic scenario in the *PV-dyn-curt* setup.

According to the procedure detailed in Fig. 5.18, the battery installed capacity is recalculated for each scenario as displayed in Fig. 5.30. As expected, considerable differences can be obtained between the simulation results (red and blue stars) and preliminary optimization results (red and blue circles). The higher differences is obtained in the *PV-dyn-inst* configuration for the RC, HFC and LCC scenarios with -7 MW.

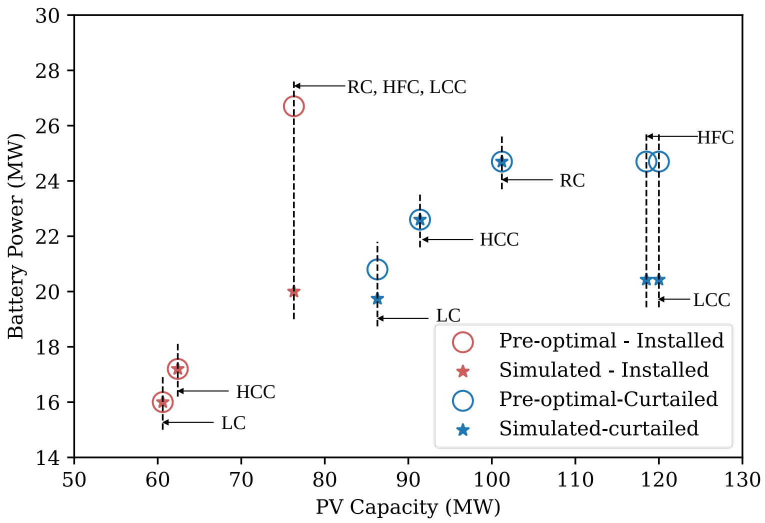

Figure 5.30: Battery capacity requirements for each economic scenario after pre-optimization (pre-optimal) and after grid simulation.

5.4.3.3 *Final architectures*

Tables 5.15 and 5.16 report the final architectures and their characteristics in "installed" and "curtailed" modes respectively.

Scenario/Unit	PV MW	Cloud Bat MW	N1 Bat MW	CAPEX m$	OPEX m$/year	Total Costs B$	CO2 kt/year
RC	76.3	19.7	40.4	69.8	229.3	4.7	746.3
HCC	62.4	17.2	40.4	97.0	229.0	4.7	745.2
HFC	76.3	19.7	40.4	69.8	310.3	6.3	749.4
HC	0	0	44	26.4	333.9	0.4	803.8
LC	60.6	16	40.4	41.2	65.2	1.3	750.8
LCC	76.3	19.8	40.4	48.5	230.2	4.7	749.3

Table 5.15: Final architecture and economic performances for the (*PV-dyn-inst* setup.

The PV integration allows saving from 15.6% to 19.8% of CO$_2$ emissions. The difference in costs and CO$_2$ savings between lowest and highest PV capacities remains relatively low (+4.2% of CO2 savings for +60 MW of installed capacities). This is also confirmed with the RC and HFC scenario in curtailed mode where the 20MW of additional

Scenario/Unit	PV MW	Cloud Bat MW	N1 Bat MW	CAPEX m$	OPEX m$/year	Total Costs B$	CO2 kt/year
RC	101.2	24.7	40.4	86.8	219.3	4.5	713.8
HCC	91.4	22.6	40.4	129.2	223.0	4.6	725.6
HFC	118.5	20.43	40.4	95.4	295.6	6.0	713.8
HC	0	0	44.0	26.4	333.9	0.42	803.8
LC	86.3	19.74	40.4	52.6	63.1	1.3	727.1
LCC	120.0	20.43	40.4	66.2	219.3	4.5	713.8

Table 5.16: Final architectures and economic performances for the *PV-dyn-curt* setup.

PV capacity have negligible impact in CO_2 savings This is mostly explained by the low flexibility of the SGT800 gas turbine (this has been highlighted in Chapter 4). Replacing gas turbines by better performing fossil generators would allow to improve the performance of the hybrid power plant. Such analysis require the integration of fossil unit investment decisions in the formulation which will be studied in the future.

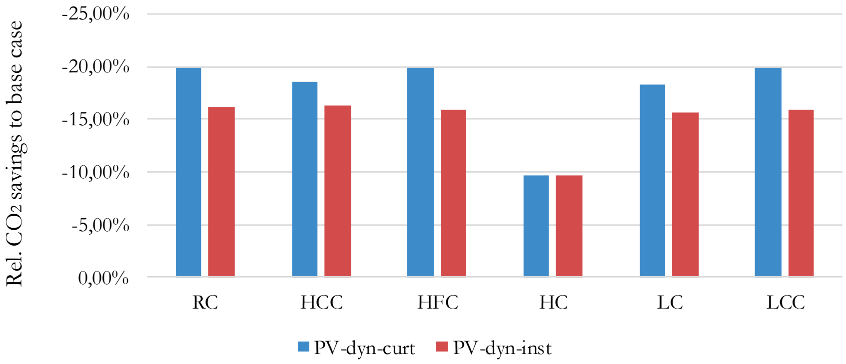

Figure 5.31: Relative CO_2 savings as compares to base case for each scenario in "installed" (red) and curtailed (blue) modes.

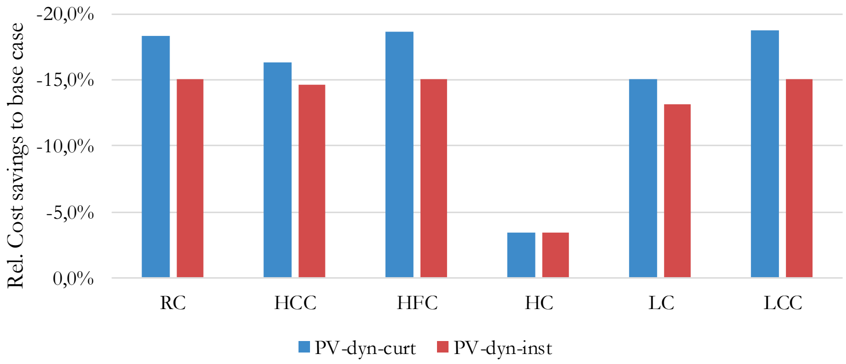

Figure 5.32: Relative total costs savings as compares to base case for each scenario in "installed" (red) and curtailed (blue) modes.

Figure 5.31 and 5.32 display the relative CO_2 and costs savings as compared to base cases both in *PV-dyn-inst* and *PV-dyn-curt* configurations. The result show that *PV-dyn-curt* perform better for every scenarios featuring PV capacities. In the LCC, RC and HFC scenario, the CO_2 reduction is improved from 16.7% up to 19.8% which is substantial and emphasize the interest of accounting for ramp constraints in the operational optimization layer.

In the preliminary optimization step, 6 optimizations were performed per constraint setup (*base case* ,*PV-dyn-curt* and *PV-dyn-inst*). Thanks to the linear optimization framework, all optimal solutions were found in less than 3 hours. This is a considerable improvement of computational time as compared to the use of the simulator for screening a wide range of PV and battery capacities. To validate the architecture and refine the total costs, a single simulation per scenario was necessary. This brings the overall process of the sensitivity analysis to a computational time of 11 h with a standard computer and less than 2h with a more advanced computer [7]. This must be compared to generation of a stability map as proposed in chapter 4 which required 15h with PV capacity increments of 10MW and battery capacity increments of 1MW whereas the MILP approach considered wider continuous intervals.

---

[7] standard computer : 4 cores 8Go RAM intel i5 CPU; advanced computer : 40 cores, 128Go Ram intel Xeon computer

5.5 CONCLUSION

In this chapter, a methodology for the optimal and robust integration of PV power plant in industrial microgrids has been proposed. After a pre-treatment of solar input data thanks to solar variability smoothing, timeseries clustering and convex hull identification, a robust pre-optimization is carried to evaluate the optimal PV and battery capacities.

The pre-optimal sizing is formulated as a MILP problem based on operational constraints developed in Chapter 4 which ensures the consistency with operational management strategies. The resiliency to fossil unit contingency is ensured thanks to spinning reserve constraints and allows evaluating the potential of an N+1 storage unit to reduce the fuel consumption. The main contribution of this work is the formulation of cloud passage resiliency constraint to ensure that no grid instability will appear during solar power drops. As opposed to [135], resiliency constraints were based on linear approximation of the equation of motion which allows fully taking advantage of the MILP formulation in terms of computational times and optimality gaps. By considering worst-case linear solar drops, the frequency constraint integrates sub-minute frequency stability into an high level energy formulation which was not proposed in the literature.

Thanks to the robust sizing at the pre-optimization phase, a single detailed simulation is necessary to refine battery capacity and fuel consumption. This simplifies the sizing process and reduces the computational burden of the methodology as compared to state-of-the art approaches such as developed in [184] were every potential solutions are simulated by detailed dynamic models.

The case study investigated in this chapter illustrates the ability of the method to provide optimal capacities for PV, N+1 storage and cloud passage storage for several economic scenarios. In the reference case, the total CO_2 savings were estimated at 16.19% against 24% when frequency constraints are ignored with 76.3 MW of installed PV capacity instead of 196 MW and a cloud passage storage capacity of 19.7 MW instead of 0 MW. This shows that neglecting cloud passage effect leads to unstable architectures and an overestimation of the power plant performances.

The integration of the frequency constraint within the operational management of the plant allowed to increase the CO_2 saving potential up to 19.85%. This demonstrates the interest of investigating reliability constrained operational management to improve the PV penetration.

6

GENERAL CONCLUSION

6.1 CONCLUSION

This doctoral dissertation addresses the integration of large scale PV systems in industrial power plants. The main research challenge is to integrate short-term solar variability in the simulation and sizing methodologies to help power plants developers in the preliminary assessment process. The main contributions of this work is to develop a simulation framework for the assessment of operational performances of the system using optimal management strategies and to propose a sizing methodology for the optimal and robust sizing of PV and storage systems.

Thanks to variability quantifiers and irradiance time series preprocessing, the solar variability is addressed to better anticipate electrical perturbations. A scenario reduction method is applied to reduce the number of daily simulations from 365 to 6 timeseries which significantly reduces the computational burden of the proposed tools. Ramp detection and convex hull representation are used to generate a set of worst-case solar ramps. These scenarios are employed to evaluate electrical perturbation and reduce the time windows from 5.4 10^5 seconds (5am to 8pm) down to 300 seconds.

The operational simulation framework proposed in this work is composed of a single-line active power electrical model which calculates the frequency shift caused by solar variability. This model is interfaced with a two-layer energy management optimization which provides optimal operating status and setpoints to fossil units. The CO_2 emissions, fuel costs and cumulated frequency disturbances are calculated and aggregated into yearly indicators thanks to the reduced set of scenarios. The battery requirement guaranteeing electrical stability is evaluated and refined according to the user's tolerance in terms of frequency shifts.

A sizing methodology evaluates the optimal investment decisions for PV systems and two storage units dedicated to contingency resiliency and cloud passage management. The sizing process is composed of a MILP optimization ensuring robust evaluation of storage requirements thanks to linear frequency constraints and worst case solar ramps. The results of the pre-optimization are refined by the multi layer simulation. The case study of an LNG power plant is investigated and results shows that up to 19% of CO_2 can be saved while ensuring electrical stability under highly variable irradiance conditions.

6.2 LIMITATIONS

In the development process of these methods, keeping the model complexity to a suitable level for preliminary studies was one of the main challenge. This led to make assumptions for component description. Consequently, the following limitations can be formulated:

A single line model reduction has been proposed to avoid using the 3-phase model. One of the key assumption is to neglect voltage variations and to consider that frequency stability is a sufficient condition for the whole stability of the system. This assumption is hard to verify in preliminary studies since the grid topology is not available (especially the contribution of PV inverters to voltage support).

The fossil controllers developed in the reduced order model is designed to track optimal setpoints and frequency stability during cloud passage. Hence, this model is not valid during fast transient such as load step or generator contingency. Evaluating the system's stability over large load steps would require using the detailed electrical model.

For the sake of simplicity, a proper modeling of the PV system has not been performed. Notably, temperature effect and modules performance degradation were not considered. This is likely to bring errors in the evaluation of the injected solar energy and consequently, inaccurate fuel savings evaluation.

An hourly averaged load profile has been considered for operational simulation and optimization. This is a reasonable assumption in normal operation since industrial processes tends to be less variable than residential loads. However, the connection of large consumers can happen and cause large grid perturbations. The resiliency of the grid in case of simultaneous load step and cloud passage is not addressed. The probability of such situations should be evaluated to verify the validity of this assumption.

In the energy management simulation proposed in chapter 4, no forecast system has been used to generate solar irradiance timeseries which is a major deviation from reality. This is not so much an issue for frequency stability as short-term ramps are unforecastable. But, spinning reserve requirements forces to use a forecast system in real life conditions. In this work, the spinning reserve requirement has been calculated as the maximum deviation between the hourly averaged value and the 1-second profile which means that the hourly averaged valued is considered as the predicted value. The use of a forecast system should improve the accuracy of the method and avoid a potential mismatch at low PV production time especially when the plant is operated without a N+1 fossil generator.

In the optimization model, solar variations are assumed to be linear. One could challenge the validity of this assumption since the gradient of solar perturbation is not constant during cloud passage. Additionally, the smoothing effect of the power plant is addressed by a single

WVM pre-processing of the time-series. The solar variability of higher power plant can be over-estimated which penalizes high PV installed capacities.

Finally, the operational simulation considers that each days are independent. The storage system is assumed to be fully charged at the beginning of the day and fossil unit operating status decision have no impact have no consequences on the next days. Such assumption would most certainly be invalid if an energy-shifting storage system or wind power are integrated in the future.

6.3 RECOMMENDATIONS FOR INDUSTRIAL MICROGRID DEVELOPMENT

The conclusions of this thesis leads to formulate a few recommendations to the attention of power plant developers.

First, the role of solar variability in the power quality degradation and storage sizing shows that electrical stability during cloud passage should be integrated sooner in preliminary sizing studies

Secondly, the role of fossil generation flexibility in the performance of the hybrid power plants have highlighted the need for a change in the selection process of future fossil units. The following factors shall be considered to maximize the renewable penetration and reduce the storage investments:

- Better performing units at part-load.
- Wider operational margins.
- Low minimum up and down times.
- High ramp rates.

This promotes the use of small units and preferably gas engines which were found to be more flexible as compared to large industrial gas turbines.

Thirdly, in an industrial development perspective of the proposed tools, additional factors may be integrated to model the plant with more accuracy. Notably, the temperature profile at site allows calculating the temperature effect of PV system as well as the gas turbine maximum power output limitation. This last factor is crucial to refine the spinning reserve capabilities of gas turbines.

Finally, the development of industrial microgrid would benefit from reducing the uncertainties related to solar variability scenarios. In this work, a worst-case data-set has been used. Performing measurement studies as soon as possible may refine the sizing and bring subsequent storage investment costs savings.

6.4 RECOMMENDATIONS FOR FUTURE RESEARCH WORK

Fossil generation performance during transient operation

One of the main research perspective for this work is to investigate the impact of extended transient operation on fossil generation performance (fuel consumption and lifetime degradation).

A data-driven investigation has been performed thanks to gas turbine commissioning records. A comparison between the fuel mass flow during transient operation and steady-state operation showed that the heat-rate may increase up to 12.5% higher during ramp operation. After applying this factor to a simulation results, it was found that the fuel consumption during day-time could be around 5% higher.

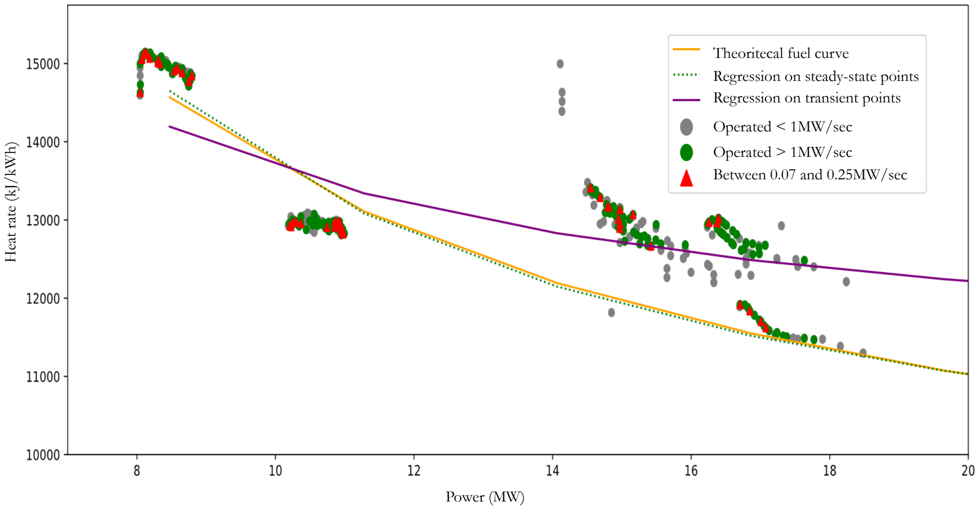

Figure 6.1: Comparison between steady-state and transient heat-rates thanks to commissioning records on Rolls Roys RB211 GT. The theoretical fuel curve is obtained from the manufacturer's steady state data whereas the blue and purple curve shows the results of a polynomial interpolation using records under transient operation.

The lack of a large amount of reliable data did not allow using these results within the present work but highlights the relevance of further investigations. Since only a few thermodynamic models have attempted to address transient operations performances, an experimental approach should provide lots of benefits for the calibration of a generic model. One option could be to generate transient running lines in the compressor performance map thanks to a detailed physical model. These lines could be interpolated in the operational simulator to integrate transient performances while avoiding heavy thermodynamic simulation.

Integration of advanced management strategies in operational simulation

In the simulation simulation framework developed in 4, a sequential structure is used for carrying energy management optimizations and grid simulation. This reproduces the operational strategy of an industrial microgrid. Another advantage of such approach is to allow integrating feedback variables from grid simulation into the optimization of the next time slice. This could be useful for handling battery state-of-charge management (see Fig. 6.2).

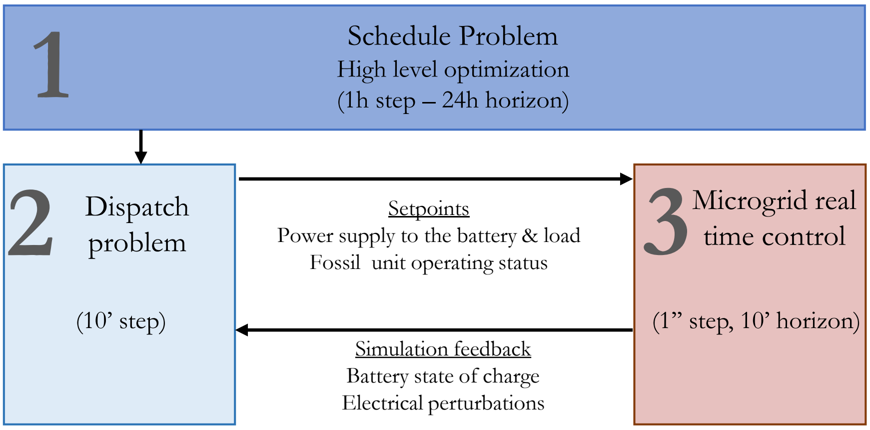

Figure 6.2: Feedback variable integration in the operational simulator

In chapter 5, the integration of solar ramp risks in the management strategy showed promising perspective to increase the penetration rate of the PV system and increase the CO_2 savings (+1.4%). More advanced management strategies could be integrated to smartly manage uncertainties related to solar production and variability. A first, a deterministic approach could be carried by integrating the convex hull corresponding to each day instead of a worst-case set obtained from one year of data. Then, variability forecasts may be used for the optimal management of the PV curtailment capacity and fossil unit dispatch. For example the ramp rate prediction method proposed in [216] paves the way for variability forecast integration. Such approach requires a deep investigation of currently available solutions. Considering reliability constraints, robust optimization approaches will be probably the most relevant to manage the uncertainties when performing the unit commitment.

Enrich the sizing optimization problem for broader use

To use the sizing optimization method in more industrial applications, the formulation shall be extended and include investments on fossil units. This could be done by adding a new binary decision variable $\mu_{m,i}$ associated to the investment costs c_m in the objective function.

The following constraint shall ensures that investment decision is made if the unit is turned on at least once :

$$\forall h \quad \mu_{m,i} \geqslant \omega_{m,i} \tag{6.1}$$

The possible synergies between buffer storage and energy shifting storage could be explored which would require to formulate the role of each block in spinning reserve and frequency constraints. If an energy shifting storage is used for solar ramp mitigation, the charging strategy will undoubtedly play an important role in the reliability of the system. However, the integration of new decision variables and a new set of constraint may significantly increase the computational complexity. To ensure faster calculation, decomposition methods for MILP programming can be employed such as column generation or Benders decomposition.

These proposals only give a glimpse of the possibilities for future research on industrial microgrids. But the coming developments of real-life projects and their practical implementation will undoubtedly bring new exciting challenges to the scientific community.

7

APPENDIX

7.1 PROOF OF CONVEX HULL PROPERTIES

The convex enveloppe of $\mathcal{R}^{max}$ allows reducing the set of events to consider. The Carathéodory's theorem[206] defines $\mathcal{H}^{max} = conv(\mathcal{R}^{max})$ as follows :

All elements $p \in \mathcal{H}^{max}$ can be written as a convex combination of k points of $\mathcal{R}^{max}$ with $k \leqslant 1 + dim(\mathcal{R}^{max})$.

Since $dim(\mathcal{R}^{max}) = 2$, this gives $p = r_1 t_1 + ... r_k t_k$ with $\sum_{k=1}^{3} t_k = 1$ and $r_k \in \mathcal{R}^{max}$

PROPERTIES

Let h_1, u_2 be two consecutive elements of $\mathcal{H}^{max}$ and $u' \in [h_1, u_2]$ such as $u' = \tau u_1 + (1 - \tau) u_2$ with $\tau \in [0, 1]$

Property 1 (P1) : The power imbalance $\Upsilon_{u'}$ of each point in the segment $[h_1, u_2]$ higher or equal than the power imbalance of every element of lower irradiance drop Υ_r
$\forall r = (\Delta T_{u'}, \Delta I_r) \quad | \quad \Delta I_r \leqslant \Delta I_{u'}$
$\Upsilon(r) \leqslant \Upsilon(u')$

Proof :

$$\Upsilon(u') = \Delta I_{u'}.\eta_{PV}.Q_{PV} - T_{u'}.rr_{fossil} \tag{7.1}$$

$$\Upsilon(r) = \Delta I_r.\eta_{PV}.Q_{PV} - T_{u'}.rr_{fossil} \tag{7.2}$$

$$\Delta I_r \leqslant \Delta I_{u'} \quad \Rightarrow \quad \Upsilon(r) \leqslant \Upsilon(u') \tag{7.3}$$

Property 2 (P2) : The power imbalance of each point of the segment $[h_1, u_2]$ is lower or equal than one of the two closely located point of the convex hull (u_1 or u_2)
$\Upsilon(u') \leqslant \Upsilon(u_1)$ or $\Upsilon(u') \leqslant \Upsilon(u_2)$

Proof :

$$\Upsilon(u_1) = \Delta I_{u_1}.\eta_{PV}.Q_{PV} - T_{u_1}.rr_{fossil} \tag{7.4}$$

$$\Upsilon(u_2) = \Delta I_{u_2}.\eta_{PV}.Q_{PV} - T_{u_2}.rr_{fossil} \tag{7.5}$$

$$\Upsilon(u') = (1-\tau)\Upsilon(u_1) + \tau\Upsilon(u_2) \tag{7.6}$$

$$\Upsilon(u_2) \leqslant \Upsilon(u_1) \quad \Rightarrow \Upsilon(u') \leqslant \Upsilon(u_1) \tag{7.7}$$

$$\Upsilon(u_1) \leqslant \Upsilon(u_2) \quad \Rightarrow \Upsilon(u') \leqslant \Upsilon(u_2) \tag{7.8}$$

7.2 GGOV MODEL

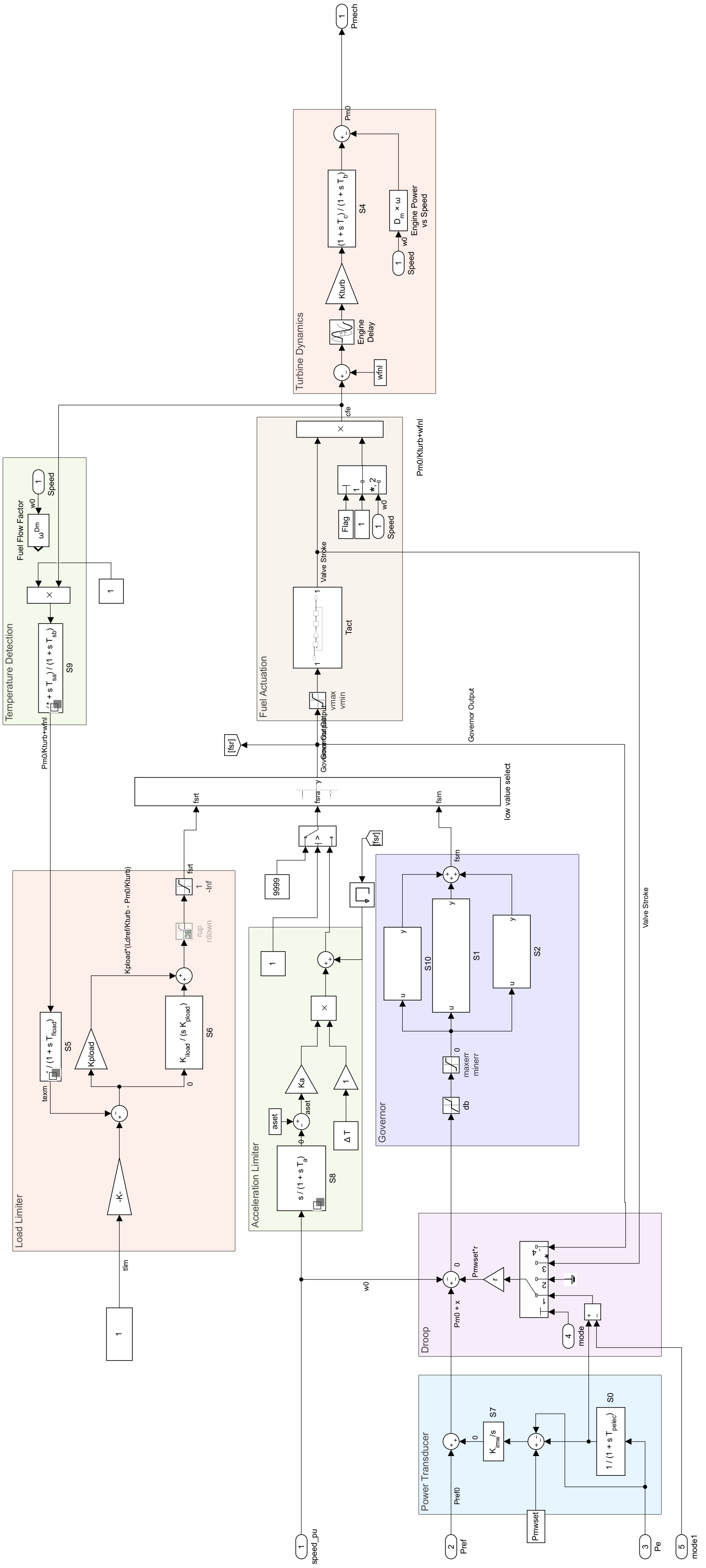

Figure 7.1: The GGOV Model

7.3 LISTS OF PARAMETERS FOR GT DETAILED ELECTRICAL MODELING

Name	Desciption	Unit	Value
Type	AVR Type	-	AC8C
Ts	Sample time (-1 for inherited)	-	0
R_C	Resistive component of load compensation	pu	0
X_C	Reactance component of load compensation	pu	0,04
T_R	Regulator input filter time constant	s	0,02
K_PR	Voltage regulator proportional gain	pu	36,3
K_IR	Voltage regulator integral gain	pu/s	15,58
K_DR	Voltage regulator derivative gain	pu*s	8,09
T_DR	Lag time constant for derivative channel of PID controller	s	0,3
V_{PIDmax}	Maximum voltage regulator output	pu	7,736
V_{PIDmin}	Minimum voltage regulator outputn	pu	0,1553
K_A	Rectifier bridge gain	pu	1
T_A	Rectifier bridge time constant	s	0
V_{Rmax}	Maximum regulator output	pu	12,243
V_{Rmin}	Minimum regulator output	pu	0
V_S	Alternate PSS input locations	-	Voltage error calculation
V_{OEL}	Alternate OEL input locations	-	Unused
V_{UEL}	Alternate UEL input locations	-	Unused
V_{SCL}	Alternate SCL input locations	-	Unused
K_E	Exciter field proportional constant, K_E	pu	1
T_E	Exciter field time constant, T_E	s	0,75
K_C	Rectifier loading factor proportional to commutating reactance, K_C	pu	0,79
K_D	Demagnetizing factor, function of exciter alternator reactances, K_D	pu	0,37
E_1	Exciter output voltage for saturation factor S_E(E_1), E_1	pu	6,6
$S_{E_E}1$	Exciter saturation factor at exciter output voltage	-	0,02
E_2	Exciter output voltage for saturation factor	pu	4,2
$S_{E_E}2$	Exciter saturation factor at exciter output voltage	-	0,02
V_{FEmax}	Maximum exciter field current,	pu	13,47
V_{Emin}	Minimum exciter output limit,	pu	0
K_P	Potential circuit gain coefficient,	pu	1
θ_P	Potential circuit phase angle (degrees)	degrees	0
K_I	Potential circuit (current) gain coefficient	pu	0
X_L	Reactance associated with potential source	pu	0
K_{C1}	Rectifier loading factor proportional to commutating reactance	pu	0
SW1	Logical switch 1	-	Position B: power source
V_{Bmax}	Maximum available exciter field voltage,	pu	1,25

Table 7.1: AVR AC7B data

Name	Description	Unit	Value
Type	Governor reference	-	GGOV1
Tpelec	Electrical Power Transducer Time Constant	s	1
Kpgov	Proportional Gain	-	5,3
Kigov	Integral Gain	-	1,9
Kdgov	Derivative Gain	-	4,9
Tdgov	Derivative Time Constant	s	1
minerr	Speed Error Limits Minimum value	pu	-0,2
maxerr	Speed Error Limits Maximum value	pu	0,2
vmin	Valve Limits Minimum value	pu	0,09
vmax	Valve Limits Maximum value	pu	0,689
r	Permanent droop	pu	0,1
rselect	Feedback for Droop	-	Electrical Power
Tact	Actuator Time Constant	s	0,2
Kturb	Turbine Gain	pu	1,999
wfnl	No Load Fuel Flow	pu	0,17
Tb	Lag Time Constant	s	0,1
Tc	Lead Time Constant	s	0
Teng	Transport Lag for Diesel	s	0
Flag	Fuel Source Characteristic	-	Fuel Flow Independent of Speed
Tfload	Time Constant	s	0
Kpload	Proportional Gain	-	10
Kiload	Integral Gain	-	0
Ldref	Load Limiter Reference Value	pu	2
Dm	Speed Sensitivity Coefficient	pu	0
rclose	Valve Closing Rates	pu/s	-3,3
ropen	Valve Opening Rates	pu/s	3,3
Kimw	Power Controller Gain	-	0
Pmwset	Power Controller Setpoint	MW	0
aset	Acceleration Limiter Setpoint	pu/s	1
Ka	Acceleration Limiter Gain	-	10
Ta	Acceleration Limiter Time Constant	s	0
db	Speed Governor Dead Band	pu	0
Tsa	Temperature Detection Lead	s	0
Tsb	Temperature Detection Lag	s	0
rdown	Load Limit Rates	pu	-1
rup	Load Limit Rates	pu	1
Tau	Algebraic Loop Time Constant	s	1,00E-06

Table 7.2: GGOV data

Name	Description	Unit	Value
Type	Machine reference	-	48.6MW 11kV
Sn	Rated apparent power	V*A	4,86E+07
Vn	Rated voltage	V	1,10E+04
fn	Rated electrical frequency	Hz	50
Xd	d-axis reactance	pu	1,5
Xd_{trans}	d-axis transient reactance	pu	0,476
$Xd_{subtrans}$	d-axis subtransient reactance	pu	0,263
Xq	q-axis reactance	pu	1,37
$Xq_{subtrans}$	q-axis subtransient reactance	pu	0,243
Xl	Stator leakage reactance	pu	0,031
Td_{trans}	d-axis transient short-circuit	s	4,349
$Td_{subtrans}$	d-axis subtransient short-circuit	s	0,031
$Tq_{subtrans}$	q-axis subtransient short-circuit	s	0,074
Rs	Stator resistance	pu	0,0042
M	Inertia constant	s*W/V/A	10,1
D	Per-unit damping coefficient	pu	0
p	Number of pole pairs	-	2

Table 7.3: Synchronous machine data

BIBLIOGRAPHY

[1] L Polleux, G Guerassimoff, JP Marmorat, J Sandoval-Moreno, and T Schuhler. "An overview of the challenges of solar power integration in isolated industrial microgrids with reliability constraints." In: *Renewable and Sustainable Energy Reviews* 155 (Mar. 1, 2022), p. 111955.

[2] UNG Assembly. "Political declaration of the high-level political forum on sustainable development convened under the auspices of the General Assembly." In: Sustainable Development Goals Summit. New York, Oct. 15, 2019.

[3] U Communications. *COP25 to Be the Launchpad for Significantly more Climate Ambition | UNFCCC*. Nov. 29, 2019. URL: `https://unfccc.int/news/cop25-to-be-the-launchpad-for-significantly-more-climate-ambition-0` (visited on 03/09/2020).

[4] UNDP. *What is the Multidimensional Poverty Index? | Human Development Reports*. URL: `http://hdr.undp.org/en/content/what-multidimensional-poverty-index` (visited on 03/10/2020).

[5] IEA. *Access to electricity – SDG7: Data and Projections – Analysis*. IEA. 2020. URL: `https://www.iea.org/reports/sdg7-data-and-projections/access-to-electricity` (visited on 12/19/2021).

[6] MS Alam, MD Miah, S Hammoudeh, and AK Tiwari. "The nexus between access to electricity and labour productivity in developing countries." In: *Energy Policy* 122 (Nov. 2018), pp. 715–726.

[7] P Alby, JJ Dethier, and S Straub. "Firms Operating under Electricity Constraints in Developing Countries." In: *The World Bank Economic Review* 27.1 (2013), pp. 109–132.

[8] H Allcott, A Collard-Wexler, and SD O'Connell. "How Do Electricity Shortages Affect Industry? Evidence from India." In: *American Economic Review* 106.3 (Mar. 2016), pp. 587–624.

[9] IEA. *Data & Statistics*. IEA. Library Catalog: www.iea.org. 2019. URL: `https://www.iea.org/data-and-statistics` (visited on 03/12/2020).

[10] IEA. *Africa Energy Outlook 2019 – Analysis*. IEA. 2019. URL: `https://www.iea.org/reports/africa-energy-outlook-2019` (visited on 03/09/2020).

[11] R Deshmukh, JP Carvallo, and A Gambhir. *Sustainable Development of Renewable Energy Mini-grids for Energy Access: A Framework for Policy Design*. LBNL–6222E, 1171612. Mar. 1, 2013, LBNL–6222E, 1171612.

[12] IRENA. *Policies and regulations for Renewable energy mini-grids*. Nov. 2018.

[13] N Hatziargyriou, ed. *Microgrids: architectures and control*. OCLC: 931500678. Chichester: Wiley-IEEE Press, 2014. 317 pp.

[14] G Guerassimoff and E du Mastère OSE. *Microgrids : pourquoi, pour qui ?* Développement durable 28. Presses des Mines, 2017.

[15] P Bornard. "Conduite d'un système de production-transport." In: *Techniques de l'ingénieur Réseaux électriques de transport et de répartition* base documentaire : TIB263DUO. (ref. article : d4080 2000).

[16] F Katiraei and M Iravani. "Power Management Strategies for a Microgrid With Multiple Distributed Generation Units." In: *IEEE Transactions on Power Systems* 21.4 (Nov. 2006), pp. 1821–1831.

[17] *Eigg Electric*. The Isle of Eigg. Library Catalog: isleofeigg.org. URL: `http://isleofeigg.org/eigg-electric/` (visited on 03/10/2020).

[18] B Lab. *UCSD | Building Microgrid*. Microgrids at Berkeley Lab. URL: `https://building-microgrid.lbl.gov/ucsd` (visited on 03/10/2020).

[19] A Roy. "Gestion optimale d'un système multi-sources pour un site isolé en mer." PhD thesis. Université Bretagne Loire, Dec. 2019.

[20] S Parhizi, H Lotfi, A Khodaei, and S Bahramirad. "State of the Art in Research on Microgrids: A Review." In: *IEEE Access* 3 (2015), pp. 890–925.

[21] A Hirsch, Y Parag, and J Guerrero. "Microgrids: A review of technologies, key drivers, and outstanding issues." In: *Renewable and Sustainable Energy Reviews* 90 (July 2018), pp. 402–411.

[22] R Rigo-Mariani. "Méthodes de conception intégrée "dimensionnement-gestion" par optimisation d'un microréseau avec stockage." PhD thesis. Université Toulouse, Dec. 2014.

[23] *World Energy Outlook 2018*. IEA, Nov. 13, 2018.

[24] IEA. *Tracking Industry*. Paris: IEA, May 2019.

[25] ARENA. *Weipa solar farm - Australian Renewable Energy Agency (ARENA)*. Australian Renewable Energy Agency. URL: `https://arena.gov.au/projects/weipa-solar-farm/` (visited on 04/23/2019).

[26] L Riboldi and L Nord. "Offshore Power Plants Integrating a Wind Farm: Design Optimisation and Techno-Economic Assessment Based on Surrogate Modelling." In: *Processes* 6.12 (Dec. 4, 2018), p. 249.

[27] ME Hamedani Golshan, MA Masoum, and SY Derakhshandeh. "Profit-based unit commitment with security constraints and fair allocation of cost saving in industrial microgrids." In: *IET Science, Measurement & Technology* 7.6 (Nov. 1, 2013), pp. 315–325.

[28] SM Nosratabadi, RA Hooshmand, E Gholipour, and S Rahimi. "Modeling and simulation of long term stochastic assessment in industrial microgrids proficiency considering renewable resources and load growth." In: *Simulation Modelling Practice and Theory* 75 (June 2017), pp. 77–95.

[29] M Soshinskaya, WHJ Crijns-Graus, J van der Meer, and JM Guerrero. "Application of a microgrid with renewables for a water treatment plant." In: *Applied Energy* 134 (Dec. 1, 2014), pp. 20–34.

[30] V Subramanyam, T Jin, and C Novoa. "Sizing a renewable microgrid for flow shop manufacturing using climate analytics." In: *Journal of Cleaner Production* 252 (Apr. 10, 2020), p. 119829.

[31] MA Cole, RJR Elliott, G Occhiali, and E Strobl. "Power outages and firm performance in Sub-Saharan Africa." In: *Journal of Development Economics* 134 (Sept. 1, 2018), pp. 150–159.

[32] HA Pasha, A Ghaus, and S Malik. "The economic cost of power outages in the industrial sector of Pakistan." In: *Energy Economics* 11.4 (Oct. 1, 1989), pp. 301–318.

[33] O Erdinc, NG Paterakis, and JPS Catalão. "Overview of insular power systems under increasing penetration of renewable energy sources: Opportunities and challenges." In: *Renewable and Sustainable Energy Reviews* 52 (Dec. 1, 2015), pp. 333–346.

[34] N Maïzi, V Mazauric, E Assoumou, S Bouckaert, V Krakowski, X Li, and P Wang. "Maximizing intermittency in 100% renewable and reliable power systems: A holistic approach applied to Reunion Island in 2030." In: *Applied Energy*. Transformative Innovations for a Sustainable Future – Part III 227 (Oct. 1, 2018), pp. 332–341.

[35] WW Anderson and OA Yakimenko. "Comparative analysis of two microgrid solutions for island green energy supply sustainability." In: *2017 IEEE 6th International Conference on Renewable Energy Research and Applications (ICRERA)*. 2017 IEEE 6th International Conference on Renewable Energy Research and Applications (ICRERA). ISSN: 2572-6013. Nov. 2017, pp. 245–250.

[36] S Favuzza, MG Ippolito, R Musca, M Navarro Navia, ER Sanseverino, G Zizzo, and M Bongiorno. "An Analysis of the Intertial Response of Small Isolated Power Systems in Presence of Generation from Renewable Energy Sources." In: *2018 IEEE 4th International Forum on Research and Technology for Society and Industry (RTSI)*. 2018 IEEE 4th International Forum on Research and Technology for Society and Industry (RTSI). Palermo: IEEE, Sept. 2018, pp. 1–6.

[37] KM Banjar-Nahor, L Garbuio, V Debusschere, N Hadjsaid, TTH Pham, and N Sinisuka. "Study on Renewable Penetration Limits in a Typical Indonesian Islanded Microgrid Considering the Impact of Variable Renewables Integration and the Empowering Flexibility on Grid Stability." In: *2018 IEEE PES Innovative Smart Grid Technologies Conference Europe (ISGT-Europe)*. 2018 IEEE PES Innovative Smart Grid Technologies Conference Europe (ISGT-Europe). Sarajevo, Bosnia and Herzegovina: IEEE, Oct. 2018, pp. 1–6.

[38] IRENA. "Innovation Outlook: Renewable: Mini-grids." In: (2016), p. 184.

[39] X Liang. "Emerging Power Quality Challenges Due to Integration of Renewable Energy Sources." In: *IEEE Transactions on Industry Applications* 53.2 (Mar. 2017). Conference Name: IEEE Transactions on Industry Applications, pp. 855–866.

[40] Aria. *Base Aria : Perturbation d'alimentation électrique*. Ministère du Développement Durable, 2009, p. 6.

[41] M Krasich. "How to estimate and use MTTF/MTBF would the real MTBF please stand up?" In: *2009 Annual Reliability and Maintainability Symposium*. 2009 Annual Reliability and Maintainability Symposium. ISSN: 0149-144X. Jan. 2009, pp. 353–359.

[42] "IEEE Recommended Practice for the Design of Reliable Industrial and Commercial Power Systems." In: *IEEE Std 493-2007 (Revision of IEEE Std 493-1997)* (June 2007). Conference Name: IEEE Std 493-2007 (Revision of IEEE Std 493-1997), pp. 1–383.

[43] RTE. *Documentation Technique de Référence, Article 3.1- Plages de tension et de réquence normales et exceptionnelles*. Aug. 3, 2020.

[44] MS Masnadi et al. "Global carbon intensity of crude oil production." In: *Science* 361.6405 (Aug. 31, 2018), pp. 851–853.

[45] OGCI. *A report from the Oil and Gas Climate Initiative*. Sept. 2018, p. 60.

[46] Equinor. *Enova supporting pioneer project - equinor.com*. Aug. 10, 2021. URL: `https://www.equinor.com/en/news/enova-supporting-pioneer-project.html` (visited on 01/03/2022).

[47] E Alves, S Sanchez, D Brandao, and E Tedeschi. “Smart Load Management with Energy Storage for Power Quality Enhancement in Wind-Powered Oil and Gas Applications.” In: *Energies* 12.15 (Aug. 2, 2019), p. 2985.

[48] J Wang, J O’Donnell, and AR Brandt. “Potential solar energy use in the global petroleum sector.” In: *Energy* 118 (Jan. 1, 2017), pp. 884–892.

[49] M Absi Halabi, A Al-Qattan, and A Al-Otaibi. “Application of solar energy in the oil industry—Current status and future prospects.” In: *Renewable and Sustainable Energy Reviews* 43 (Mar. 1, 2015), pp. 296–314.

[50] AR Ardal, K Sharifabadi, O Bergvoll, and V Berge. “Challenges with integration and operation of offshore oil & gas platforms connected to an offshore wind power plant.” In: *2014 Petroleum and Chemical Industry Conference Europe*. 2014 Petroleum and Chemical Industry Conference Europe (PCIC Europe). Amsterdam, Netherlands: IEEE, June 2014, pp. 1–9.

[51] L Bigarelli, A Lidozzi, M di Benedetto, L Solero, and S Bifaretti. “Model Predictive Energy Management for Sustainable Off-Shore Oil and Gas Platforms.” In: *2019 21st European Conference on Power Electronics and Applications (EPE ’19 ECCE Europe)*. 2019 21st European Conference on Power Electronics and Applications (EPE ’19 ECCE Europe). Genova, Italy: IEEE, Sept. 2019, P.1–P.10.

[52] D Hu, X Zhao, Xu Cai, and Jianfeng Wang. “Impact of wind power on stability of offshore platform power systems.” In: *2008 Third International Conference on Electric Utility Deregulation and Restructuring and Power Technologies*. 2008 Third International Conference on Electric Utility Deregulation and Restructuring and Power Technologies. Nanjing, China: IEEE, Apr. 2008, pp. 1688–1692.

[53] AR Årdal, S D’Arco, RE Torres-Olguin, T Undeland, and K Shrarifabadi. “Parametric sensitivity of transients in an islanded system with an offshore wind farm connected to an oil platform.” In: (), p. 10.

[54] N Anglani, SRD Salvo, G Oriti, and AL Julian. “Renewable Energy Sources and Storage Integration in Offshore Microgrids.” In: *2020 IEEE International Conference on Environment and Electrical Engineering and 2020 IEEE Industrial and Commercial Power Systems Europe (EEEIC / I CPS Europe)*. 2020 IEEE International Conference on Environment and Electrical Engineering and 2020 IEEE Industrial and Commercial Power Systems Europe (EEEIC / I CPS Europe). June 2020, pp. 1–6.

[55] E Global. *ETN R&D recommendation report*. ETN Global, Oct. 2018.

[56] Warstila. *Combustion Engine vs Gas Turbine: Ramp Rate*. 2019.

[57] HIH Saravanamuttoo, H Cohen, and GFC Rogers. *Gas turbine theory*. OCLC: 476334045. Harlow: Prentice Hall, 2001.

[58] AMY Razak. *Industrial gas turbines: performance and operability*. Woodhead Publishing in mechanical engineering. OCLC: 255544738. Boca Raton, Fla.: CRC Press [u.a.], 2007. 602 pp.

[59] P Jansohn. *Modern gas turbine systems: high efficiency, low emission, fuel flexible power generation*. OCLC: 957507212. 2016.

[60] Thermoflow. *Thermoflow, Inc. (Home)*. URL: https://www.thermoflow.com/ (visited on 04/23/2019).

[61] EA EA Internacional. *EcosimPro | PROOSIS Modelling and Simulation Software*. EcosimPro | PROOSIS. URL: https://www.ecosimpro.com/ (visited on 04/23/2019).

[62] F Alobaid, N Mertens, R Starkloff, T Lanz, C Heinze, and B Epple. "Progress in dynamic simulation of thermal power plants." In: *Progress in Energy and Combustion Science* 59 (Mar. 2017), pp. 79–162.

[63] A Mehrpanahi, A Hamidavi, and A Ghorbanifar. "A novel dynamic modeling of an industrial gas turbine using condition monitoring data." In: *Applied Thermal Engineering* 143 (Oct. 2018), pp. 507–520.

[64] SK Yee, JV Milanovic, and FM Hughes. "Overview and Comparative Analysis of Gas Turbine Models for System Stability Studies." In: *IEEE Transactions on Power Systems* 23.1 (Feb. 2008), pp. 108–118.

[65] E Tsoutsanis and N Meskin. "Dynamic performance simulation and control of gas turbines used for hybrid gas/wind energy applications." In: *Applied Thermal Engineering* 147 (Jan. 2019), pp. 122–142.

[66] A Chaibakhsh and S Amirkhani. "A simulation model for transient behaviour of heavy-duty gas turbines." In: *Applied Thermal Engineering* 132 (Mar. 2018), pp. 115–127.

[67] E Tsoutsanis, N Meskin, M Benammar, and K Khorasani. "Dynamic Performance Simulation of an Aeroderivative Gas Turbine Using the Matlab Simulink Environment." In: *Volume 4A: Dynamics, Vibration and Control*. ASME 2013 International Mechanical Engineering Congress and Exposition. San Diego, California, USA: ASME, Nov. 15, 2013, V04AT04A050.

[68] E Tsoutsanis, M Hamadache, and R Dixon. “Real-Time Diagnostic Method of Gas Turbines Operating Under Transient Conditions in Hybrid Power Plants.” In: *Journal of Engineering for Gas Turbines and Power* 142.10 (Oct. 1, 2020), p. 101002.

[69] J Blondeau and J Mertens. “Impact of intermittent renewable energy production on specific CO2 and NO emissions from large scale gas-fired combined cycles.” In: *Journal of Cleaner Production* 221 (June 2019), pp. 261–270.

[70] G Sujesh and S Ramesh. “Modeling and control of diesel engines: A systematic review.” In: *Alexandria Engineering Journal* 57.4 (Dec. 2018), pp. 4033–4048.

[71] LLJ Mahon. *Diesel generator handbook*. Oxford ; Boston: Butterworth-Heinemann, 1992. 646 pp.

[72] JB Heywood. *Internal combustion engine fundamentals*. McGraw-Hill series in mechanical engineering. New York: McGraw-Hill, 1988. 930 pp.

[73] W Finland. “Wärtsilä 32 Product guide.” In: (2018), p. 284.

[74] L Guzzella and CH Onder. “Introduction to Modeling and Control of Internal Combustion Engine Systems.” In: (), p. 362.

[75] Rakopoulos, Constantine, Giakoumis, and Evangelos. *Diesel Engine Transient Operation : principles of operation and simulation analysis*. Springer-Verlag London, 2009.

[76] H Bastida, CE Ugalde-Loo, and M Abeysekera. “Dynamic Modelling and Control of a Reciprocating Engine.” In: *Energy Procedia* 142 (Dec. 2017), pp. 1282–1287.

[77] A Kuznetsov, S Kharitonov, and V Ryzhov. “Experimental and Calculation Study of Diesel-Generator Performance in Transient Conditions.” In: *Journal of Engineering for Gas Turbines and Power* 140.12 (Oct. 24, 2018), p. 121009.

[78] E Semshchikov, J Hamilton, L Wu, M Negnevitsky, X Wang, and S Lyden. “Frequency control within high renewable penetration hybrid systems adopting low load diesel methodologies.” In: *Energy Procedia* 160 (Feb. 2019), pp. 483–490.

[79] G Stavrakakis and G Kariniotakis. “A general simulation algorithm for the accurate assessment of isolated diesel-wind turbines systems interaction. I. A general multimachine power system model.” In: *IEEE Transactions on Energy Conversion* 10.3 (Sept. 1995), pp. 577–583.

[80] M Yu, X Tang, Y Lin, and X Wang. “Diesel engine modeling based on recurrent neural networks for a hardware-in-the-loop simulation system of diesel generator sets.” In: *Neurocomputing* 283 (Mar. 2018), pp. 9–19.

[81] D Nikolic, M Negnevitsky, and M de Groot. “Effect of the diesel engine delay on stability of isolated power systems with high levels of renewable energy penetration.” In: *2015 International Symposium on Smart Electric Distribution Systems and Technologies (EDST)*. 2015 International Symposium on Smart Electric Distribution Systems and Technologies (EDST). Vienna, Austria: IEEE, Sept. 2015, pp. 70–73.

[82] J Hamilton, M Negnevitsky, and X Wang. “The potential of variable speed diesel application in increasing renewable energy source penetration.” In: *Energy Procedia* 160 (Feb. 2019), pp. 558–565.

[83] J Hamilton, M Negnevitsky, X Wang, and S Lyden. “High penetration renewable generation within Australian isolated and remote power systems.” In: *Energy* 168 (Feb. 2019), pp. 684–692.

[84] J Hamilton, A Tavakoli, M Negnevitsky, and X Wang. “Investigation of no load diesel technology in isolated power systems.” In: *2016 IEEE Power and Energy Society General Meeting (PESGM)*. 2016 IEEE Power and Energy Society General Meeting (PESGM). Boston, MA, USA: IEEE, July 2016, pp. 1–5.

[85] A Benato, S Bracco, A Stoppato, and A Mirandola. “LTE: A procedure to predict power plants dynamic behaviour and components lifetime reduction during transient operation.” In: *Applied Energy* 162 (Jan. 2016), pp. 880–891.

[86] H Energy. *HOMER - Hybrid Renewable and Distributed Generation System Design Software*. URL: `https://www.homerenergy.com/` (visited on 03/19/2019).

[87] A Dobos. *PVWatts Version 5 Manual*. NREL/TP-6A20-62641, 1158421. Sept. 1, 2014, NREL/TP–6A20–62641, 1158421.

[88] GN Tiwari, AK Tiwari, and Shyam. *Handbook of Solar Energy: Theory, Analysis and Applications*. Energy Systems in Electrical Engineering. OCLC: 959403981. Singapore: Springer Singapore, 2016. 764 pp.

[89] M Sengupta and A Andreas. *Oahu Solar Measurement Grid (1-Year Archive): 1-Second Solar Irradiance; Oahu, Hawaii (Data)*. type: dataset. 2010.

[90] J Stein, C Hansen, and MJ Reno. *The variability index: A new and novel metric for quantifying irradiance and PV output variability*. Sandia National Laboratories, 2012.

[91] R Blaga and M Paulescu. “Quantifiers for the solar irradiance variability: A new perspective.” In: *Solar Energy* 174 (Nov. 2018), pp. 606–616.

[92] M Lave. “Solar variability zones: Satellite-derived zones that represent high-frequency ground variability.” In: *Solar Energy* (2017), p. 10.

[93] P Lauret, R Perez, L Mazorra Aguiar, E Tapachès, HM Diagne, and M David. “Characterization of the intraday variability regime of solar irradiation of climatically distinct locations.” In: *Solar Energy* 125 (Feb. 1, 2016), pp. 99–110.

[94] A Mills et al. “Dark Shadows.” In: *IEEE Power and Energy Magazine* 9.3 (May 2011), pp. 33–41.

[95] D Cormode, AD Cronin, W Richardson, AT Lorenzo, AE Brooks, and DN DellaGiustina. “Comparing ramp rates from large and small PV systems, and selection of batteries for ramp rate control.” In: *2013 IEEE 39th Photovoltaic Specialists Conference (PVSC)*. 2013 IEEE 39th Photovoltaic Specialists Conference (PVSC). Tampa, FL, USA: IEEE, June 2013, pp. 1805–1810.

[96] J Marcos, L Marroyo, E Lorenzo, D Alvira, and E Izco. “From irradiance to output power fluctuations: the PV plant as a low pass filter.” In: *Progress in Photovoltaics: Research and Applications* 19.5 (2011). _eprint: https://onlinelibrary.wiley.com/doi/pdf/10.1002/pip.1063, pp. 505–510.

[97] TE Hoff and R Perez. “Quantifying PV power Output Variability.” In: *Solar Energy* 84.10 (Oct. 1, 2010), pp. 1782–1793.

[98] M Lave, J Kleissl, and JS Stein. “A Wavelet-Based Variability Model (WVM) for Solar PV Power Plants.” In: *IEEE Transactions on Sustainable Energy* 4.2 (Apr. 2013). Conference Name: IEEE Transactions on Sustainable Energy, pp. 501–509.

[99] S University. *PV Performance Modeling Collaborative | Wavelet Variability Model*. Library Catalog: pvpmc.sandia.gov. 2012. URL: `https://pvpmc.sandia.gov/applications/wavelet-variability-model/` (visited on 03/23/2020).

[100] JM Bright, CJ Smith, PG Taylor, and R Crook. “Stochastic generation of synthetic minutely irradiance time series derived from mean hourly weather observation data.” In: *Solar Energy* 115 (May 1, 2015), pp. 229–242.

[101] CM Fernández-Peruchena and M Gastón. “A simple and efficient procedure for increasing the temporal resolution of global horizontal solar irradiance series.” In: *Renewable Energy* 86 (Feb. 1, 2016), pp. 375–383.

[102] W Zhang, W Kleiber, AR Florita, BM Hodge, and B Mather. “Modeling and Simulation of High-Frequency Solar Irradiance.” In: *IEEE Journal of Photovoltaics* 9.1 (Jan. 2019). Conference Name: IEEE Journal of Photovoltaics, pp. 124–131.

[103] A Ahmed and M Khalid. “A review on the selected applications of forecasting models in renewable power systems.” In: *Renewable and Sustainable Energy Reviews* 100 (Feb. 2019), pp. 9–21.

[104] E Cirés, J Marcos, I de la Parra, M García, and L Marroyo. “The potential of forecasting in reducing the LCOE in PV plants under ramp-rate restrictions.” In: *Energy* 188 (Dec. 1, 2019), p. 116053.

[105] J Antonanzas, N Osorio, R Escobar, R Urraca, FJ Martinez-de Pison, and F Antonanzas-Torres. “Review of photovoltaic power forecasting.” In: *Solar Energy* 136 (Oct. 15, 2016), pp. 78–111.

[106] L Vallance. “Synergie des mesures pyranométriques et des images hémisphériques in-situ avec des images satellites météorologiques pour la prévision photovoltaïque.” PhD thesis. PSL Research University, Nov. 9, 2018.

[107] K Lappalainen, GC Wang, and J Kleissl. “Estimation of the largest expected photovoltaic power ramp rates.” In: *Applied Energy* 278 (Nov. 15, 2020), p. 115636.

[108] S Pro. *HelioClim-3 Real Time and Forecast - www.soda-pro.com*. URL: `http://www.soda-pro.com/fr/web-services/radiation/helioclim-3-real-time-and-forecast` (visited on 01/27/2020).

[109] M Abuella and B Chowdhury. “Forecasting of solar power ramp events: A post-processing approach.” In: *Renewable Energy* 133 (Apr. 2019), pp. 1380–1392.

[110] P Mathiesen, D Rife, and C Collier. “Forecasting solar irradiance variability using the analog method.” In: *2016 IEEE 43rd Photovoltaic Specialists Conference (PVSC)*. 2016 IEEE 43rd Photovoltaic Specialists Conference (PVSC). June 2016, pp. 1207–1211.

[111] J Huang and RJ Davy. “Predicting intra-hour variability of solar irradiance using hourly local weather forecasts.” In: *Solar Energy* 139 (Dec. 1, 2016), pp. 633–639.

[112] Y Chu, HTC Pedro, M Li, and CFM Coimbra. “Real-time forecasting of solar irradiance ramps with smart image processing.” In: *Solar Energy* 114 (Apr. 1, 2015), pp. 91–104.

[113] C Gauchet, P Blanc, B Espinar, B Charbonnier, and D Demengel. “Surface solar irradiance estimation with low-cost fish-eye camera.” In: (2012), p. 5.

[114] P Zhang, W Li, S Li, Y Wang, and W Xiao. “Reliability assessment of photovoltaic power systems: Review of current status and future perspectives.” In: *Applied Energy* 104 (Apr. 1, 2013), pp. 822–833.

[115] A Sangwongwanich, Y Yang, D Sera, F Blaabjerg, and D Zhou. "On the Impacts of PV Array Sizing on the Inverter Reliability and Lifetime." In: *IEEE Transactions on Industry Applications* 54.4 (July 2018). Conference Name: IEEE Transactions on Industry Applications, pp. 3656–3667.

[116] M Faisal, MA Hannan, PJ Ker, A Hussain, MB Mansor, and F Blaabjerg. "Review of Energy Storage System Technologies in Microgrid Applications: Issues and Challenges." In: *IEEE Access* 6 (2018). Conference Name: IEEE Access, pp. 35143–35164.

[117] O Krishan and S Suhag. "An updated review of energy storage systems: Classification and applications in distributed generation power systems incorporating renewable energy resources." In: *International Journal of Energy Research* 43.12 (2019). _eprint: https://onlinelibrary.wiley.com/doi/pdf/10.1002/er.4285, pp. 6171–6210.

[118] PD Lund, J Lindgren, J Mikkola, and J Salpakari. "Review of energy system flexibility measures to enable high levels of variable renewable electricity." In: *Renewable and Sustainable Energy Reviews* 45 (May 1, 2015), pp. 785–807.

[119] Neoen Australia. *HPR fully installed and energised ! – Hornsdale Power Reserve*. Library Catalog: hornsdalepowerreserve.com.au. Nov. 28, 2019. URL: `https://hornsdalepowerreserve.com.au/hpr-fully-installed-and-energised/` (visited on 04/28/2020).

[120] H Hesse, M Schimpe, D Kucevic, and A Jossen. "Lithium-Ion Battery Storage for the Grid—A Review of Stationary Battery Storage System Design Tailored for Applications in Modern Power Grids." In: *Energies* 10.12 (Dec. 11, 2017), p. 2107.

[121] AAK Arani, H Karami, GB Gharehpetian, and MSA Hejazi. "Review of Flywheel Energy Storage Systems structures and applications in power systems and microgrids." In: *Renewable and Sustainable Energy Reviews* 69 (Mar. 1, 2017), pp. 9–18.

[122] MAM Ramli, A Hiendro, and S Twaha. "Economic analysis of PV/diesel hybrid system with flywheel energy storage." In: *Renewable Energy* 78 (June 1, 2015), pp. 398–405.

[123] HF Habib, AAS Mohamed, M El Hariri, and OA Mohammed. "Utilizing supercapacitors for resiliency enhancements and adaptive microgrid protection against communication failures." In: *Electric Power Systems Research* 145 (Apr. 1, 2017), pp. 223–233.

[124] U Akram, M Khalid, and S Shafiq. "An Innovative Hybrid Wind-Solar and Battery-Supercapacitor Microgrid System—Development and Optimization." In: *IEEE Access* 5 (2017). Conference Name: IEEE Access, pp. 25897–25912.

[125] E Mohammadi, R Rasoulinezhad, and G Moschopoulos. "Using a Supercapacitor to Mitigate Battery Microcycles Due to Wind Shear and Tower Shadow Effects in Wind-Diesel Microgrids." In: *IEEE Transactions on Smart Grid* 11.5 (Sept. 2020). Conference Name: IEEE Transactions on Smart Grid, pp. 3677–3689.

[126] PS Kundur. *Power system stability and control*. Ed. by NJ Balu and MG Lauby. Indian edition. The EPRI power system engineering series. OCLC: 636758162. Mc Graw Hill Education (India) Private Limited, 1994. 1176 pp.

[127] T shift project. *Power Systems 2050 – Power System operation V1.1*. Feb. 2020.

[128] IRENA. *Planning for the renewable future : Long-term modelling and tools to expand variable renewable power in emerging economies*. OCLC: 1054400681. Abu Dhabi: International Renewable Energy Agency (IRENA), 2017.

[129] JL Fraisse and L Karsenti. "Raccordement de la production décentralisée aux réseaux de distribution - Conditions d'intégration." In: (2014), p. 41.

[130] FM Uriarte, C Smith, S VanBroekhoven, and RE Hebner. "Microgrid Ramp Rates and the Inertial Stability Margin." In: *IEEE Transactions on Power Systems* 30.6 (Nov. 2015), pp. 3209–3216.

[131] DE Olivares et al. "Trends in Microgrid Control." In: *IEEE Transactions on Smart Grid* 5.4 (July 2014), pp. 1905–1919.

[132] N Soni, S Doolla, and MC Chandorkar. "Improvement of Transient Response in Microgrids Using Virtual Inertia." In: *IEEE Transactions on Power Delivery* 28.3 (July 2013). Conference Name: IEEE Transactions on Power Delivery, pp. 1830–1838.

[133] JM Guerrero, JC Vasquez, J Matas, LG de Vicuna, and M Castilla. "Hierarchical Control of Droop-Controlled AC and DC Microgrids—A General Approach Toward Standardization." In: *IEEE Transactions on Industrial Electronics* 58.1 (Jan. 2011), pp. 158–172.

[134] UB Tayab, MAB Roslan, LJ Hwai, and M Kashif. "A review of droop control techniques for microgrid." In: *Renewable and Sustainable Energy Reviews* 76 (Sept. 1, 2017), pp. 717–727.

[135] CC Arteaga. "Optimisation of power system security with high share of variable renewables: Consideration of the primary reserve deployment dynamics on a Frequency Constrained Unit Commitment model." Thèse de doctorat. Paris, France: Univertié Paris-Saclay, Mar. 10, 2016. 282 pp.

[136] F Katiraei, K Mauch, M Vandenbergh, and L Arribas. *PV Hybrid Mini-Grids: Applicable Control Methods for Various Situations*. IEA, 2012, p. 104.

[137] T Morstyn, B Hredzak, and VG Agelidis. "Control Strategies for Microgrids With Distributed Energy Storage Systems: An Overview." In: *IEEE Transactions on Smart Grid* 9.4 (July 2018). Conference Name: IEEE Transactions on Smart Grid, pp. 3652–3666.

[138] J Li, R Xiong, Q Yang, F Liang, M Zhang, and W Yuan. "Design/test of a hybrid energy storage system for primary frequency control using a dynamic droop method in an isolated microgrid power system." In: *Applied Energy* 201 (Sept. 1, 2017), pp. 257–269.

[139] I Serban and C Marinescu. "Control Strategy of Three-Phase Battery Energy Storage Systems for Frequency Support in Microgrids and with Uninterrupted Supply of Local Loads." In: *IEEE Transactions on Power Electronics* 29.9 (Sept. 2014). Conference Name: IEEE Transactions on Power Electronics, pp. 5010–5020.

[140] M Toge, Y Kurita, and S Iwamoto. "Supplementary load frequency control with storage battery operation considering SOC under large-scale wind power penetration." In: *2013 IEEE Power & Energy Society General Meeting*. 2013 IEEE Power & Energy Society General Meeting. Vancouver, BC: IEEE, 2013, pp. 1–5.

[141] GO Suvire, MG Molina, and PE Mercado. "Improving the Integration of Wind Power Generation Into AC Microgrids Using Flywheel Energy Storage." In: *IEEE Transactions on Smart Grid* 3.4 (Dec. 2012). Conference Name: IEEE Transactions on Smart Grid, pp. 1945–1954.

[142] C Abbey and G Joos. "Supercapacitor Energy Storage for Wind Energy Applications." In: *IEEE Transactions on Industry Applications* 43.3 (May 2007). Conference Name: IEEE Transactions on Industry Applications, pp. 769–776.

[143] W Gu, W Liu, C Shen, and Z Wu. "Multi-stage underfrequency load shedding for islanded microgrid with equivalent inertia constant analysis." In: *International Journal of Electrical Power & Energy Systems* 46 (Mar. 2013), pp. 36–39.

[144] M Hajiakbari Fini and ME Hamedani Golshan. "Frequency control using loads and generators capacity in power systems with a high penetration of renewables." In: *Electric Power Systems Research* 166 (Jan. 2019), pp. 43–51.

[145] A Arif, Z Wang, J Wang, B Mather, H Bashualdo, and D Zhao. "Load Modeling—A Review." In: *IEEE Transactions on Smart Grid* 9.6 (Nov. 2018). Conference Name: IEEE Transactions on Smart Grid, pp. 5986–5999.

[146] M Dreidy, H Mokhlis, and S Mekhilef. “Inertia response and frequency control techniques for renewable energy sources: A review.” In: *Renewable and Sustainable Energy Reviews* 69 (Mar. 1, 2017), pp. 144–155.

[147] A Hoke and D Maksimović. “Active power control of photovoltaic power systems.” In: *2013 1st IEEE Conference on Technologies for Sustainability (SusTech)*. 2013 1st IEEE Conference on Technologies for Sustainability (SusTech). Aug. 2013, pp. 70–77.

[148] G Dickeson, L McLeod, A Dobb, L Frearson, B Herteleer, and D Scheltus. “RAMP RATE CONTROL FOR PV PLANT INTEGRATION: EXPERIENCE FROM KARRATHA AIRPORT’S HYBRID POWER STATION.” In: (), p. 6.

[149] J Matevosyan et al. “Grid-Forming Inverters: Are They the Key for High Renewable Penetration?” In: *IEEE Power and Energy Magazine* 17.6 (Nov. 2019). Conference Name: IEEE Power and Energy Magazine, pp. 89–98.

[150] S Sasmono, J Chandra, A Wijaya, and N Hariyanto. “Transient Stability Method to Determine Maximum Intermittent Power Plant Penetration to Small Island Isolated System.” In: *2018 IEEE PES Asia-Pacific Power and Energy Engineering Conference (APPEEC)*. 2018 IEEE PES Asia-Pacific Power and Energy Engineering Conference (APPEEC). Kota Kinabalu: IEEE, Oct. 2018, pp. 498–501.

[151] R Rossi and MAS Masoum. “Application of swing equation and equal area criteria to determine maximum penetration of wind generation in an islanded network.” In: *2013 Australasian Universities Power Engineering Conference (AUPEC)*. 2013 Australasian Universities Power Engineering Conference (AUPEC). Hobart, Australia: IEEE, Sept. 2013, pp. 1–8.

[152] MC Magro, M Giannettoni, P Pinceti, and M Vanti. “Real time simulator for microgrids.” In: *Electric Power Systems Research* 160 (July 2018), pp. 381–396.

[153] L Polleux, J Sandoval-Moreno, G Guerassimoff, and JP Marmorat. “Impact of thermal generation flexibility on power quality and LCOE of industrial off-grid power plants.” In: *Proceedings of 11th International Conference on Applied Energy, Part 2*. Vol. 3. Västeraas, Sweden, Aug. 2019.

[154] MF Zia, E Elbouchikhi, and M Benbouzid. “Microgrids energy management systems: A critical review on methods, solutions, and prospects.” In: *Applied Energy* 222 (July 2018), pp. 1033–1055.

[155] A Ahmad Khan, M Naeem, M Iqbal, S Qaisar, and A Anpalagan. "A compendium of optimization objectives, constraints, tools and algorithms for energy management in microgrids." In: *Renewable and Sustainable Energy Reviews* 58 (May 2016), pp. 1664–1683.

[156] A Zakaria, FB Ismail, MSH Lipu, and MA Hannan. "Uncertainty models for stochastic optimization in renewable energy applications." In: *Renewable Energy* 145 (Jan. 1, 2020), pp. 1543–1571.

[157] JD Lara, DE Olivares, and CA Cañizares. "Robust Energy Management of Isolated Microgrids." In: *IEEE Systems Journal* 13.1 (Mar. 2019). Conference Name: IEEE Systems Journal, pp. 680–691.

[158] A Mohammed, J Pasupuleti, T Khatib, and W Elmenreich. "A review of process and operational system control of hybrid photovoltaic/diesel generator systems." In: *Renewable and Sustainable Energy Reviews* 44 (Apr. 2015), pp. 436–446.

[159] H Kanchev, D Lu, F Colas, V Lazarov, and B Francois. "Energy Management and Operational Planning of a Microgrid With a PV-Based Active Generator for Smart Grid Applications." In: *IEEE Transactions on Industrial Electronics* 58.10 (Oct. 2011). Conference Name: IEEE Transactions on Industrial Electronics, pp. 4583–4592.

[160] A Chaouachi, RM Kamel, R Andoulsi, and K Nagasaka. "Multiobjective Intelligent Energy Management for a Microgrid." In: *IEEE Transactions on Industrial Electronics* 60.4 (Apr. 2013). Conference Name: IEEE Transactions on Industrial Electronics, pp. 1688–1699.

[161] A Askarzadeh. "A Memory-Based Genetic Algorithm for Optimization of Power Generation in a Microgrid." In: *IEEE Transactions on Sustainable Energy* 9.3 (July 2018). Conference Name: IEEE Transactions on Sustainable Energy, pp. 1081–1089.

[162] A Maulik and D Das. "Optimal operation of microgrid using four different optimization techniques." In: *Sustainable Energy Technologies and Assessments* 21 (June 1, 2017), pp. 100–120.

[163] M Marzband, F Azarinejadian, M Savaghebi, and JM Guerrero. "An Optimal Energy Management System for Islanded Microgrids Based on Multiperiod Artificial Bee Colony Combined With Markov Chain." In: *IEEE Systems Journal* 11.3 (Sept. 2017). Conference Name: IEEE Systems Journal, pp. 1712–1722.

[164] C Ju, P Wang, L Goel, and Y Xu. "A Two-Layer Energy Management System for Microgrids With Hybrid Energy Storage Considering Degradation Costs." In: *IEEE Transactions on Smart*

Grid 9.6 (Nov. 2018). Conference Name: IEEE Transactions on Smart Grid, pp. 6047–6057.

[165] M Mohiti, M Mazidi, AA Moghaddam, and JM Guerrero. "Microgrid optimal energy and reserve scheduling considering frequency constraints." In: *2019 International Conference on Smart Energy Systems and Technologies (SEST)*. Sept. 2019, pp. 1–6.

[166] A N'Goran, B Daugrois, M Lotteau, and S Demassey. "Optimal engagement and operation of a grid-connected PV/battery system." In: *2019 IEEE PES Innovative Smart Grid Technologies Europe (ISGT-Europe)*. 2019 IEEE PES Innovative Smart Grid Technologies Europe (ISGT-Europe). Sept. 2019, pp. 1–5.

[167] DE Olivares, CA Canizares, and M Kazerani. "A Centralized Energy Management System for Isolated Microgrids." In: *IEEE Transactions on Smart Grid* 5.4 (July 2014), pp. 1864–1875.

[168] N Rezaei and M Kalantar. "Economic–environmental hierarchical frequency management of a droop-controlled islanded microgrid." In: *Energy Conversion and Management* 88 (Dec. 2014), pp. 498–515.

[169] SR Cominesi, AL Bella, M Farina, and R Scattolini. "A multilayer control scheme for microgrid energy management." In: *IFAC-PapersOnLine*. IFAC Workshop on Control of Transmission and Distribution Smart Grids CTDSG 2016 49.27 (Jan. 1, 2016), pp. 256–261.

[170] S Cominesi, M Farina, L Giulioni, B Picasso, and R Scattolini. "A Two-Layer Stochastic Model Predictive Control Scheme for Microgrids." In: *IEEE Transactions on Control Systems Technology* 26.1 (Jan. 2018), pp. 1–13.

[171] J Hu, Y Shan, JM Guerrero, A Ioinovici, KW Chan, and J Rodriguez. "Model predictive control of microgrids – An overview." In: *Renewable and Sustainable Energy Reviews* 136 (Feb. 1, 2021), p. 110422.

[172] E Mayhorn, W Zhang, S Lu, and N Samaan. "Optimal Control of Distributed Energy Resources using Model Predictive Control." In: *IEEE Power and Energy Society General Meeting* (2012), p. 8.

[173] L Moretti, S Polimeni, L Meraldi, P Raboni, S Leva, and G Manzolini. "Assessing the impact of a two-layer predictive dispatch algorithm on design and operation of off-grid hybrid microgrids." In: *Renewable Energy* 143 (Dec. 1, 2019), pp. 1439–1453.

[174] B Wang. "Intelligent control and power flow optimization of microgrid." PhD thesis. Université de Technologie de Compiègne, 2013.

[175] S Mashayekh and KL Butler-Purry. “An Integrated Security-Constrained Model-Based Dynamic Power Management Approach for Isolated Microgrids in All-Electric Ships.” In: *IEEE Transactions on Power Systems* 30.6 (Nov. 2015). Conference Name: IEEE Transactions on Power Systems, pp. 2934–2945.

[176] MA Fotouhi Ghazvini, H Morais, and Z Vale. “Coordination between mid-term maintenance outage decisions and short-term security-constrained scheduling in smart distribution systems.” In: *Applied Energy*. Smart Grids 96 (Aug. 1, 2012), pp. 281–291.

[177] D Rebollal, M Chinchilla, D Santos-Martín, and JM Guerrero. “Endogenous Approach of a Frequency-Constrained Unit Commitment in Islanded Microgrid Systems.” In: *Energies* 14.19 (Jan. 2021). Number: 19 Publisher: Multidisciplinary Digital Publishing Institute, p. 6290.

[178] Y Yin, T Liu, L Wu, C He, and Y Liu. “Frequency-constrained multi-source power system scheduling against N-1 contingency and renewable uncertainty.” In: *Energy* 216 (Feb. 1, 2021), p. 119296.

[179] Y Wen, W Li, G Huang, and X Liu. “Frequency Dynamics Constrained Unit Commitment With Battery Energy Storage.” In: *IEEE Transactions on Power Systems* 31.6 (Nov. 2016). Conference Name: IEEE Transactions on Power Systems, pp. 5115–5125.

[180] S Mashayekh, M Stadler, G Cardoso, and M Heleno. “A mixed integer linear programming approach for optimal DER portfolio, sizing, and placement in multi-energy microgrids.” In: *Applied Energy* 187 (Feb. 2017), pp. 154–168.

[181] K Anoune, M Bouya, A Astito, and AB Abdellah. “Sizing methods and optimization techniques for PV-wind based hybrid renewable energy system: A review.” In: *Renewable and Sustainable Energy Reviews* 93 (Oct. 2018), pp. 652–673.

[182] S Sinha and S Chandel. “Review of software tools for hybrid renewable energy systems.” In: *Renewable and Sustainable Energy Reviews* 32 (Apr. 2014), pp. 192–205.

[183] J Lian, Y Zhang, C Ma, Y Yang, and E Chaima. “A review on recent sizing methodologies of hybrid renewable energy systems.” In: *Energy Conversion and Management* 199 (Nov. 1, 2019), p. 112027.

[184] L Riboldi, EF Alves, M Pilarczyk, E Tedeschi, and LO Nord. “Optimal Design of a Hybrid Energy System for the Supply of Clean and Stable Energy to Offshore Installations.” In: *Frontiers in Energy Research* 8 (2020). Publisher: Frontiers.

[185] R Rigo-Mariani, B Sareni, and X Roboam. “Integrated Optimal Design of a Smart Microgrid With Storage.” In: *IEEE Transactions on Smart Grid* 8.4 (July 2017). Conference Name: IEEE Transactions on Smart Grid, pp. 1762–1770.

[186] E Cuisinier. “Techno-economic modelling and optimisation methods for the planning of multi-energy systems.” PhD thesis. Université Grenoble Alpes, Dec. 2021.

[187] S Chalil Madathil, E Yamangil, H Nagarajan, A Barnes, R Bent, S Backhaus, SJ Mason, S Mashayekh, and M Stadler. “Resilient Off-Grid Microgrids: Capacity Planning and N-1 Security.” In: *IEEE Transactions on Smart Grid* 9.6 (Nov. 2018), pp. 6511–6521.

[188] S Mashayekh, M Stadler, G Cardoso, M Heleno, SC Madathil, H Nagarajan, R Bent, M Mueller-Stoffels, X Lu, and J Wang. “Security-Constrained Design of Isolated Multi-Energy Microgrids.” In: *IEEE Transactions on Power Systems* 33.3 (May 2018), pp. 2452–2462.

[189] V Krakowski. “Intégration du renouvelable et stratégie de déploiement du réseau électrique: réconciliation d’échelles spatio-temporelles dans des exercices prospectifs de long terme.” PhD thesis. Paris Sciences et Lettres, 2016.

[190] M Drouineau, N Maïzi, and V Mazauric. “Impacts of intermittent sources on the quality of power supply: The key role of reliability indicators.” In: *Applied Energy* 116 (Mar. 1, 2014), pp. 333–343.

[191] T Schittekatte, M Stadler, G Cardoso, S Mashayekh, and N Sankar. “The Impact of Short-Term Stochastic Variability in Solar Irradiance on Optimal Microgrid Design.” In: *IEEE Transactions on Smart Grid* 9.3 (May 2018), pp. 1647–1656.

[192] P Mathiesen, M Stadler, J Kleissl, and Z Pecenak. “Techno-economic optimization of islanded microgrids considering intra-hour variability.” In: *Applied Energy* 304 (Dec. 15, 2021), p. 117777.

[193] A Khodaei, S Bahramirad, and M Shahidehpour. “Microgrid Planning Under Uncertainty.” In: *IEEE Transactions on Power Systems* 30.5 (Sept. 2015). Conference Name: IEEE Transactions on Power Systems, pp. 2417–2425.

[194] A Billionnet, MC Costa, and PL Poirion. “Robust optimal sizing of a hybrid energy stand-alone system.” In: *European Journal of Operational Research* 254.2 (Oct. 16, 2016), pp. 565–575.

[195] P Gabrielli, F Fürer, G Mavromatidis, and M Mazzotti. “Robust and optimal design of multi-energy systems with seasonal storage through uncertainty analysis.” In: *Applied Energy* 238 (Mar. 15, 2019), pp. 1192–1210.

[196] L Polleux, t schuhler, G Guerassimoff, JP Marmorat, and J Sandoval-Moreno. "Increasing the accuracy of PV plants and power system dynamic models: a comparison of benefits for battery capacity sizing." In: *12th International Conference on Applied Energy (ICAE2020)*. Bangkok, Thailand, Dec. 2020.

[197] L Polleux, T Schuhler, G Guerassimoff, JP Marmorat, J Sandoval-Moreno, and S Ghazouani. "On the relationship between battery power capacity sizing and solar variability scenarios for industrial off-grid power plants." In: *Applied Energy* 302 (Nov. 15, 2021), p. 117553.

[198] J Stein, C Hansen, and M Reno. *Global horizontal irradiance clear sky models : implementation and analysis.* SAND2012-2389, 1039404. Mar. 1, 2012, SAND2012–2389, 1039404.

[199] K Lappalainen and S Valkealahti. "Recognition and modelling of irradiance transitions caused by moving clouds." In: *Solar Energy* 112 (Feb. 1, 2015), pp. 55–67.

[200] M Lave, MJ Reno, and RJ Broderick. "Characterizing local high-frequency solar variability and its impact to distribution studies." In: *Solar Energy* 118 (Aug. 1, 2015), pp. 327–337.

[201] M Lave and J Kleissl. "Cloud speed impact on solar variability scaling – Application to the wavelet variability model." In: *Solar Energy* 91 (May 1, 2013), pp. 11–21.

[202] K Fahy, M Stadler, ZK Pecenak, and J Kleissl. "Input data reduction for microgrid sizing and energy cost modeling: Representative days and demand charges." In: *Journal of Renewable and Sustainable Energy* 11.6 (Nov. 1, 2019). Publisher: American Institute of Physics, p. 065301.

[203] CS Lai, Y Jia, MD McCulloch, and Z Xu. "Daily Clearness Index Profiles Cluster Analysis for Photovoltaic System." In: *IEEE Transactions on Industrial Informatics* 13.5 (Oct. 2017). Conference Name: IEEE Transactions on Industrial Informatics, pp. 2322–2332.

[204] J Zhao, C Wan, Z Xu, and J Li. "Impacts of large-scale photovoltaic generation penetration on power system spinning reserve allocation." In: *2016 IEEE Power and Energy Society General Meeting (PESGM)*. 2016 IEEE Power and Energy Society General Meeting (PESGM). ISSN: 1944-9933. July 2016, pp. 1–5.

[205] F Domínguez-Muñoz, JM Cejudo-López, A Carrillo-Andrés, and M Gallardo-Salazar. "Selection of typical demand days for CHP optimization." In: *Energy and Buildings* 43.11 (Nov. 1, 2011), pp. 3036–3043.

[206] F LEMONNIER. *Développements pour l'aggregation externe - Théorème de Carathéodory.*

[207] A Makibar, L Narvarte, and E Lorenzo. "On the relation between battery size and PV power ramp rate limitation." In: *Solar Energy* 142 (Jan. 15, 2017), pp. 182–193.

[208] W F. Holmgren, C W. Hansen, and M A. Mikofski. "pvlib python: a python package for modeling solar energy systems." In: *Journal of Open Source Software* 3.29 (Sept. 7, 2018), p. 884.

[209] M Simulink. *Model dynamics of three-phase round-rotor or salient-pole synchronous machine using standard parameters in pu units - Simulink - MathWorks France*. URL: `https://fr.mathworks.com/help/physmod/sps/powersys/ref/synchronousmachinepustandard.html?s_tid=doc_ta` (visited on 03/02/2022).

[210] Y Wen, W Li, G Huang, and X Liu. "Frequency Dynamics Constrained Unit Commitment With Battery Energy Storage." In: *IEEE Transactions on Power Systems* 31.6 (Nov. 2016). Conference Name: IEEE Transactions on Power Systems, pp. 5115–5125.

[211] O Abrishambaf, P Faria, L Gomes, J Spínola, Z Vale, and JM Corchado. "Implementation of a Real-Time Microgrid Simulation Platform Based on Centralized and Distributed Management." In: *Energies* 10.6 (June 2017). Number: 6 Publisher: Multidisciplinary Digital Publishing Institute, p. 806.

[212] EF Alves, G Bergna, DI Brandao, and E Tedeschi. "Sufficient Conditions for Robust Frequency Stability of AC Power Systems." In: *IEEE Transactions on Power Systems* (2020). Conference Name: IEEE Transactions on Power Systems, pp. 1–1.

[213] S Mashayekh, M Stadler, G Cardoso, M Heleno, SC Madathil, H Nagarajan, R Bent, M Mueller-Stoffels, X Lu, and J Wang. "Security-Constrained Design of Isolated Multi-Energy Microgrids." In: *IEEE Transactions on Power Systems* 33.3 (May 2018), pp. 2452–2462.

[214] IRENA. *Utility-scale batteries – Innovation Landscape Brief*. 2019, p. 24.

[215] "Renewable Power Generation Costs 2020." In: (2020), p. 180.

[216] GC Wang, B Kurtz, JL Bosch, i de la Parra, and J Kleissl. "Maximum expected ramp rates using cloud speed sensor measurements." In: *Journal of Renewable and Sustainable Energy* 12.5 (Sept. 2020), p. 056302.

COLOPHON

This document was typeset using the typographical look-and-feel `classicthesis` developed by André Miede and Ivo Pletikosić. The style was inspired by Robert Bringhurst's seminal book on typography "*The Elements of Typographic Style*".

Final Version as of February 26, 2023 (V1.0).

RÉSUMÉ

L'intégration de centrales photovoltaïques dans les réseaux électriques industriels hors réseau pose de nouveaux défis liés à la variabilité de l'ensoleillement. La planification des micro-réseaux industriels doit désormais tenir compte de la relation entre la pénétration des énergies renouvelables, la variabilité court terme et la qualité de la fourniture électrique.

Cette thèse vise à intégrer la variabilité court-terme de l'ensoleillement dans le processus d'optimisation des micro-réseaux industriels. Dans un premier temps, une procédure d'analyse de la variabilité des séries temporelles d'ensoleillement est proposée. Ensuite, la performance des stratégies de gestion optimale est évaluée grâce à un cadre de simulation composé d'une couche d'optimisation couplée à un modèle électrique dynamique. Enfin, un problème de dimensionnement optimal et robuste est formulé. Il assure à la fois la résilience face au passage nuageux et aux pannes des générateurs fossiles.

MOTS CLÉS

Optimisation, Energie photovoltaïque, Mathématiques appliquées, Systèmes électriques

ABSTRACT

The integration of a large-scale solar power plant in off-grid industrial power systems brings new challenges related to the short-term variability. The long-term planning and management of industrial microgrids must now consider the relationship between renewable penetration, short-term variability, and power quality.

This thesis aims to integrate the short-term solar photovoltaic variability in the optimization process of off-grid industrial microgrids. To ensure the resiliency of the grid against renewable variation, a procedure for the variability analysis of irradiance time series is proposed. Then, the performance of optimal management strategies is evaluated thanks to a multi-layer simulation framework that reproduces scheduling decisions and power quality control. Finally, optimal and robust sizing of the power plant is performed and ensures both resiliency to cloud passage and to fossil generators contingencies.

KEYWORDS

Optimization, Solar Energy, Applied Mathematics, Power systems